

NAVAL POSTGRADUATE SCHOOL

Monterey, California



DISSERTATION

DTIC QUALITY INSPECTED 4

**INVESTIGATION OF THE EFFECT OF TWO-
DIMENSIONAL CAVITIES ON BOUNDARY
LAYERS IN AN ADVERSE PRESSURE
GRADIENT**

By

Richard J. Margason

March 1996

Dissertation Supervisor:

Max F. Platzer

Approved for public release; distribution is unlimited

19960705 081

REPORT DOCUMENTATION PAGE

Form Approved
OMB No. 0704-0188

Public reporting burden for this collection of information is estimated to average 1 hour per response, including the time for reviewing instructions, searching existing data sources, gathering and maintaining the data needed, and completing and reviewing the collection of information. Send comments regarding this burden estimate or any other aspect of this collection of information, including suggestions for reducing this burden, to Washington Headquarters Services, Directorate for Information Operations and Reports, 1215 Jefferson Davis Highway, Suite 1204, Arlington, VA 22202-4302, and to the Office of Management and Budget, Paperwork Reduction Project (0704-0188), Washington, DC 20503.

1. AGENCY USE ONLY (Leave blank)

2. REPORT DATE

March 1996

3. REPORT TYPE AND DATES COVERED

Ph.D. Dissertation

4. TITLE AND SUBTITLE

INVESTIGATION OF THE EFFECT OF TWO-DIMENSIONAL CAVITIES ON BOUNDARY LAYERS IN AN ADVERSE PRESSURE GRADIENT

5. FUNDING NUMBERS

6. AUTHOR(S)

Margason, Richard J.

7. PERFORMING ORGANIZATION NAME(S) AND ADDRESS(ES)

Naval Postgraduate School
Monterey, CA 93943-5000 and
NASA Ames Research Center
Moffett Field, CA 94035-1000

8. PERFORMING ORGANIZATION
REPORT NUMBER

9. SPONSORING/MONITORING AGENCY NAME(S) AND ADDRESS(ES)

10. SPONSORING/MONITORING
AGENCY REPORT NUMBER

11. SUPPLEMENTARY NOTES

The views expressed in this thesis are those of the author and do not reflect the official policy or position of the Department of Defense or the U.S. Government

12a. DISTRIBUTION / AVAILABILITY STATEMENT

Approved for public release; distribution is unlimited.

12b. DISTRIBUTION CODE

13. ABSTRACT (Maximum 200 words)

The present investigation evaluated one aspect of the feasibility of the use of multiple cavities as an airfoil high-lift device. The effects of cavities on the boundary layer characteristics in several pressure gradients were determined experimentally and computationally. Experimentally, it was found that up to four cavities could be deployed with only a small change to the boundary layer profiles downstream of the cavities and without significantly modifying the resultant streamwise pressure distribution. From the computational results for both of the wind tunnel test section lengths used in the experimental investigation, it was found that a grid which provided a converged solution in less than a few hundred iterations was needed before a reasonable comparison with experimental data could be obtained. It was also found for these converged solutions that the appropriate grid clustering and density as well as the cell size required for a satisfactory solution was not always apparent before comparing computational results with experimental data. Overall, the investigation results show that a multiple cavity high-lift concept may be feasible.

14. SUBJECT TERMS

MULTIPLE CAVITY HIGH LIFT CONCEPT, HIGH LIFT, CAVITY, BOUNDARY LAYER, PRESSURE GRADIENT

15. NUMBER OF PAGES

287

16. PRICE CODE

17. SECURITY CLASSIFICATION
OF REPORT

Unclassified

18. SECURITY CLASSIFICATION
OF THIS PAGE

Unclassified

19. SECURITY CLASSIFICATION
OF ABSTRACT

Unclassified

20. LIMITATION OF ABSTRACT

UL

Approved for public release; distribution is unlimited.

**INVESTIGATION OF THE EFFECT OF TWO-DIMENSIONAL CAVITIES
ON BOUNDARY LAYERS IN AN ADVERSE PRESSURE GRADIENT**

Richard J. Margason

Aeronautical Engineer, National Aeronautics and Space Administration

B.S., San Jose State University, 1960

M.S., Virginia Polytechnic Institute and State University, 1968

Submitted in partial fulfillment of the
requirements for the degree of

DOCTOR OF PHILOSOPHY IN AERONAUTICAL ENGINEERING

from the

NAVAL POSTGRADUATE SCHOOL

March 1996

Author: *Richard J. Margason*
Richard J. Margason

Approved by:

Raymond P. Shreeve
Raymond P. Shreeve
Professor of Aeronautics and
Astronautics

Knox P. Millsaps
Knox Millsaps,
Assistant Professor of Mechanical
Engineering

Beny Neta
Beny Neta
Professor of Mathematics

Max F. Platzer
Max F. Platzer
Distinguished Professor of
Aeronautics and Astronautics
Dissertation Supervisor

Daniel J. Collins
Daniel J. Collins
Professor of Aeronautics and
Astronautics

Approved by:

Daniel J. Collins

Daniel J. Collins, Chairman, Department of Aeronautics and Astronautics

Approved by:

Maurice D. Weir
Maurice D. Weir, Associate Provost for Instruction

ABSTRACT

Investigation of the Effect of Two-Dimensional Cavities on Boundary Layers in an Adverse Pressure Gradient

by

Richard J. Margason

The present investigation evaluated one aspect of the feasibility of the use of multiple cavities as an airfoil high-lift device. The effects of cavities on the boundary layer characteristics in several pressure gradients were determined experimentally and computationally. Experimentally, it was found that up to four cavities could be deployed with only a small change to the boundary layer profiles downstream of the cavities and without significantly modifying the resultant streamwise pressure distribution. From the computational results for both of the wind tunnel test section lengths used in the experimental investigation, it was found that a grid which provided a converged solution in less than a few hundred iterations was needed before a reasonable comparison with experimental data could be obtained. It was also found for these converged solutions that the appropriate grid clustering and density as well as the cell size required for a satisfactory solution was not always apparent before comparing computational results with experimental data. Overall, the investigation results show that a multiple cavity high-lift concept may be feasible.

TABLE OF CONTENTS

I. INTRODUCTION	1
II. PREVIOUS CAVITY FLOW RESEARCH	5
A. MEAN FLOW CHARACTERISTICS	6
B. FLOW INDUCED OSCILLATIONS	12
C. CAVITY DRAG	24
D. NUMERICAL PREDICTIONS	29
E. MULTIPLE CAVITIES	35
III. EXPERIMENTAL PROCEDURE AND RESULTS	45
A. WIND TUNNEL AND APPARATUS	45
1. Wind Tunnel	45
2. Test Hardware	52
a. Single and Multiple Cavity Hardware	52
b. Traverse	53
c. Boundary Layer Probe	55
d. Computer and Data Acquisition System.....	56
B. WIND TUNNEL RESULTS	68
1. Test Section Boundary Layer	68
a. Zero Longitudinal Pressure Gradient	68
b. Adverse Pressure Gradient	82
2. Open Cavity Configurations	105
a. Effects on the Boundary Layer Characteristics.....	105
b. Effects on the Surface Pressure Distribution.....	108
3. Cavity With a Door	147
IV. INCOMPRESSIBLE NAVIER-STOKES COMPUTATIONS	155
A. INCOMPRESSIBLE NAVIER-STOKES CODE	157
B. GRID GENERATION	159
C. CFD RESULTS	164
1. Wind Tunnel Flow Computation	165
a. 24 Inch Test Section	165
b. 120 Inch Test Section	172
2. Driven Cavity Computations	177
3. Open Cavity Flow Computations	180

V. CONCLUSIONS AND RECOMMENDATIONS	185
REFERENCES	189
APPENDIX A - TEST RUN SCHEDULE	199
APPENDIX B - SURFACE PRESSURE TAP LOCATIONS	211
APPENDIX C - CAVITY PRESSURES	217
APPENDIX D - BOUNDARY-LAYER PROFILES	247
INITIAL DISTRIBUTION LIST	269

NOMENCLATURE

a	freestream speed of sound, ft/s
A	test section cross-section flow area, ft ² ; elemental area, ft ²
AR	wing aspect ratio, b ² /S
b	wing span, ft
bc	boundary condition
BL	experimental boundary-layer data run
c	airfoil chord, ft; speed of sound, ft/s
c _f	local skin-friction coefficient, $c_f = \frac{\tau}{q} = \frac{2\tau}{\rho U^2}$
c _p , C _p	pressure coefficient, (p _l -p _∞)/q
C _f	local skin-friction coefficient integrated over a specified distance
C ₁	constant of integration in the log law equation, $U^+ = \frac{1}{\kappa} \ln(y^+) + C_1$
C _D	drag coefficient, D/qS
C _F	cavity drag or friction coefficient, D/qLW
C _L	lift coefficient, L/qS
CFD	computational fluid dynamics
CP	experimental pressure coefficient data run
D	cavity depth, ft; drag force, lbf; or body diameter, ft; finite difference delta term
D, E, F	convection terms in the incompressible Navier-Stokes equations
e	span efficiency, from $1/\pi AR e$
f	frequency, 1/s
FLIC	fluid-in-cell method
G	ratio of first universal moment to the second universal moment, $\int_0^\infty \left(\frac{U-u}{u^*} \right)^2 d(y/\Delta)$
GFLOP	billion floating-point-operations per second
GUI	graphic user interface

h	step height or tunnel height, ft
H	von Kármán shape factor, δ_1/δ_2
ins2d	incompressible two-dimensional Navier-Stokes code
I	identity vector
J	Jacobian
k	speed of vortices over a cavity ratioed to freestream velocity
K	ratio of convection velocity of vortices to freestream velocity
l,l	length or mixing length, ft; local
L	length, cavity length, or run length, ft; or lift force, lbf
m	mode number for the peak amplitude frequency in the cavity, m_a+m_v , integer
m_a	complete wavelengths of acoustic radiation, integer
m_v	complete wavelengths of vortex motion, integer
M	Mach number, U/a
MB	million bytes
MHz	million Hertz, 1/ sec
MW	million words
n	number of cavities
N	number of wavelengths of the fundamental frequency contained by the cavity length, integer
NC	number of grid points in a given direction
N_S	Strouhal number, equation 1
p,P	pressure, lb/ft ²
PMARC	panel method - Ames Research Center
q	dynamic pressure, lbf/ft ²
ram	random access memory
R	run number; residual vector
Re, R_x	Reynolds number, $\rho U_x / \mu$
R_y	Reynolds number, $\rho U_y / \mu$
$R_{uu}(\tau)$	autocorrelation between two velocity measurements separated by time τ
S	reference area or wing area, ft ²
SF	tangential grid spacing scale factor
SJSU	San Jose State University

SV	scanivalve
t	time, s
t'	cycle time between arrivals of a specified phase of acoustic radiation at the front cavity wall lip just as a shear layer vortex leaves, s
T	temperature, °F
u, v, \bar{u} , \bar{v}	time-averaged local streamwise or normal velocity components, ft/s
u', v'	fluctuating streamwise or normal velocity components, ft/s
u*	friction velocity, $\sqrt{\tau/\rho}$, ft/s
U, V	velocity, ft/s
U _c	phase velocity of fundamental frequency, ft/s
U ⁺	non-dimensional inner layer velocity, u/u*
w	Coles universal wake function, equation 32
W	cavity width (spanwise in a tunnel), ft
x, y, z	distance in the X, Y, or Z directions, ft
X, Y, Z	Cartesian axis system
\bar{x}	normalized grid dimension in the x direction
y _{org}	initial upstream y coordinate, ft
y ⁺	non-dimensional inner layer distance normal to the wall, yu*/ν
\bar{y}	normalized grid dimension in the y direction, y/h
α	constant of proportionality in acoustic frequency relation, f =
α/L,	ft/s; angle-of-attack or diffuser angle, deg.; grid refinement factor, equation 36.
β	Clauser equilibrium parameter, $\frac{\delta_1}{\tau_0} \frac{dp}{dx}$; Robert's transformation stretching parameter, equation 36; pseudocompressibility constant, equation 30.
δ	boundary-layer thickness where u = 0.99 U _e , ft
δ ₁	boundary-layer displacement thickness, $\int_0^\infty \left(1 - \frac{u}{U_\infty}\right) dy$, ft
δ ₂	boundary-layer momentum thickness, $\int_0^\infty \frac{u}{U_\infty} \left(1 - \frac{u}{U_\infty}\right) dy$, ft

$\delta\eta$	uniform grid spacing before transformation to physical space
Δ	Clauser defect thickness, i.e.: the first universal moment about $\zeta = 0$, $-\delta \int_0^\infty f(\eta) d\eta$
ϕ	phase difference between two probes, s; test section diffuser angle, deg. η grid dimension before transformation to physical space
γ	time lag factor to account for the time increment between the passage of a vortex and the emission of a sound pulse at the downstream cavity edge, s
η	grid dimension before transformation to physical space
κ	von Kármán constant used in log-law equation, $U^+ = \frac{1}{\kappa} \ln(y^+) + C_1$
λ	wavelength, ft
λ_a	cavity sound wave length, ft
λ_v	vortex spacing over a cavity, ft
Λ	wing sweep, deg.
μ	coefficient of viscosity, lbf-s/ft ²
ρ	density, lbf-s/ft ⁴
Π	Coles wake parameter, $0.8(\beta + 0.5)^{0.75}$
ζ, η	Clauser non-dimensional variables, $(u - U)/u^*$ and y/δ
τ	shear stress, lbf/ft ² ; time increment, s
ν	kinematic viscosity, μ/ρ , ft ² /s
Ω	velocity boundary condition vector, equation 33
ψ	stream function

subscripts:

a	acoustic radiation
atm	atmospheric
c	calculated
D	diameter
e	boundary-layer edge
g.c.	cavity geometric center
i	step

l, l	laminar, local, or length
L	cavity length
m, min	minimum
max	maximum
M	momentum
n	cavity number
o	wall or flat plate; initial value or location
p	pitot probe
P	pressure
ref	reference
s	static
surf	tunnel surface
S	shear stress
t	turbulent; or total
tun	tunnel
v	vortex motion; viscous
v.c.	cavity vortex center
x	streamwise
y	normal to the wall
1, 2, ...	stations; positions
∞	freestream

superscript:

n	pseudotime step
---	-----------------

ACKNOWLEDGEMENTS

The research topic was conceived by Professor Max Platzer and supported by both the Naval Postgraduate School and the NASA Ames Research Center. In addition to the direction and support of Dr. Platzer, the author is grateful to his NASA supervisor, Dr. Larry E. Olson, for making available the needed time and NASA resources used for this investigation. The San Jose State University (SJSU) low speed wind tunnel was made available for the experimental investigation by Dr. Dick Desautel and Dr. Nikos Mourtos. The experimental data were acquired using NASA owned instrumentation, a desktop computer, and a LABVIEW data acquisition system which was programmed by Douglas A. Wardwell. A former SJSU student, Gino Paglia, volunteered many hours over two and a half years to help build the test hardware, calibrate the instrumentation, conduct the test, reduce and evaluate the experimental data, and prepare the data Appendices. His strong interest and desire to participate provided a needed stimulus to get me on the ball and get this thing done. Additional help for the input data preparation and computations using the ins2d Navier-Stokes code were provided by its author, Dr. Stuart E. Rogers. The continuing beneficial interaction with two former NPS students, Bob VanDyken and Jerry Higman, is also acknowledged. The most important understanding and support was provided by my partner in life and loving wife, Jennifer. She provided vital encouragement and has made it possible for me to spend many more hours over the course of this effort than I originally anticipated.

I. INTRODUCTION

Aircraft wings are usually sized by their cruise requirements which occur at a relatively low lift coefficient. The increased lift coefficient needed for low-speed flight, including take-off and landing, usually requires the deployment of high-lift devices. These devices increase either wing area and/or lift coefficient at a given angle-of-attack. Several examples of high-lift devices are shown in Figure 1. Most modern aircraft use slats and flaps (Figure 1(a)) which extend to increase wing area and deflect to increase camber (i.e., lift coefficient). Additionally, less conventional high-lift concepts include trailing-edge tabs (Figure 1(b)), variable-camber airfoils (Figure 1(c)), and spanwise blowing. The pressure coefficient on airfoils typically has a favorable gradient from flow stagnation location near the leading edge to the minimum negative pressure coefficient peak which is usually located several percent of the chord length from the leading edge.

For high-lift conditions, the pressure coefficient rises from the negative pressure peak back to the ambient static pressure near the trailing edge. This is the adverse pressure-gradient region ($dp/dx > 0$). If the pressure gradient is too large the lift is reduced because the flow will separate on the wing upper surface and the suction pressure peak is reduced and moves toward the leading edge. A cavity or multiple cavities could be useful in delaying separation to a more adverse pressure gradient. The usefulness of multiple cavities for maintaining attached flow in an adverse pressure gradient is determined by their effect on the viscous flow in the boundary layer downstream of the cavities. Maintenance of attached flow requires that the flow over the cavities and downstream of them retain enough momentum to overcome the loss due to an adverse pressure gradient, shear layer flow gradients, and viscous dissipation. The effects are greater near the wall because of the reduced velocity near the surface. If the velocity at the wall is reduced to zero the flow separates and produces flow forward, opposite the freestream direction. As a result, boundary layer assumptions are no longer valid.

High-lift aerodynamics has been the subject of numerous investigations as described in a classic review by A. M. O. Smith [Ref. 1] about twenty years ago. This review described conventional high-lift devices and included a list of the ten

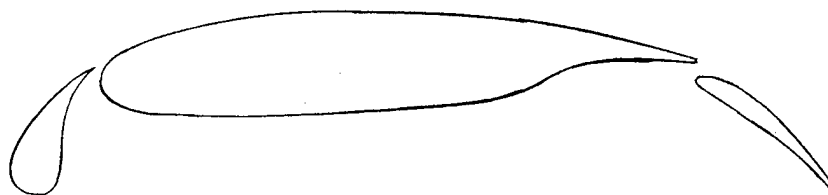
most important basic theoretical problems of high-lift aerodynamics. The list emphasized development of computational methods capable of representing three-dimensional flow with boundary-layer separation and merging multi-element airfoil boundary layers. There have been many experimental investigations and applications of computational methods to high-lift aerodynamics during the past twenty years. As a consequence, there has been significant progress toward the solution of the basic research needs listed by Smith. Additionally, the review indicated the need for new "inventions" such as spanwise blowing and trapped-vortex concepts to provide improved lifting-surface flow control.

There have been several attempts to develop the trapped-vortex concept. Even Leonardo da Vinci observed and sketched very realistic recirculating eddies due to a bluff obstacle (or spoiler) in the fifteenth century. Recently it was suggested [Ref. 2] that several spoilers located at different chordwise locations could be deployed to form several cavities in the chordwise direction (Figure 1(d)). This may provide a means of increasing upper surface camber and thereby increase wing lift. The spoilers could be deployed as a high-lift device for steady flow conditions. In other scenarios, the spoilers could be deployed either for transient maneuvers of a combat aircraft at high angles-of-attack or for increasing the lift of a retreating rotorcraft blade. In still another application, the sudden opening of a cavity near the leading edge (Figure 1(e)) of a retreating rotorcraft blade may suppress or delay dynamic stall. Cavity flows may also be caused by finned surfaces, windows, bomb bays, landing gear bays, finned heat transfer surfaces, and other surface imperfections. Some cavity flow research has been conducted specifically to study the more general problem of flow separation.

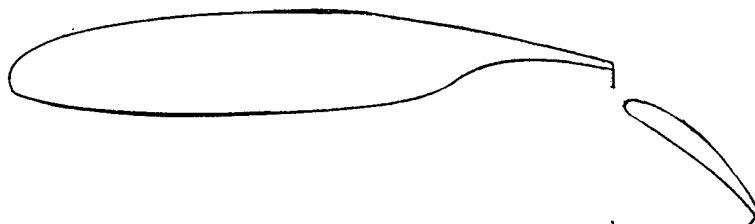
Detailed cavity experiments were first reported in the early 1950's. Since then a large number of investigations of cavity flow have been conducted. This research has most often concentrated on a single, two-dimensional rectangular cavity in a uniform freestream flow with no streamwise static-pressure gradient. A survey of the literature was made to locate investigations of either the effect of cavities on boundary-layer characteristics, especially for high-lift conditions; i.e., in an adverse pressure-gradient. No experimental data were found in the literature search which documented the effect of either adverse pressure gradients or multiple cavities on the boundary-layer development or on the pressure

distributions in or near the cavities. No data for either single or multiple cavities were found which documented their effect on the local flow in the vicinity of the cavities. These effects include the influence of a door or spoiler which closes the cavity opening.

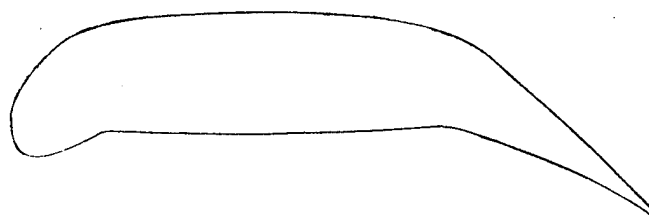
A basic understanding is needed to determine how multiple cavities could be used on an airfoil to either delay flow separation or to increase its camber and obtain an increased lift at a given angle-of-attack with suitable drag characteristics. The present investigation simulated a lifting airfoil using a wind tunnel with test section liners to represent different pressure-gradients which could be associated with an airfoil at selected angles-of-attack. This investigation concentrated on the effect of cavity flow on the attached surface boundary-layer characteristics in adverse pressure-gradients. Conditions where flow separation was present were not considered. The purpose of the present investigation was to experimentally and computationally evaluate the effect of 1, 2, or 4 two-dimensional spanwise cavities with square cross-sections on the boundary-layer characteristics in both a constant pressure flow and for two adverse pressure gradient flows. The experimental investigation was conducted in the San Jose State University (SJSU) 12" by 12" low speed tunnel. Computational results were also obtained using a numerical solution to the incompressible Navier-Stokes equations.



(a) Flap and slat with chord extension.



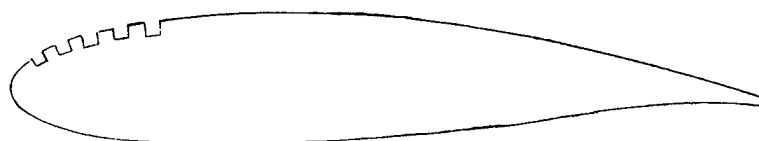
(b) Tabs on airfoil and flap trailing edges.



(c) Variable camber airfoil.



(d) Multiple spoilers used to form multiple cavity concept.



(e) Leading edge cavities to delay dynamic stall.

Figure 1. High lift concepts.

II. PREVIOUS CAVITY FLOW RESEARCH

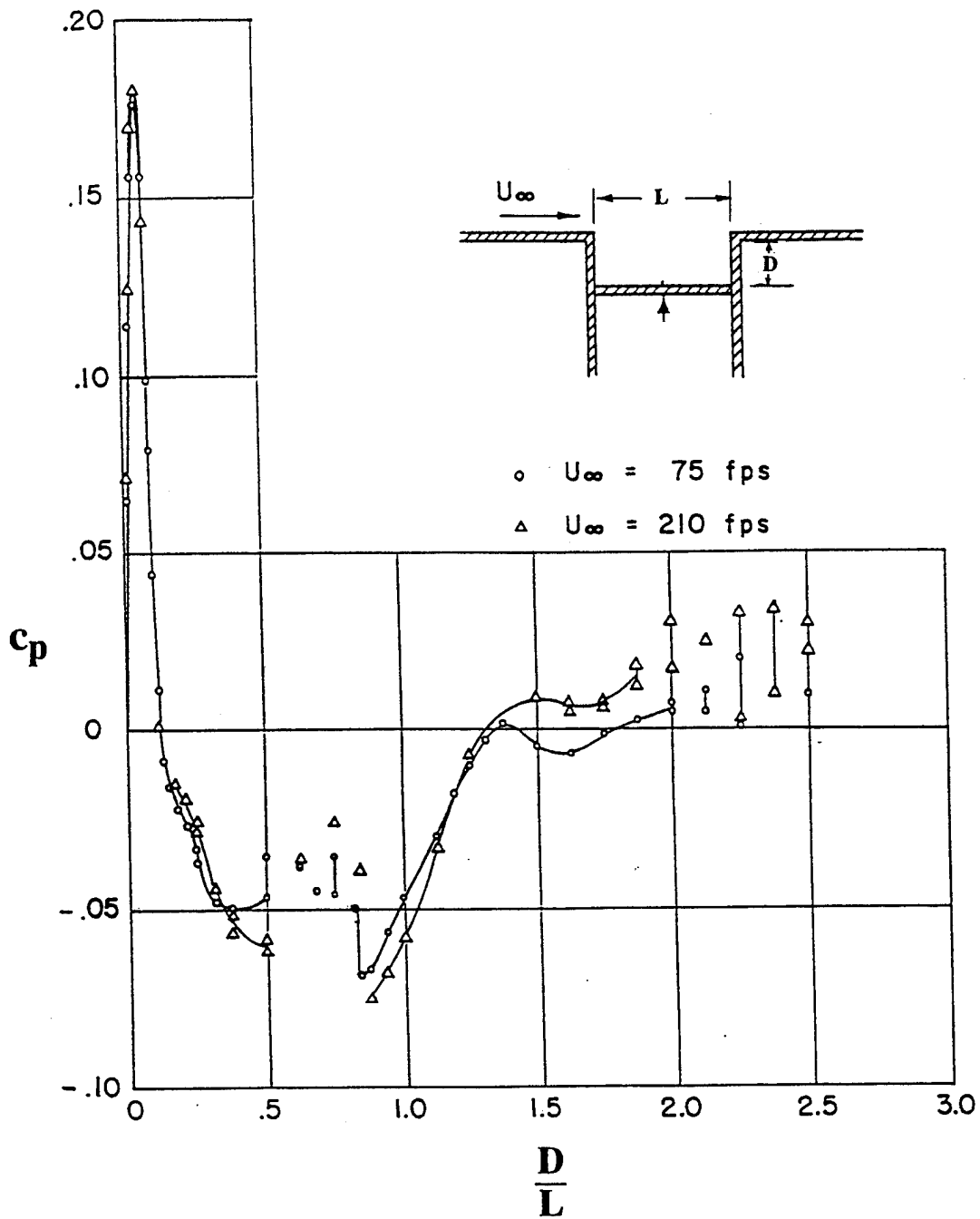
Two-dimensional boundary layers in subsonic flow are well defined as described in a very complete survey paper by Ligrani [Ref. 3] and textbooks such as Schlichting [Ref. 4], White [Ref. 5], and Cebeci and Smith [Ref. 6]. At low Reynolds numbers, i.e. short run lengths, in low-turbulence flow the boundary layer is usually laminar. For high-lift applications, the boundary layer rapidly transitions to a fully turbulent boundary layer whose mean velocity profile may be represented by the $1/7$ power law ($u/U_\infty = (y/d)^{1/7}$). Additional work on boundary layers and the effects of skin friction, adverse pressure gradient, surface roughness, and shear-layer flow are described in References 17 through 31.

Nearly 40 years ago, Roshko [Ref. 32] and Krishnamurty [Ref. 33] conducted two of the first relatively-detailed investigations of cavity flow. These experiments did a good job of identifying the important flow characteristics associated with a single cavity. In the present paper, the cavity streamwise dimension, length, is designated as L ; the dimension normal to the freestream, depth, is D ; and the distance across the tunnel and normal to the flow direction, width, is W . In general, cavity flows exhibit various steady and unsteady phenomena. The upstream boundary layer separates at the cavity lip to form a shear layer over the cavity. The shear layer then reattaches (1) either on the cavity floor or (2) on the downstream cavity wall or downstream of the cavity. The cavity is considered to be closed if the shear layer reattaches on the cavity floor and then recirculates within the upstream end of the cavity. Typically this flow can occur when $L/D > 4$. The cavity is considered to be open when the shear layer reattaches near the rear lip or downstream of the cavity. This flow is typical of deeper cavities where $L/D < 1$. For L/D values between 1 and 4, the d_2/L strongly influences whether a cavity is open or closed. At certain conditions disturbance waves are fed back to the upstream cavity lip, the original disturbance source. This feedback loop can amplify the disturbance waves and create large oscillating pressure waves and noise. In these circumstances the unsteady flow can dominate the cavity flowfield.

A. MEAN FLOW CHARACTERISTICS

Roshko [Ref. 32] used a cavity length L of 4 inches and systematically varied the cavity depth D to study the time-averaged flow at low Mach numbers (0.06 to 0.20) for D/L ranging from 0.02 to 2.50. Pressure coefficients on the cavity walls and floor were measured and the skin-friction coefficients were calculated. The structure of the flow in the cavity was also observed and found to be a function of the cavity depth-to-length ratio D/L . For very shallow cavities ($D/L < 0.1$) the shear layer above the cavity reattached to the cavity floor forming a recirculation region on the upstream corner of the cavity. As the varying cavity D/L approached 1, the shear layer attachment location moved aft along the cavity floor to the rear-wall intersection and up the wall to near its intersection with the freestream surface. For a cavity with a square cross section ($D/L \sim 1$) there was steady flow in a single predominant vortex with secondary vortices in the corners of the cavity. For D/L from 1 to 2.5, a single vortex continued to dominate the cavity flow.

It was concluded that the drag due to the cavity was almost entirely due to the pressure on the cavity walls. The drag contribution from changes in the skin friction coefficient on the cavity surfaces was relatively small. Further, the friction forces on the cavity walls were found to be small compared with the pressure forces. The drag is analyzed in detail in section II.C. While the friction forces due to the cavity vortex were negligible compared to the pressure drag, they do play a role in determining the vortex stability. An indication of this stability is shown in Figure 2(a) by the variation of the pressure coefficient measured at the middle of the cavity floor as the cavity depth was increased from D/L of 0.02 to 2.50. Steady pressures were measured when D/L was less than 0.50 and when D/L was between 0.87 and 2.00. For D/L from 0.50 to 0.87 and $D/L >$



(a) Variation of pressure coefficient measured at the middle of the cavity floor [Ref. 32].

Figure 2. Effect of cavity D/L ratio on local pressure-coefficients.

2.00 the pressures were unsteady. The change from unstable flow to stable flow as D/L was varied through 0.87 was quite distinct. There were two stable states for this range of D/L . When the cavity vortex was steady ($D/L < 0.50$ and $0.87 < D/L < 2.00$), the flow over the cavity was also steady.

A single, stable vortex was formed by the deflection of a portion of the shear layer at the downstream cavity edge into the square cross-section cavity. The relatively high pressure on the cavity wall in that vicinity accounts for most of the drag. The pitot pressure at the top back corner is shown in Figure 2(b). This pressure measurement is analogous to a Preston-tube measurement and it is related to the local skin-friction coefficient. It is intended to give a measure of the pressure near the top of the rear cavity wall. There is an unsteadiness shown for D/L between 0.50 and 0.87. Above D/L of 1 there is a hysteresis which shows that the pressure coefficient is dependent upon whether D is increasing or decreasing. For the square cavity ($L/D = 1$), the skin-friction coefficient was calculated from the boundary-layer profiles with the following results:

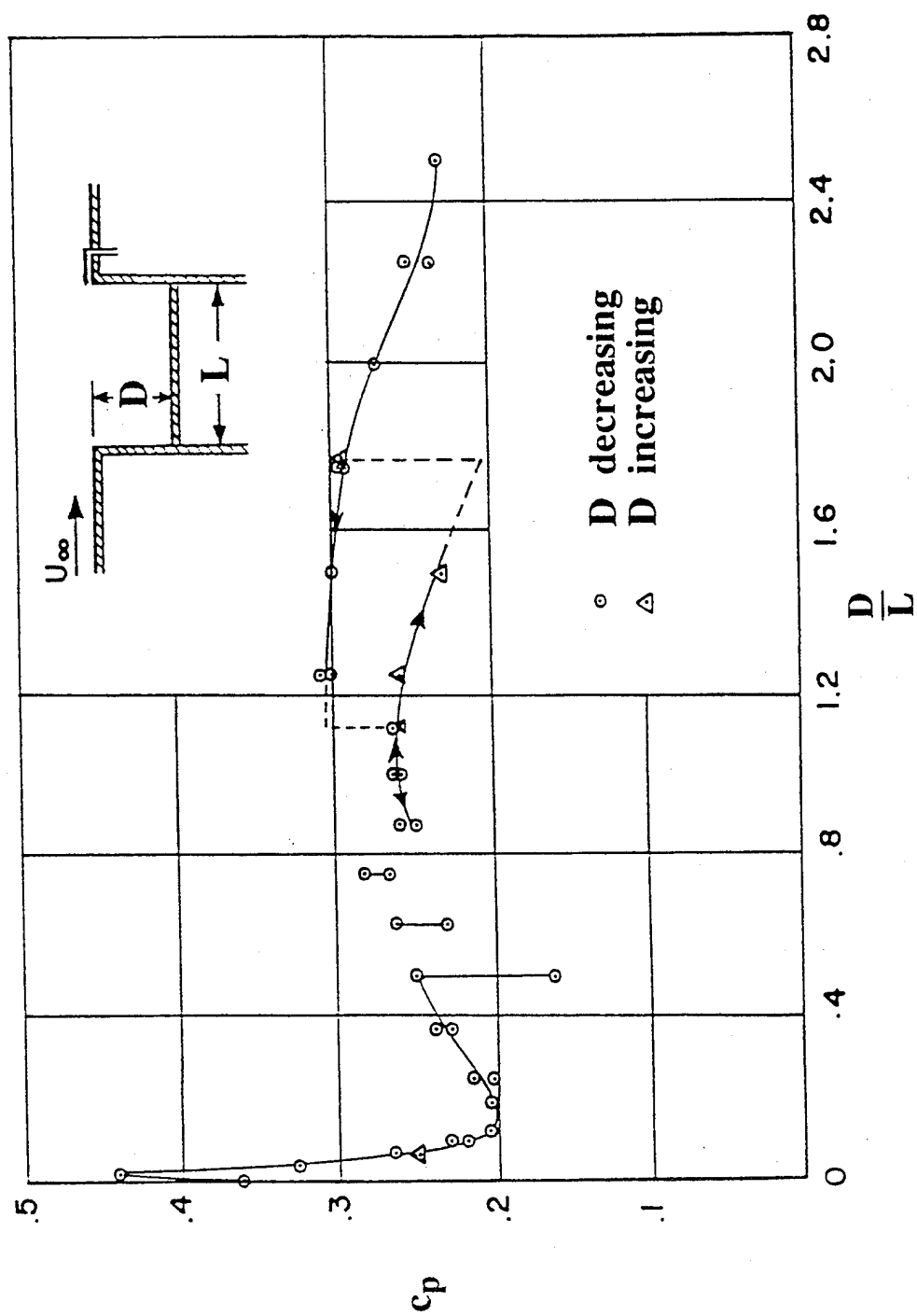
Boundary-Layer Profile Location	c_f
I - 0.375 L upstream of the cavity front wall	0.0015
II - 0.125 L downstream of the cavity rear wall	0.0011
III - 0.375 L downstream of the cavity rear wall	0.0012
IV - 0.375 L downstream of the cavity rear wall location without the cavity in place	0.0014

Another investigation by Maull and East [Ref. 34] studied cavities at low subsonic velocities using oil-flow and surface static-pressure distributions. They found that the flow steadiness depended on cavity width as well as streamwise length and depth. For a cavity width-to-length ratio W/L of 9, a non-uniform spanwise variation of pressure coefficient was most notable below D/L of

0.85 and between D/L of 1.5 to over 2. These regions are roughly consistent with the steadiness of Roshko's pressure coefficient data in Figure 2. There were regions of uniform pressure distribution near D/L of 1 and 2.5. There was a very rapid switch from non-uniform pressure-coefficient variation for $D/L = 0.85$ to a nearly uniform pressure-coefficient distribution for $D/L = 0.86$. These results appeared to also depend on the ratio of boundary-layer thickness to cavity length δ/L .

Rossiter [Ref. 35] investigated the flow over rectangular cavities at subsonic and transonic speeds. The investigation was conducted in a 2' by 1.5' transonic tunnel. The cavity had a 4" width, an 8" length, and a depth which was varied from 0.8 to 8.0 inches. Steady and unsteady pressures were recorded on the cavity floor and downstream of the cavity. While the flow was highly unsteady, it was useful to briefly discuss the nature of the time-average flow over cavities. For very shallow cavities, the flow over the front and rear walls may be considered independently as the flow down and up a step, respectively. The airflow will separate from the front edge and reattach at some point along the floor of the cavity. The pressure in the separated region will be lower than the freestream pressure. This occurs because the freestream flow speeds up as it enters the cavity. Then the pressure rises at the attachment point. As the airflow approaches the rear wall, it is slowed and then the pressure increases until a position is reached where the boundary layer separates to form the boundary layer ahead of the rear wall. The boundary layer will usually reattach at a location downstream of the cavity. As the depth-to-length ratio of the cavity increases, the attachment and separation points on its floor will move closer together until a reverse flow develops between the high pressure region ahead of the rear wall and the low pressure region behind the front wall. A large vortex then forms within the cavity.

As shown by Roshko [Ref. 32] the mean flow pattern depends on the length-to-depth ratio L/D of the cavity. Rossiter compared his data with Roshko's as shown in Figure 3. The results are not directly comparable between these tests because of different length-to-depth ratios and the relatively thicker boundary layer approaching the cavity in Rossiter's investigation. For the very shallow



(b) Pressure coefficient measured at the top back corner of a cavity for a range of depth-to-length ratios [Ref. 32].

Figure 2. Concluded.

cavities ($L/D > 8$) the two pressure rises associated with flow attachment and with separation on the floor of the cavities may be seen. Immediately behind the cavity front wall the pressure reaches a low value. The pressure increases from the center of the closed vortex in the corner at the front wall to the rear end of the vortex. The pressure levels off and then increases again as the downstream wall is approached. At a length-to-depth ratio of 8, the two pressure rises have merged and extend from $x/L \sim 0.4$ to 0.9. At a length-to-depth ratio of 6, the pressure is

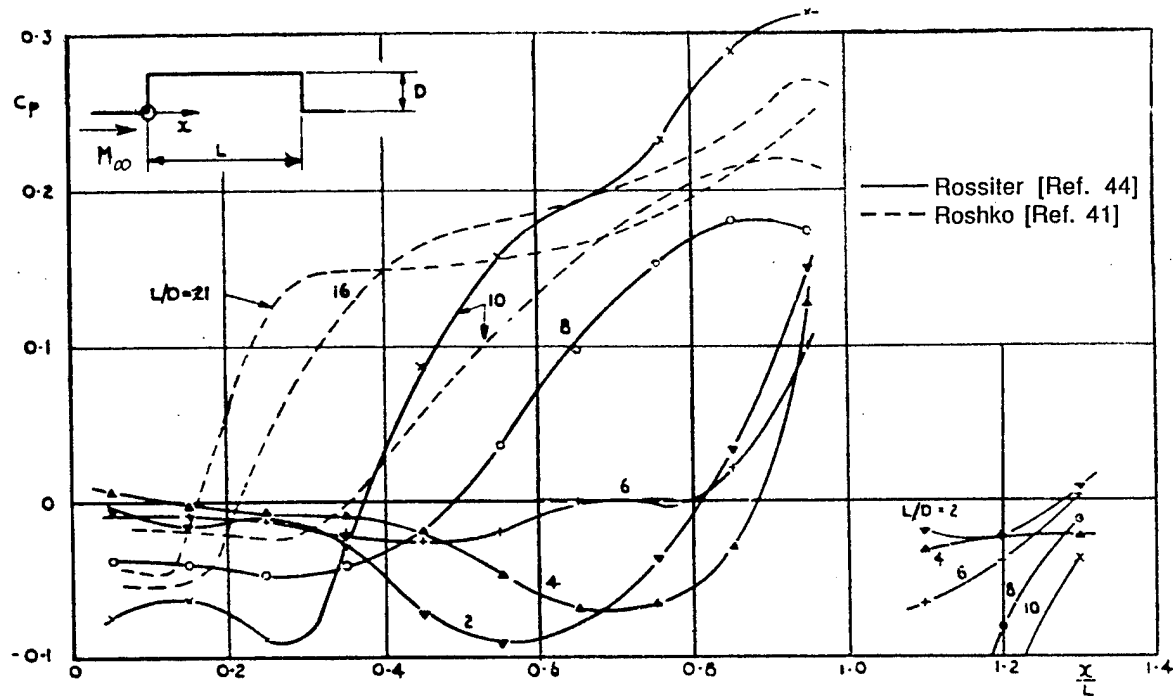


Figure 3. Comparison of Pressure coefficients measured on cavity floors and on the surface downstream of the cavity by Rossiter [Ref. 35] and Roshko [Ref. 32].

almost constant ($C_p \sim -0.02$) along the floor of the cavity indicating that the two separations have combined. For the deeper cavities (L/D of 4 and 2) there is a decrease in the pressure on the floor associated with the high airspeeds at the periphery of the cavity vortex. As Mach number is increased, the flow attachment point on the floor of the shallower cavities moves downstream so that the cavities

become effectively deeper. As a result, the pressure distributions for the shallower cavities show a large variation with Mach number whereas the pressure distributions in the deeper cavities are comparatively independent of Mach number.

Other investigations, such as Charwat et al [Ref. 36 and 37], have studied cavities in supersonic flow and found that the same general flows exist as those found at subsonic speeds. Three-dimensional cavities which relate to landing gear or weapons bays were studied by Plentovich [Ref. 38]. Greater unsteadiness was found at the highest Reynolds number and the pressure distributions were found to be sensitive to the thickness of the boundary layer entering the cavity. Another application of cavities is found in aircraft where telescopes are used for various observations. The objective of the investigation by Buell [Ref. 39] was to minimize the shear-flow disturbance using an antiresonance device. Devices were developed which suppressed cavity shear-flow resonance and produced thinner shear layers. This shear-layer flow suppression enabled better light transmission to the telescope. However, the suppression of resonance also made the boundary layer downstream of the cavity more susceptible to flow separation.

B. FLOW INDUCED OSCILLATIONS

There have been reviews by Rockwell and Naudascher [Ref. 40] and by Komerath, Ahufa, and Chambers [Ref. 41] which emphasize cavity flow-induced oscillations. Both papers used the classification of self-sustaining flow oscillation over cavities first presented by Rockwell and Naudascher and reproduced in Figure 4 from reference 40. Three flow-interaction categories were identified: (1) fluid dynamic, (2) fluid resonant, and (3) fluid elastic. In many situations more than one of these interactions may be involved. The fluid-dynamic interactions involve coupling between oscillations of the shear layer over the cavity with the flow inside the cavity. Many of the oscillating flows at low speeds over shallow cavities ($L/D > 1$) fall under this category. The mechanisms involved are believed to arise from shear-layer instability and vortex shedding. Large-scale coherent

structures present in the shear layer are known to play the major role in such interactions. Fluid-resonant interactions are flow oscillations which appear to be controlled by the acoustic modes of the cavity. These are usually encountered in cavities which have large depths normal to the flow direction ($L/D < 1$). These fluid-resonant oscillations are observed in flows over cavities at high Mach numbers. Fluid-elastic flows involve interactions between the shear layer over the cavity and the elastic boundaries of the cavity. These interactions may cause sonic-fatigue problems.

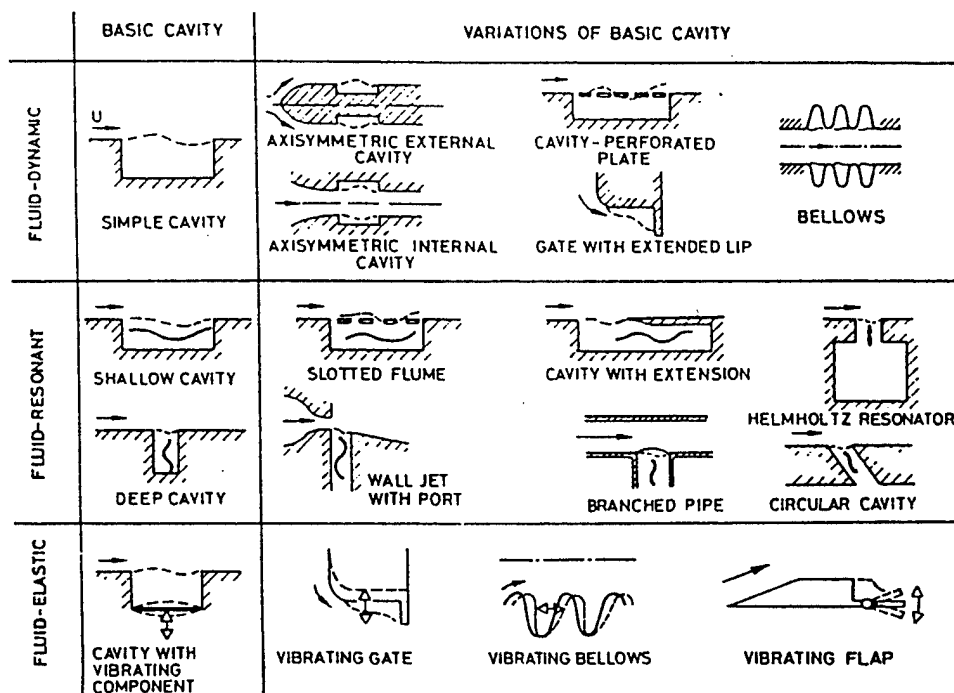


Figure 4. Classification of cavity flows by Rockwell and Naudascher [Ref. 40].

Krishnamurty [Ref. 33] varied the rectangular cavity L/D ratio in a study of the sound radiated by cavity flow. The cavity had a constant depth of 0.1" and was located in a flat plate. A trip wire and the flat-plate angle-of-attack were varied to change the boundary layer from laminar to turbulent. The cavity length was varied from 0 to 2 inches. The investigation was conducted in a blowdown

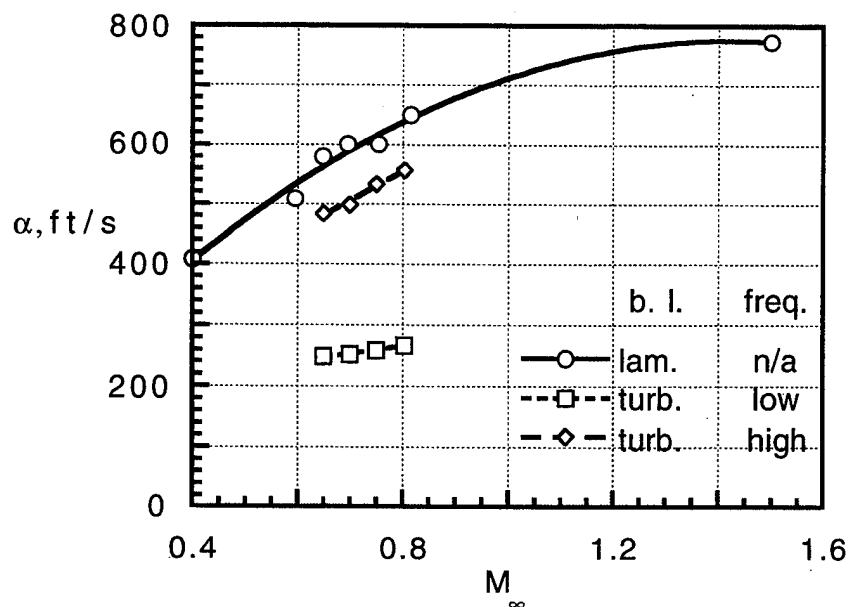
wind tunnel over a Mach number range from 0.4 to 1.5. Data included hot wire measurements of the boundary layer, magnitude and directionality of the radiated sound, as well as, schlieren and interferometer flow visualization. Below a minimum cavity length it was found that the shear layer flowed over the cavity and reattached downstream of the rear cavity wall. For these conditions there were no acoustic oscillations.

Above this cavity length, the acoustic frequency was inversely proportional to the cavity length $f = \alpha / L$. The constant of proportionality α was different for laminar and turbulent boundary layers. This dependence is presented in Figure 5 for both laminar and turbulent boundary layers. While there was a dominant frequency for laminar flow, there were two frequencies, low and high, for the turbulent case. Krishnamurty used Strouhal number to obtain a dimensionless frequency. If the freestream velocity is used as the characteristic velocity, the Strouhal number becomes

$$N_S = f L / U_\infty = \alpha / U_\infty \quad (1)$$

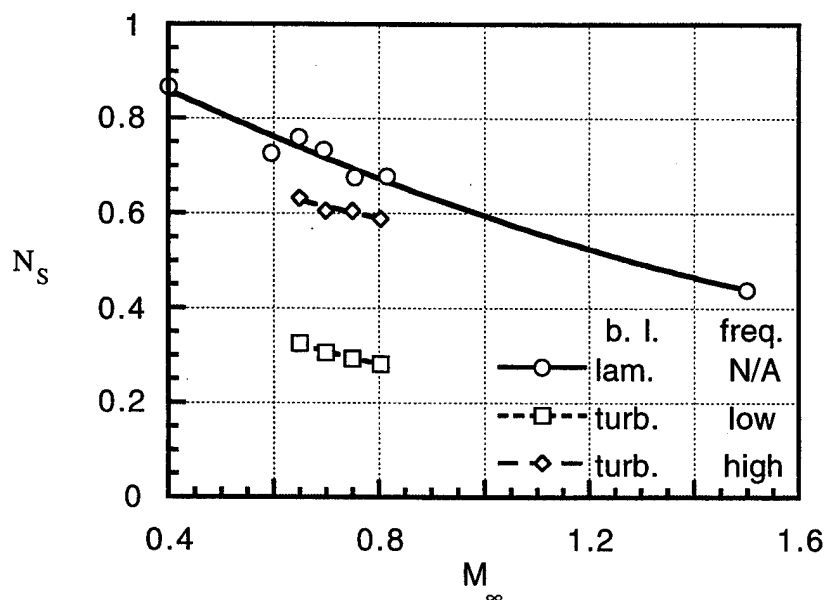
At low Mach numbers there was little sound radiation directionality; at increased Mach numbers the sound became more intense and directional. The radiation pattern was observed using a schlieren system. It was shown that the unsteady pressure oscillations were greater in a laminar boundary layer than in a turbulent boundary layer.

Rossiter [Ref. 35] found that the unsteady pressures contain both random and periodic components. The random component predominates in the shallower cavities ($L/D > 4$) and was most intense near the rear wall. The unsteady pressure had a smooth spectrum over a broad frequency band showing the random character in shallow cavities. For very shallow cavities, a local region of intense pressure fluctuations was found where the shear layer flow attaches to the floor of the



(a) Proportionality constant α .

Figure 5. Effect of Mach number on the acoustic field due to a cavity.



(b) Strouhal number N_S .

Figure 5. Concluded.

cavity. There were usually two peaks of almost equal magnitude. The periodic component predominates in the deeper cavities ($L/D < 4$) and may form standing wave patterns with one peak whose magnitude is much larger than any other. It is suggested that the periodic component is due to an acoustic resonance within the cavity excited by a phenomenon similar to that causing edge-tones. The periodic pressure fluctuations may be very large. Mean values up to 0.35 times the freestream dynamic-pressure were measured. These results indicated the predominance of the periodic component over the random oscillation. Increasing Mach number caused an increased periodic component. The periodic component was reduced in the thicker boundary-layer. This suggests that the lack of periodic pressure fluctuations in shallow cavities is partially due to a large ratio of boundary layer thickness to cavity depth δ/D . This result suggested a means to reduce the magnitude of the pressure fluctuations. The suppression was achieved using a small spoiler located upstream of the cavity to effectively increase the boundary-layer thickness.

In this investigation, Rossiter identified experimentally the principal characteristics of the periodic pressure fluctuations as the following:

- (1) The pressure fluctuations may contain a number of periodic components or modes which occur at specific frequencies and are designated as $m = 1, 2, 3, \dots$
- (2) The frequency of any component is inversely proportional to the cavity length and increases with freestream velocity. Dimensionally this suggests

$$f\left(\frac{U}{L}\right) = g(M, R_e) \quad (2)$$

Over the Reynolds number range investigated it was found that the effect of cavity length was small.

- (3) Shadowgraphs showed that the pressure fluctuations are accompanied by the periodic shedding of vortices from the front lip of the cavity while the principal acoustic source is close to the rear lip of the cavity.

- (4) Under some conditions, standing wave patterns occur in the cavity which are probably due to an acoustic resonance within the cavity.

The regular shedding of vortices found in flow over cavities is a feature of the edge tone phenomenon as well as the strong acoustic-radiation. A connection was assumed between these two acoustic features. Further it was assumed that the acoustic radiation initiates the vortex shedding and that the passage of the vortices over the rear lip of the cavity is responsible for the acoustic radiation. If the average speed of the vortices over the cavity is K times the freestream velocity and sound waves travel upstream in the cavity at a mean velocity c then

$$f = \frac{KU_{\infty}}{\lambda_v} = \frac{c}{\lambda_a} \quad (3)$$

where λ_v was assumed to equal λ_a . The phase relation between the two motions is unknown.

A solution was found by identifying the particular phase of the acoustic radiation which reaches the front lip of the cavity at the instant that a vortex is shed. It is assumed that a vortex is $\gamma \lambda_v$ behind the rear lip when this particular phase of the acoustic radiation leaves the source at the rear lip. It was assumed that there were m_v complete wavelengths of the vortex motion and m_a complete wavelengths of acoustic radiation. Further it was assumed that there is a time interval t' between arrivals of an identified phase of the acoustic radiation at the front lip just as a vortex is shed. Therefore the vortex pattern moves downstream a distance $KU_{\infty}t'$ in this time interval so that

$$m_v \lambda_v = L + \gamma \lambda_v + KU_{\infty}t' \quad (4)$$

Also in time t' the internal wave system has moved a distance ct' so that

$$L = m_a \lambda_a + ct' \quad (5)$$

Then t' is eliminated between equations 4 and 5. The freestream velocity U_{∞} was replaced by Ma ; further, it was assumed the acoustic velocities internal, c , and external, a , to the cavity were equal; and that the total number of wavelengths, $m_v + m_a$, equal the mode number, m .

These assumptions led to a physical model of the flow which may be represented by the empirical frequency equation

$$f = \frac{U_{\infty}}{L} \frac{(m - \gamma)}{\left(\frac{1}{K} + M\right)} \quad (6)$$

where K equals 0.57, m is an integer, and γ equals 0.25. When the frequency of one of the components $(m - \gamma)$ is close to the natural frequency of the volume of air in the cavity, resonance occurs. Both cavity length and depth influence which mode number is dominant for a particular cavity geometry.

Additional investigations of flow induced cavity pressure oscillations and acoustic resonance to refine Rossiter's work were conducted by East [Ref. 42], Heller et al [Ref. 43], Bilanin and Covert [Ref. 44], Miles [Ref. 45], Block [Ref. 46], Sarohia [Ref. 47], Yu [Ref. 48], and Gharib and Roshko [Ref. 49]. The investigation by Tam and Block [Ref. 50] obtained experimental data for the tone-frequency characteristics for flow Mach numbers less than 0.4. It was observed that there was a transition from the normal mode resonance mechanism to a feedback instability mechanism for discrete tone generation as flow Mach number increases. A mathematical model of acoustic-feedback oscillations was developed which, in contrast to the Bilanin and Covert model, accounted for the shear-layer thickness. Compared with the Rossiter model, the Tam and Block model added two parameters; (1) the cavity length-to-depth ratio L/D ; and (2) the ratio of the momentum thickness of the shear layer to the cavity length δ_2/L .

The acoustic-wave generation process sketched in Figure 6 (from Ref. 51) for a supersonic freestream was adopted. Flow-induced cavity oscillations are caused by the interaction of the free shear layer and the complex internal cavity wavetrains. The shear layer oscillated up and down near the trailing edge of the cavity. During the upward motion of the cycle, the fluid of the shear layer shields the trailing edge of the cavity from the external flow and the predominant flow is over the cavity with no pressure waves. When the shear layer deflects downward, there is flow of the freestream into the cavity which causes a transient high pressure region near the cavity trailing edge, which forces propagation of a compression wave in all directions. The convection effect of the freestream

modifies the shape of the wave front as it radiates away from the cavity trailing-edge.

In Figure 6, the essential features of a typical oscillation cycle are divided into six time-sequential parts, identified by the letters A through F. The external-flow Mach waves represent a freestream Mach number of 1.5. Each part sketched in Figure 6 should be viewed as a typical phase of the oscillation cycle. The direction of the motion of each wave is indicated by an arrow. The exact wave representation depends on the cavity geometry (L , D , and W), the external Mach number, the boundary layer characteristics at the upstream end of the cavity, and the freestream turbulence. The starting point for the cycle is arbitrarily selected. It is helpful to review the entire cycle to gain a good understanding of cavity flow phenomena. This cycle is now discussed starting at A:

(A) The pressure wave from the previous trailing-edge disturbance reaches the front of the cavity and reflects. Another wave, moving from the front wall approaches the rear wall. The shear layer is above the cavity trailing edge, so the external flow does not produce a disturbance at the cavity trailing edge. Some fluid leaves the cavity at the rear.

(B) The shear-layer waveform travels rearward and reduces the height of the shear layer above the trailing edge. A new compression wave begins to form at the rear as the flow interacts with the trailing edge and fluid is added to the cavity. The front compression wave has reflected off the front wall and moves rearward nearly in phase with the shear layer displacement. The previous rearward wave has reached the trailing edge.

(C) The wave reflected off the front wall continues to move rearward in phase with the shear-layer displacement. The shear layer, which is now below the trailing edge at the rear of the cavity, forms a new forward-traveling compression wave as the external flow impinges on the back of the cavity.

(D) The newly-generated, forward-traveling compression wave and the reflected, rearward-traveling compression wave meet and interact near the cavity center.

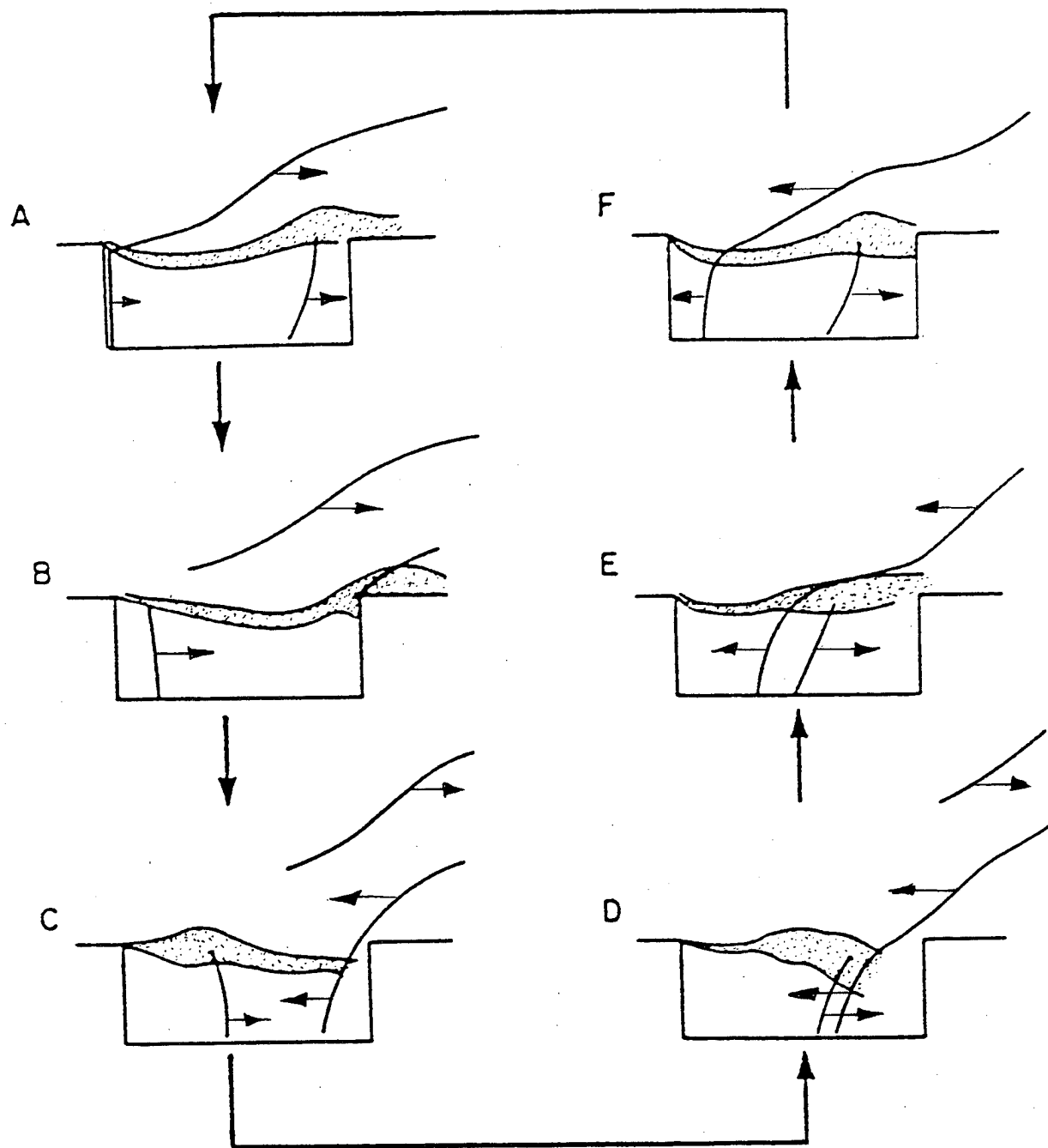


Figure 6. Typical oscillation cycle for cavity flow [from Ref. 51].

(E) After interaction, the waves continue in their respective directions. The external part of the forward-traveling wave moves into the supersonic flow, thus causing it to be tipped more than the external flow angle. The rearward wave moves in the same direction as the external flow and travels at a subsonic speed relative to it. This subsonic relative speed explains why the rearward-traveling wave stops at the shear layer. At the rear, the shear layer reaches the trailing edge height.

(F) The shear layer is now above the trailing-edge height. The wave generated at the trailing edge approaches the front of the cavity, and the reflected wave nears the rear of the cavity. The next step is the same as (A), and the oscillation cycle repeats.

For subsonic flow, the process is essentially the same, particularly as regards the internal wave structure. The forward-traveling wave will still be supersonic with respect to the external flow. The external wave structure will usually be non-existent. Instead, the shear layer will tend to roll into transverse vortices with the number dependent primarily on the cavity geometry (L/D) and on the freestream Mach number. Typically there will be either two (mode II) or three (mode III) vortical structures present.

For the purpose of computing the phases of the acoustic waves generated at the trailing edge of the cavity, Tam and Block [Ref. 50] made the size of the noise source very small. A periodic line source was used to produce this flow pattern. Inside the cavity the mean velocity was zero. The mathematical model of the effect of the interaction of the acoustic-wave field on the instabilities of the shear layer was assumed to be convective. A mean shear-layer momentum thickness was used in the model. The resultant equations, which are fairly complex, are presented in Reference 50. This model provided good agreement between predicted discrete-tone frequencies and Rossiter's data ($0.4 \leq M \leq 1.2$) and Tam & Block's data ($M < 0.2$). For the very low Mach numbers, $M < 0.2$, it appeared that the tones were generated by the normal-mode resonance mechanism. The transition between the feedback mechanism and the normal-mode resonance was rather gradual. This suggested that the Tam and Block model may provide the

basis for a unified model of the flow-induced tone phenomenon to include cavity-tone frequencies throughout the Mach number range.

Ziada and Rockwell [Ref. 52] found that impingement of mixing layers on solid boundaries enhanced the organization of all harmonic modes in a shear layer. This effect was investigated by Rockwell and Knisely [Ref. 53] specifically for cavity flow using a laser velocimeter. As shown in Figure 7, inserting a downstream cavity-impingement edge makes a large change in the unsteady nature of the shear flow. Autocorrelations were taken along the edge of the shear layer where $u/U_\infty \cong 0.95$ using an average of six sequential samples. These results are presented in Figure 7; note that the ordinate scale changes for each curve. Both data sets were taken at the same shear layer location of $x/\delta_0 = 134$. For the backward facing cavity, there were large variations in the autocorrelations. The typical period of oscillation is quite irregular and tends to increase with downstream location. For the cavity flow, the enhanced organization of the flow is quite dramatic. In addition, there are no apparent variations in the oscillation frequency. This enhancement of the shear layer organization extended along the entire length of the shear layer. This finding substantiates the concept of disturbance feedback. The perturbations propagated upstream from the impingement surface affected the amplitude of the locally-induced pressure fluctuations and the resultant shear layer deformation.

A few examples of the many additional cavity-flow investigations are cited below to illustrate some results pertinent to the present investigation. Franke and Carr [Ref. 54] investigated the effect of geometry on modification of flow-induced oscillations for open cavity flow in the Mach number range from 0.6 to 3.3. It was found that ramps at the leading and trailing edges of the rectangular cavities could be effective in reducing pressure amplitudes under some conditions. Some of the cavity configurations studied by Franke and Carr included two cavities in tandem. Tandem cavities were also investigated by Zhang and Edwards [Ref. 55] in supersonic flow. They examined both the mean and unsteady flowfields. It was found that two cavities whose L/D was either 1 or 3 had little effect on each other. In contrast, a $L/D = 3$ cavity completely altered the flow in a downstream $L/D = 1$ cavity.

Betts [Ref. 56] experimentally evaluated the effect of slotted walls on flow in a rectangular water-channel. It was found that the effect of geometry on flow oscillations could be modeled by empirical relations. Sarno and Franke [Ref. 57] evaluated several devices located upstream of a cavity which attempted to reduce flow oscillation. Like Buell [Ref. 39] it was found that stationary fences at the cavity leading edge were the most effective flow-suppression device since they effectively reduced L/δ_0 .

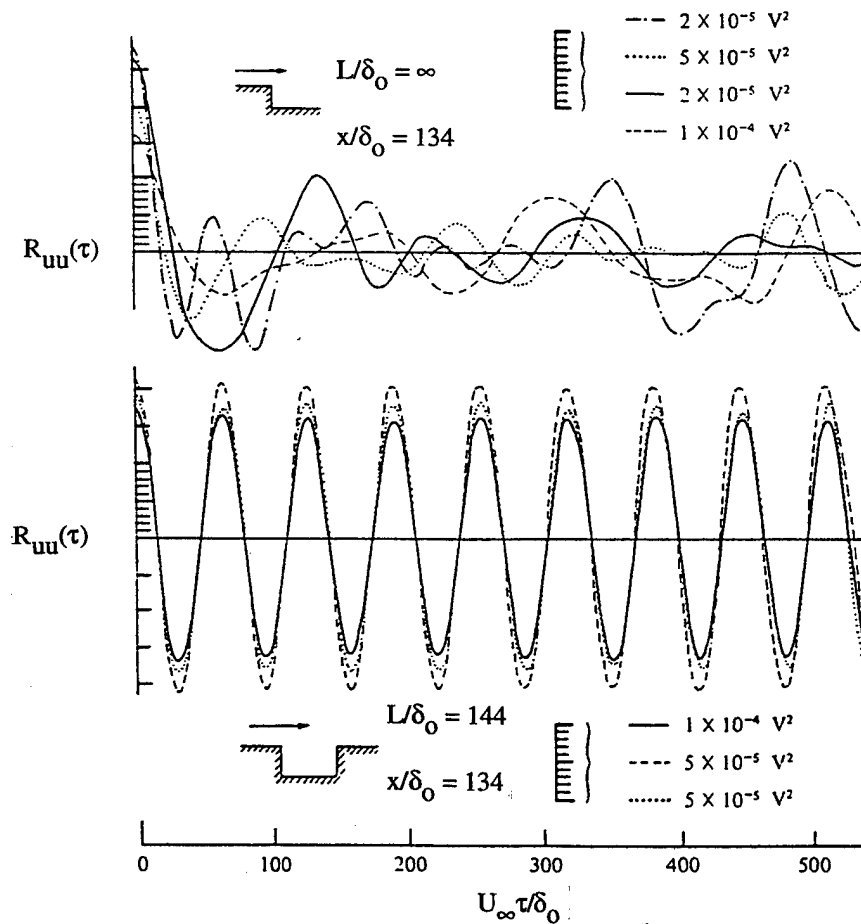


Figure 7. Comparison of autocorrelations taken with and without the cavity impingement edge at corresponding locations in the cavity shear-layer [Ref. 62].

C. CAVITY DRAG

The drag of cavities, holes, and gaps were discussed by Hoerner [Ref. 13] in his book on fluid-dynamic drag. Cavity drag is relatively small compared to the overall aircraft drag. The cavity drag coefficient C_F was typically less than 0.01 based on a reference area equal to the cavity opening, LW. For comparison, complete aircraft drag coefficient is usually based on wing area; the cavity opening area LW of landing gear or a stores cavity is usually at least one or two orders of magnitude less than wing area so that the C_F contribution to aircraft drag coefficient is of the order of 0.001 to 0.0001 or less. The shape of the edges of the cavities have a major influence on the magnitude of the drag as shown in Figure 8. For square cavities, $L/D = 1$ such as those used in the present investigation, C_F was 0.0083. When the slope on the top of the rear wall was changed to -5° , C_F was reduced to 0.0072. Rounding the rear slope reduced C_F to 0.0060. The other sketches in Figure 8 show a cavity with the same opening area but a larger

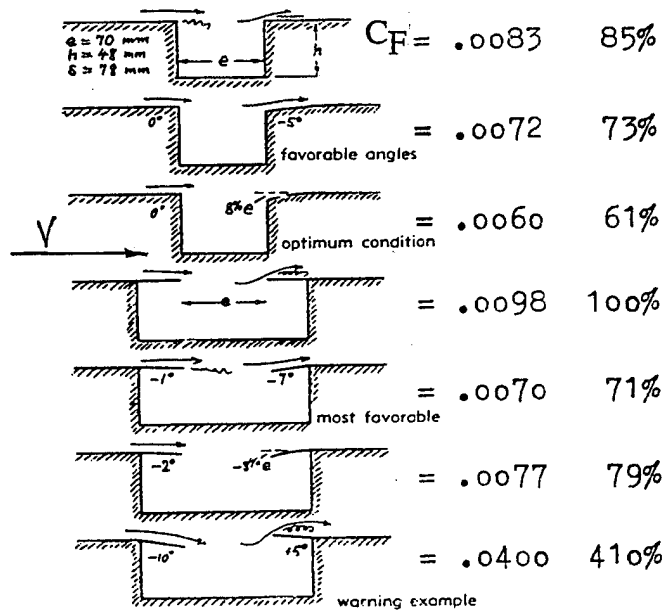
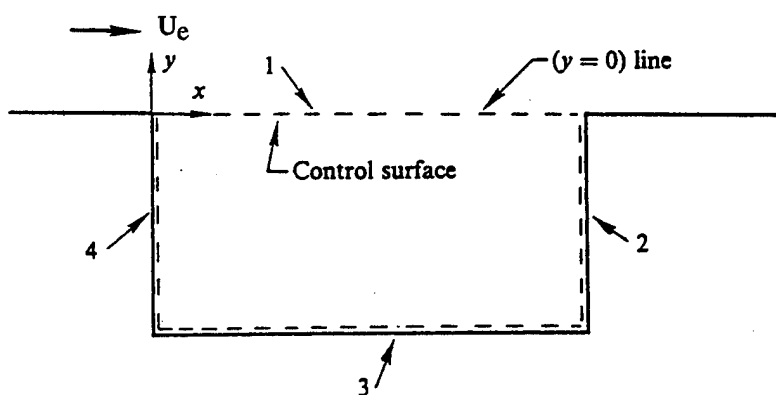


Figure 8. Cavity drag coefficient C_F measured for several edge shapes [Ref. 13].

cavity volume with variations in the slopes into and out of the cavity. It is shown that the value of C_F can be varied from 0.0070 to as high as 0.0400 by changing these slopes. Cavities with front slopes which direct freestream flow into the cavity and with rear wall slopes which inhibit flow out of the cavity greatly increase the drag. For minimum drag, the upstream edge should be nearly parallel with the freestream and the downstream edge should be bent at a small angle into the cavity.

The maximum shear stress increases with the cavity L/D . Gharib and Roshko [Ref. 49] measured the maximum c_f as 0.013. This c_f value compares closely with 0.0125 measured by Liepmann and Laufer [Ref. 58] for a two-dimensional shear layer and 0.012 measured by Kistler and Tan [Ref. 59] for a two-dimensional cavity shear layer. The maxima of cavity c_f profiles did not have a constant value. In contrast, c_f was found to be constant in two-dimensional, self-similar free turbulent shear layers.

Cavity drag is defined as the net force in the flow direction experienced by the cavity. The cavity control volume which can be used for the momentum balance is shown in Figure 9(a). Surface 1 is the open interface between the cavity and freestream flows where drag equals the momentum flux drag D_M occurs. On



(a) Schematic of the cavity and its control volume.

Figure 9. Cavity drag and effect of cavity length on maximum C_p .

On the upstream and downstream cavity walls (surfaces 4 and 2, respectively) the pressures are integrated to give a pressure drag D_P . On the cavity floor (surface 3) the shear stress gives a third drag force contribution D_S . These terms are summed to zero for the control volume. The drag force on walls 2, 3, and 4 is given by

$$D = D_P + D_S = D_M \quad (7)$$

The cavity drag is expressed as either the direct forces on the cavity walls and floor or the cavity momentum flux. The drag terms in equation 7 may be expanded to provide the cavity momentum-drag balance in integral form as

$$D = \int_{[2]} p dA_2 - \int_{[4]} p dA_4 + \int_{[3]} \tau_o dA_3 = \int_{[1]} \left(-\rho \bar{u} \bar{v} - \rho u' v' + \mu \frac{\partial \bar{u}}{\partial y} \right) dA_1 \quad (8)$$

Roshko [Ref. 32] found that the dynamic pressure in the recirculating cavity flow is low. On their axisymmetric experimental cavity model, which had no cavity floor at the centerline, there was a standing axisymmetric vortex. At the body centerline the vortex velocity components tended to cancel and the resultant velocity was nearly zero. As a consequence, the resultant drag due to shear stress, D_S , was negligible compared to the pressure drag, D_P . This simplified the drag equation to

$$D = D_P = D_M \quad (9)$$

This drag force can be nondimensionalized as a drag coefficient using the freestream dynamic pressure and an arbitrary reference area so that

$$C_D = \frac{D}{\frac{1}{2} \rho U_e^2 S_{ref}} = C_{D_P} = C_{D_M} \quad (10)$$

Alternatively, the reference area may be the cavity opening $S_{ref} = LW$ to obtain an equivalent average friction coefficient due to the cavity (or cavity drag)

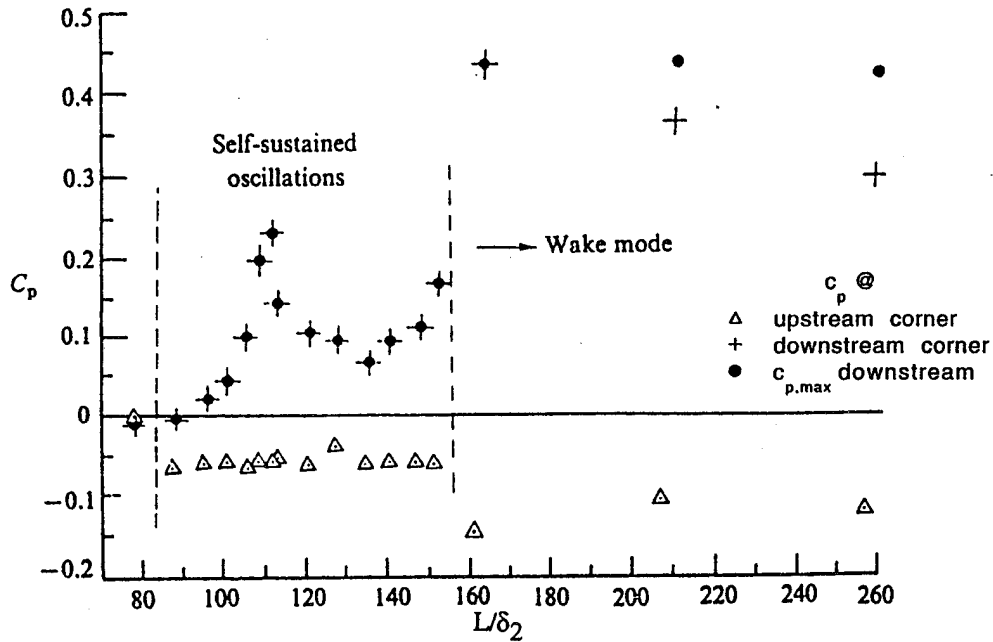
$$C_F = \frac{D}{\frac{1}{2} \rho U_e^2 LW} = C_{F_P} = C_{F_M} \quad (11)$$

coefficient). Both coefficients, C_D and C_F , give the same drag value. Gharib and Roshko [Ref. 59] choose to associate C_D with the forces on the cavity walls and C_F with cavity momentum flux. For cavities in the non-oscillation mode C_F was near 0.0001; in the self-sustained mode, the C_F was less than 0.01; and while in the wake mode ($L/\delta_2 > 155$ or $L/D > 1.25$) the C_F was between 0.06 and 0.08. For comparison, the estimated C_F based on boundary layer friction in the absence of a cavity was about 0.005.

Measurement of the pressure distribution on the solid surfaces of the cavity provides an understanding of drag generation. In short cavities with non-oscillating flow, the pressure coefficient c_p on both the upstream and downstream walls tends to be slightly negative and uniform indicating essentially no drag contribution. In cavities with flow oscillations ($84 < L/\delta_2 < 155$ or $0.68 < L/D < 1.25$) the c_p on both upstream and downstream walls approaches -0.1, except near the freestream edge of the rear wall. The c_p on the rear wall in the region from 0.1 D to the freestream surface increases to a positive value equal to a few tenths. This small region accounts for the entire pressure-drag force. For cavities in the wake mode, shear-layer impingement occurs further below the edge of the rear wall. As a result the positive pressure coefficient extends much further into the cavity. For large L/D , impingement even occurs on the cavity floor leading to positive c_p values. On the upstream wall, the negative c_p is nearly twice that for self-sustaining oscillation modes.

Examples of selected c_p values from Gharib and Roshko [Ref. 49] are presented in Figure 9(b). The plot shows the variation of maximum pressure coefficient with increasing cavity length. The c_p on the upstream corner of the cavity is nearly constant (≈ -0.07) in the self-sustained oscillation mode II and III regimes and are more negative (≈ -0.10 to -0.15) in the wake regime. In the self-sustaining oscillation regimes, the maximum c_p occurs at the downstream corner as shown by the overlap of the plus and solid-circle symbols. As cavity length increases in the wake-mode flow regime, the peak c_p on the downstream moves into the cavity from the downstream corner. This is consistent with shear-layer impingement inside the cavity, as discussed earlier.

Gharib and Roshko [Ref. 49] used a laser velocimeter to measure both the turbulent and mean shear layer velocity components. These proved to be difficult to obtain especially in the wake mode. The integral of \overline{uv} across the cavity opening represents a relatively small difference between two large contributions. It was found that the variation of $C_{F,M}$, while showing a lot of scatter, was generally consistent with $C_{F,p}$. In conclusion, it was found that the oscillating shear layer in the cavity is fundamentally different from a free shear layer. This difference is attributable to coupling between the upstream and downstream edges of the cavity.



(b) Variation of maximum pressure coefficient with cavity length L/δ_2 [Ref. 49].

Figure 9. Concluded.

In their study of coaxial flow over a combination of a disk and cylinder separated by a gap, Koenig and Roshko [Ref. 60] defined two flow regimes based on the magnitude of the drag of the combined body. These regimes were identified as low and medium drag. The medium drag is significantly lower than the drag that exists when the bodies are well separated and the downstream body has little influence on the upstream body, but in the low-drag regime drag is about an order of magnitude lower. Their study suggests that the low-drag flows appear

to be more general examples of the classical cavity flow. From the Gharib and Roshko [Ref. 49] work, it is now clear that the low-drag regime of Ref. 60 corresponds to the regime for self-sustained cavity flow oscillations while the medium-drag regime corresponds to the cavity wake mode. The flow visualizations and flowfield measurements of Ref. 49 show that in the low-drag regime the cavity shear layer always stagnates at the downstream corner. Only in the wake mode, the increased drag case, does it stagnate inside the downstream corner. The stagnation location moves further into the cavity as the cavity length increases.

In summary, the mechanism for a stable equilibrium of the shear layer may be explained. An inward displacement of the shear layer at the rear corner lowers the feedback signal and the resultant Reynolds stress. This decreases the entrainment in the initial portion of the shear layer and reduces the positive outflow. Correspondingly, the inflow at the downstream end must be reduced and the shear layer returns to its initial position. In the self-sustained flow oscillation modes the flow is very stable and resistant to moderate external disturbances until the gap becomes so large that the wake-mode instability takes over. These phenomena have been shown to determine that a cavity in the self-sustained flow oscillation modes has low drag and that a cavity in the wake mode has high drag.

D. NUMERICAL PREDICTIONS

The earliest separated-eddy and cavity-flow computations were reviewed in detail by Burggraf [Ref. 61]. These computations ranged from incompressible, inviscid such as Rossow [Ref. 62] to solutions of full Navier-Stokes equations at low Reynolds numbers. The Burggraf paper included a numerical solution to the full Navier-Stokes equations using a stream function and vorticity formulation, for the case of a square cavity in the Reynolds number (UL/ν) range from 0 to 400. From all of the studies reviewed, a fairly clear description was obtained for the overall flow characteristics. However, the detailed structure of secondary vortices was poorly represented, even for these low Reynolds number flows. Pan and

Acrivos [Ref. 63] calculated steady flow in rectangular cavities (L/D from 0.25 to 5) where the flow was driven by a uniform translation of the top wall of the cavity. These creeping flow solutions were obtained using a relaxation technique in a formulation similar to that of Burggraf. Computed streamline contours of the secondary corner vortices were an improvement upon earlier solutions. However, a minimum grid size of $0.01L$ was too coarse to represent detailed streamline patterns inside the corner eddies. It should be noted that these corner vortices occupied only about 0.5 percent of the total area of the cavity cross-sectional area. Unfortunately, the numerical method had serious instabilities for Reynolds numbers greater than 400, which made those results invalid.

The flow in a two-dimensional channel with a rectangular cavity was studied numerically by Metha and Lavan [Ref. 64]. For simplification, the length of the channel was taken to be infinite and the upper wall of the channel was moved with a constant velocity. This kept the flow approaching the cavity identical in all cases. Steady laminar, incompressible flow in two-dimensional channels with a rectangular cutout cavity were computed using an explicit numerical solution of the Navier-Stokes equations in a stream function and vorticity formulation. Solutions were obtained for cavity L/D of 0.5, 1.0, and 2.0 and for Reynolds numbers of 1, 10, 100, and 500. These cavity L/D ratios were chosen to give reattachment of the flow over the cavity and not inside. One vortex was observed for cavities with L/D of 1 and 2. For a L/D of 0.5 there were two vortices present, one on top of the other. The streamline dividing the external flow and the cavity flow was concave for very low Reynolds numbers and convex for the higher Reynolds numbers. As the Reynolds was increased, the vortex center moved downstream and upward, creating a thin shear layer. The shear layer on top of the cavity and along the cavity wall was not very thin, even at the larger Reynolds number. This result suggested that a relatively coarse grid may be adequate to define the flow features.

Borland [Ref. 65] obtained numerical solutions for the oscillating flowfield in an open cavity exposed to a high subsonic freestream for comparison with both wind tunnel and flight test data. Two-dimensional Euler equations for time-dependent inviscid compressible flow were formulated and solved using two different numerical algorithms. A first-order, fluid-in-cell method (FLIC) which

used an entirely Eulerian scheme provided the fundamental-frequency pressure-oscillation mode results. The grid cells were control volumes where the equations for conservation of mass, momentum, and energy were solved subject to appropriate boundary conditions. A second-order, fluid-in-cell MacCormack predictor-corrector method was also used in an attempt to predict some of the higher-frequency oscillation modes. These finite-difference equations were used for cell boundaries which were within the computational region. Upstream or inflow boundary conditions (b.c.'s) used the freestream variables. Downstream or outflow b.c.'s assumed that the gradients of the basic flow variables vanish. This is a more complex b.c.'s and sometimes produces less reliable results. The solid wall b.c.'s used cell boundaries which were coincident with the physical boundaries. For inviscid flow, reflective conditions were used where the normal velocities at the solid walls are cancelled by assuming a fictitious grid cell with an opposing velocity just beyond the physical boundary. All of the other primitive flow variables are also duplicated by the fictitious grid cell. The first-order FLIC results gave a good correlation with the fundamental oscillation frequency and the magnitude of the pressure oscillations observed experimentally. The second-order predictor-corrector method showed a capability to predict higher-order harmonics as well as the fundamental. It was found that this computation was not stable and the oscillatory flow field damped out with increasing numbers of iterations and was not observed late in the computation. The outflow b.c. was suspected to be the cause of this computational instability.

Hankey and Shang [Ref. 66] analyzed pressure oscillations in an open cavity using time-dependent numerical computations of supersonic flow over an open cavity with a L/D equal to 2.25. The unsteady Navier-Stokes equations were solved by the MacCormack finite-difference explicit method for a freestream Mach number of 1.50, and a Reynolds number of 2.6×10^7 . The most obvious feature was that the flowfield within the cavity is subsonic, except in the vicinity of the cavity opening. The orderly development of the shear layer above the cavity was shown. An attached turbulent boundary layer upstream of the cavity separates at the front wall to form the shear layer over the cavity. The shear layer then reattaches downstream of the cavity. The pressure oscillation was also predicted, and both the fundamental frequency and magnitude were in agreement

with experimental data [Ref. 51]. However, the numerical solution would be needed for a longer period to completely verify the experimental spectral analysis. This paper provided the first complete viscous solution of the pressure oscillating cavity.

Ghia, Ghia, and Shin [Ref. 67] used a multigrid method to solve the Navier-Stokes equations for incompressible flow in a cavity. The laminar incompressible flow was computed in a square cavity whose top wall moved with a uniform velocity in its own plane for moderately high values of Reynolds number (100 to 10,000). The objective of the paper was to achieve the solutions in a greatly reduced computational time. The two-dimensional cavity flow was represented mathematically by a stream function and vorticity form of the Navier-Stokes equations. The non-slip boundary conditions were applied at the cavity walls by requiring zero normal velocities at all of the boundaries. The two-dimensional cavity space was discretized by a uniform mesh. Second-order accurate central finite-difference approximations were employed for all of the second-order derivatives. The convective terms were represented by a first-order upwind difference scheme. In the multigrid method, the mesh density is cycled from low to high, iteratively, to smooth the results by damping the high frequency errors. The solutions used the coupled, strongly-implicit procedure of Rubin and Khosla [Ref. 68].

An example of the computational results from Reference 67 is presented in Figure 33 which shows the streamline contours in Figure 33 for a Reynolds number of 10,000 using a uniform grid (257 x 257). The center of the primary vortex was offset towards the top right corner at a Reynolds number of 100 ($x = 0.6172$ and $y = 0.7344$). It moves toward the geometric center of the cavity with increase of the Reynolds number. Above a Reynolds number of 5000 the movement ceases and the primary vortex was located at $x = 0.5117$ and $y = 0.5233$. As the Reynolds number increased from 100 to 10,000 the vorticity strength at the vortex center decreased from 3.17 to 1.88.

This solution shows the presence of additional counter-rotating vortices in or near the cavity corners. The notation shown in Figure 10 uses the letters T, B, L, and R to denote top, bottom, left, and right, respectively. For example, BR_2

refers to the second in the sequence of secondary vortices that occur in the bottom right corner of the cavity. At a Reynolds number of 100 there were only two secondary vortices; as the Reynolds number was increased to 10,000 the number of secondary vortices increased to the six shown in Figure 10. Initially, all of the secondary vortices are located very near the cavity corners. With increasing Reynolds number the secondary vortices move, very slowly, toward the cavity center. Figure 33 includes magnified views of the contours of the secondary vortices. The values of the stream function for each contour on the figure are listed below:

contour letter	ψ	contour number	ψ
a	-1×10^{-10}	0	1×10^{-8}
b	-1×10^{-7}	1	1×10^{-7}
c	-1×10^{-5}	2	1×10^{-6}
d	-1×10^{-4}	3	1×10^{-5}
e	-0.0100	4	5×10^{-5}
f	-0.0300	5	1×10^{-4}
g	-0.0500	6	2.5×10^{-4}
h	-0.0700	7	5×10^{-4}
i	-0.0900	8	1×10^{-3}
j	-0.1000	9	1.5×10^{-3}
k	-0.1100	10	3×10^{-3}
l	-0.1150		
m	-0.1175		

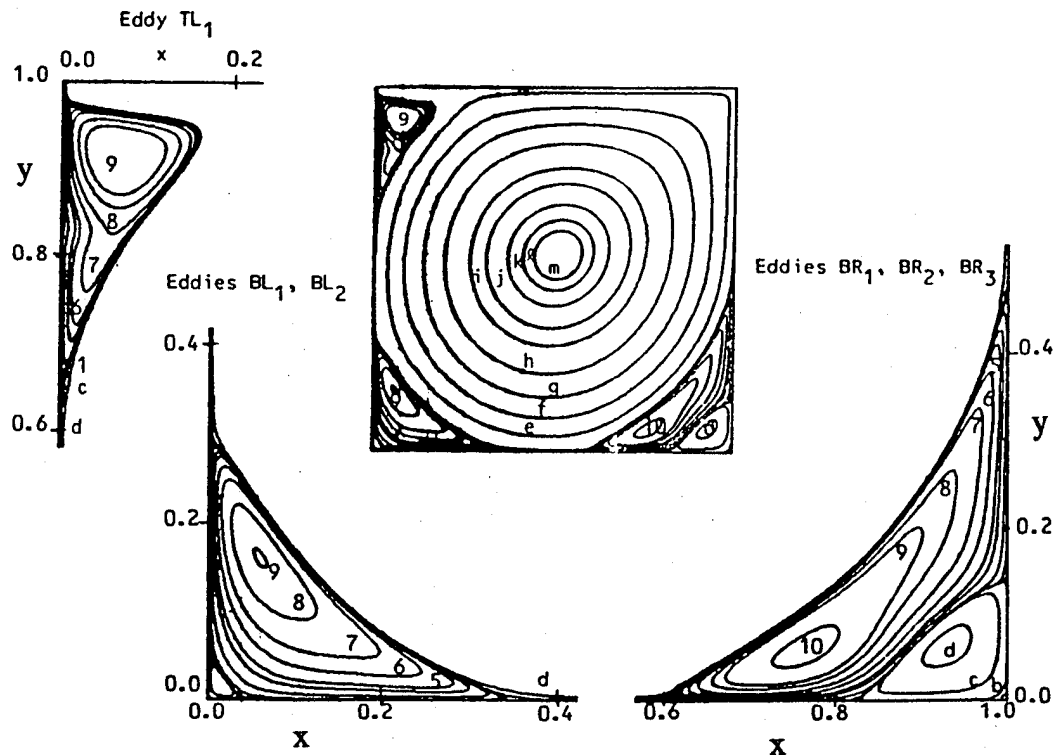


Figure 10. Streamline pattern for primary, secondary, and additional corner vortices for a Reynolds number of 10,000 using a uniform grid (257 x 257).

In the last ten years there have been many additional computational solutions of the cavity flow problem [Ref. 69 through 78]. These efforts covered a wide range of flow conditions. In spite of this large amount of computational activity there are still some major deficiencies. The extensive regime of unsteady and oscillatory flow over and inside cavities still contains many unresolved problems. Prediction of the possible modes, amplitudes, and frequencies have been very difficult to obtain accurately. Many of these prediction efforts have not adequately modeled the effect of the initial boundary layer thickness on the shear

layer interaction with the cavity flow oscillations. Attempts to get around the details of the shear layer have usually succeeded only in situations where the shear layer is not the controlling factor, such as for deep cavities and large enclosures with small openings. Improvements upon these deficiencies will require a significant development effort.

E. MULTIPLE CAVITIES

A two-dimensional inviscid, incompressible computational investigation of the aerodynamics of an airfoil with a vortex trapped by two spanwise fences was conducted by Rossow [Ref. 62]. To evaluate the concept, computed results were obtained for a Clark-Y airfoil using a variety of fence geometries at several angles-of-attack to determine the aerodynamic characteristics of these trapped-vortex, high-lift devices. These computational results suggested that two spanwise fences should be used to enclose a trapped vortex. The two fence heights were adjusted so that an equilibrium condition could more easily be achieved than using only a single fence. Little or no mass removal from the core region of the vortex was required to stabilize the trapped vortex. The lift increase was found to be inversely proportional to the chordwise spacing of the fences. It appeared that for two fences there would be no profile drag penalty, that the vortex would be easier to form and would be more stable than for a single fence. The results also showed that the vortex bubble could be moved fore and aft on the airfoil to control the pitching moment. It was suggested that an extension of the single trapped-vortex geometry to two or more trapped vortices on the upper surface of an airfoil may provide the same lift with less cumbersome equipment.

The progression in complexity from the two-dimensional configurations studied above to the full three-dimensional flowfield of a wing requires examination of several additional factors. Such devices were recently studied in an unpublished experimental investigation by Rossow and Ross [Ref. 79] using a low-aspect-ratio, highly-swept-back ($\Lambda = 60^\circ$) wing (Figure 11) with a semispan of 24.76 inches and a chord of 18.98 inches. There were differences between the

actual wing area and the resultant aspect ratio and the values used in the aerodynamic coefficients as the reference geometry as shown below:

	actual geometry	reference geometry
S, in^2	783.90	467.66
AR	3.13	5.24

This test was conducted in the NASA Ames Research Center 7- by 10- Foot Tunnel using a semispan model. The model was mounted on a metric balance frame. Force data were obtained from an external floating-frame system of beam balances located below the test-section floor.

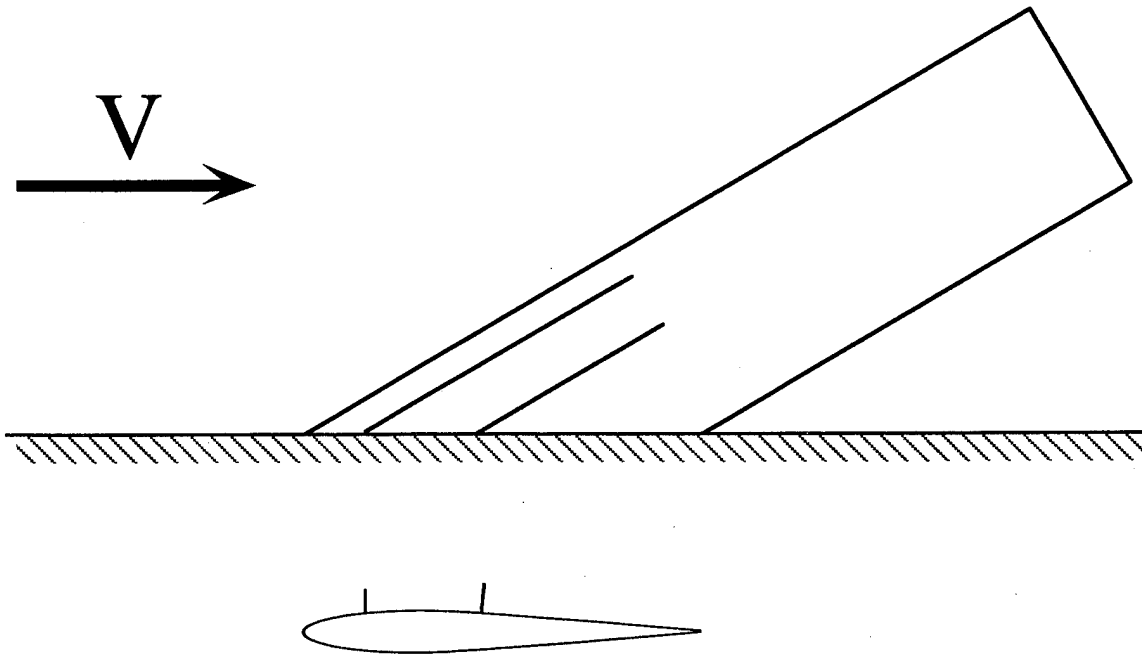
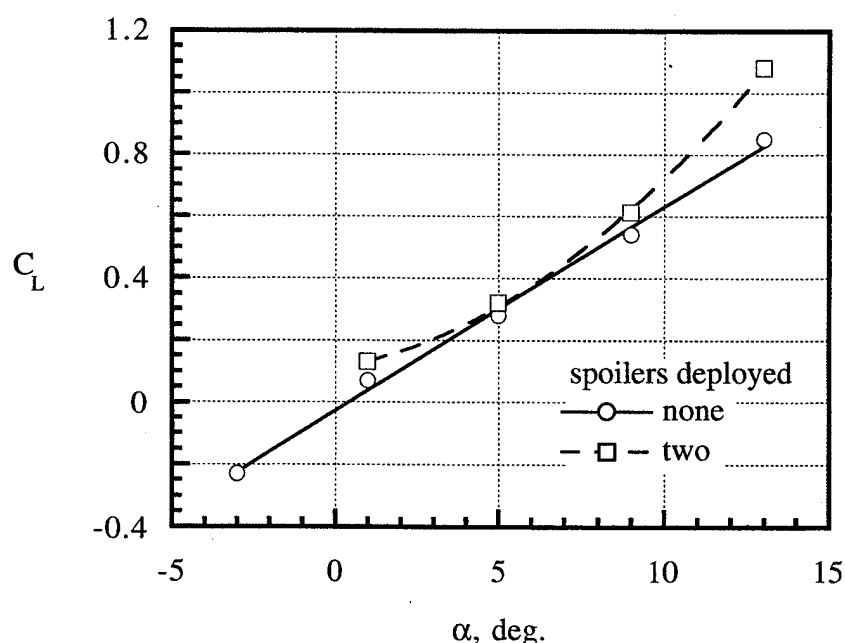


Figure 11. Semispan wing (NACA 0012 airfoil normal to the leading edge) with two part-span spoilers tested by Rossow and Ross [Ref. 79].

A variety of spoiler configurations were tested. As a sample of results from this investigation, the following data were obtained using a pair of spoilers (0.08c high at 0.15c and 0.10c high at 0.45c) which were used to form a single cavity

swept along the local chord line. The spoilers extended from the root chord to approximately 1/3 of the wing span. The intent was to take advantage of the inherent spanwise flow to form a standing vortex and to avoid active mass removal from the core region of the vortex. If the spoilers are effective, then the flow over the upper surface would be displaced passively to increase the wing camber. This experimental investigation found that below 8° angle-of-attack there was little or no lift increase. However, there was a lift benefit as high as 30% at an angle-of-attack greater than 10° (Figure 12(a)).

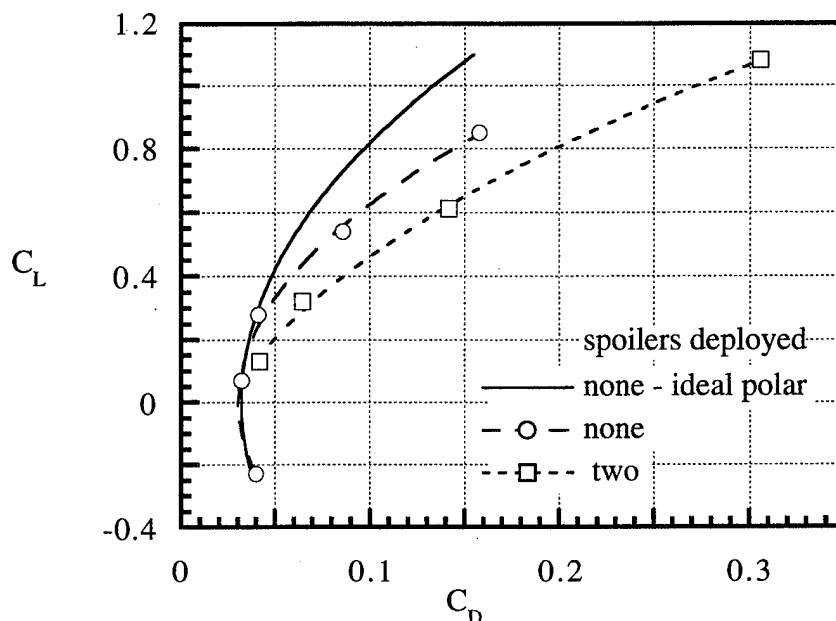


(a) Lift curve.

Figure 12. Rossow-Ross experimental data [Ref. 79].

However, there was an unexpected and undesired drag increase over a wider angle-of-attack range as shown by the polar plot in Figure 12(b). For reference, the ideal polar ($1/\pi AR e$) is shown by a solid line, where the span efficiency factor e is 1, which corresponds to an elliptic spanload distribution. An efficient transport wing will typically have a span efficiency factor greater than 0.9. Lower-aspect-ratio fighter aircraft have a span efficiency which drops into the 0.7 or 0.8 range. Even lower span-efficiency factors indicate either an inefficient

spanload distribution or the presence of flow separation. The polar for the wing without spoilers shows a drag increase above the ideal drag polar for $C_L > 0.3$ (or $\alpha > 5^\circ$). The drag for the spoiler-deployed configuration is increased even further. In an attempt to quantify the drag increase the experimentally determined span efficiency factor, e , is tabulated in the following table:



(b) Lift-drag polar.

Figure 12. Concluded.

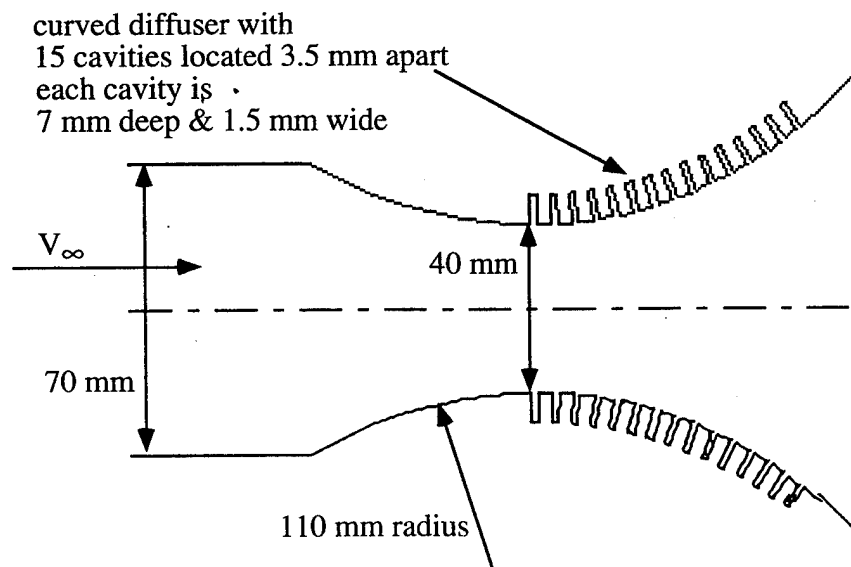
C_L	spoilers deployed	
	none	two
0.4	0.57	0.31
0.6	0.56	0.33
0.8	0.58	0.38
1.0	-----	0.42

These adverse drag results suggest the presence of flow separation and indicate the need for a better understanding of the flow phenomena involved.

In the early 1960's, Migay [Ref. 80] conducted a series of investigations which evaluated the effect of multiple transverse cavities in a diffuser (Figure 13(a)). The diffuser surface had a constant radius of 11 centimeters. The first cavity was located at the entrance to the diffuser ($\alpha = 0^\circ$). Up to 12 transverse cavities distributed along the flow direction through the diffuser (at $\alpha > 0^\circ$) were tested. Pressure taps were distributed along the diffuser in the direction of the flow. The pressures were non-dimensionalized using a pressure coefficient referenced to atmospheric pressure

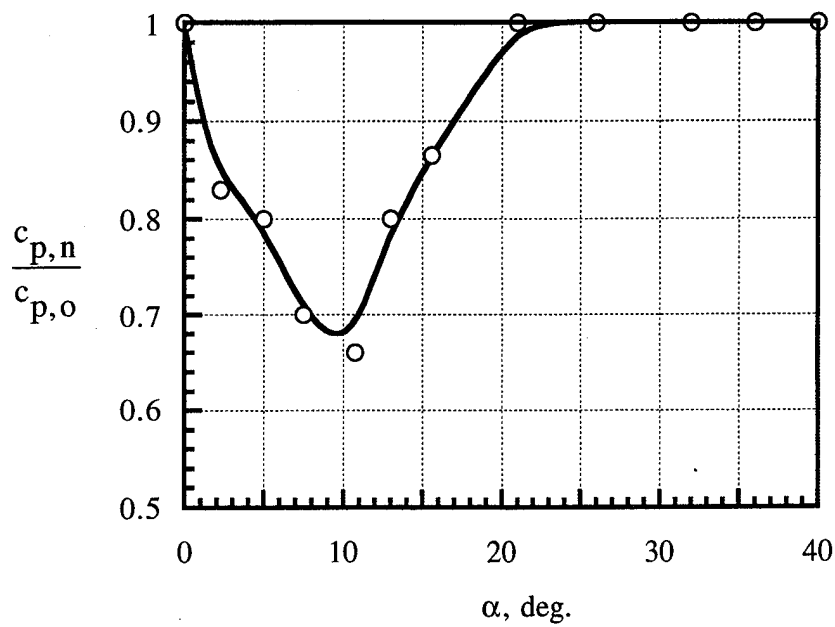
$$c_p = \frac{P_1 - P_{atm}}{\frac{1}{2} \rho (U|_{\alpha=0})^2} \quad (12)$$

where $U|_{\alpha=0}$ is the velocity in the test section upstream of the diffuser. The pressure data were presented as the ratio of the pressure coefficient measured at a particular tap location to the pressure coefficient measured at $\alpha = 0$. The measured pressure distribution is presented in Figure 13 (b) and it is seen that the largest

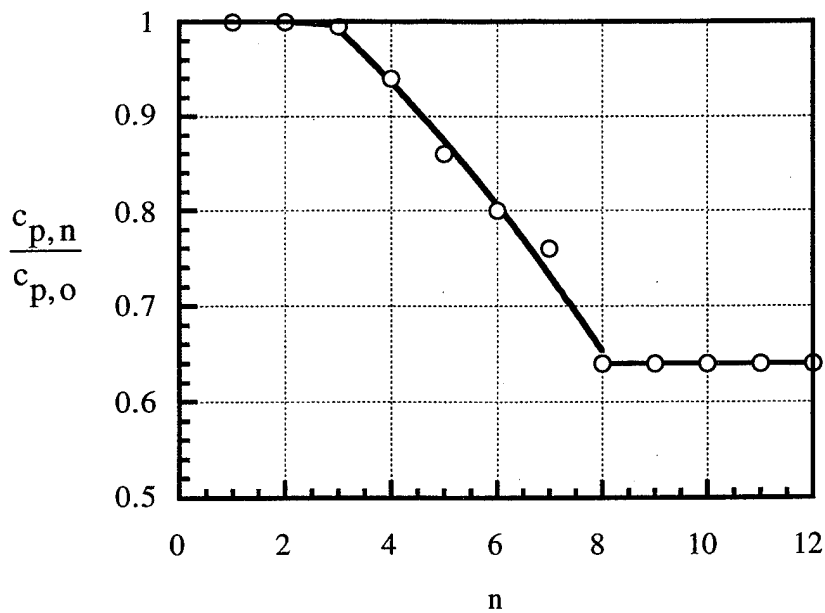


(a) Sketch of curved diffuser.

Figure 13. Results of Migay investigation [Ref. 80].



(b) Effect of diffuser angular position.
Figure 13. Continued.



(c) Effect of the total number of cavities
Figure 13. Concluded.

pressure reduction occurred near $\alpha = 10^\circ$. It appeared that the surface flow separated downstream of the $\alpha = 10^\circ$ location. It was found that the cavities were effective in preventing flow separation as long as the first cavity was located at an α between 0° and 10° . When the first cavity was located further downstream, the cavities had no beneficial effect on the location of flow separation. The effect of the number of cavities is presented in Figure 13 (c) where the ratio of pressure coefficients is shown as a function of the number of cavities. No effect was found for up to three cavities. Then there was an increasing pressure coefficient reduction from four to eight cavities with no additional change for more than eight cavities. These results indicate that the cavity benefit can be achieved with a limited number of cavities if they are properly located in the diffuser.

An investigation by Lin et al [Ref. 81-86] evaluated in some detail the potential of multiple cavities as a base-drag reduction device. An example of these results is presented in Figure 14 for an axisymmetric body with a modified bluff base which had up to 13 circumferential grooves. The transition from the axisymmetric body to the tapered base used a radius on the shoulder at the intersection of the body and the base. For the results in Figure 14, the shoulder radius was one-half of the body radius. The downstream edge of the first groove was located at the start of the shoulder radius. The grooves were numbered from 1 to 13 as their location varied from the shoulder to more downstream positions. The bluff-body base had a 30° angle; a streamline body with a base angle of 10° was also tested. Both bodies had a diameter of 2.39 inches; the bluff body was 3 diameters long while the streamline body was nearly 5 diameters long.

The data in Figure 14 present the variation of drag coefficient with Reynolds number for axisymmetric-body configurations with and without circumferential grooves. They show that the streamline body had the lowest drag and that the ungrooved bluff body had one of the highest drag coefficients. The effect of the grooves was determined by opening the grooves one at a time. Groove number 1 was opened at the shoulder location. Then groove number 2 was also opened at the next downstream location. This process was continued until all 13 grooves were open. When one groove was opened the drag increased above that for the ungrooved body. When a second groove was opened there was a drag reduction. However, for 1, 2, or 3 grooves open, the drag was greater than

for the ungrooved body. As the number of grooves was increased from 4 to 10 the drag was increasingly reduced below that for the ungrooved body.

The largest drag reduction was achieved with either 10 or 13 grooves open. For these two configurations the lowest drag occurred in the Reynolds number range from about 80,000 to 100,000 and then drag tended to increase slowly with further Reynolds number increase. It was found that the boundary layer transitioned on the base from laminar to turbulent in this Reynolds number range. As a result, these circumferential grooves on the body with a shoulder radius appear to only be effective for a laminar boundary layer approaching the shoulder. The reason for this Reynolds-number sensitivity was not identified. This investigation also evaluated many other devices and found several which were as good or better than multiple cavities without being limited to a particular Reynolds-number range. This study also indicated a need to improve the understanding of the flow changes due to the cavities.

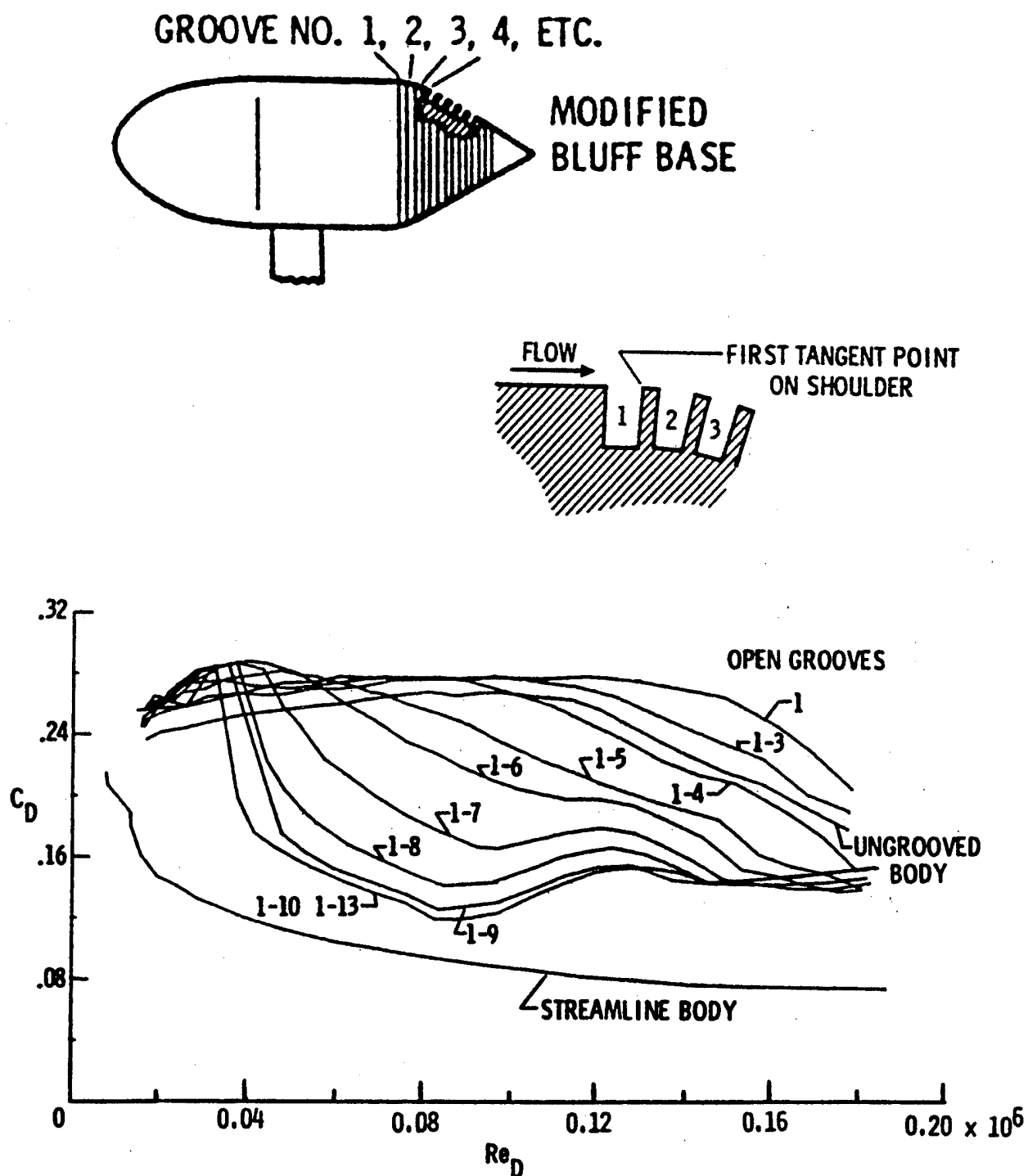


Figure 14. Effect of circumferential grooves on the afterbody on the axisymmetric bluff-body drag; shoulder radius is 0.2 body radius [Ref. 86].

III. EXPERIMENTAL PROCEDURE AND RESULTS

The present investigation included a wind tunnel test where the effect of single and multiple cavities on the boundary layer development and the pressure distributions were measured in both a zero and two adverse pressure gradients. The boundary layer profiles were measured at four or five longitudinal stations in the vicinity of the cavity(s). One station was located immediately upstream of the first cavity and the rest were either between the multiple cavities and/or downstream of the cavities.

A. WIND TUNNEL AND APPARATUS

The experimental investigation was conducted in the San Jose State University (SJSU) Low Speed Wind Tunnel. The test apparatus included a three-dimensional traverse from the Naval Postgraduate School as well as a computer and data acquisition system from the NASA Ames Research Center. The test hardware for the cavity configurations and the test section diffusers were specifically fabricated for this investigation in the SJSU tunnel.

1. Wind Tunnel

A sketch of the SJSU tunnel is presented in Figure 15. This is a continuous flow tunnel with an Eiffel-type return. The flow enters the 30" square entrance section, shown on the left in Figure 16, and then goes through a honeycomb and two screens into the 36" long contraction. The contraction ratio is 6.25. The test section is 12" high, 12" wide, and 24" long. The contraction, test section, and

diffuser are mounted on a fixed frame. The drive motor-fan assembly is located on a movable frame located on the right side of the sketch. There is also a honeycomb upstream of the motor. Between the downstream end of the diffuser and the honeycomb there is a variable gap which is used to control the tunnel speed. As the gap was varied from 6" to 0" the test section speed U_{∞} increased from 40 feet per second (fps) ($q = 1.9$ psf) to the maximum tunnel speed, 142 fps ($q = 24$ psf). The present test was conducted using a speed of 130 feet per second. A 96" long test section extension was constructed for this investigation to increase the boundary layer thickness for a portion of the tests. Longitudinal position in the test section was measured from the test section entrance: station 0" through 24" for the 24" test section; and stations 0" through 120" for the 120" test section. In the longer test section the original 24" long test section was located between the 96" and 120" stations. Photographs of the SJSU tunnel with each test section length are presented in Figure 17.

To achieve adverse pressure gradients in the 24" long test section, the first 6" was reduced in height. Then the increased contraction ratio was faired using an insert on the tunnel bottom in the 16" immediately upstream of the test section ($x < 0$ "). A test section diffuser was installed between 6" and 24" stations on the floor of the test section. One diffuser had a constant 7° angle and the second test section diffuser had a constant 14° angle. The test section extension height was variable to accomodate the reduced height upstream of the same test section diffusers used in the 24" test section. The contraction ratios for the test section with the 7° and 14° test section diffusers were 9.38 and 10.13, respectively. Coordinates are presented in Figure 36 for the original test section (solid lines) and for the two test section diffusers (dashed lines). The x and y scales exaggerate the y dimensions relative to the x dimensions. Tests were conducted in each of the three configurations shown; (1) original test section, $y = 6$ " (top) and -6 " (bottom); (2) 7° test section diffuser, $y = 6$ " (top) and varying from -4 " to -6 " (bottom); and 14° test section diffuser, $y = 6$ " (top) and varying from -1.4 " to -6 " (bottom). The same test section top was used for each of the basic tunnel configurations. For the 120" test section the same test section diffusers were used. As mentioned in the previous paragraph their x locations were increased by 96", the length of the test

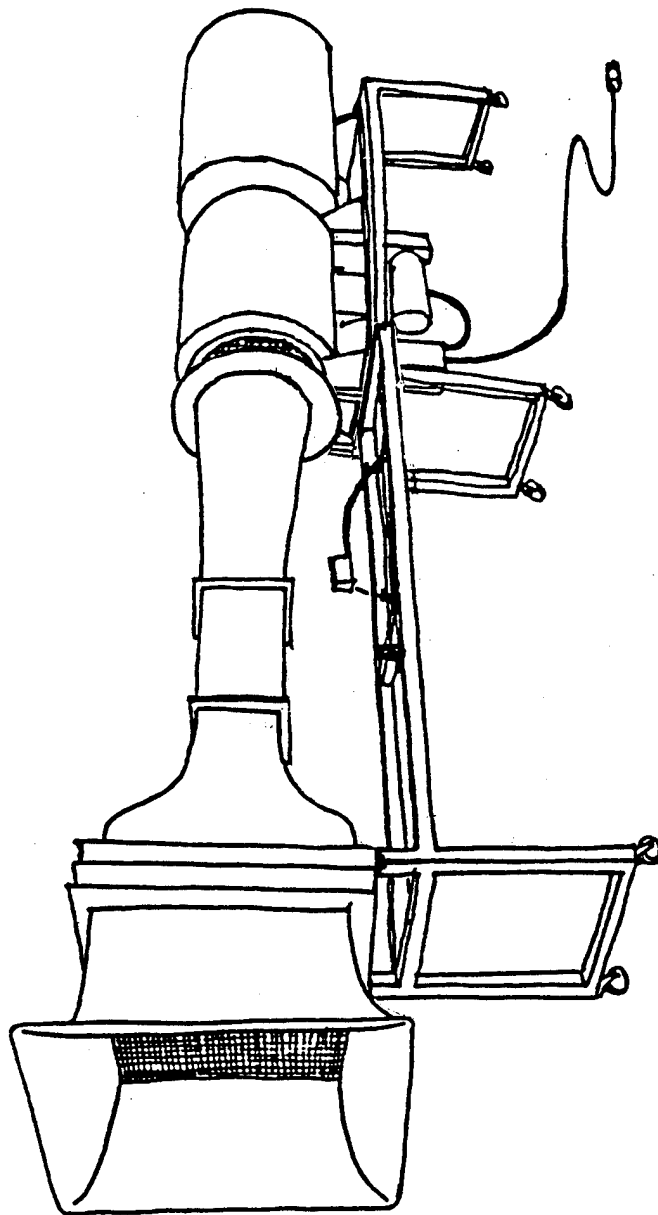


Figure 15. Perspective sketch of the San Jose State University Low Speed Tunnel.

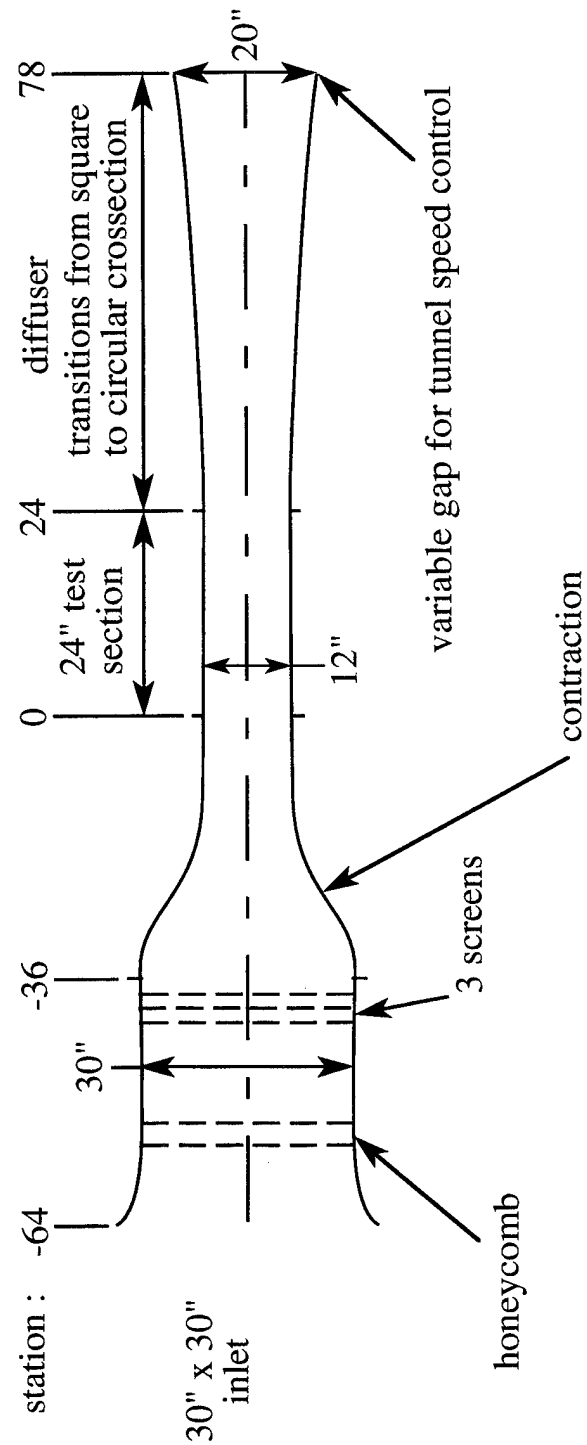
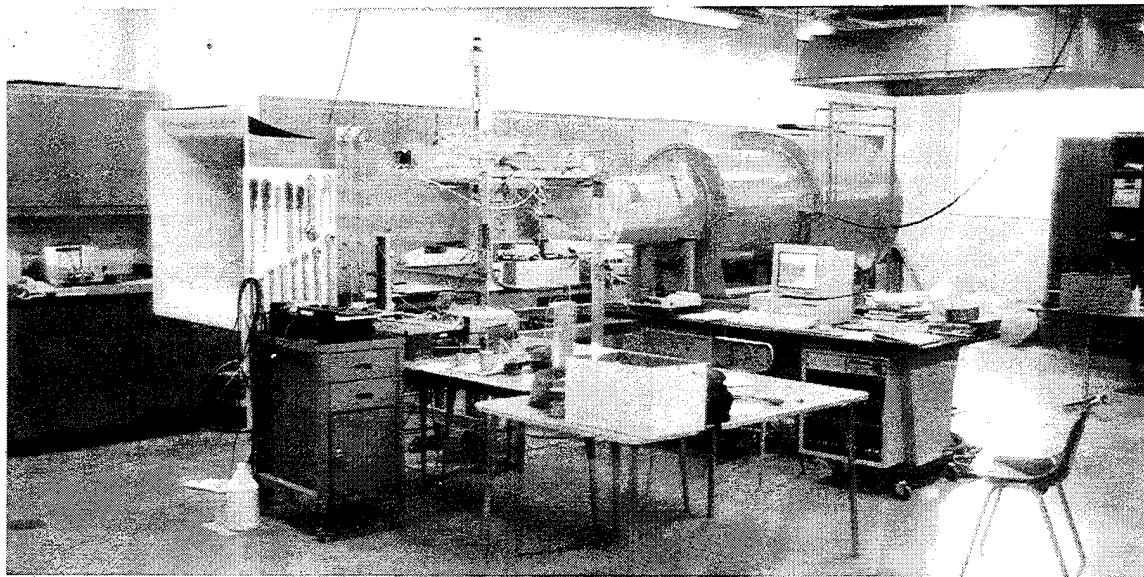
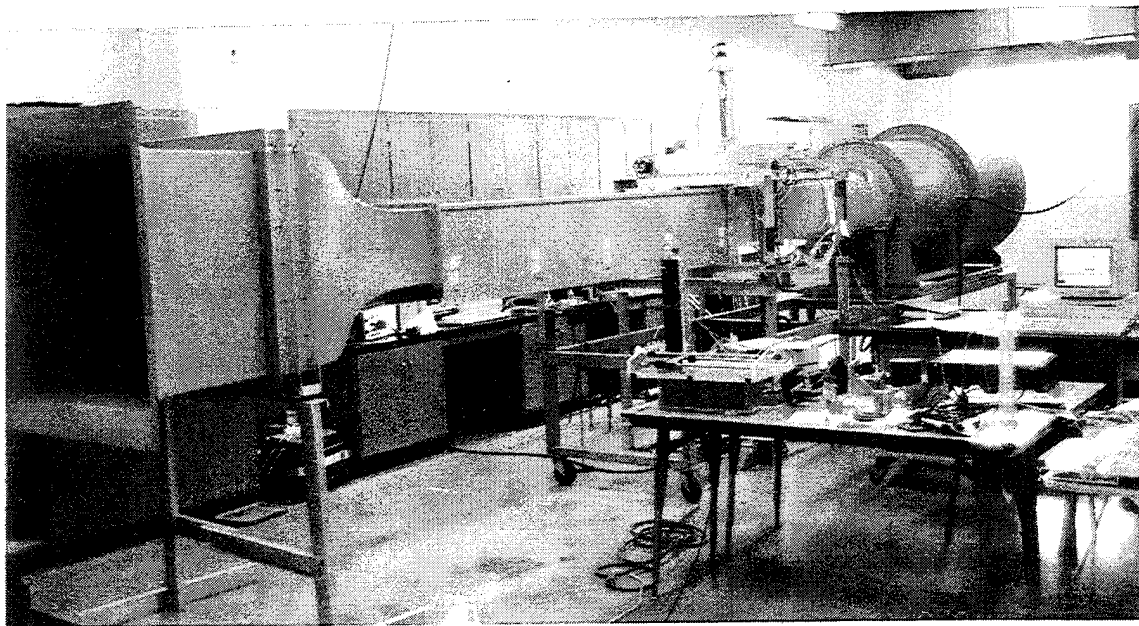


Figure 16. Sideview of the San Jose State University low speed tunnel.



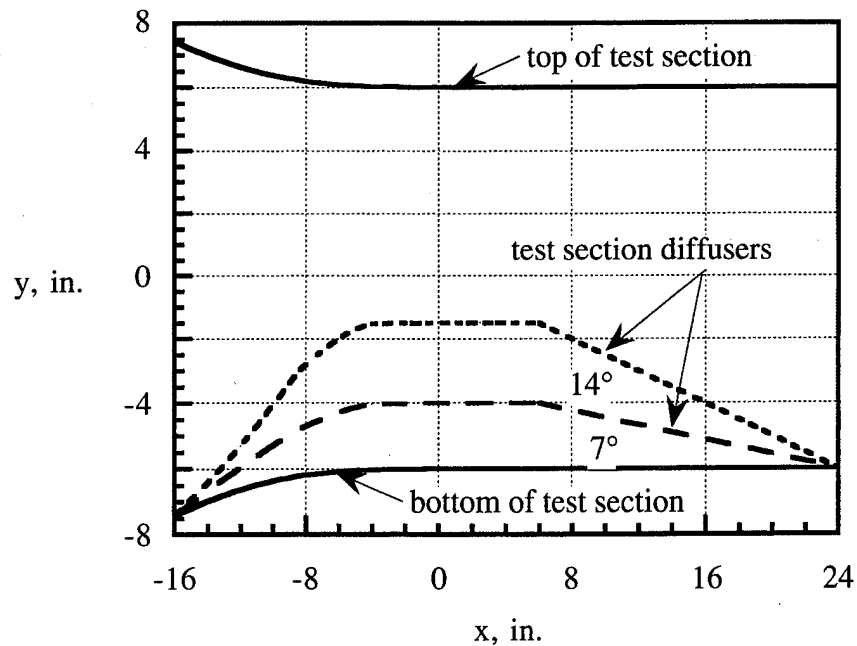
(a) Standard 24" long test section configuration.

Figure 17. Photograph of the San Jose State University Low Speed Tunnel.



(b) Extended 120" long test section configuration.

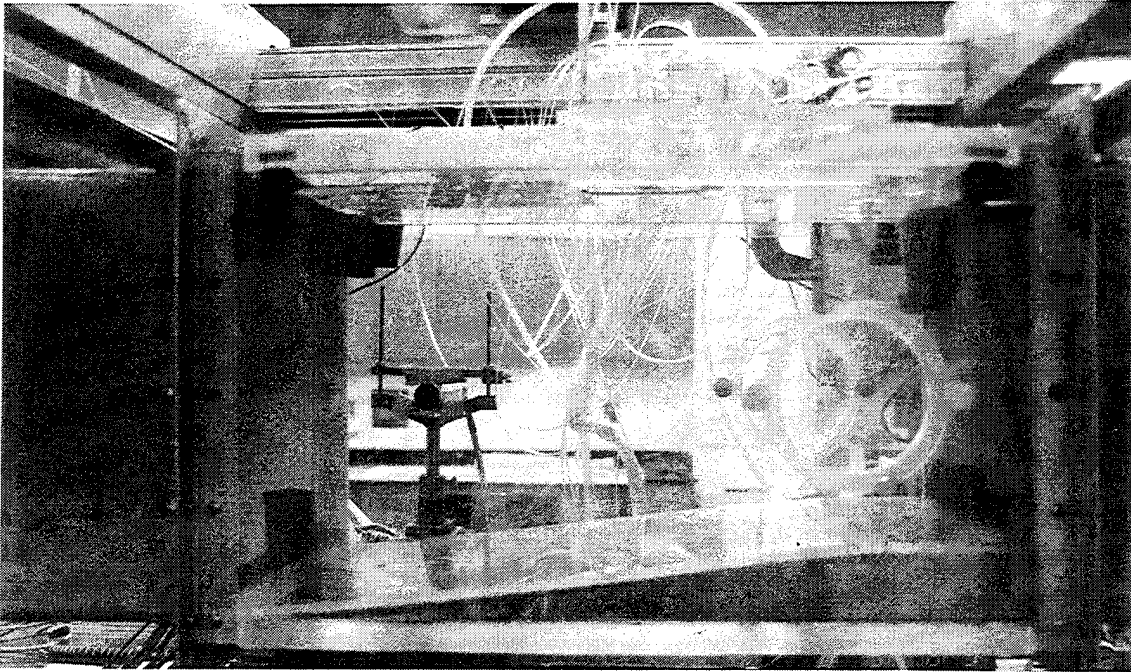
Figure 17. Concluded



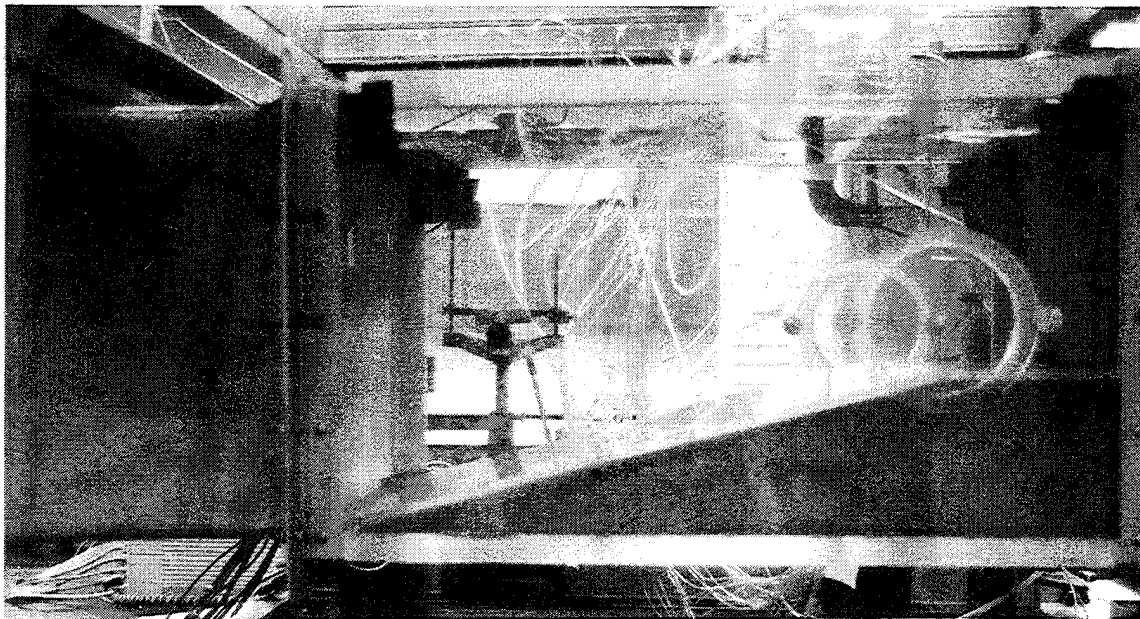
(a) Coordinates of the 24 " test section and for the 7° and 14° test section diffusers.
Figure 18. Test section diffusers used to generate an adverse dp/dx .

section extension which was added to the front of the original test section and downstream of the modified contraction ratio ($x < 0$).

Photographs of the SJSU tunnel are also presented in Figure 18 which shows the 7° test section diffuser with four one inch cavities (Figure 18(b)) and the 14° test section diffuser with one two inch cavity (Figure 18(c)). The test section diffusers were fabricated using plywood frames mounted in the streamwise direction and covered by 0.25" thick clear acrylic sheets. The photograph for the 7° test section diffuser also shows the four cavity configuration mounted on the top of the test section. The photograph for the 14° test section diffuser also shows the single two inch cavity configuration mounted on the top of the test section. Some of the clutter in the background of the photographs is the tygon tubing used for the pressure distribution measurements on the tunnel top and bottom. The vertical portion of the pitot-static probe used for tunnel reference dynamic pressure measurement is visible above the circular access window. The boundary layer



(b) Photograph of the 7° test section diffuser with flow from the right.
Figure 18. Continued.



(c) Photograph of the 14° test section diffuser with flow from the right.
Figure 18. Concluded

total pressure probe is near the downstream cavity in Figure 18(b) or near the two inch cavity in Figure 18(c) adjacent to the tunnel ceiling in both photographs.

2. Test Hardware

The test hardware built assembled specifically for the present investigation consisted of the test section diffuser, the cavity configurations (1, 2, and 4 cavities), the three-dimensional traverse mechanism, and the computer with its data acquisition program.

a. Single and Multiple Cavity Hardware

There were four cavity configurations built for the investigation of the effect of the number of cavities on the boundary layer profiles. As shown by the photographs in Figure 18 the cavities were mounted in the test section ceiling in the adverse pressure gradient portion of the test section diffuser. For nomenclature purposes, the edge of the cavity adjacent to the freestream is called the top and the cavity horizontal surface parallel to the freestream is called the floor. For each cavity the upstream vertical surface is called the front wall and the downstream vertical surface is called the rear wall. Each cavity had a nominal length to depth ratio L/D of 1. Each of these cavity configurations was equipped with a distribution of surface pressure taps both in the cavities and on the ceiling surface both upstream and downstream of the cavities. The coordinates of all of these pressure taps are presented in Appendix B, Pressure Tap Locations. The cavity test hardware which was fabricated for this investigation is summarized in the following table:

number of cavities	cavity number (from upstream)	cavity depth, D, in.	cavity length, L, in.	longitudinal location of cavity front wall, in.
1	1	2.00	1.94	7.50
1	1	0.94	1.00	6.50
2	1	1.00	0.94	6.00
2	2	1.00	0.94	8.00
4	1	0.94	0.94	6.00
4	2	0.99	0.94	7.95
4	3	1.00	0.94	9.94
4	4	0.99	0.95	11.95

b. Traverse

The three-dimensional traverse assembly from the Naval Postgraduate School is shown in Figure 19. It was used to support and traverse a pitot probe used to measure the boundary layer profile. A 0.375 inch circular hole in the ceiling provided clearance for the 0.25 inch diameter probe support. The probe was used to survey the boundary layer profile adjacent to the test section ceiling. The traverse was mounted on top of a frame which wrapped around the tunnel test section and did not touch the wind tunnel. Three electric motors powered the gear-driven screws which moved the traverse independently in each Cartesian direction. The following traverse ranges were available: streamwise,

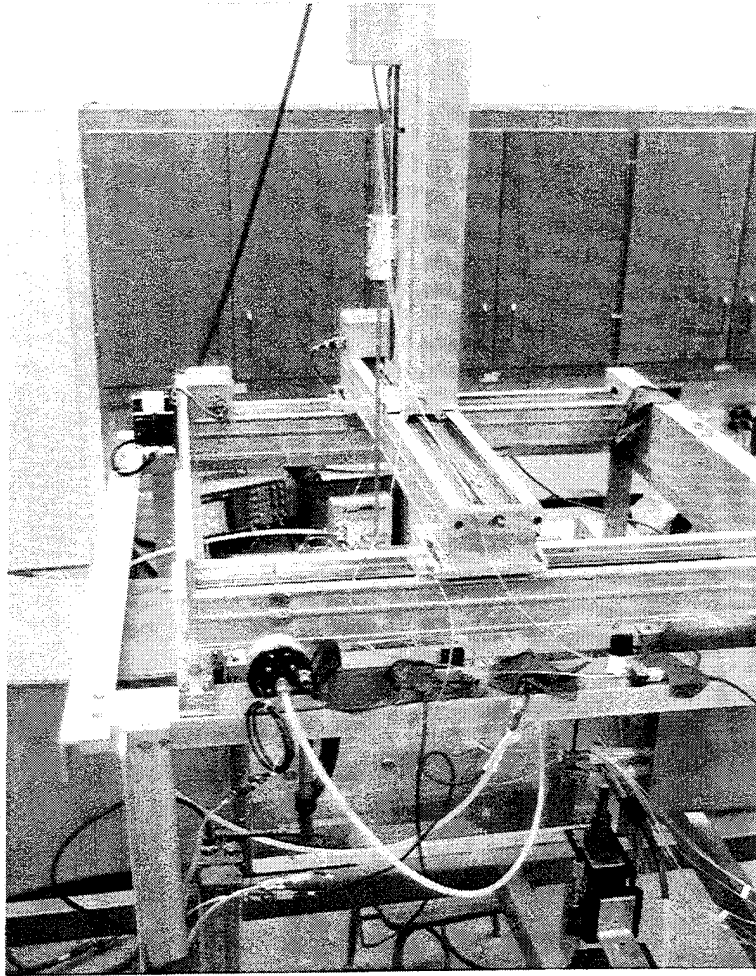


Figure 19. Photograph of the traverse mechanism mounted at the SJSU tunnel.

20"; laterally, 22.5"; and vertically, 12". These movements were executed by manually entering the desired movement direction (X, Y, or Z) and the movement distance. The repeatability of probe positioning was determined by moving the probe ten inches and then moving back to the starting point. There was less than 0.002 inch error in returning to the original position. Significantly no backlash due to reversing the movement direction was observed. To assure the best positioning accuracy, all of the boundary layer traverses were obtained by moving in one direction from the ceiling into the freestream to avoid any possibility of backlash. For the next run, the probe was then returned to a position hard against

the test section ceiling. The direction was then reversed to a position where the probe just touched the ceiling prior to the next traverse.

c. Boundary Layer Probe

The boundary layer total pressure was measured using a total pressure probe which was made by flattening a circular stainless steel tube. Using a 0.060 inch diameter tube, a probe tip height of 0.022 inch was used for runs 101 through 254. This probe was damaged and replaced by another probe with a tip height of 0.034 inch for runs 255 through 380. The probe location for plotting boundary layer profiles was taken to be one-half of the probe tip height when it touched the wall. For the tests, this half height was identified as zero on the probe traverse position data display.

The pressure was measured using a 0.5 psid transducer. The NASA Ames calibration laboratory found that this particular transducer had a standard deviation equal to 0.141% of full scale. This translated to a 0.5% (0.102 psf) error for differential pressures measured at a freestream dynamic pressure of 20 psf. After the probe was installed, the calibration was checked using an electronic pressure calibration device. Regression analyzes of repeated calibrations gave a correlation coefficient r^2 of between 0.9986 and 0.9997. This represented a maximum repeatability error of 0.07% of full scale or 0.05 psf. A third error source was the electronic zero shift between the beginning and end of a run. In 154 runs this shift averaged 0.03 psf. If these errors were summed the maximum error becomes 0.18 psf or 0.9% of the freestream dynamic pressure.

A final error source was the effect of the wall proximity or boundary layer displacement effect. The work of Coles [Ref. 9] was applied to the present data. It was found that this error was negligible when used to correct the displacement thickness δ_1 and the momentum thickness δ_2 . Application of this correction to the measured velocity adjacent to the wall indicated a velocity error

$\Delta V/V$ of 0.0145. At a freestream dynamic pressure of 20 psf, this was an error of 0.004 psf or 0.02%. This was considered to be negligible.

d. Computer and Data Acquisition System

The digital data acquisition system was controlled by a desktop computer through a graphical user interface (GUI) computer program and two dedicated data acquisition circuit boards. Each data channel had its own amplifier which conditioned the data signal and amplified its voltage so that it could be sampled with the greatest possible accuracy and then multiplexed to the computer. The computer had 8 megabytes (Mb) of random access memory (RAM), an 40 Mb internal hard disk, and a removable 44 Mb hard disk which was used to store the experimental data.

The application program for the GUI was a set of virtual instruments (VI) which each consisted of three parts: (1) the front panel; (2) the block diagram; and (3) the icon/connector. The first two parts were visible on the computer screen as windows. The front panel was the user interface to the VI and was used during data acquisition by the program operator to interact with it. It included input objects called controls and output objects called indicators. The objects were portrayed on the computer screen as command buttons and status indicators. Data was also be displayed in either tabular and/or graphical forms. The block diagram was a VI source code which was created using a graphical programming language. This was a virtual wiring diagram for connecting the program modules which were called nodes to the terminals for the controls and indicators. The icon was a representation of the VI. The connector acted as the port through which the data passed. The icon/connector together represented the VI in a manner analogous to a subroutine call statement when the VI was used as a subVI in another VI's block diagram. Many layers of subVIs could be used in higher order VIs.

The present investigation GUI used a main panel (Figure 20(a)), a boundary layer measurements panel (Figure 20(b)), and a pressure distribution

measurements panel (Figure 20(c)). The data acquisition/reduction program was executed by first loading the GUI program application code and then launching the cavity flow experiment main panel VI and all of the related subVIs. At the completion of these steps the computer screen displayed the main panel shown in Figure 20(a). There were nine command buttons shown on the top portion of this panel and status indicators for each data channel. The data acquisition was initiated by sequentially using the computer's mouse to select the clear acquisition button, then select the initialize acquisition button, and finally select the take zeros button. Then there were five choices available: (1) data acquisition setup button which was used to add or remove data channels; (2) on-line monitoring button to view data output for each channel; (3) boundary layer measurements button; (4) pressure distribution measurements button; and (5) quit button to terminate and exit the program.

In this investigation four groups of data measurements were taken and recorded in data files: (a) tunnel conditions; (b) boundary layer profiles; and (c) static pressure distributions. An example of the data recorded for a boundary layer profile run is presented in Figure 21. This particular run was identified as R0105BL which stands for run R, number 0105 and boundary layer profile BL, respectively. Subsequent boundary layer profile runs have different run numbers. As shown in Figure 21, the data file generated by the GUI program started with the run number, the date and time of the run, and the tunnel code (see Appendix A for a detailed description). Then there was an additional line of group 1 data which consisted of the freestream conditions measured by a pitot probe located at $x = 1$ " and $y = 2.5$ " and then averaged over the entire run. These data include the tunnel reference values for pitot probe static $P_{s,tun}$ and total pressures $P_{t,tun}$, as well as their difference, the calculated dynamic pressure q_c . For an independent measurement, the dynamic pressure was also measured by a separate pressure

riches main panel
Friday, August 5, 1994 2:17 PM

Front Panel

Cavity Flow Experimental Main Panel

Data Acquisition Setup

Boundary Layer Measurements

Initialize Acquisition

On-Line Monitoring

Dynamic Data

Pressure Distribution Measurements

Take Zeros

Clear Acquisition

Quit

Zeros

0

CHANNEL	Name	Description	K0	K1	K2	K3	K4
0	Ps	Tunnel Static Pressure	22	55	1	1	1
1	Pt	Tunnel Total Pressure					
2	Tt	Tunnel Total Temperature					
3	Pt-Ps	Tunnel Dynamic Pressure					
4	Pscan1	Pressure 1 Scanivalve					
5	Pscan2	Pressure 2 Scanivalve					
6	Pscan3	Pressure 3 Scanivalve					
7	Pscan4	Pressure 4 Scanivalve					
8	Pcf	Pressure, Preston Tube					
9							
10							
11							
12							

(a) Cavity flow experimental main panel.

Figure 20. Front panels used as the GUI in the present investigation.

[illegible]

Figure 20. Continued.

Front Panel

Pressure Distribution Measurements

Channel Setup

$P_{s\infty}$ (tunnel static) psfg
 $P_{t\infty}$ (tunnel total) psfg
 $T_{t\infty}$ (tunnel total) °F

$P_{s,p}$ (wall static) psfg
 $P_{t,p}$ (probe total) psfg
 q_{∞} (tunnel q) psfg

P_{amb} , psfa
 $q_{\infty,c}$ ($P_{t\infty}-P_{s\infty}$) psfg
 SV #1 psfg

P_{amb} , " Hg
 q_{∞} ($P_{t\infty}-P_{s\infty}$) psfg
 SV #2 psfg

$A2$
 SV #3 psfg

$B1$
 SV #4 psfg

Change Set-Up

Test Section/Cavity Config.

Tunnel Configuration Code

Data 1

Data 2

Data 3

Data 4, actual EU

Take Cp Data

Return

Change Run/Point

Run #

Point

Scanivalve Control

Step ☐

Home ☐

Continue

Scanivalve Port

Scanivalve Control

Step ☐

Home ☐

Continue

(c) Pressure distribution measurement panel.
Figure 20. Concluded

transducer and displayed as q . For pressure coefficients this value of dynamic pressure was used to non-dimensionalize the static pressures. Finally the tunnel total temperature $T_{t,tun}$ and atmospheric pressure P_{atm} were listed. The tunnel conditions were always measured along with one of the other three groups of data described above.

Shown in Figure 21 is a group of boundary layer probe data, identified as group 2 data. The number of data points varied from run to run. In this example from run 105, 15 points were recorded. Then seven columns of data measurements were displayed for each boundary layer height: (1) the height from the bottom of the boundary layer total pressure probe to the tunnel ceiling ($y = 6.00$ ") Y_{bl} ; (2) the boundary layer total pressure $P_{t,p}$; (3) the ratio of local u velocity to estimated local freestream velocity u/U ; (4) pitot probe dynamic pressure q_{tun} ; (5) tunnel total temperature $T_{t,tun}$; (6) pitot probe total pressure $P_{t,tun}$; and (7) pitot probe static pressure $P_{s,p}$. The height of the boundary layer measurement was the sum of the probe height Y_{bl} plus one-half of the probe vertical thickness $\Delta y_p/2$ which was 0.011 inch for runs 100-257 and 0.017 inch for runs 258-380. The four measured pressures and the measured temperature were tabulated in the engineering units shown in Figure 21. The boundary layer profile in run 105 was taken at $x = 9$ ", which is downstream of the location of the single cavity configurations. The boundary layer profile is expressed as the ratio of boundary layer velocity computed from the total pressure measured by the boundary layer probe $p_{t,p}$ at the height $Y_{bl} + \Delta y_p/2$ divided by the freestream velocity at the x station where the profile was measured. The velocity within the boundary layer at a given height was computed from the Bernoulli equation as

$$u = \sqrt{\frac{2}{\rho} (P_{t,p} - P_{s,ceiling})} \quad (13)$$

where the static pressure measured at a static pressure orifice located on the ceiling at the x station of the boundary layer profile was p_{surf} . The quantity $P_{t,p} - P_{surf}$ was measured as the pressure difference across a pressure transducer.

During the on-line measurements the local freestream velocity was estimated by the GUI program. For tunnel configurations without the diffuser

inserts, the local freestream velocity was assumed to be constant along the length of the test section. For tunnel configurations with a diffuser the local velocity U or U_x was computed using the incompressible continuity equation

$$U_x = U_\infty \frac{A_\infty}{A_x} \quad (14)$$

where either; (1) $A_x = 12 * y_{@x=5}$ for A_∞ or for A_x where $x \leq 6$ or; (2) $A_x = 12(y_{@x=5} + (x - 6)\sin(\alpha))$ for A_x when $x > 6$. The test section diffuser had a constant height from $x = 0$ " to $x = 6$ ". From $x = 6$ " to $x = 24$ " the diffuser had a constant slope of either 7° or 14° . For the final processed data, U_x was replaced by the velocity at the edge of the boundary layer U_e which was computed from the boundary layer probe measurements at $y \geq d$ where the maximum value of $p_{t,p} - p_{surf}$ was measured.

An example of group 3 data from run 173 is presented in Figure 22. This particular run was identified as R0173CP which stands for run R, run number 0173 and pressure coefficient data CP, respectively. The run heading, run-date-time-tunnel code, and group 1 data are displayed the same way they were shown in Figure 21. The group 3 data, pressure distributions, are grouped by the scanivalve module that measured a group of pressure taps. Each section of these data is headed by the scanivalve number (1, 2, or 3) and the number of pressures recorded. Notice that the number of pressures is one greater than the number of taps for each scanivalve. The extra pressure is a reference pressure which represents zero return after the group of taps were sampled and indicates whether there is any electrical drift in the pressure data during the data sample period.

Scanivalve 1 (Figure 22(a)) measured the 16 taps located on the test section diffuser between $x \approx 2$ " and $x \approx 21$ ". When there was no test section diffuser installed, scanivalve 1 was not sampled; only the test section ceiling pressures were measured. For run 173 scanivalve 2 (Figure 22(b)) measured the 17 taps located on the test section ceiling upstream (from $x \approx 2$ ") and downstream of the two inch cavity (to $x \approx 22$ "). Notice that pressure tap 13 measured a pressure nearly equal to zero for this run. Since this was not seen in measurements of this tap in other runs, this measurement was interpreted as faulty data for this

run and omitted from the final data plots. Scanivalve 3 (Figure 22(c)) measured the 21 taps located in and near the two inch cavity. As seen in the data listing, the upstream cavity wall was located at $x = 7"$ and the downstream wall was located at $x = 9"$. The floor of the cavity was located at $z = 8"$ (for the 2" cavity). The data listing for each scanivalve includes the following information: (1) tap number; (2) tap x location; (3) tap y location; (4) the surface static pressure P_{surf} ; (5) the pressure coefficient C_p which is defined as

$$C_p = \frac{P_{surf} - P_{s,tun}}{q} \quad (15)$$

The complete list of runs completed in this investigation is presented in Appendix A. The surface tap locations for all of the test configurations are listed in Appendix B. The cavity pressure data are presented in Appendix C for all of the measured data. The boundary layer profile data are presented in Appendix D for all of the measured data.

Run		105												
Date		2/23/94												
Time		11:44 AM												
Tunnel Code		0000												
Group 1 Data (average)														
P _{s,tun} (psfg)		Pt,tun (psfg)		Tt,tun (°F)		q (psfa)		qc (psfa)			P atm (psfa)			
-29.7175		-13.1453		63.0198		16.7807		16.5722			2116.2416			
Group 2 Data						Boundary Layer Probe Data								
# of Points		15												
Y bl		Pt,p (psfg)		u/U		qt,tun (psfa)		Tt,tun (°F)		Pt,tun(psf g)		Ps,p (psfg)		u/ue
0		-22.27		0.6204		16.8513		62.9		-13.1562		-28.76		0.6213531
0.01		-21.23		0.6692		16.8696		62.6		-13.1809		-28.79		0.670023
0.02		-20.49		0.6992		16.8032		63		-13.1562		-28.7		0.7001066
0.04		-19.45		0.7418		16.8019		62.6		-13.155		-28.7		0.743127
0.06		-18.59		0.7757		16.77		63.1		-13.1573		-28.68		0.776600
0.08		-17.76		0.8061		16.7568		62.9		-13.1343		-28.65		0.807524
0.1		-17.05		0.8319		16.7813		63		-13.1494		-28.67		0.833652
0.15		-15.4		0.8893		16.7602		63.3		-13.1426		-28.66		0.8908068
0.2		-13.98		0.9366		16.7879		63		-13.158		-28.7		0.937446
0.25		-12.86		0.9705		16.7523		63.1		-13.1199		-28.64		0.972356
0.3		-12.27		0.9889		16.7562		63.2		-13.1344		-28.65		0.990372
0.35		-12.05		0.9953		16.7758		63.1		-13.1348		-28.67		0.997005
0.4		-11.96		0.9974		16.7402		63		-13.1157		-28.62		0.999700
0.45		-12.01		0.9976		16.7606		63.4		-13.1666		-28.69		0.998206
0.5		-11.95		0.9979		16.7434		63.3		-13.118		-28.63		1

[illegible]

[illegible]

(c) Group 3 scanivalve (SV) 3 pressure data
Figure 22. Concluded.

B. WIND TUNNEL RESULTS

The experimental wind tunnel data described in the previous section and presented in the appendices are analyzed in this section in three parts: (1) boundary layer profile analyses; (2) static surface and cavity pressure data analyses; and (3) dynamic flow due to cavity opening. The entrance velocity profile was surveyed in the 24 inch test section at the $x = 4$ " station using the boundary layer total pressure probe. It was found that the flow dynamic pressure was uniform (less than 0.2 percent variation) with an increase of about 0.8 percent in dynamic pressure at the edge of the ceiling and floor boundary layers. A single hot-wire probe was located at the tunnel centerline of the 24" test section at the $x = 4$ " station to measure the streamwise flow turbulence. These data found that the $\Delta u/u$ was approximately 0.003.

1. Test Section Boundary Layer

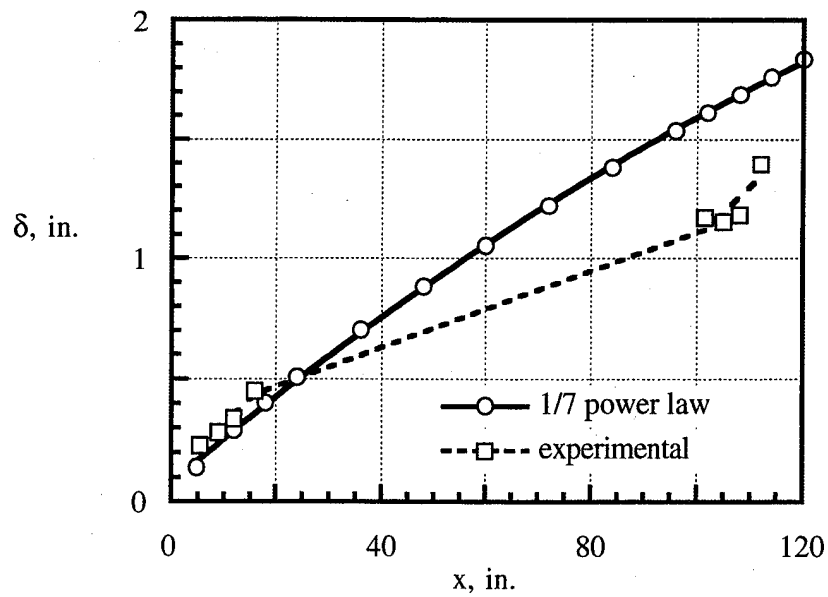
For the plain test section ceiling, the boundary layers were measured at four longitudinal locations in the original 24" test section ($x = 5.5$ ", 9.0 ", 12.0 ", and 16 "") and in the extended 120" test section ($x = 101.5$ ", 105.0 ", 108.0 ", and 112.0 ""). The test-section configurations included the basic 12" by 12" cross section test section with essentially zero pressure gradient ($dp/dx \approx 0$) and the two test section diffuser configurations with adverse pressure gradients ($dp/dx > 0$). These data are analyzed in the following section to evaluate how representative the present basic tunnel data are of a two-dimensional boundary layer over a flat plate.

a. Zero Longitudinal Pressure Gradient

For a two-dimensional, turbulent boundary layer in a zero pressure gradient, the velocity profile may be estimated using the $1/7$ power law

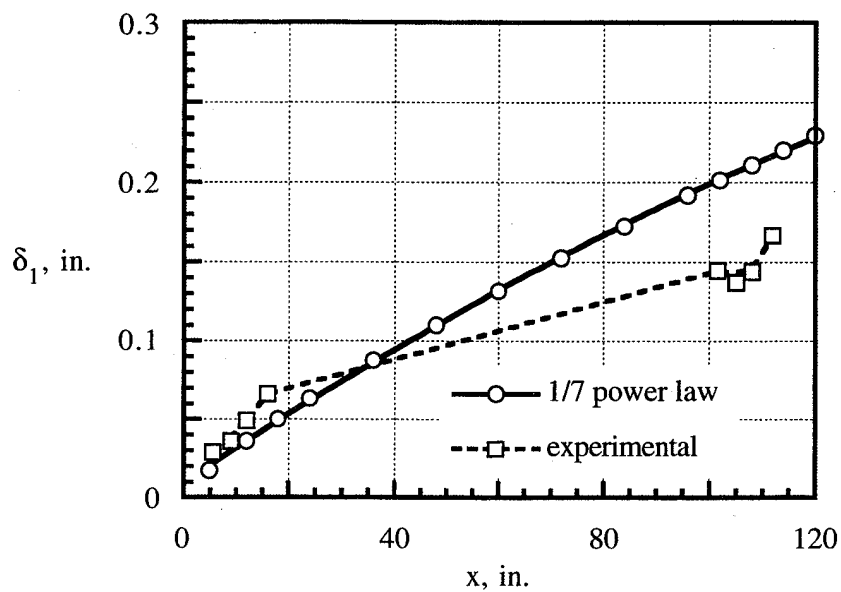
$u/U_\infty = (y/\delta)^{(1/7)}$. The 1/7 power law may then be integrated [Ref. 4] to obtain the above boundary layer thickness quantities as $\delta/x = 0.37 R_x^{-(1/5)}$, $\delta_1/x = 0.37 R_e^{-(1/5)} / (1+n)$ where $n = 7$, and $\delta_2/x = 0.036 R_x^{-(1/5)}$. In the present investigation these relations only apply to the cases where the velocity is constant with increasing run length x ; that is for zero pressure gradient, the tunnel configurations without the 7° and 14° diffusers in the test section.

These three boundary layer thickness parameters (δ , δ_1 , and δ_2) were computed using both the 1/7 power law relations and the experimental data from the SJSU tunnel for both the basic 24" long test section (at $x = 5.5"$, $9"$, $12"$, and $16"$) and the 120" long test section (at $x = 101.5"$, $105"$, $108"$, and $112"$). The results are compared in Figure 23. In the 24" test section data all three experimental thicknesses were found to be slightly greater than the 1/7 power law thicknesses. This could be due to the fact that x was measured from the start of the test section. Ahead of the test section in the contraction the pressure was decreasing ($dp/dx < 0$) so that the boundary layer thicknesses were decreasing. However, they almost certainly do not go to zero at the $x = 0$ station. If the initial station were moved upstream 3 or 4 inches to a virtual origin for application of the 1/7 power law (to more adequately represent the equivalent zero thickness location) then the experimental data would agree with the 1/7 power law relations. The experimental boundary layer profiles for all four stations where the boundary layer was measured in the 24" test section agree with the 1/7 power law profile. As the Reynolds number increases the boundary layer profiles are more nearly one-eighth or one-ninth or a lower power profile. In the 120" test section the boundary layer thicknesses are well below those obtained from the 1/7 power law. If a one-eleventh power law is used to compute the momentum thickness δ_1 agreement with the experimental data can be achieved. For the thicker boundary layer in the 120" test section, the presence of four walls may be the reason that the boundary layer thickness does not grow as large as a two-dimensional boundary layer. While all of the reasons for the difference between the 24" and 120" test sections have not been identified, these effects, especially for the longer test section, will be evaluated numerically in a later section using the incompressible Navier-Stokes equations.



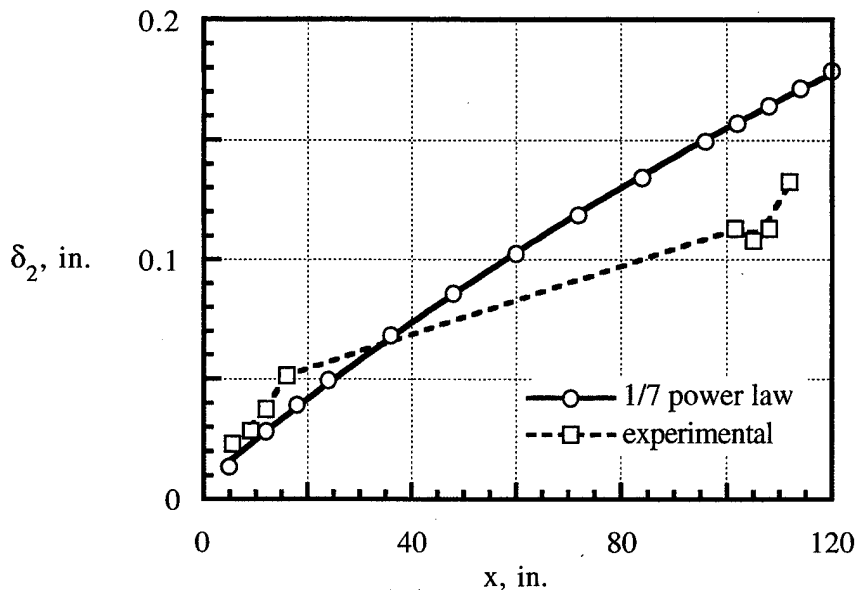
(a) Boundary-layer thickness, δ .

Figure 23. Comparison of experimental data from present investigation using the 24" and 120" test sections with the 1/7 power-law boundary-layer thicknesses.



(b) Boundary-layer-displacement thickness, δ_1 .

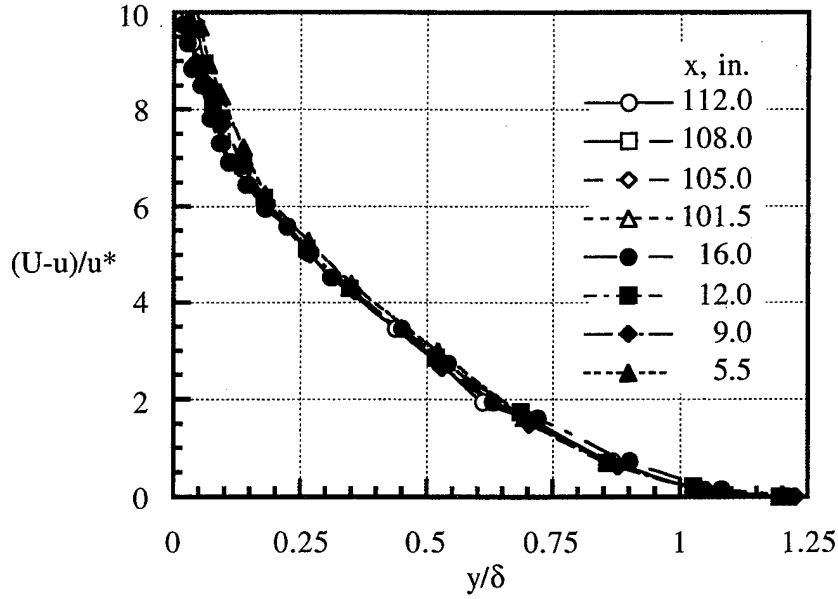
Figure 23. Continued.



(c) Boundary-layer-momentum thickness, δ_2 .

Figure 23. Concluded.

Rotta's analysis [Ref. 9] introduced universal similarity parameters which were later demonstrated by Clauser [Ref. 8]. Clauser plotted data from three separate investigations as u/U versus y/δ which appeared to lack similarity. He then replotted these data using a universal similarity-parameter plot $((u-U)/u^*)$ versus y/δ . This change greatly reduced the data scatter and convincingly demonstrated similarity independent of both Reynolds number and roughness. A similar correlation was done using the data from the present investigation where the 24" test section data (Figure D1) deviated from the 1/7 power law and the 120" test section data (Figure D2) tended to agree with the 1/7 power law. The universal similarity parameter form of these data is presented in Figure 24(a). The data provide a good correlation for most of the boundary-layer profile with only a limited dispersion at heights below 0.15 for the shortest run length data ($x = 5.5$ inches). This correlation provides confidence that these boundary layer profiles are similar and representative of those measured in a two-dimensional boundary-layer.



(a) Experimental data from present investigation.
Figure 24. Universal velocity distribution law comparisons.

In Schlichting [Ref. 4] the velocity defect laws of both von Kármán

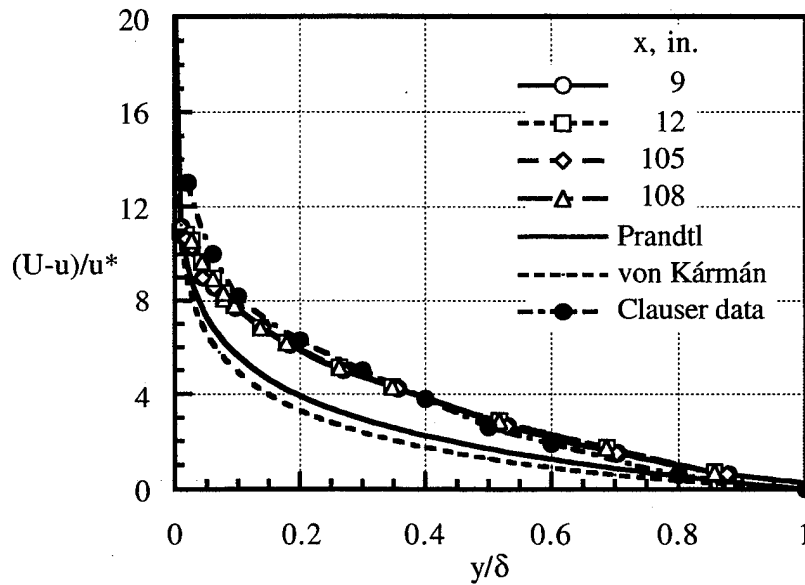
$$\frac{u - U_e}{u^*} = \frac{1}{x} \left\{ \ln \left[1 - \sqrt{1 - \frac{y}{\delta}} \right] + \sqrt{1 - \frac{y}{\delta}} \right\} \quad (16)$$

and Prandtl

$$\frac{U_e - u}{u^*} = \frac{1}{\kappa} \ln \left(\frac{1}{y/\delta} \right) \quad (17)$$

compared favorably with experimental data from both smooth and rough pipes. It is stated that both laws were obtained for two-dimensional flow in a channel. They were found to agree with both two-dimensional and axisymmetric experimental data. Both of these equations are compared in Figure 24(b) with zero pressure gradient, flat plate experimental data both from the present investigation

(Figure 24(a)) and from the experimental data correlation done by Clauser [Ref. 8]. The two sets of experimental data correlate. In contrast to Ref. 4, there is a difference between the two velocity defect laws (equations 16 and 17) and the two sets of experimental data in Figure 24 (b).



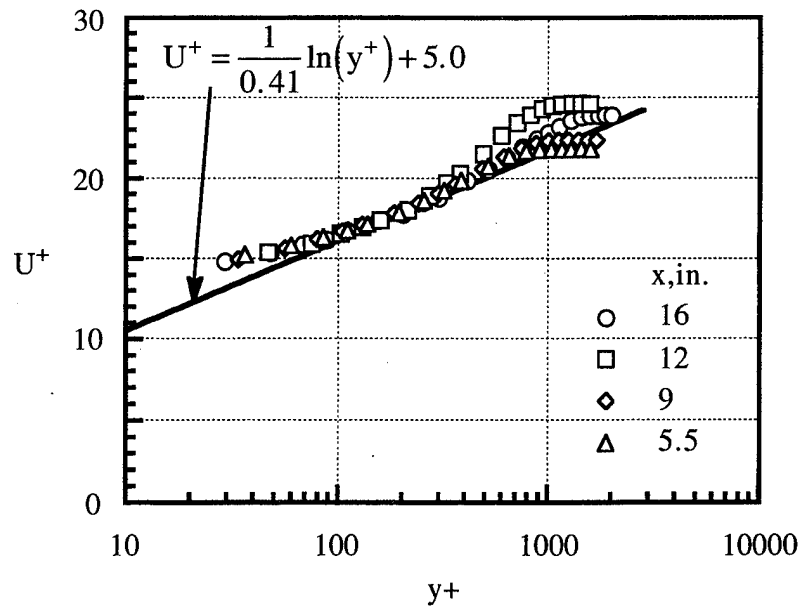
(b) Prandtl and von Kármán equations compared with present investigation and with experimental data correlated by Clauser [Ref. 17].

Figure 24. Concluded.

The data from the SJSU low speed tunnel is compared with log-law relation

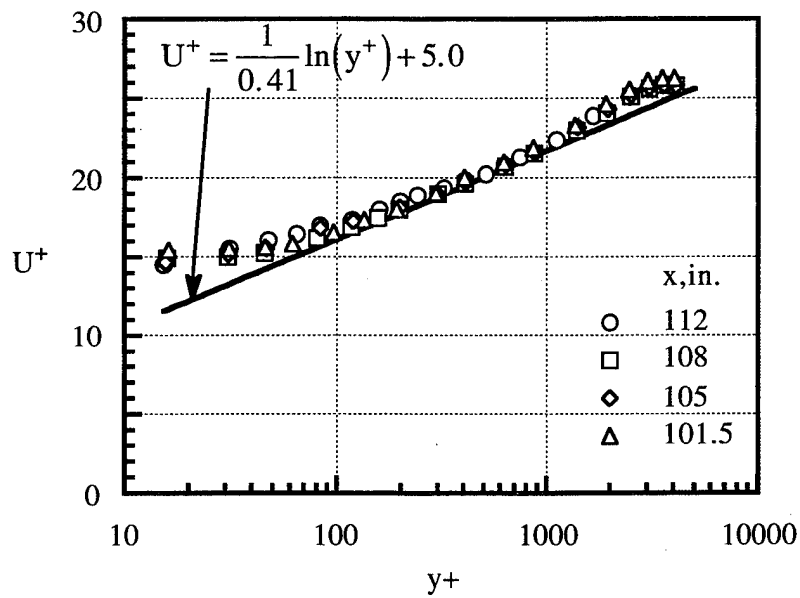
$$U^+ = \frac{1}{\kappa} \ln(y^+) + C_1 \quad (18)$$

in Figure 25 (a) for the standard 24" long test section (where $\delta = 0.23$ at $x = 5.5$ " and $\delta = 0.45$ " at $x = 16$ ") and in Figure 25 (b) for the extended 120" long test section ($\delta \sim 1.17$ " at the locations where the measurements were taken). The comparison is typical of the expected agreement in the log-law region. There is a



(a) 24" test section

Figure 25. Log-law relation using inner variables compared with experimental data from the San Jose State University low speed tunnel.



(b) 120" test section.

Figure 25. Concluded.

boundary layer probe displacement effect at y^+ for low heights in the inner region; and there is a wake effect at y^+ for the greater heights. The wake is characterized by a region at heights approaching the edge of the boundary layer region where the measured velocity is greater than that given by the log law. The specific locations for these effects are given below:

test section length, inches	24	120
boundary layer probe displacement effect below y^+	100	100
boundary layer wake effect at y^+ greater than	300	1000

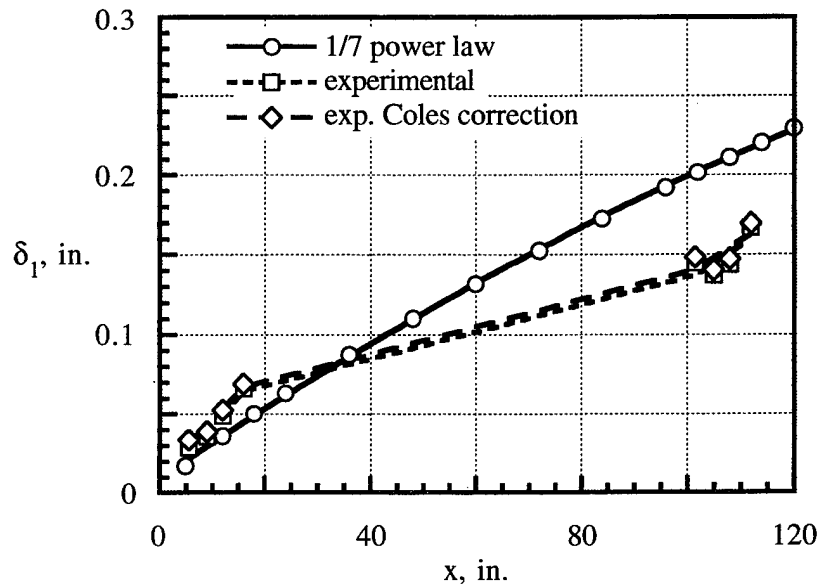
In Figure 25 (a) for the 24" test section there is a larger wake effect at the $x = 12"$ location than at the other locations. It should be noted that the boundary layer run lengths are relatively short and so it should not be surprising that there are differences where the boundary layer is in its initial development. In contrast, as shown in Figure 25 (b) for the 120" test section, where there is a fully developed turbulent boundary layer, there are no significant differences among the wakes. As a consequence, for the y^+ regions both below the boundary layer displacement effect limit and above the wake effect limit the experimental U^+ data is greater than the log law relation. In between these y^+ limits where equation 13 applies, the data in the log law region agrees well with the above log-law equation when the constants are $\kappa = 0.41$ and $C_1 = 5.0$.

Computation of the turbulent boundary layer was the subject of the 1968 AFSOR-IFP-Stanford Conference on Computation of Turbulent Boundary Layers [Ref. 9]. Volume II of reference 9 included a compilation of experimental boundary layer data by Coles and Hirst and a paper by Coles which was a guide to the experimental data compiled for use at the conference by the various predictive methods which were being evaluated. In this paper, Coles discussed two problems associated with evaluation of experimental data: (1) the boundary layer displacement effect where, near the wall, the data are in error because of the effects of probe wall interference and local strong turbulence; and (2) the wake

effect near the edge of the boundary layer where the data are correct but the law-of-the-wake equations are not correct as discussed earlier in this section. To account for the near wall effects, Coles used a standard sublayer profile to obtain the following standard functions to reproduce the tabulated thicknesses:

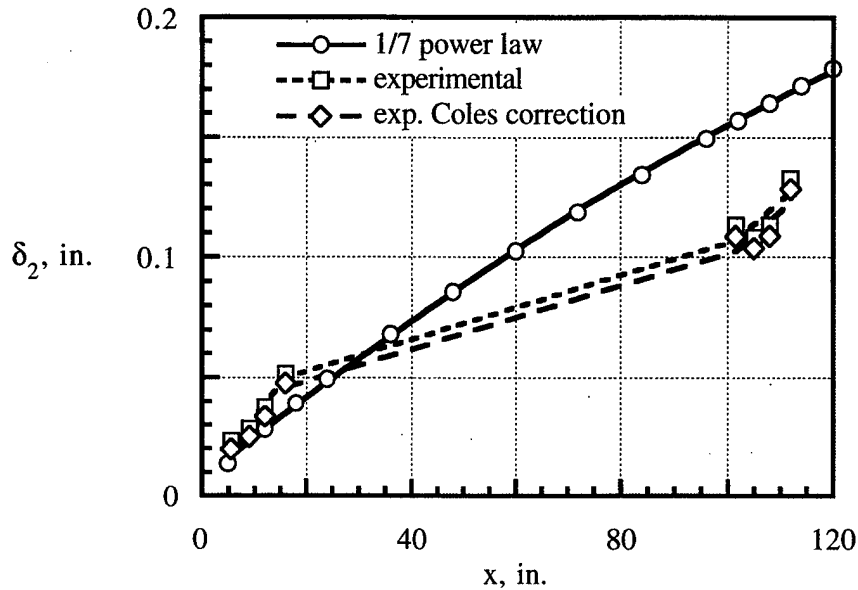
$$\int_0^{50} U^+ dy^+ = 540.6 \quad \text{and} \quad \int_0^{50} (U^+)^2 dy^+ = 6546. \quad (19)$$

The experimental boundary layer displacement thickness and the momentum thickness have been recomputed using these relations (equations 19) and are shown in Figures 26(a) and 26(b), respectively. Here the 1/7 power law results are compared with the experimental data from the SJSU tunnel for both the integrated uncorrected data and these data modified by the above correction procedure. It is shown that the corrections made only a small change to δ_1 and δ_2 . Since these changes are so small, for all of the rest of the boundary layer data in the present paper only the integrated experimental data without the Coles correction will be used.



(a) Boundary-layer displacement-thickness.

Figure 26. Comparison of 1/7 power law boundary-layer thicknesses with experimental data both with and without Coles near-wall correction.



(b) Boundary-layer momentum-thickness.
Figure 26. Concluded.

Relations for turbulent wall-friction were determined using the experimental velocity profile data. Experimentally, the skin friction coefficient may be found using a variety of skin-friction strain gauge-devices, by an obstacle block, by a heat transfer analogy [Ref. 16], by surface flow visualization, by a razor blade technique, by a sublayer fence [Ref. 14 through 17], by a Preston tube [Ref. 18], by empirical correlation [Ref. 17 and 19] or by analysis of the boundary layer profile [Ref. 8, 17, and 20]. In the present report the skin friction was determined from the boundary layer profile using a Clauser plot [Ref. 8]. The log-law equation (equation 8) may be re-arranged to become an implicit equation for skin friction coefficient, giving

$$\frac{u}{U_e} \sqrt{\frac{2}{c_f}} + \frac{1}{\kappa} \ln \sqrt{\frac{2}{c_f}} = \frac{1}{\kappa} \ln \left(\frac{y U_e}{\nu} \right) + C_1 \quad (20)$$

An example of the application of this equation to the analysis of the data from the present investigation is presented in Figure 27 for station 112 inches in the 120

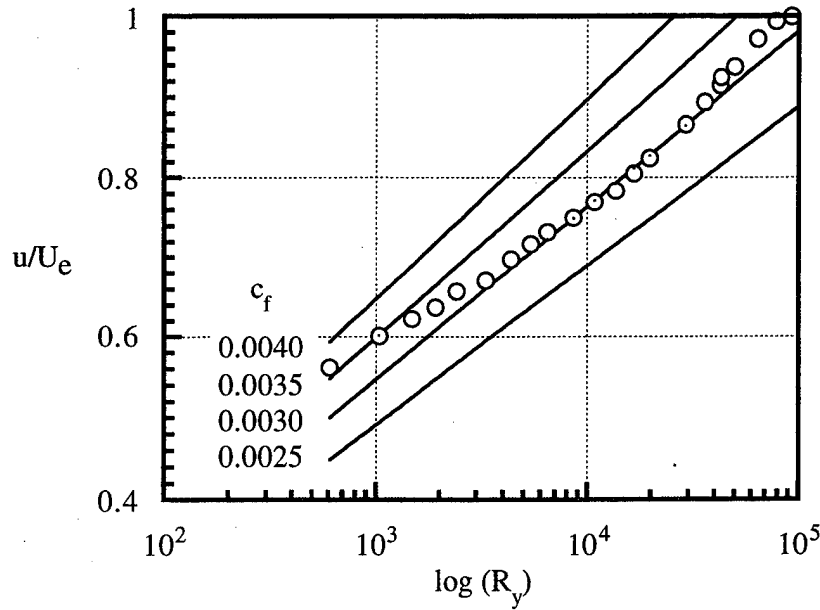


Figure 27. Application of the Clauser plot for the determination of skin-friction coefficient for data from SJSU 120" test section at station 112 inches.

inch long test section where the skin-friction coefficient was found to be 0.0030. Typically, repeat runs had differences in c_f no larger than 0.0002. These results show that while there is a small reduction in skin friction due to the cavity, the differences from the plain wall configuration were nearly within measurement accuracy. This procedure was used to obtain the skin-friction coefficient from all of the data described in the test run schedule (Appendix A).

There are a number of correlations which may be used to estimate the skin-friction coefficient on a flat plate. The equation based on the 1/7 power law has already been given as $c_f = 0.0592(R_x)^{-0.2}$. Another correlation often used is the empirically developed skin-friction equation by Schultz-Grunow [Ref. 19]

$$c_f = 0.37(\log R_x)^{-2.584} \quad (21)$$

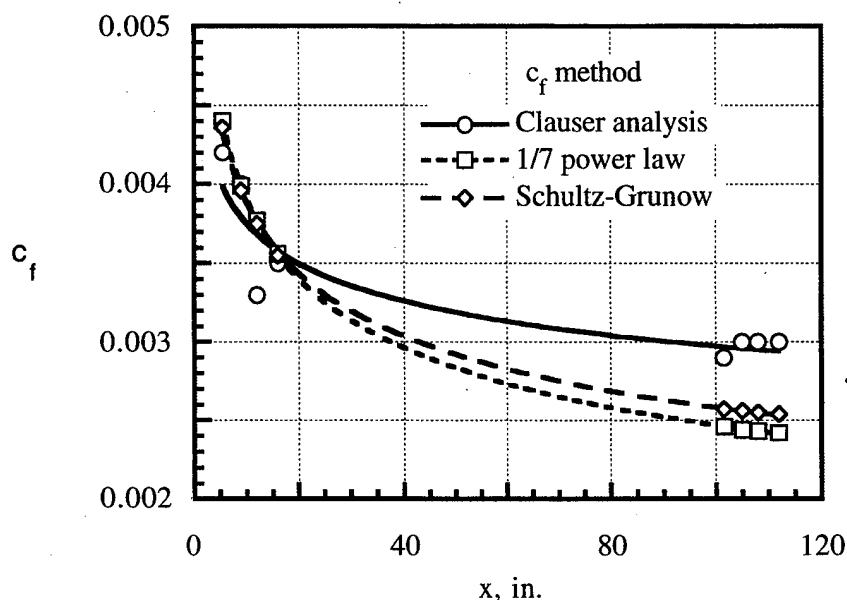
The skin friction coefficients obtained from the Clauser plots for the conditions with zero pressure gradient are compared in Figure 28 (a) with the corresponding values obtained from the 1/7 power law and with the Schultz-Grunow equation.

The correlations and the experimental data agree for the 24" test section. But for the 120" test section both c_f correlations are about 0.0005 less than the experimental data. Whether this difference may be due to surface roughness in the 96" test section extension will be evaluated in the fourth subsection of the general background section.

The following correlation by Ludwig-Tillmann [Ref. 17] was developed to account for the effect of pressure gradients

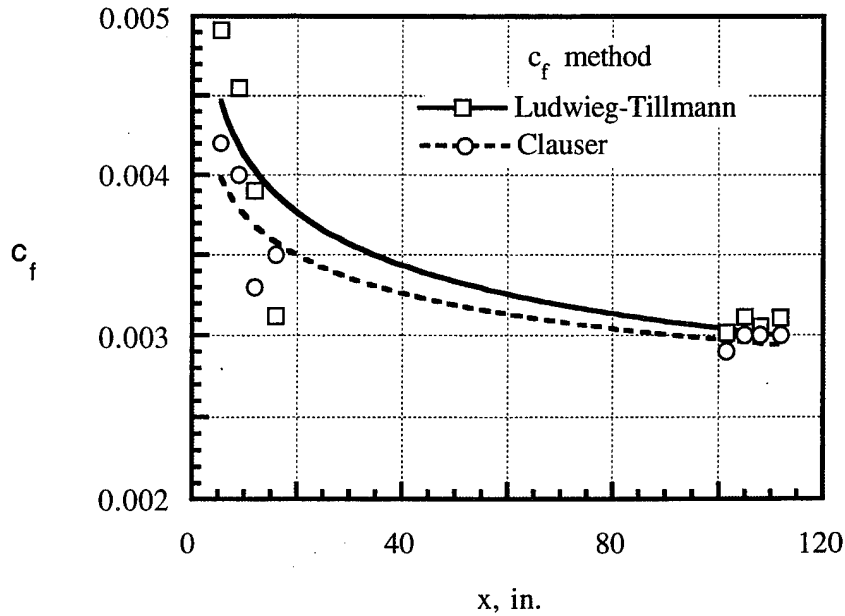
$$c_f = 0.246(R_{\delta_2})^{-0.268} 10^{-0.678H} \quad (22)$$

This correlation is compared with data from both test section lengths in Figure 28 (b). In contrast to the 1/7 power law and Schultz-Grunow correlations in Figure 28 (a), the Ludwig-Tillmann correlation demonstrates good agreement with the Clauser method results. There is scatter for the data from the 24" test section. There is agreement with the experimental data from the 120" test section. This latter comparison for $x > 100$ " represents the major difference between the



(a) Comparison of Clauser analysis of present data from both the 14" and 120" test sections with correlations from 1/7 power law and by Schultz-Grunow.

Figure 28. Comparisons of skin friction from several methods.



(b) Comparison of Clauser analysis with the Ludwig-Tillmann correlation.
Figure 28. Concluded.

Ludwig-Tillmann correlation and both the 1/7 power law and Schultz-Grunow correlation.

Initially, the pressure distributions for the 24" and 120" long test sections were measured. An example of the measured pressure distribution on the short test section ceiling is presented in Figure 29 using open circle symbols. These data show a reduction in c_p with increasing x distance from the test section entrance. The measured pressure gradient was $\frac{dc_p}{dx} = -0.000643$. This c_p decrease was caused by the small increase in local velocity due to the expected increase in displacement thickness. At an arbitrary x location the effective test section cross-section area for the flow may be expressed as the physical dimension reduced by the boundary layer displacement thickness on each surface, giving

$$A = (12.0 - 2\delta_1)^2 \quad (23)$$

and the local velocity using the incompressible continuity equation becomes

$$U_2 = U_1 A_1 / A_2 \quad (24)$$

Finally, the computed c_p is given by

$$c_p = 1 - \left(\frac{u_1}{U_\infty} \right)^2 \quad (25)$$

The c_p change due to the increasing δ_1 is called the buoyancy correction. For the four stations where the boundary-layer profile was measured, the buoyancy-induced c_p was computed and is presented in Figure 29 as solid square symbols. The two curves shown provide reasonable agreement and illustrate why the pressure gradient was negative.

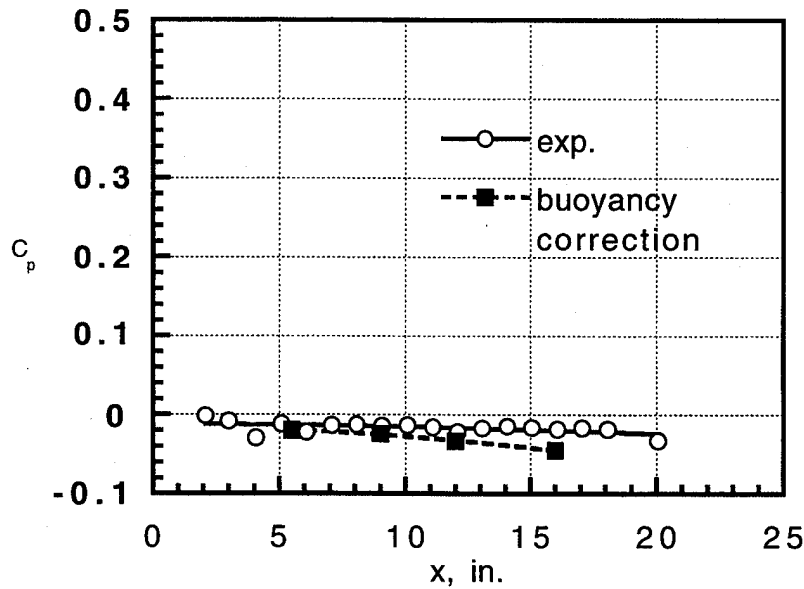
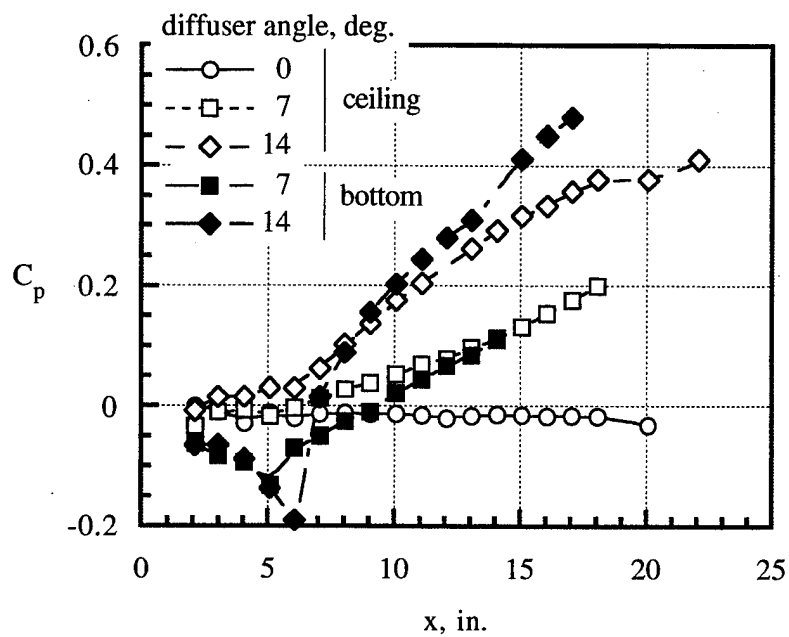


Figure 29. Effect of buoyancy on pressure distribution on the ceiling of the 24" long test section.

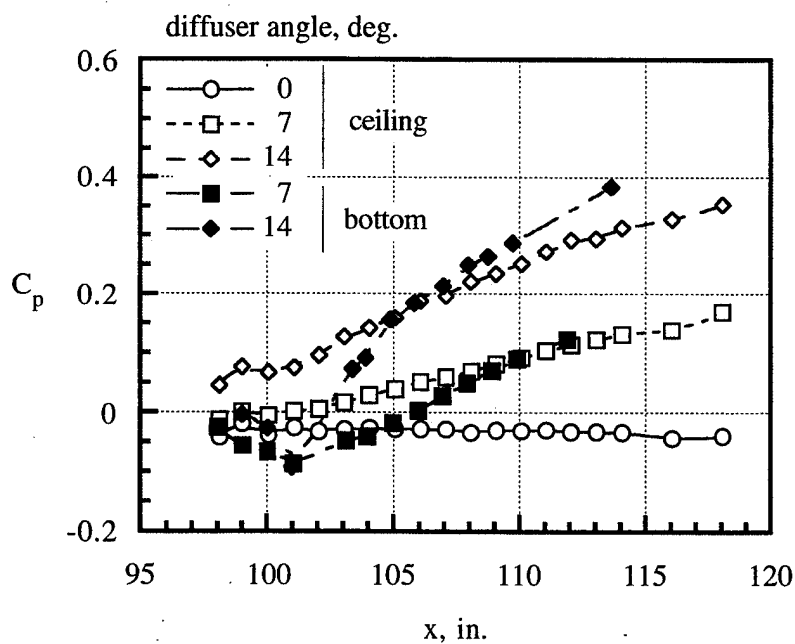
b. Adverse Pressure Gradient

The pressure distributions measured in the original test section and in the test section with the diffuser are presented in Figure 30. When either test section diffuser (7° or 14°) was installed the reference velocity (or dynamic pressure) was measured by a pitot-static probe located at station 1". The surface pressure data from both test section lengths showed a difference between the test section ceiling flat surface and the test section floor with a deflected surface. On the test section floor at station 6" (or 102"), the surface had an obtuse angle where there was an abrupt change of flow direction. As discussed in Milne-Thompson [Ref. 87] for potential flow, the velocity is locally infinite at an angle apex. The effects of a sharp corner in viscous flow also show an increased, but finite, velocity. At the angle apex, measured pressure coefficients were of the order of minus one and increased rapidly a small distance from the corner to a few tenths. These flows are discussed in greater detail by Mason [Ref. 88]. The data from the present investigation confirms the trends discussed above. The floor pressure distribution had a discontinuity near the angle apex at station 6" (or 102") where the local pressure coefficient peaked as low as -0.19 at $x = 7.4$ " for the 24" test section and at about -0.1 at $x = 5$ " for the 120" test section. These pressure coefficients correspond to 10% or 5% velocity increases, respectively.

The inviscid pressure distribution for both test section diffusers was computed using the low-order panel method PMARC [Ref. 89] and the results for the 7° diffuser are presented in Figure 31. Without viscosity the pressure peak near the bottom apex angle is seen to peak at about -0.10 for the 7° diffuser which is similar to the experimental data and at about -1.40 for the 14° diffuser which is much lower than the experimental data in Figure 31. This indicates that while the flow for the 7° diffuser was attached, the flow for the 14° diffuser may have separated near the angle apex and as a result generate a reduced pressure peak.



(a) SJSU 24" test section.
Figure 30. Measured longitudinal pressure gradient.



(b) SJSU 120" test section.
Figure 30. Concluded

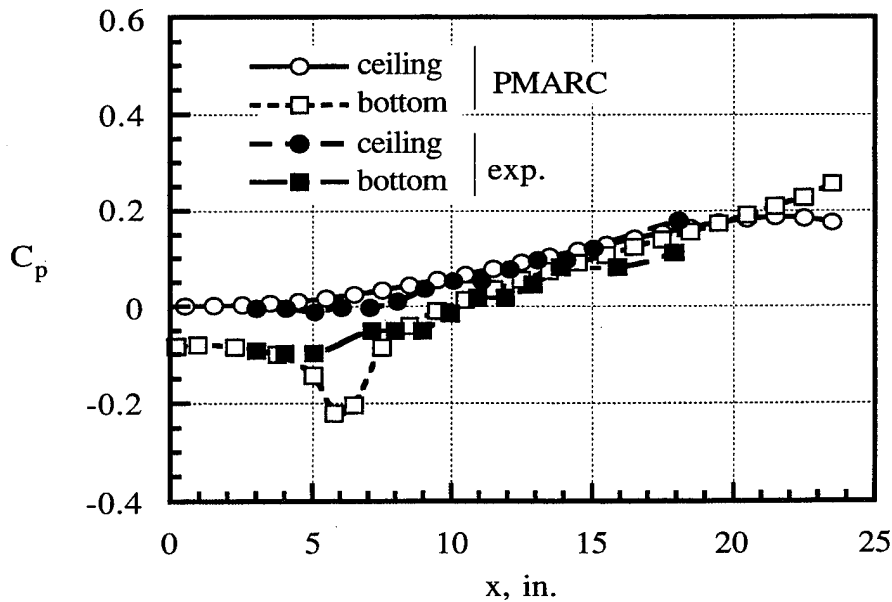
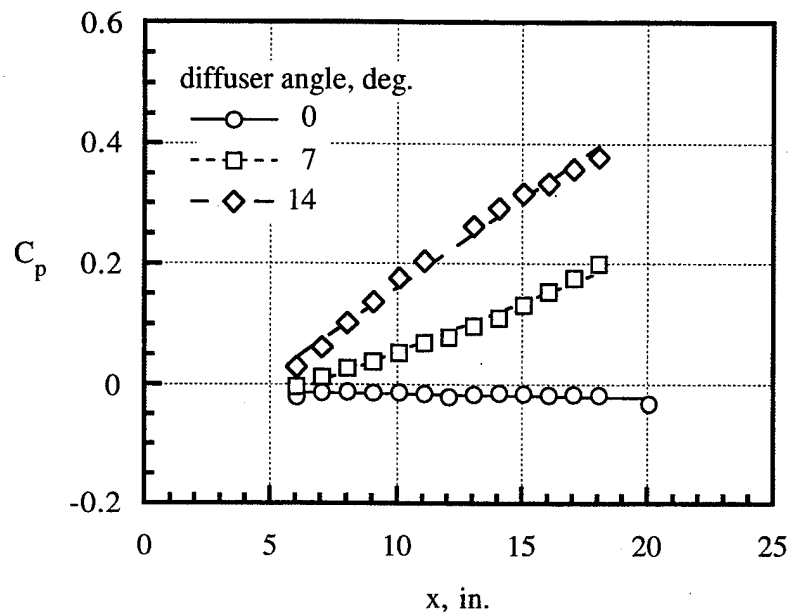


Figure 31. Test-section pressure distribution computed by the inviscid panel-method PMARC [Ref. 90] for the 24" test-section with the 7° test-section diffuser.

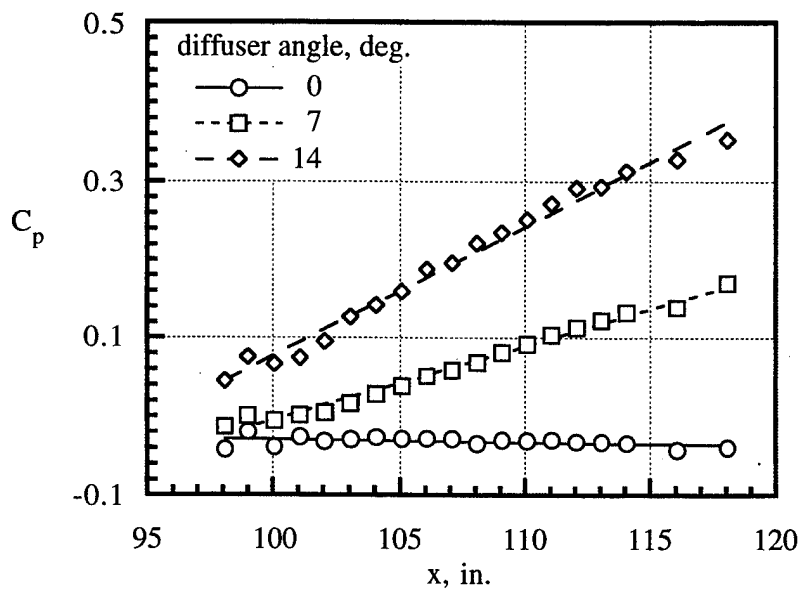
Since the velocity was subsonic, the streamlines above the angle apex should quickly smooth out, and the disturbance die down exponentially with increasing distance [Ref. 88]. The ceiling pressure-distributions for all six test section configurations show the expected and desired smooth profile in the vicinity of the cavity location(s). The 14° diffuser data still has a slope change near station 6" (or 102") and shows the effect on the ceiling pressure-distribution of the change in pressure gradient slope at station 6" (or 102"). The comparison between the two test sections shows that the thicker boundary layer (see Figure 30) in the 120" test section was more effective in smoothing the c_p distribution on the ceiling pressure-distribution. These data also show that there was no significant flow separation apparent in these experimentally measured profiles.

The experimental pressure distributions in the 0°, 7°, and 14° diffuser constant-angle portions of both the 24" and 120" long test sections are presented in Figure 32. These data show a linear variation of c_p with x location. Repeatability is shown by the data for the 14° diffuser.



(a) 24" long test section.

Figure 32. Effect of diffuser angle on the test section ceiling pressure distribution.



(b) 120" long test section.

Figure 32. Concluded.

The resultant pressure gradients are tabulated below and plotted in Figure 33.

Test Section Length, in.	Diffuser Angle, deg.	height at test section diffuser entrance(x=6"), in.	$\frac{dc_p}{dx}$, 1/in.
24.	0	12.0	-0.00064
24.	7	10.0	0.01103
24.	14	7.4	0.02443
120	0	12.0	-0.00036
120	7	10.0	0.00944
120	14	7.4	0.01653

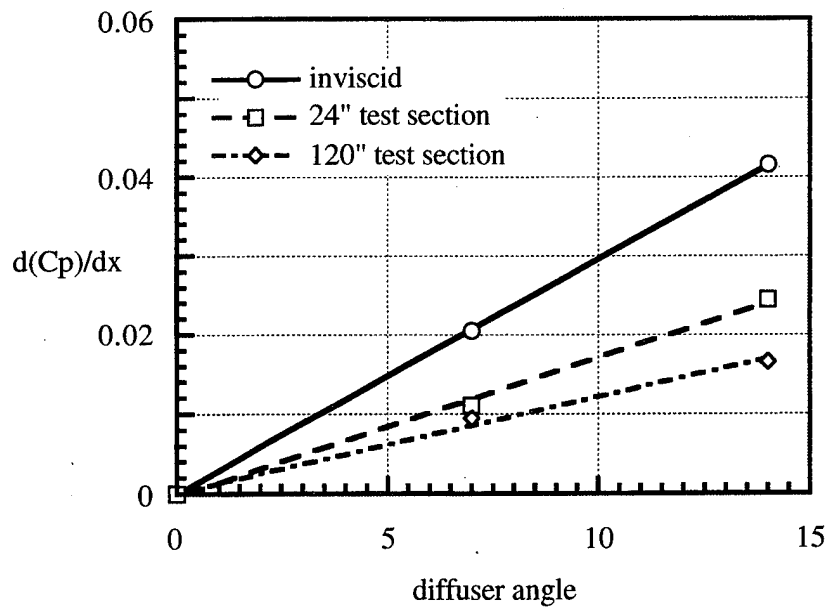


Figure 33. Test section pressure gradient as a function of the diffuser angle.

Also shown in Figure 33 is the pressure coefficient for inviscid flow. This curve was computed using equation 24 with $U_1 = U_\infty$, the velocity at the test section entrance, and equation 25. The effect of boundary layer growth is to increase local velocity above that computed inviscidly, as described above for Figure 29. The slopes shown in Figure 33 are listed below:

Case	$\left(\frac{dc_p}{dx}\right)/\phi, 1/\text{deg.}$
inviscid	0.00297
24" long test section	0.00175
120" long test section	0.00121

These data show a 41% and a 60% reduction for viscous effects on the pressure gradient per degree of diffuser angle in the 24" and 120" long test sections, respectively.

Boundary-layer profiles were measured on the ceiling of the test section at four longitudinal stations in each test section: $x = 5.5", 9", 12",$ and $16"$ in the 24" test section; or $x = 101.5", 105", 108",$ and $112"$ in the 120" test section. These boundary-layer profiles are presented in Appendix D in the following figures:

Configuration	Test Section length, in	Diffuser Angle, deg.	Figure
0000	24	0	D1
8000	120	7	D2
0700	24	14	D3
8700	120	0	D4

Configuration	Test Section length, in	Diffuser Angle, deg.	Figure
1400	24	7	D5
8400	120	14	D6

These profiles were used to compute the boundary-layer thickness δ , displacement thickness δ_1 , momentum thickness δ_2 , pressure-gradient parameter β , the ratio of Clauser defect thickness to boundary-layer thickness Δ/δ , and shape factor G which are presented in the following figures:

Parameter	δ	δ_1	δ_2	β	Δ/δ	G
Figure	34	35	36	37	38	39

The data from the 24" test section are presented in part (a) and from the 120" test section are presented in part (b) of each of the above figures.

The boundary-layer thickness, boundary-layer displacement thickness, and the boundary-layer momentum thickness data for the basic test sections (configurations 0000 and 8000) without pressure gradients were compared in Figure 23 with results from application of the 1/7 power law. While the 24" test section data were found to agree with the 1/7 power law, the higher Reynolds number 120" test section data tended to agree with a lower order 1/11 power law. For the 24" test section the addition of the 7° and 14° diffusers reduced the values of δ , δ_1 , and δ_2 at corresponding stations in the divergent section ($x = 9"$, $12"$, and $16"$). In contrast, for the 120" test section the addition of the 7° and 14° test-section diffusers increased the values of δ , δ_1 , and δ_2 at the corresponding stations in the divergent section ($x = 105"$, $108"$, and $112"$).

The Clauser equilibrium parameter β is often used to characterize the magnitude of a pressure gradient. The dominant term in this parameter is the

pressure gradient, dp/dx . This term is multiplied by the ratio of displacement thickness to skin friction. In Clauser's paper [Ref. 8], constant values of β were used to characterize equilibrium boundary layers. The results in Figure 37 show that the present investigation achieved equilibrium for configurations 0000, 8000, and 0700. The Clauser equilibrium parameter for the 24" test section presented in Figure 37(a) shows a variation similar to the actual pressures shown in Figure 32(a). The Clauser equilibrium parameter for the 120" test section presented in Figure 37(b) also shows a variation similar to the actual pressures shown in Figure 32(b) except for the 7° diffuser. Inspection of the values that make up the Clauser equilibrium parameter show that the skin friction coefficients and displacement thicknesses were nearly constant, which lead to a small variation of β .

Another measure of the pressure gradient is the Clauser shape factor [Ref. 8], which is the ratio of the second to the first moment about the axis $(U-u)/u^* = 0$. Another useful parameter is the Clauser defect thickness Δ . The relation of G to the universal parameter Δ/δ was originally shown by Clauser [Ref. 8]. Equivalent information from the present investigation are shown in Figure 38. These data indicate that the test section diffusers induced a relatively modest adverse pressure gradient.

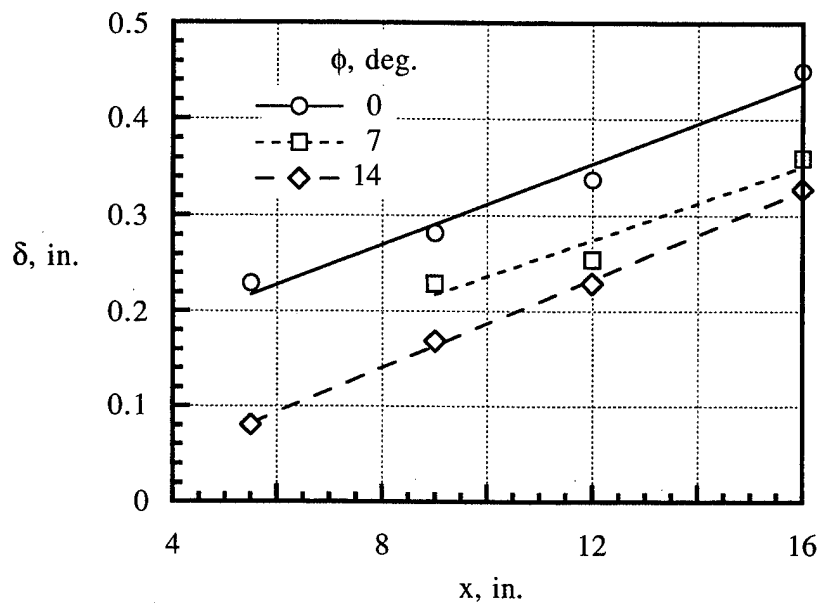
The conventional shape factor H is often used as an indication of flow separation. Schlichting [Ref. 4, page 630] indicates that separation occurs when $H \approx 1.8$ to 2.4. The data in Figure 39 show that all of the test sections gave shape factors which were well below 1.8. It is interesting to observe that the no-diffuser configuration for the 24" test section had shape factors greater than either of the two diffuser configurations. In contrast, the opposite relation was measured in the 120" test section. All of these data show that the goal of obtaining adverse pressure gradients without flow separation was achieved in the present investigation.

The log-law relation (equation 18) for the data from the SJSU low speed tunnel was presented in Figure 25 and showed the expected agreement. The corresponding data for the 7° and 14° test section diffusers are presented in Figure 40. The data for the 24" test section (Figures 40(a) and (b)) show reasonable agreement with the law-of-the wall equation using the generally-accepted

empirical constants. In contrast, the 120" test-section data fell below the law-of-the wall equation. This is consistent with the fact that the boundary layer thickness δ was less than that given by the 1/7 power law. It appears that this boundary layer thickness is characteristic of a higher Reynolds number flow consistent with a 1/9 to as low as a 1/11 power-law correlation depending on the x station of the boundary-layer survey.

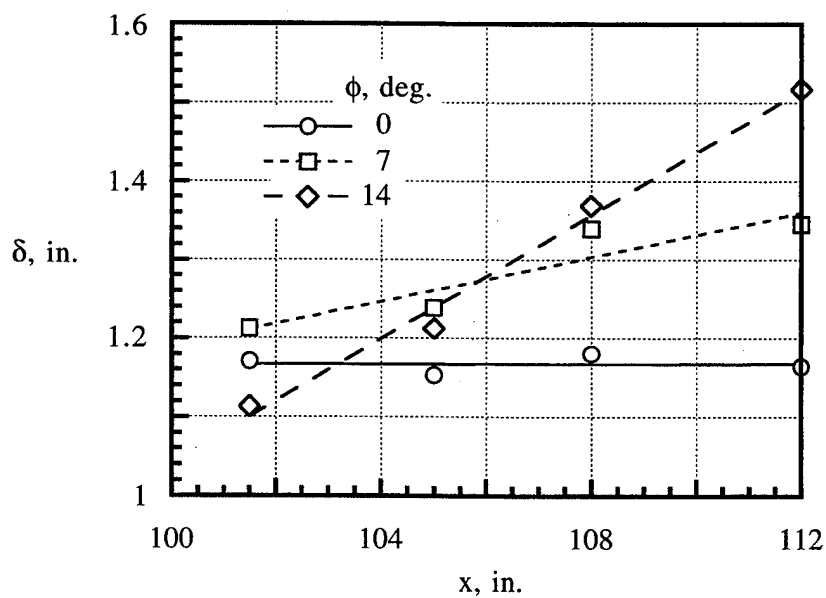
Clauser [Ref. 8] used a universal plot of equilibrium turbulent velocity profiles, $(U-u)/u^*$ versus y/Δ , to display the effect of boundary-layer run length on the boundary-layer shape. The increasing x distance was shown in Figure 37(a) to correspond to the greatest increase in the pressure-gradient parameter β achieved in this investigation. The resultant effect of the pressure gradient on the velocity profile is shown in Figure 41(b) using data from the 24" test section with the 14° diffuser. The changing velocity profile from station 5.5" to station 16" due to increasing β is consistent with the changes shown by Clauser.

Since these profiles seemed to depend more on x location than specific diffuser geometry, the data from Figure 41 was replotted at a given x location for the 24" test section in Figure 42 and for the 120" test section in Figure 43. The data at station 5.5" (Figure 42(a)) showed an anomaly in that an apparently large effect of pressure gradient was present. For this station the 7° data was apparently invalid and the 14° data showed a large profile change. The other three stations from the 24" test section showed only small profile changes consistent with the data correlation shown in Figure 38. For the 120" test section the expected larger profile changes due to the larger pressure gradient parameter variation are seen. At $x = 101.5"$ there was no pressure gradient, so the boundary layer profiles are seen to be in equilibrium. That is, all three surveys are the same. At the next three stations there was an increasing gradient in the pressure variation with increasing x which is consistent with increasing pressure gradient parameter, β .



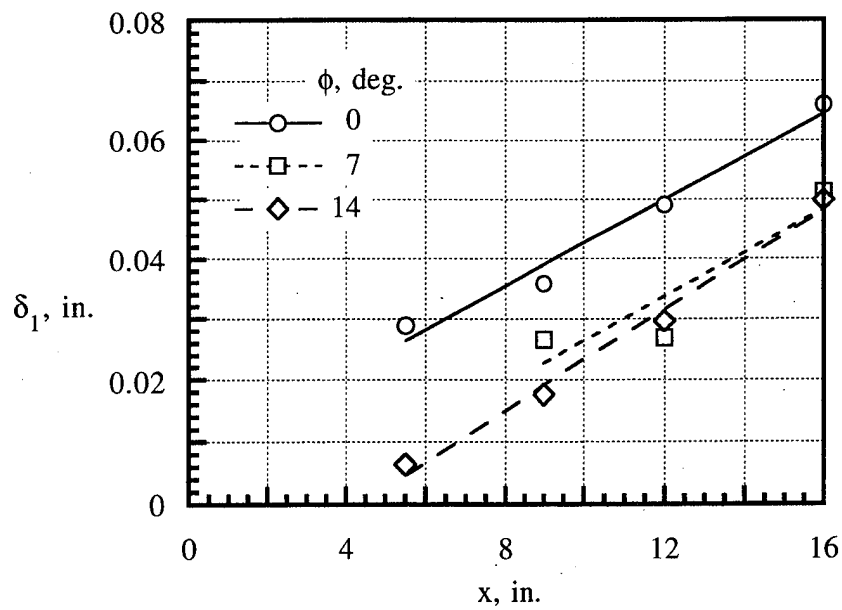
(a) 24" test section.

Figure 34. Effect of test-section diffuser angle on the variation of boundary-layer thickness as a function of longitudinal location.



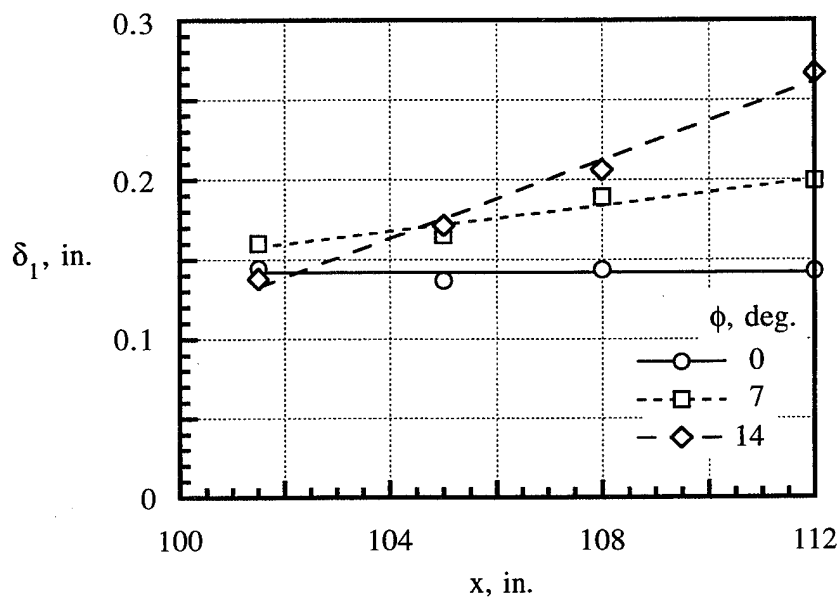
(b) 120" test section.

Figure 34. Concluded.

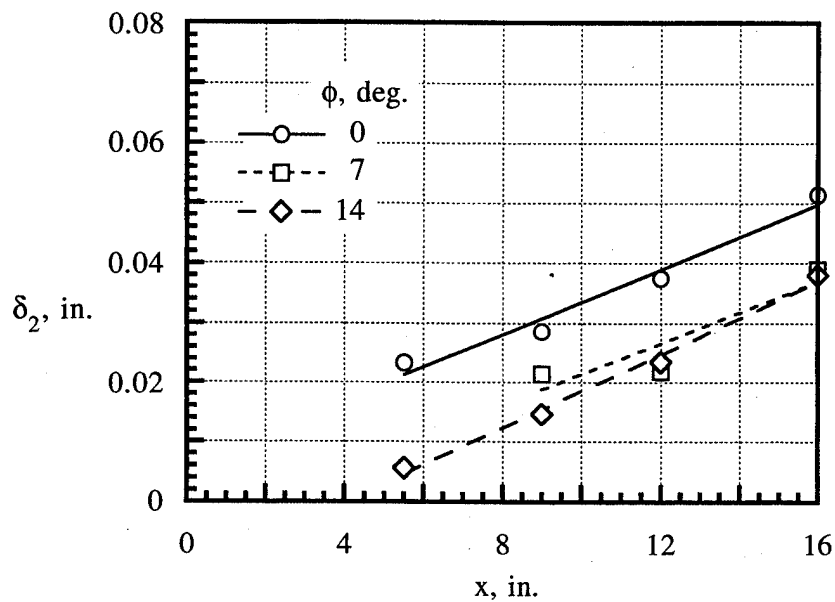


(a) 24" test section.

Figure 35. Effect of test-section diffuser angle on the variation of boundary-layer displacement thickness as a function of longitudinal location.

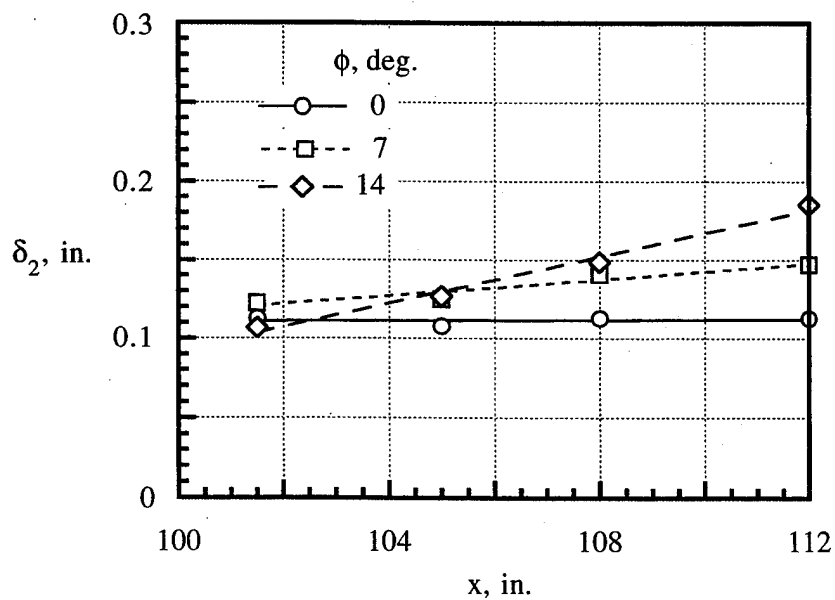


(b) 120" test section.
Figure 35. Concluded.

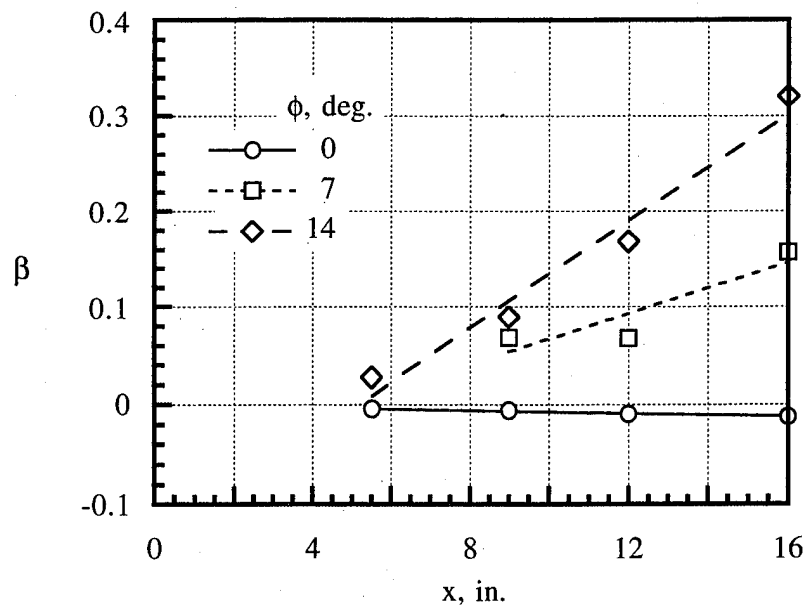


(a) 24" test section.

Figure 36. Effect of test-section diffuser angle on the variation of boundary-layer momentum thickness as a function of longitudinal location.

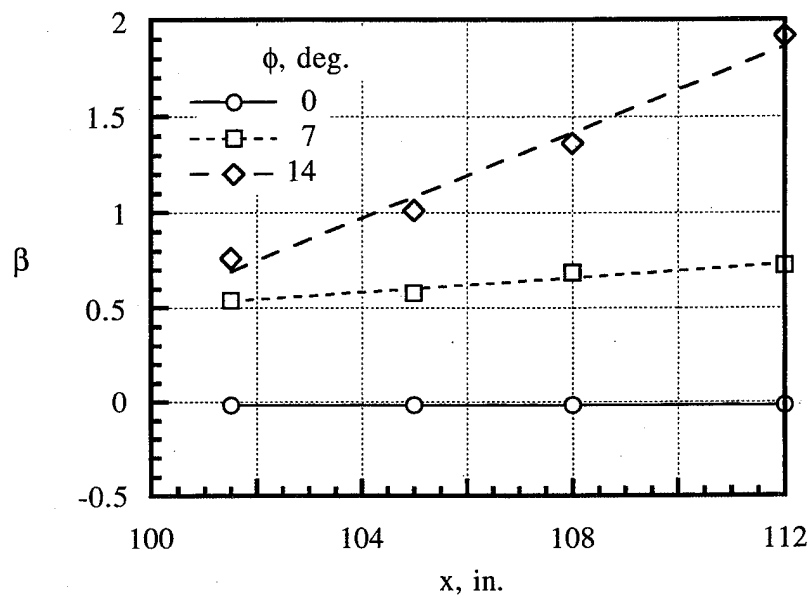


(b) 120" test section.
Figure 36. Concluded.

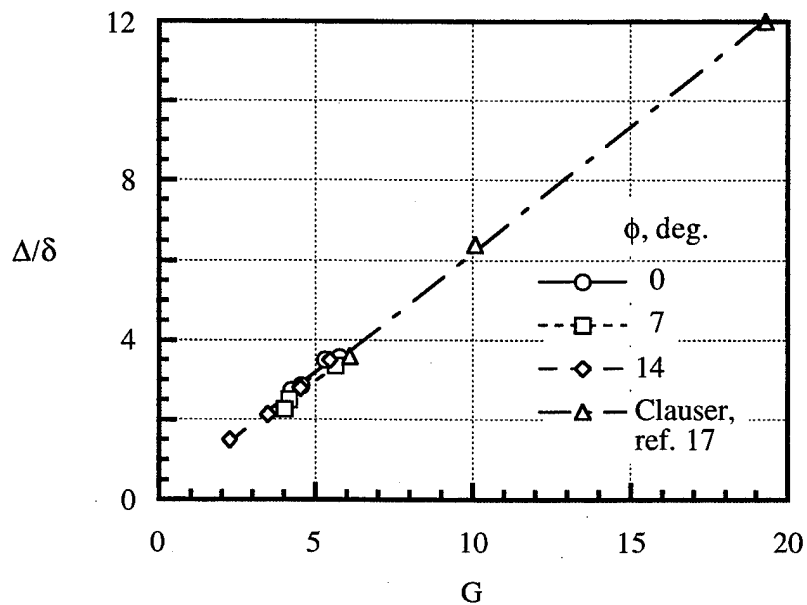


(a) 24" test section.

Figure 37. Effect of test-section diffuser angle on the variation of freestream pressure-gradient parameter as a function of longitudinal location.

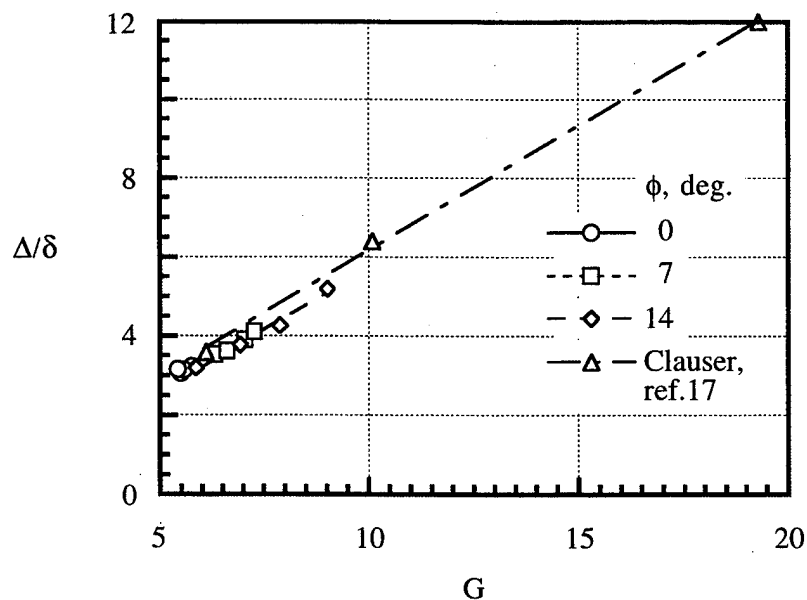


(b) 120" test section.
Figure 37. Concluded.

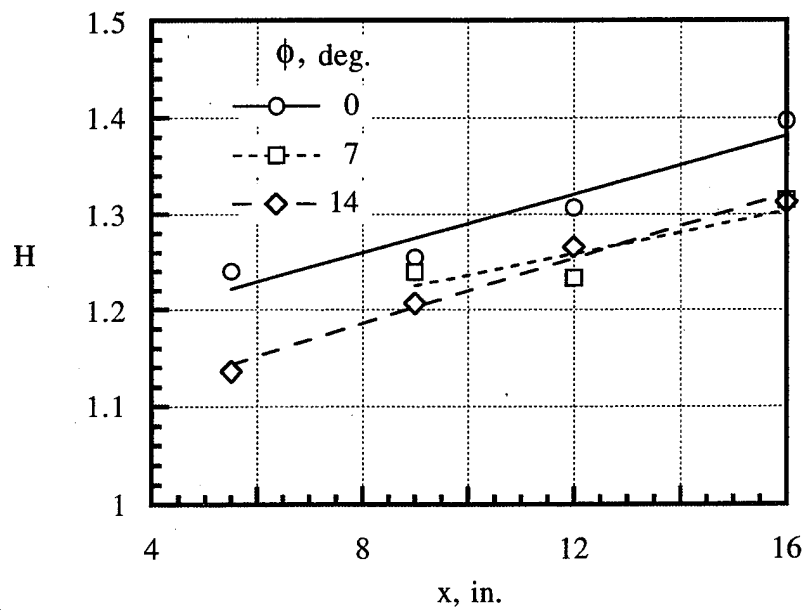


(a) 24" test section.

Figure 38. Effect of test-section diffuser angle on the ratio of the Clauser defect thickness to the boundary-layer thickness as a function of the Clauser shape factor.

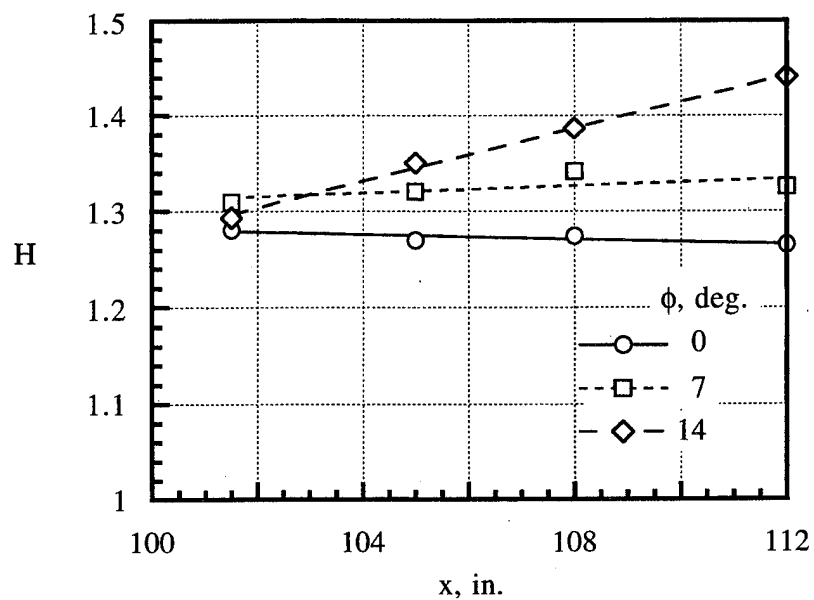


(b) 120" test section.
Figure 38. Concluded.

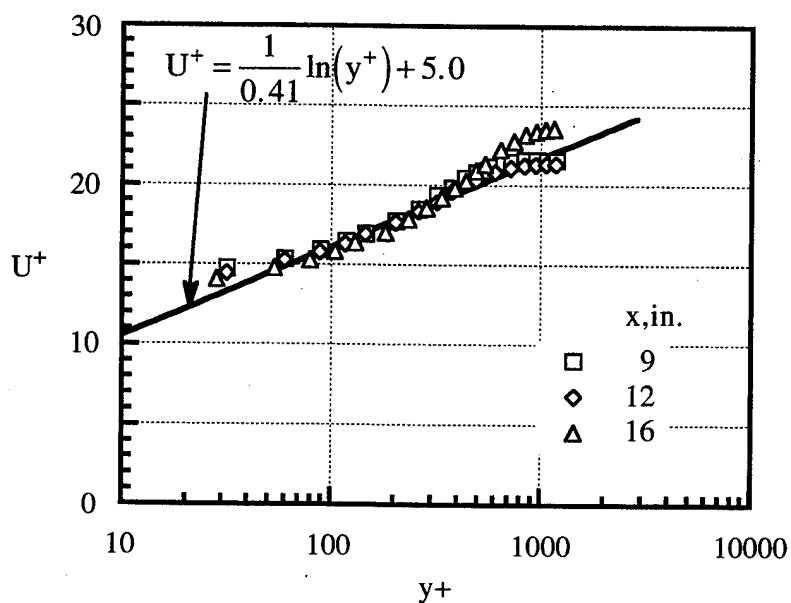


(a) 24" test section.

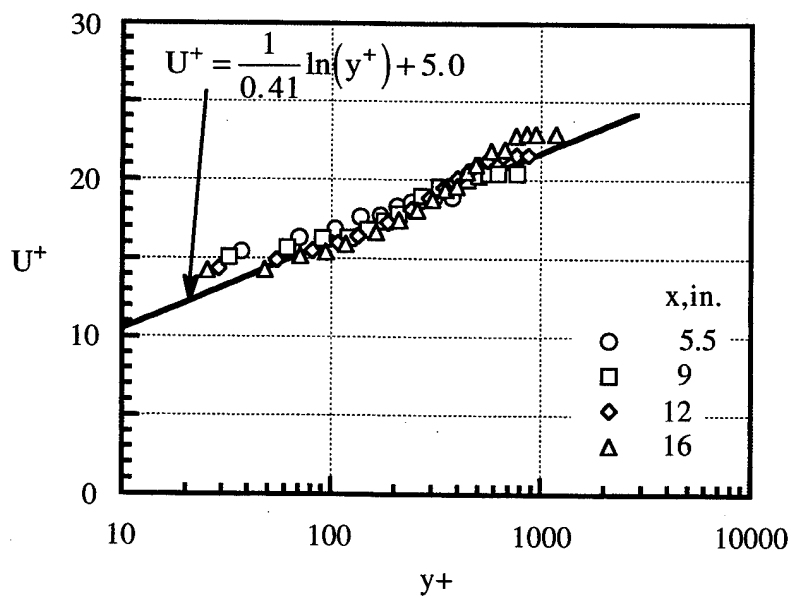
Figure 39. Effect of test-section diffuser angle on the variation of shape factor as a function of longitudinal location.



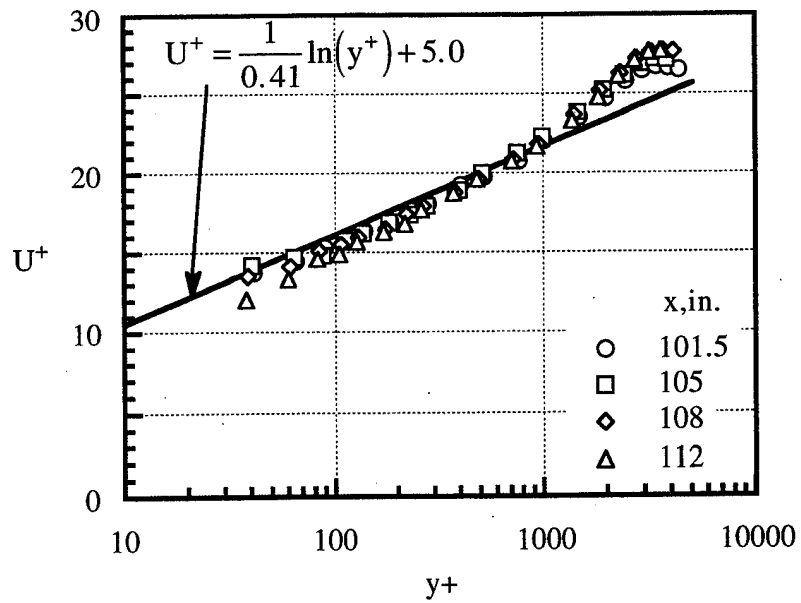
(b) 120" test section.
Figure 39. Concluded.



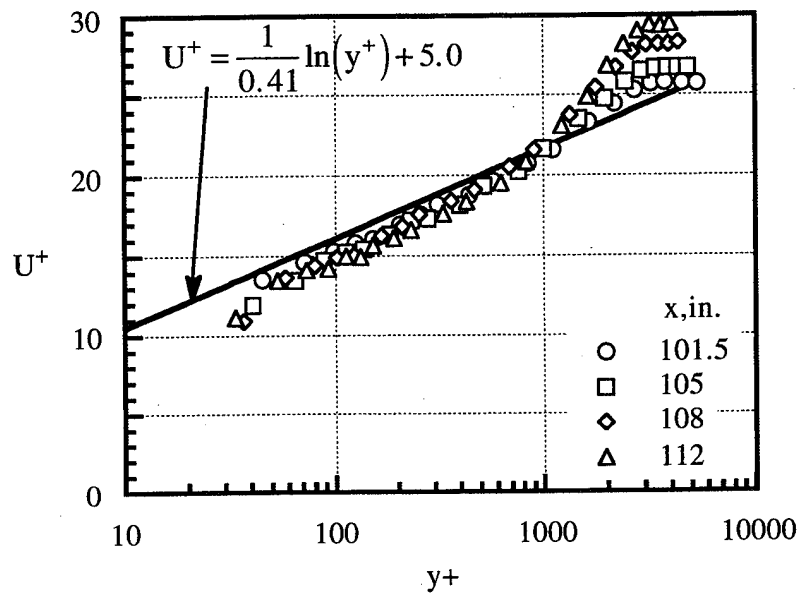
(a) 24" test section with 7° diffuser.
 Figure 40. Effect of test-section diffuser angle on the variation of boundary-layer thickness as a function of longitudinal location.



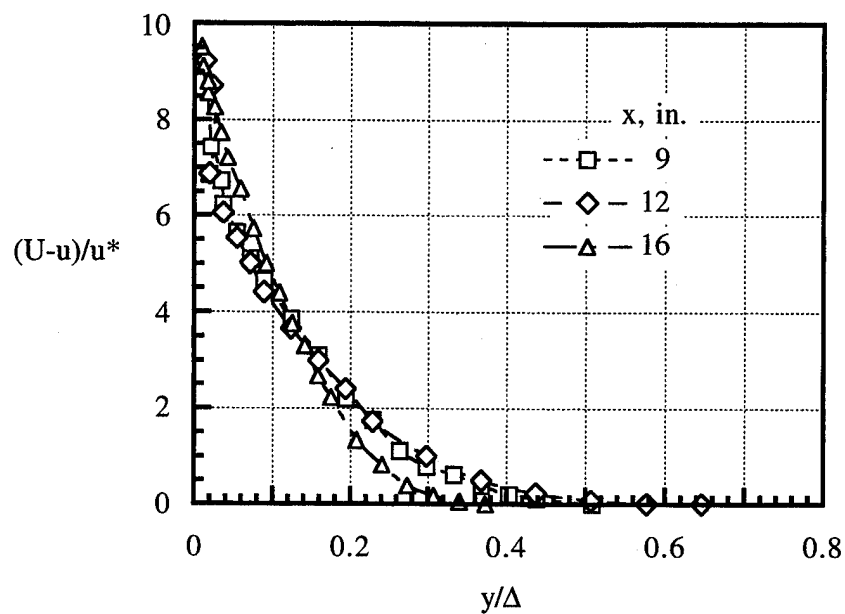
(b) 24" test section with 14° diffuser.
 Figure 40. Continued.



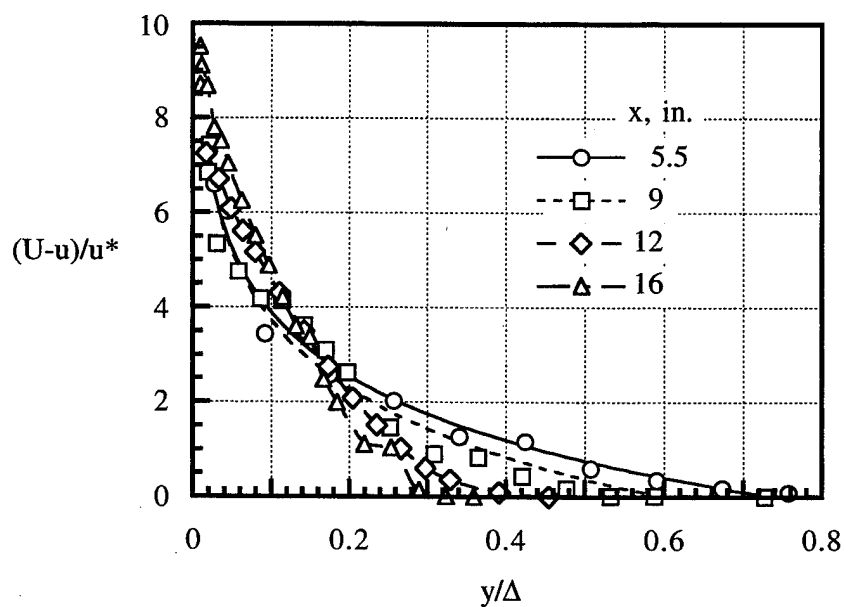
(c) 120" test section with 7° diffuser.
Figure 40. Continued.



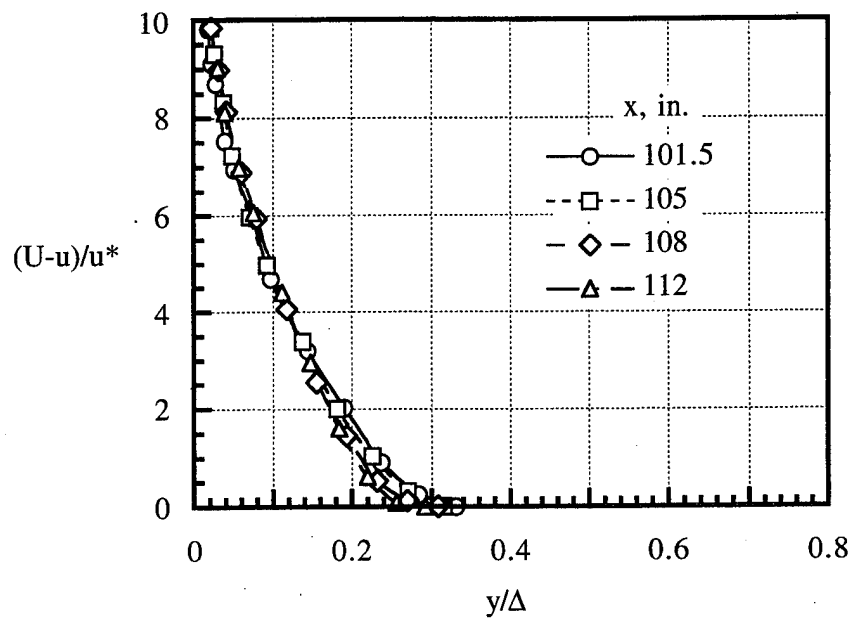
(d) 120" test section with 14° diffuser.
Figure 40. Concluded.



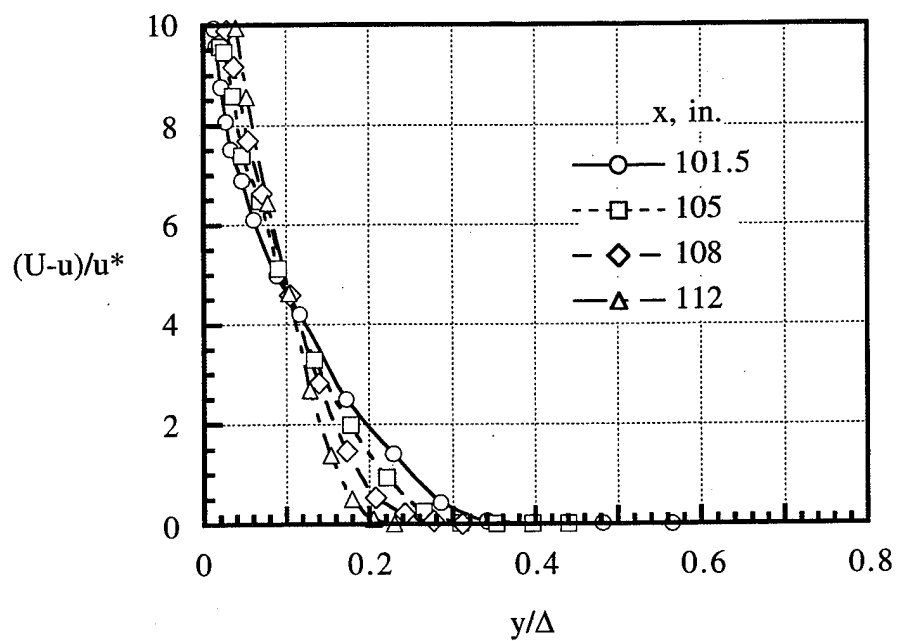
(a) 24" test section with 7° diffuser.
 Figure 41. Effect of test-section survey longitudinal position on the universal velocity distribution.



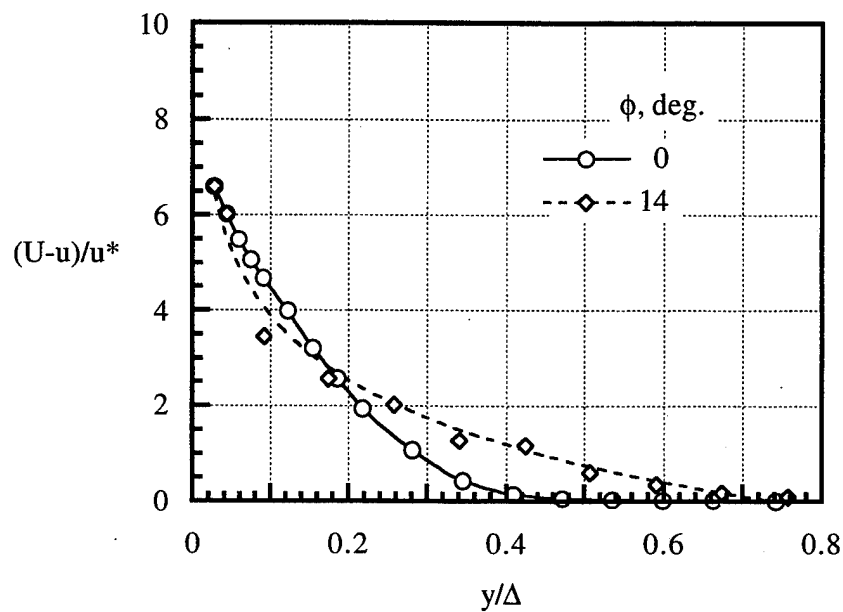
(b) 24" test section with 14° diffuser.
 Figure 41. Continued.



(c) 120" test-section with 7° diffuser.
Figure 41. Continued.

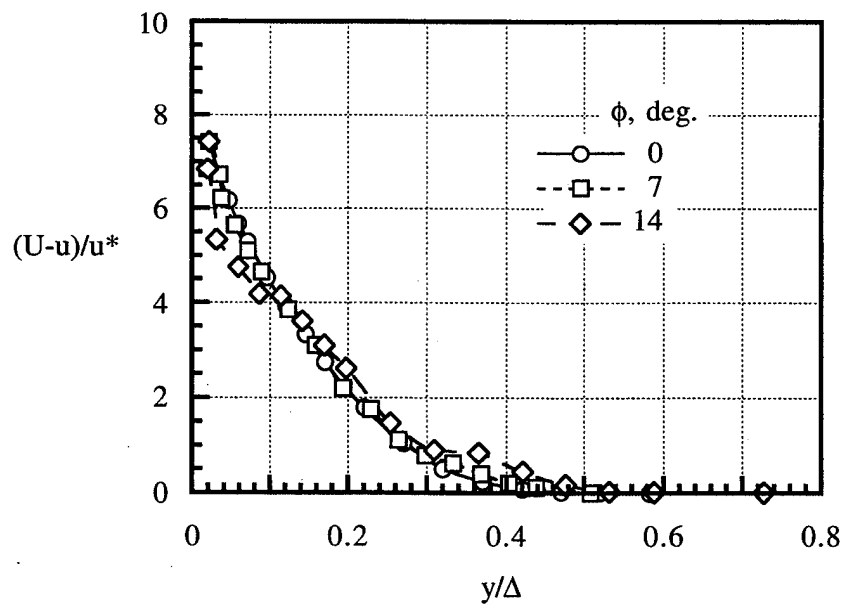


(d) 120" test-section with 14° diffuser.
Figure 41. Concluded.



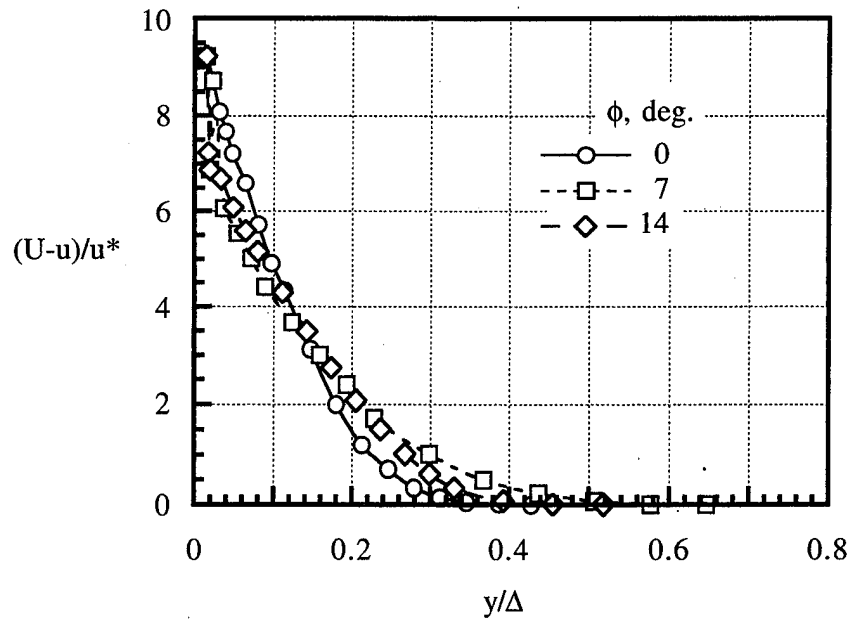
(a) Station 5.5" in the 24" test section.

Figure 42. Effect of test-section diffuser angle on the universal velocity profiles.

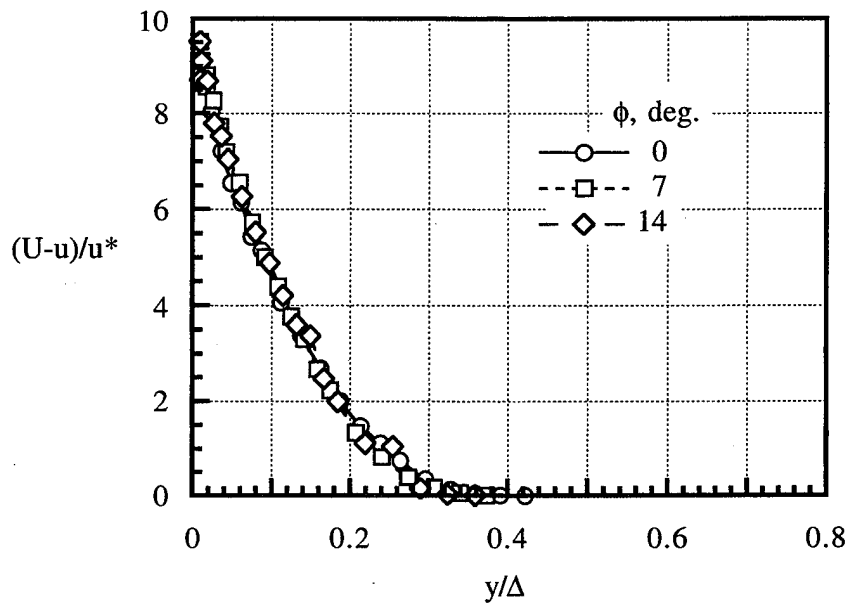


(b) Station 9" in the 24" test section.

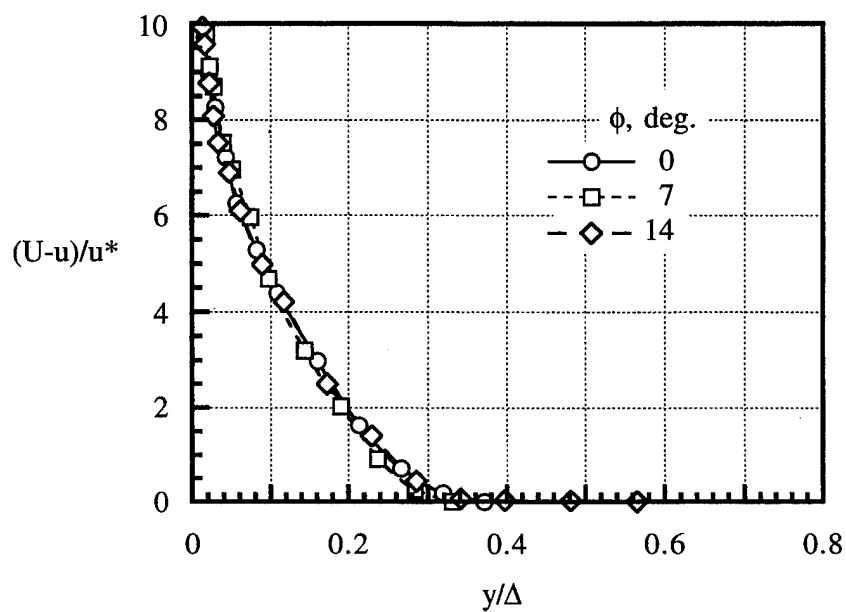
Figure 42. Continued.



(c) Station 12" in the 24" test section.
Figure 42. Continued.

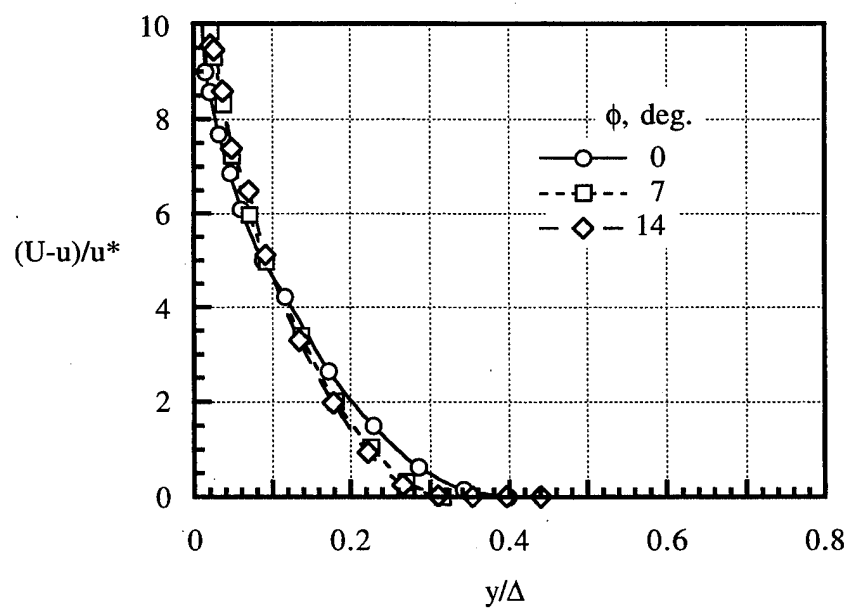


(d) Station 16" in the 24" test section.
Figure 42. Concluded.



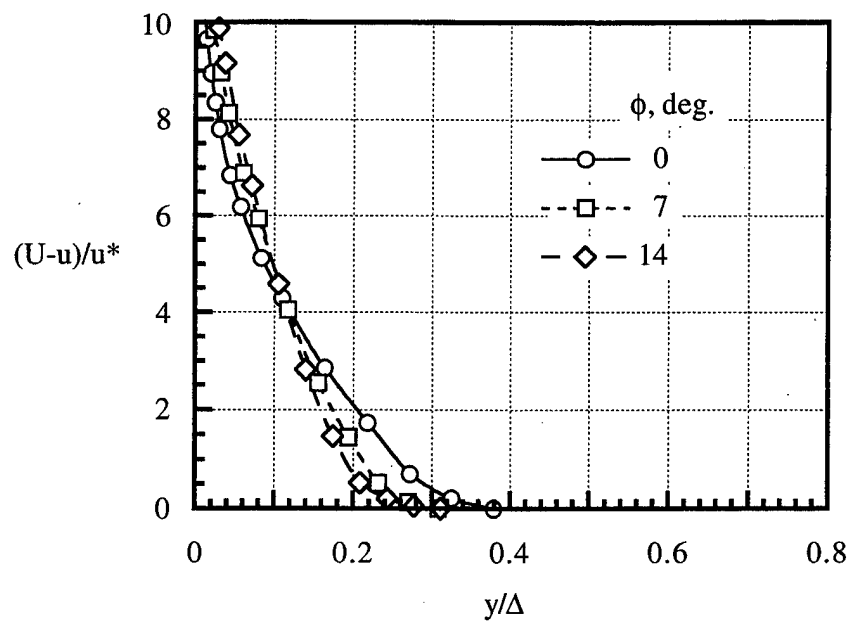
(a) Station 101.5" in the 120" test section.

Figure 43. Effect of test-section diffuser angle on the universal velocity profiles.

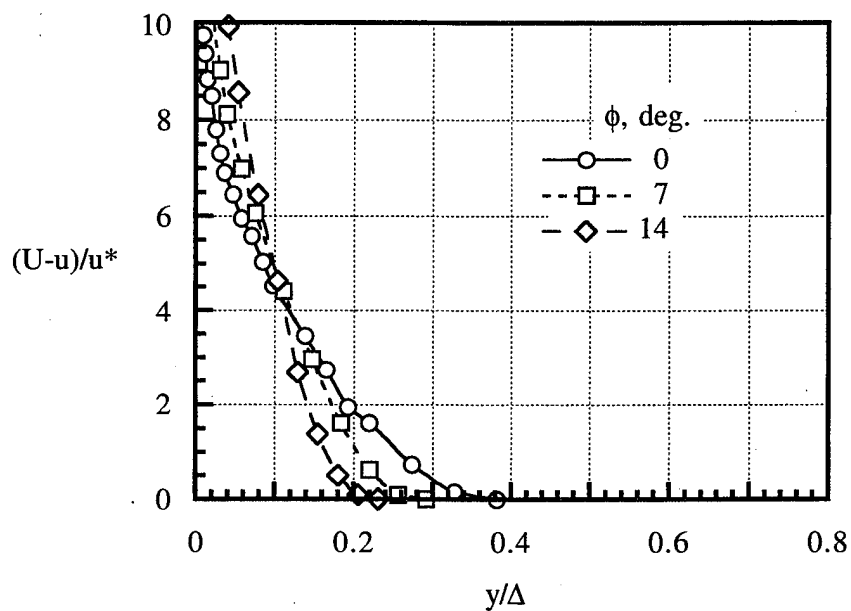


(b) Station 105" in the 120" test section.

Figure 43. Continued.



(c) Station 108" in the 120" test section.
Figure 43. Continued.



(d) Station 112" in the 120" test section.
Figure 43. Concluded.

2. Open Cavity Configurations

The purpose of the present investigation was to experimentally and computationally evaluate the effect of 1, 2, or 4 two-dimensional spanwise cavities with square cross-sections on the boundary-layer characteristics in both a constant pressure flow and two adverse pressure-gradient flows. The experimental results presented in the present section are based on the boundary-layer profiles presented in Appendix D and the surface/cavity pressure distributions presented in Appendix C. These data will be compared and analyzed in the following two subsections.

a. Effects on the Boundary-Layer Characteristics

The effects of the cavity geometry on the boundary-layer characteristics are analyzed in this subsection to identify how they are influenced by the flowfield. The boundary layer profiles measured on the tunnel ceiling in the vicinity of the cavities were used to compute the boundary layer thickness δ , displacement thickness δ_1 (equation 4), momentum thickness δ_2 , shape factor H , and skin-friction coefficient c_f which are presented in the following figures:

Parameter	δ	δ_1	δ_2	H	c_f
Figure	44	45	46	47	48

The data from the 120" test section are presented in parts (a), (b), and (c) (test section diffuser angles of 0° , 14° , and 7° , respectively) and from the 24" test section are presented in parts (d), (e), and (f) (test section diffuser angles of 0° , 14° , and 7° , respectively) of each of the above figures.

The longer 120" test section provided a fully-developed turbulent boundary layer with only small increases in the $x = 100"$ to $112"$ measurement region where the Reynolds number was large ($Re > 5 \times 10^6$). The boundary-layer thicknesses (δ , δ_1 , and δ_2) for the 120" test section with either the 0° or the 7° test

section diffusers did not change significantly with variation in the cavity configuration (parts (a) and (c) of Figures 44 through 46). Depending on the selected comparison, these data were within $\pm 2\%$ to $\pm 12\%$ for a given plot. Only the four-cavity configuration with the 14° diffuser shows a noticeable increase (up to 50%) in these thicknesses (part (b) of Figures 44 through 46).

The 24" test section had a much thinner boundary layer which is initially barely turbulent since the Reynolds number ranged from 350,000 to about 1,100,000. The boundary layer profiles presented in Appendix D tend to agree with the $1/7$ power law which is typical of a two-dimensional turbulent boundary layer. The boundary layer thicknesses (δ , δ_1 , and δ_2) for the 24" test section with either the 0° or 7° test section diffuser are typically within $\pm 10\%$. In the 14° test section diffuser, while there was more data scatter, there tended to be an increase in thickness with the increasing diffuser angle. The shape factor H (Figure 47) and skin friction coefficient c_f (Figure 48) do not show any noticeable effect of the presence of the cavities.

The boundary layer log-law profiles were compared (Figures 49 to 51) both upstream and downstream of the cavity (or cavities) in an attempt to identify their effect on the flow. It is shown that all of the data obtained without a diffuser tend to agree with the log law (equation 18) where $\kappa = 0.41$ and $C_1 = 5.0$. The data with the 7° and 14° test-section diffusers asymptote below the log-law defined by the above constants. It was found, as shown in Figure 52, that if C_1 is changed to 3.5 for the 7° diffuser and to 3.0 for the 14° diffuser that these data for the test-section diffuser geometries agree with the log-law equation.

The effect of variation of the cavity configuration (0, 1, 2, or 4 cavities) on the boundary-layer profiles at a given x station is presented in Figures 53, 54, and 55. The test-section entrance profiles (Figure 53) demonstrate boundary layer similarity for the basic test section and for the 7° test section diffuser. These profiles are in agreement with the $1/7$ power law profile. There is a significant boundary layer profile variation from the $1/7$ power law for the 14° test-section diffuser. The data from Figure 54, which are for the downstream x station, are presented in Figure 55 using the universal velocity profile. This data format demonstrates a modest variation in the boundary-layer profiles which are

typical of an adverse pressure gradient. The single and double cavities show only a small deviation from the profile measured with no cavity. The four-cavity configuration profile in most cases represents a more adverse boundary-layer profile than any other configuration.

Figure	test section length	x station	test section diffuser angle, deg.
53 a	120	≈ 101	0
53b	120	≈ 101	14
53 c	120	≈ 101	7
53 d	24	≈ 5	0
53 e	24	≈ 5	14
54 a	120	112	0
54 b	120	112	14
54 c	120	112	7
54 d	24	16	0
54 e	24	16	14
54 f	24	16	7

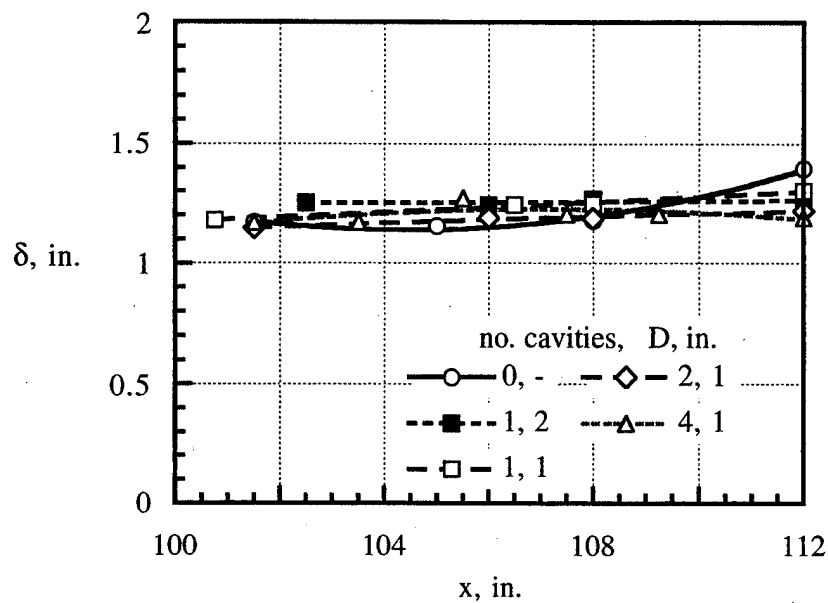
b. Effects on the Surface Pressure Distribution

The effect of the test-section diffuser on the surface-pressure distribution was discussed on page 82. The focus of the present section is the evaluation of the effect of cavities on the pressure distribution on the wind-tunnel ceiling. Several configurations were measured several times to determine the data repeatability. An example is presented in Figure 56 where the ceiling pressure distributions from five runs of configuration 8431c (120" test section with a 2" deep cavity covered by a door located between $x = 102"$ and $104"$) are plotted along with their average. Immediately downstream of the cavity the pressure coefficient is seen to be depressed. This was probably caused by a misalignment of the door with the ceiling. Most of the pressure coefficients are within ± 0.02 of the average pressure coefficient curve shown on Figure 56.

The effect of the cavities in the 24" test section is presented in Figures 57 and 58. The basic test section shows a pressure coefficient magnitude of approximately -0.02; ahead of the cavities there is a similar pressure coefficient. Downstream of the cavity the pressure coefficients drop to about -0.06. With both test section diffusers (Figures 59 through 61) in the 24" test section the general data trend is unaffected by the presence of the cavities.

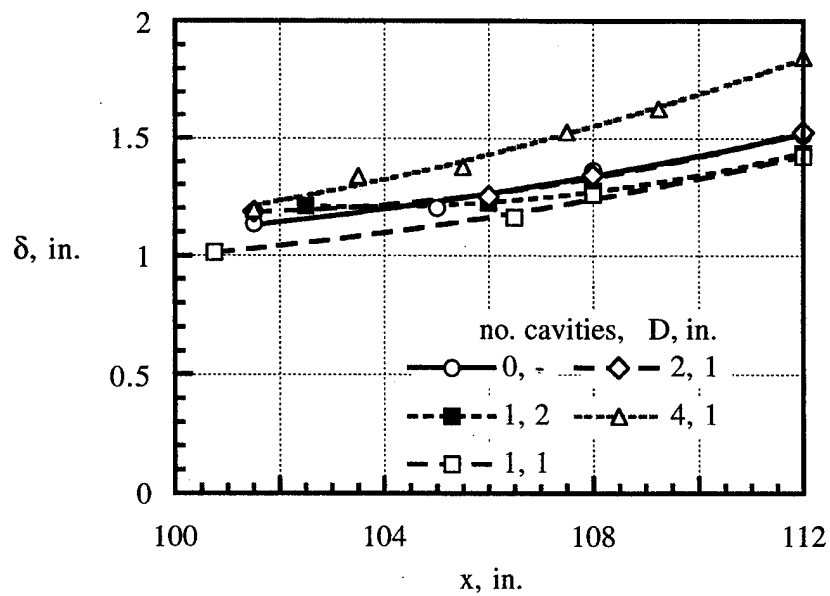
The effect of the cavities in the 120" test section is presented in Figures 62 through 66. Generally there is seen to be little effect of the cavities on the pressure distributions. The one exception is the effect of the 2" cavity downstream of that cavity where the pressure coefficient is reduced to about -0.04. With both test section diffusers there is more scatter in the data without a consistent trend.

In conclusion, all of the surface pressure data suggest that the presence of the cavities has no consistent effect. It may be concluded that cavities may be deployed without significantly modifying the resultant pressure distribution.



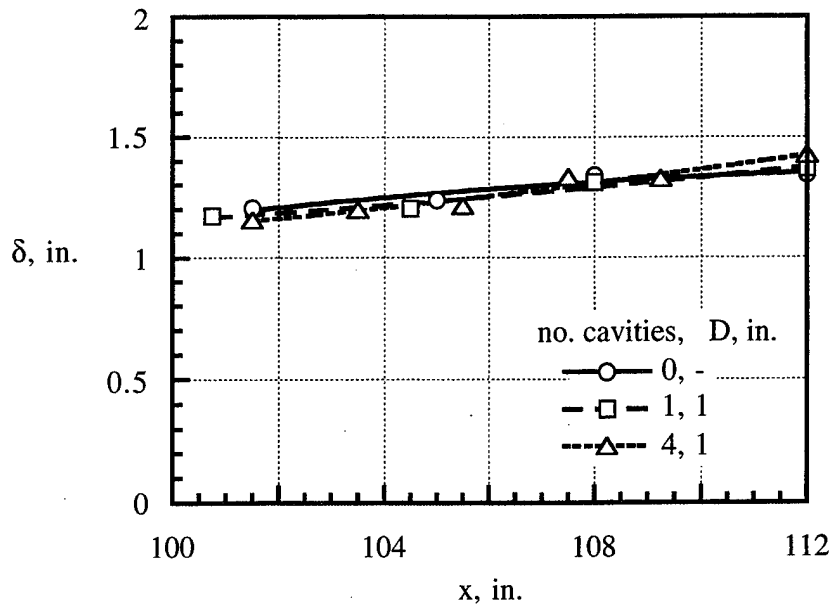
(a) 120° test section.

Figure 44. Effect of the cavity configuration on the boundary-layer thickness.



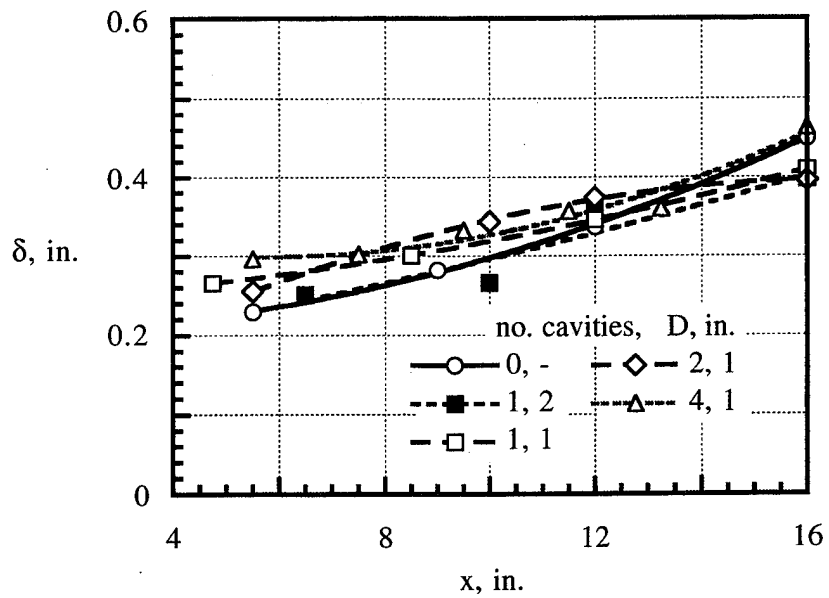
(b) 120° test section with the 14° test-section diffuser.

Figure 44. Continued.



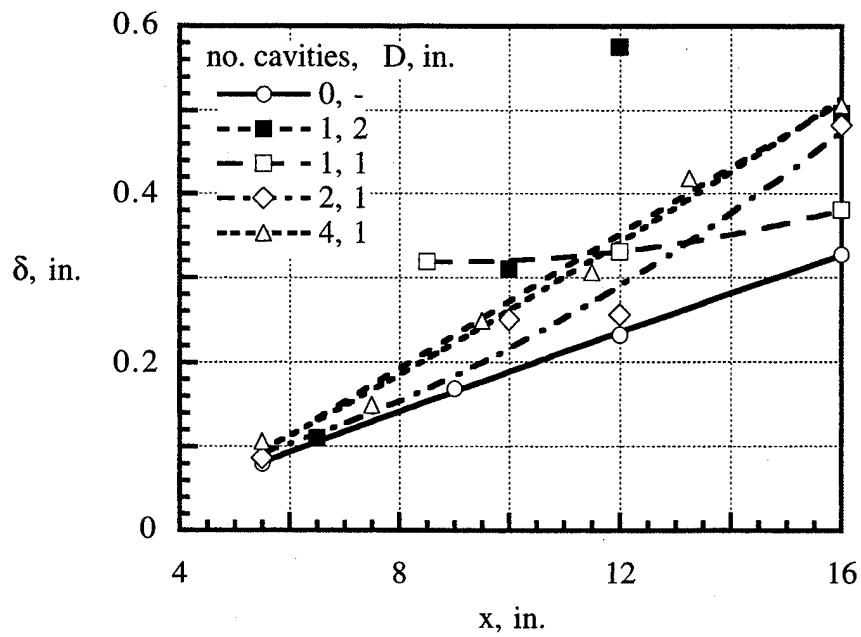
(c) 120" test section with the 7° test-section diffuser.

Figure 44. Continued.



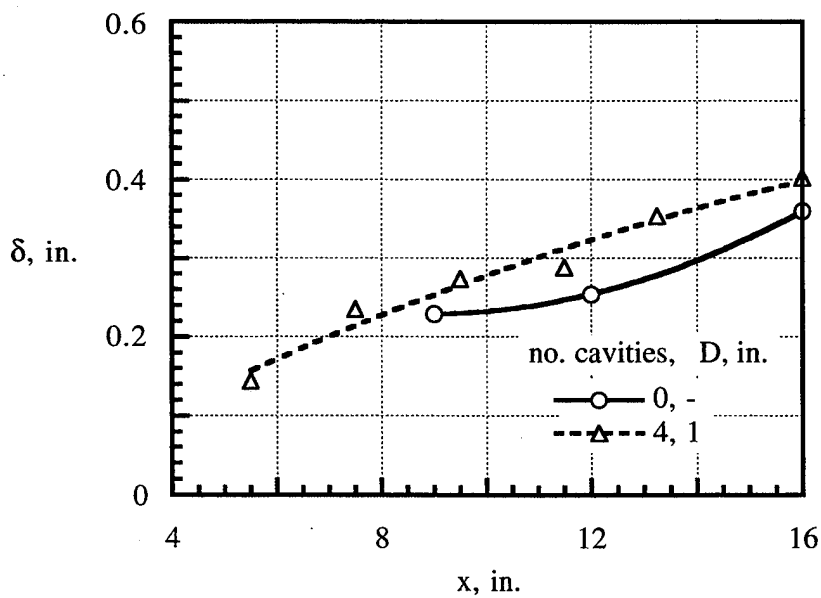
(d) 24" test section

Figure 44. Continued.



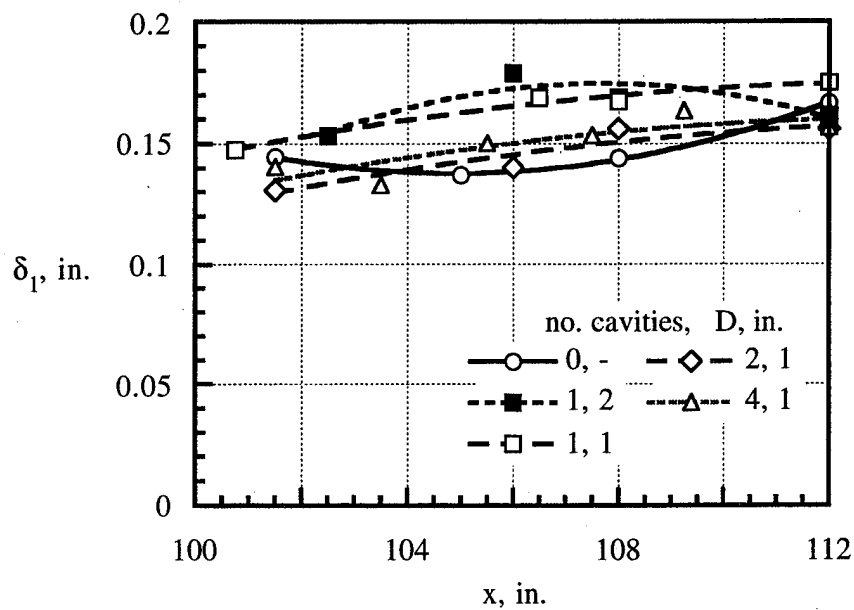
(e) 24" test section with the 14° test-section diffuser.

Figure 44. Continued.



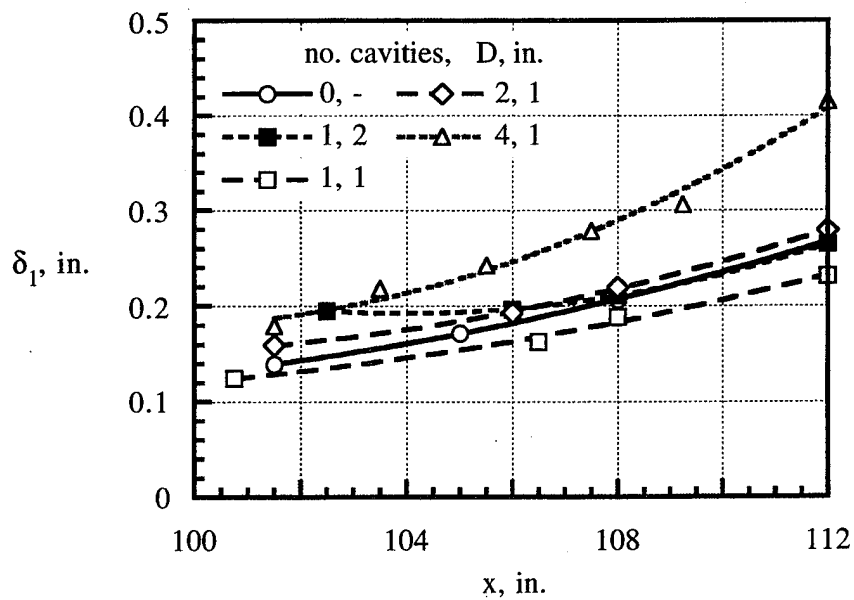
(f) 24" test section with the 7° test-section diffuser.

Figure 44. Concluded.



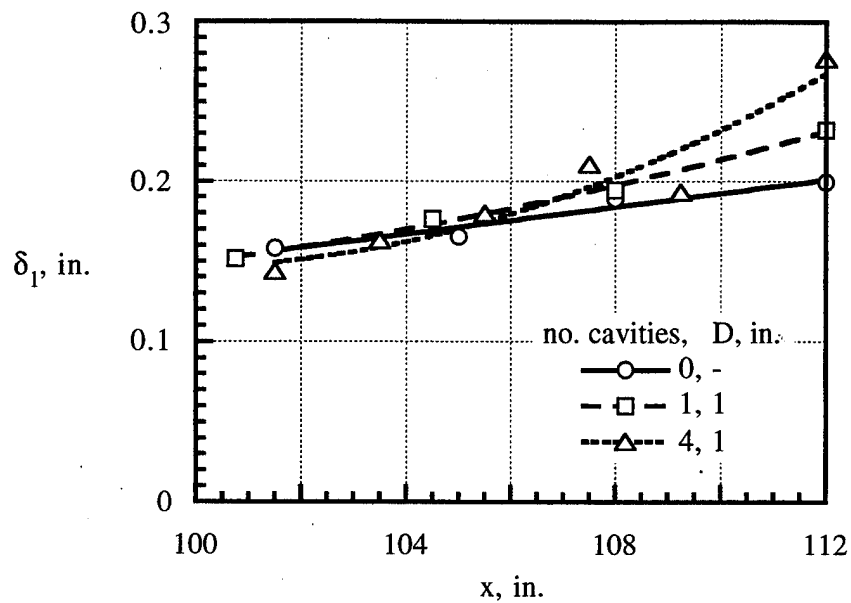
(a) 120° test section.

Figure 45. Effect of the cavity configuration on the displacement thickness.



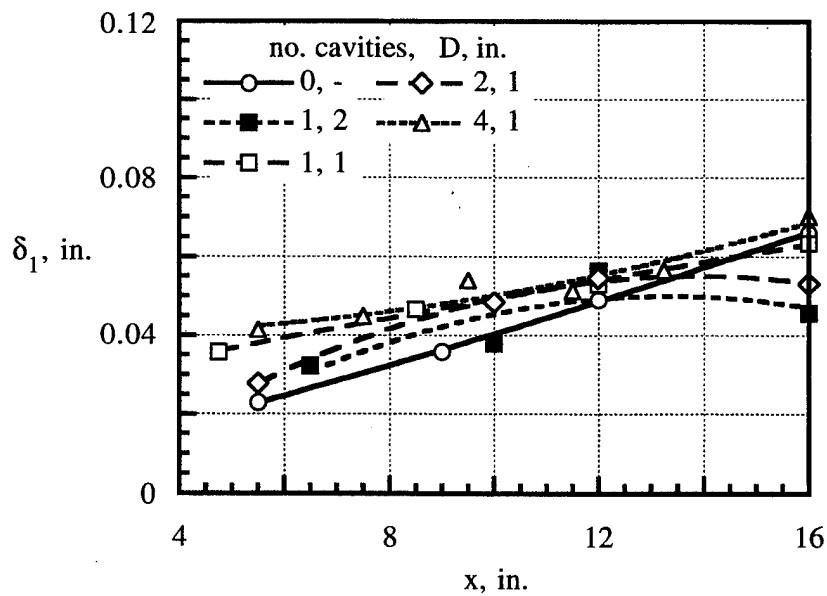
(b) 120° test section with the 14° test-section diffuser.

Figure 13. Continued.



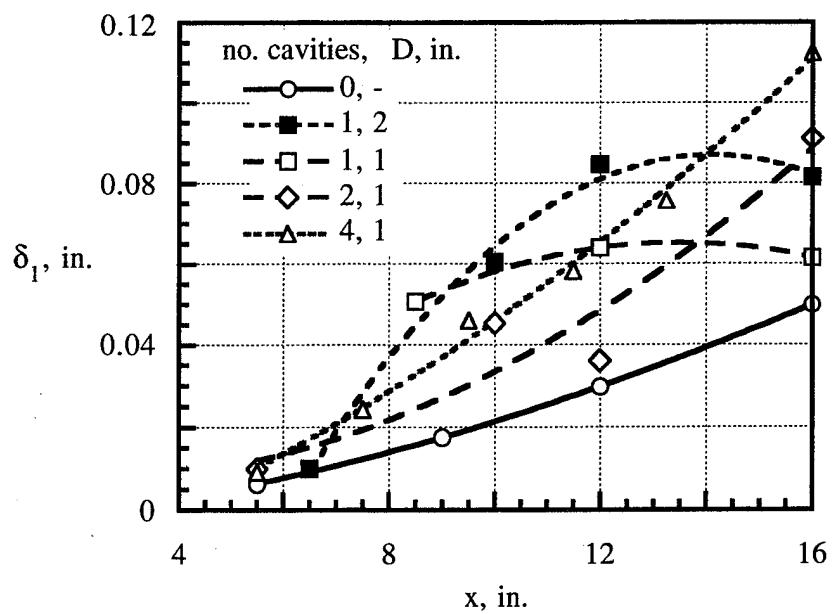
(c) 120" test section with the 7° test-section diffuser.

Figure 45. Continued.

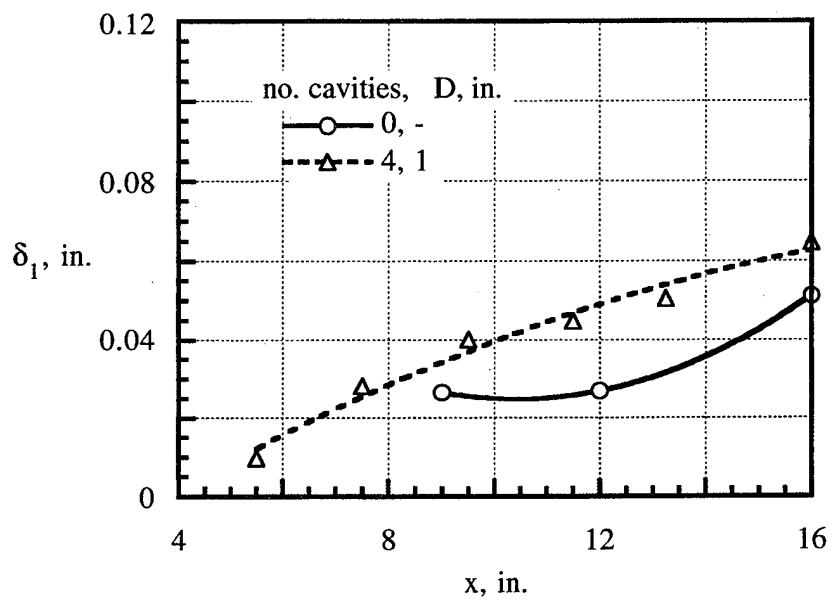


(d) 24" test section

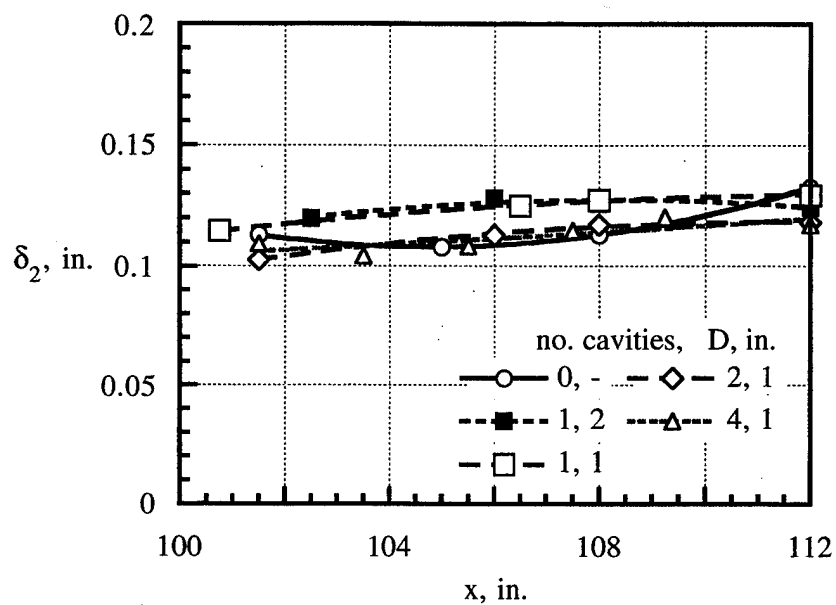
Figure 45. Continued.



(e) 24" test section with the 14° test-section diffuser.
Figure 45. Continued.

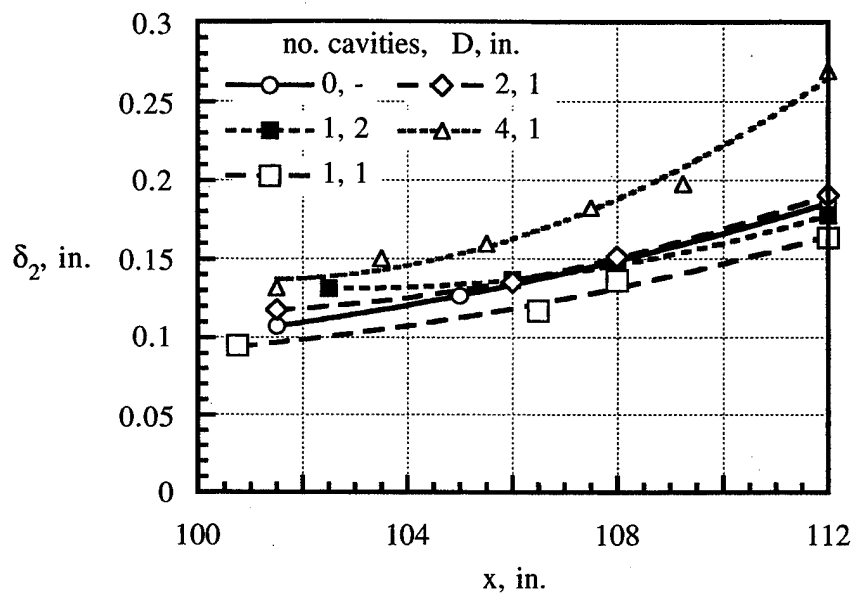


(f) 24" test section with the 7° test section diffuser.
Figure 45. Concluded.



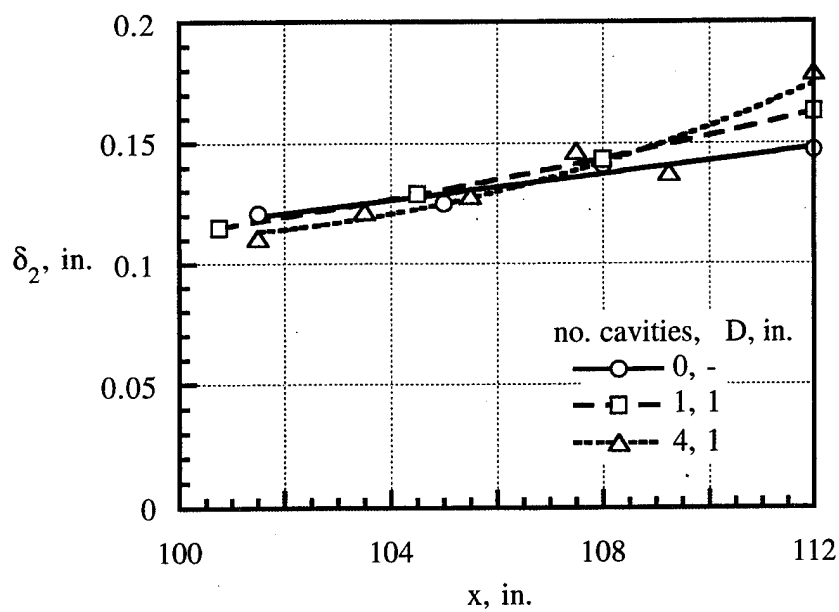
(a) 120° test section.

Figure 46. Effect of the cavity configuration on the momentum thickness.

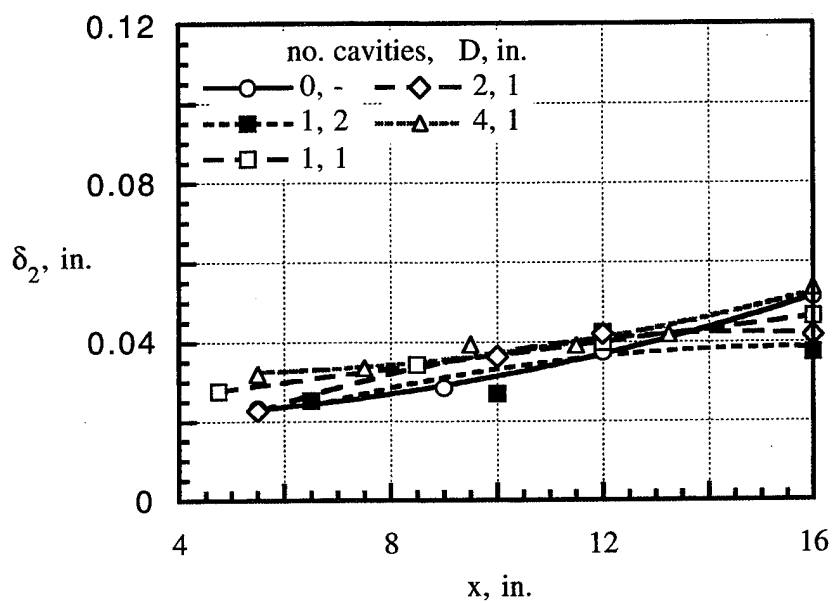


(b) 120° test section with the 14° test-section diffuser.

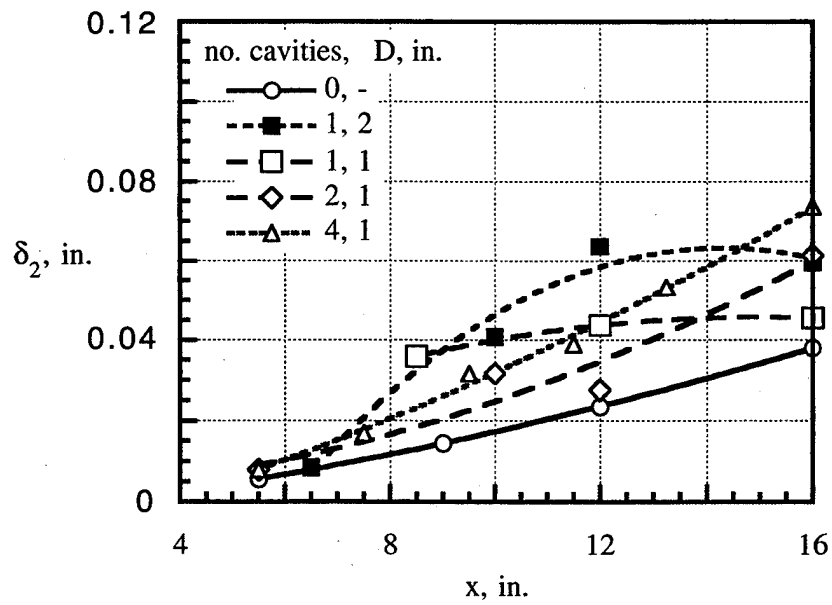
Figure 46. Continued.



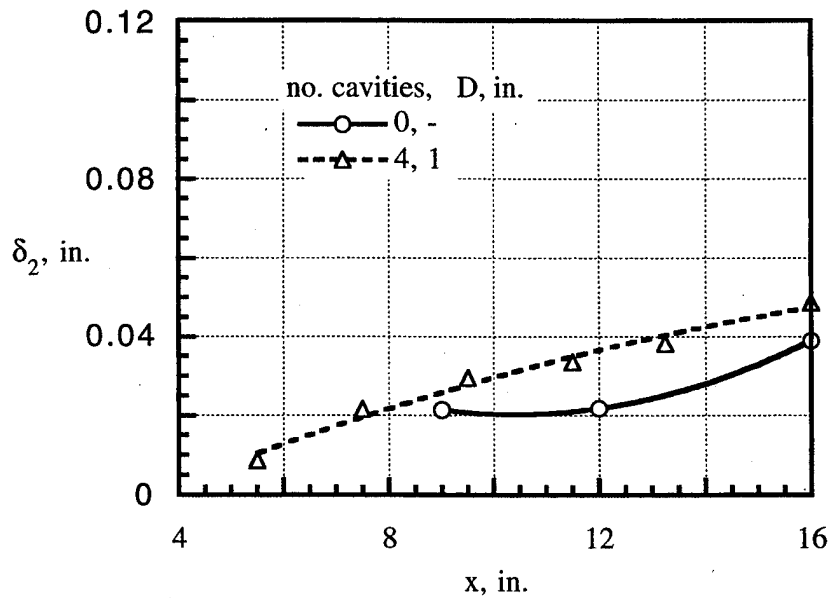
(c) 120" test section with the 7° test-section diffuser.
Figure 46. Continued.



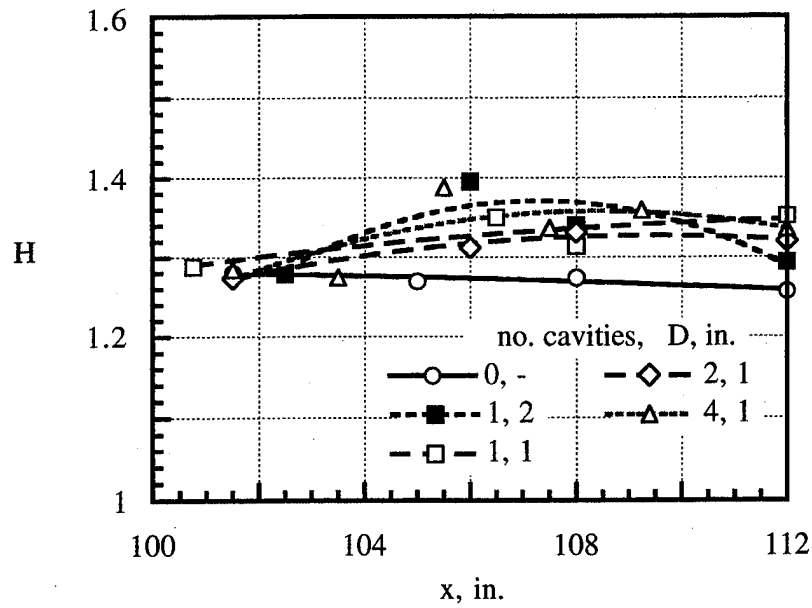
(d) 24" test section
Figure 46. Continued.



(e) 24" test section with the 14° test-section diffuser.
Figure 46. Continued.

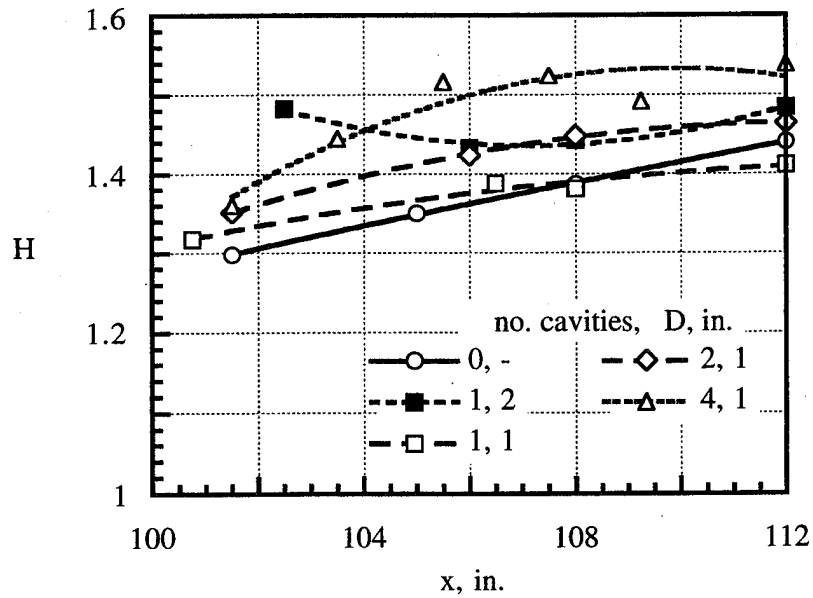


(f) 24" test section with the 7° test-section diffuser.
Figure 46. Concluded.



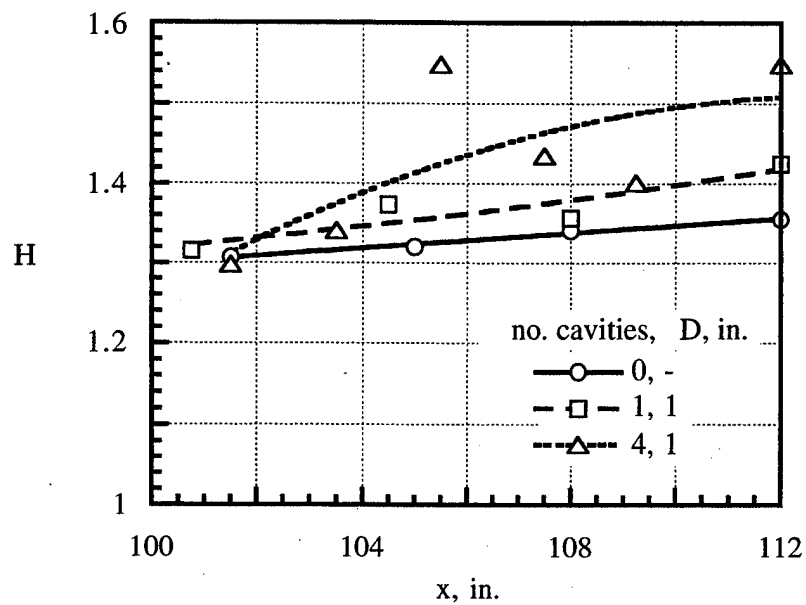
(a) 120" test section.

Figure 47. Effect of the cavity configuration on the shape factor.

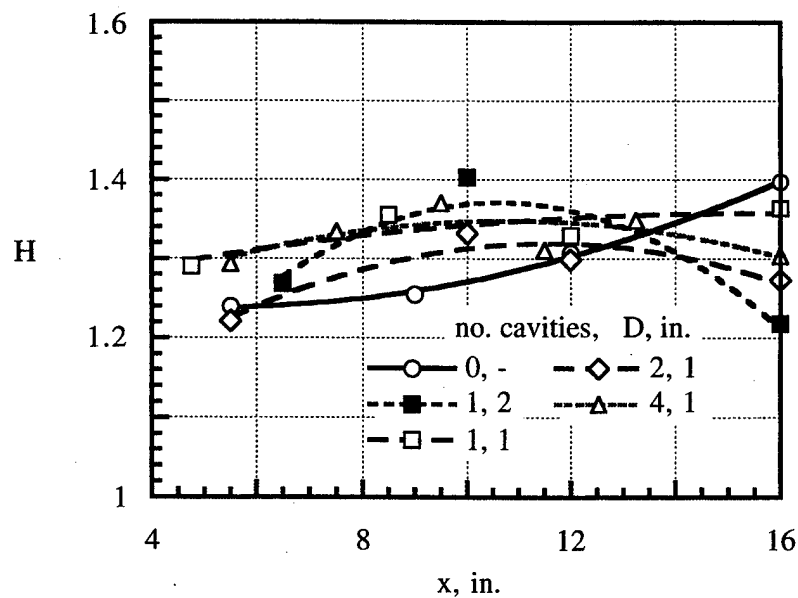


(b) 120" test section with the 14° test-section diffuser.

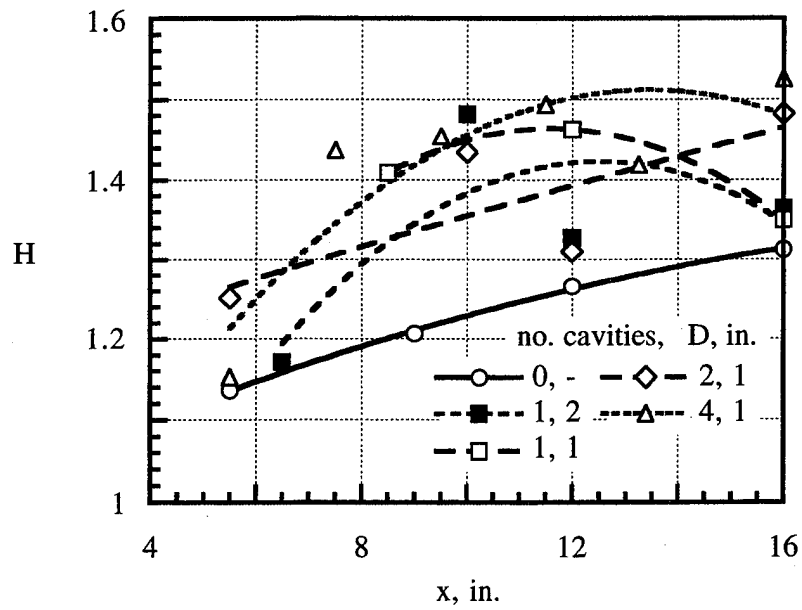
Figure 47. Continued.



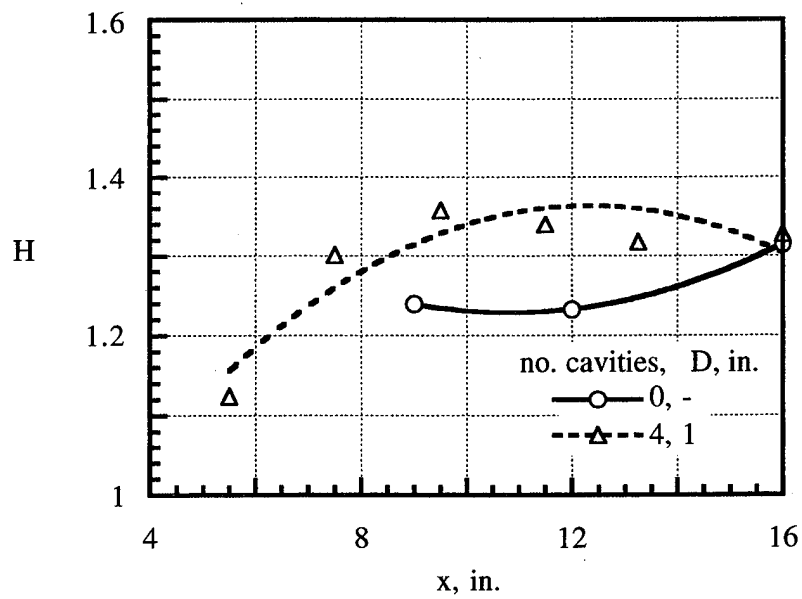
(c) 120" test section with the 7° test-section diffuser.
Figure 47. Continued.



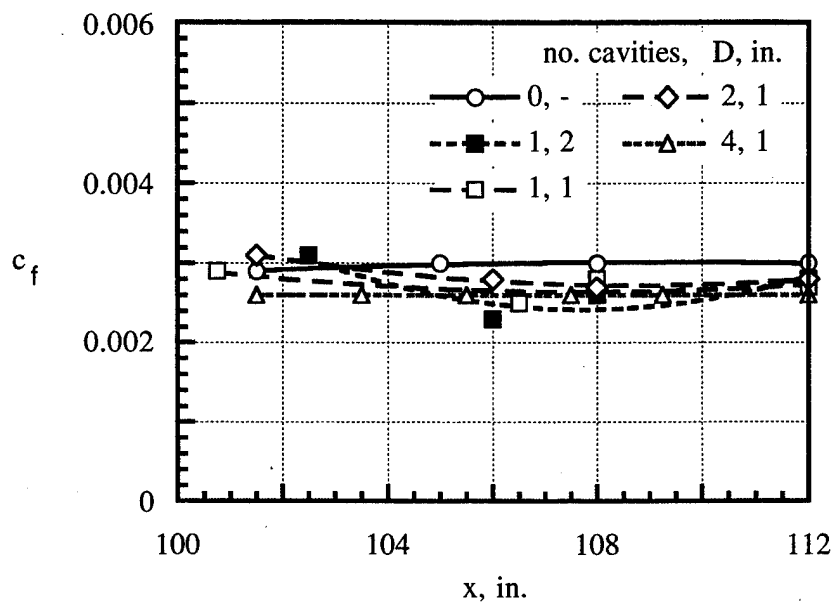
(d) 24" test section
Figure 47. Continued.



(e) 24" test section with the 14° test-section diffuser.
Figure 47. Continued.

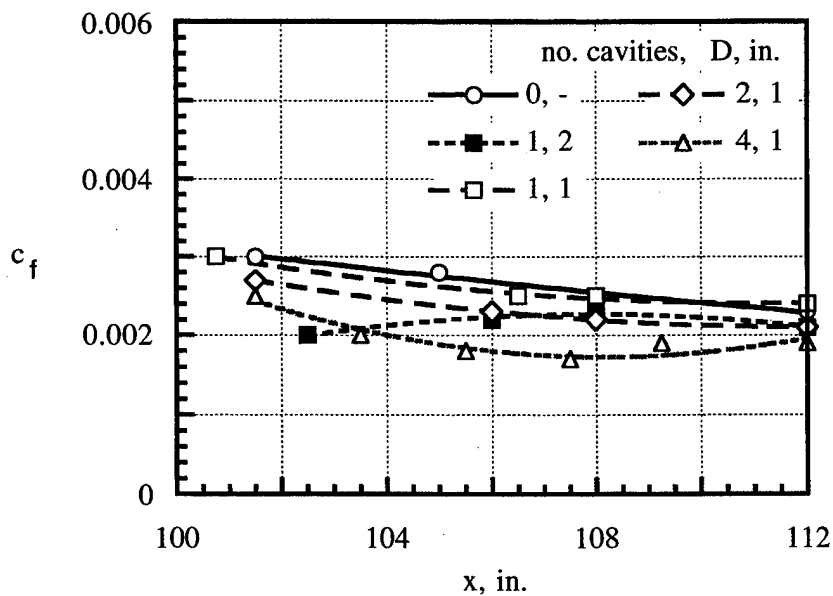


(f) 24" test section with the 7° test-section diffuser.
Figure 47. Concluded.



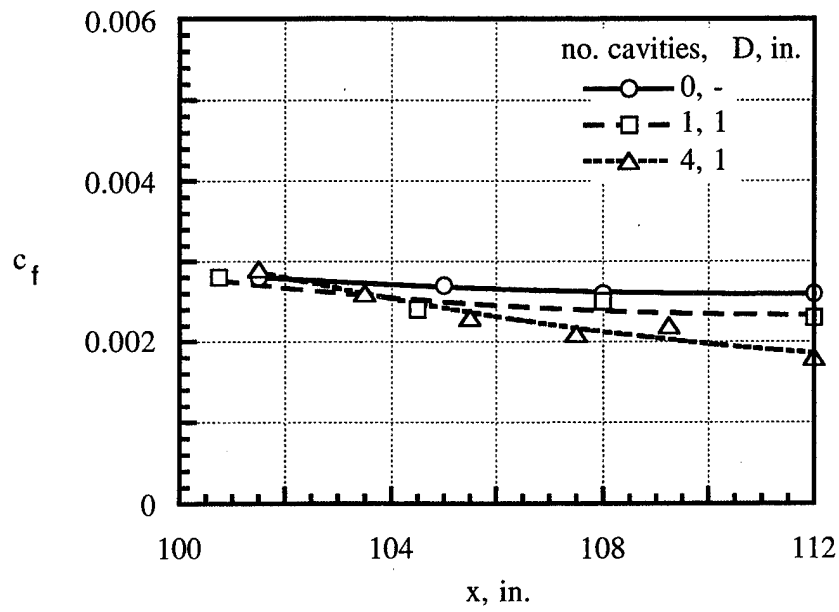
(a) 120" test section.

Figure 48. Effect of the cavity configuration on the skin-friction coefficient.

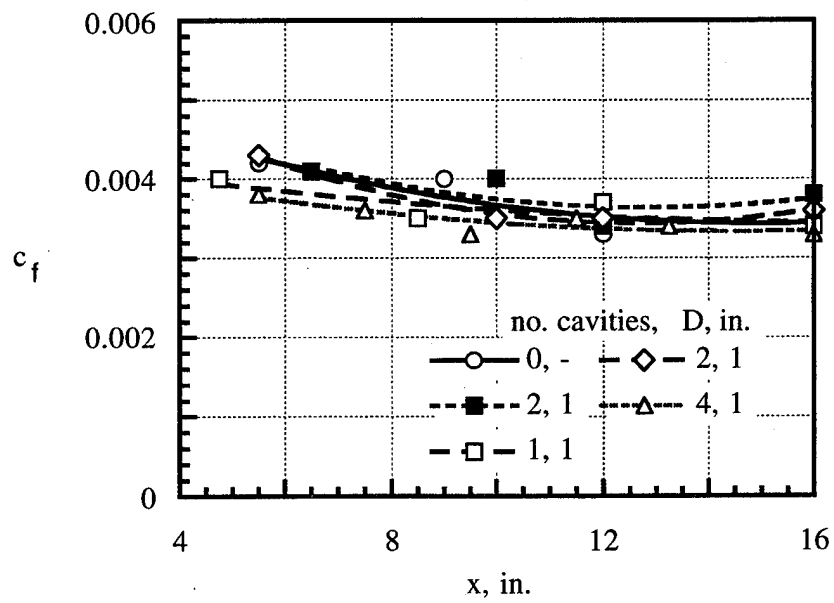


(b) 120" test section with the 14° test-section diffuser.

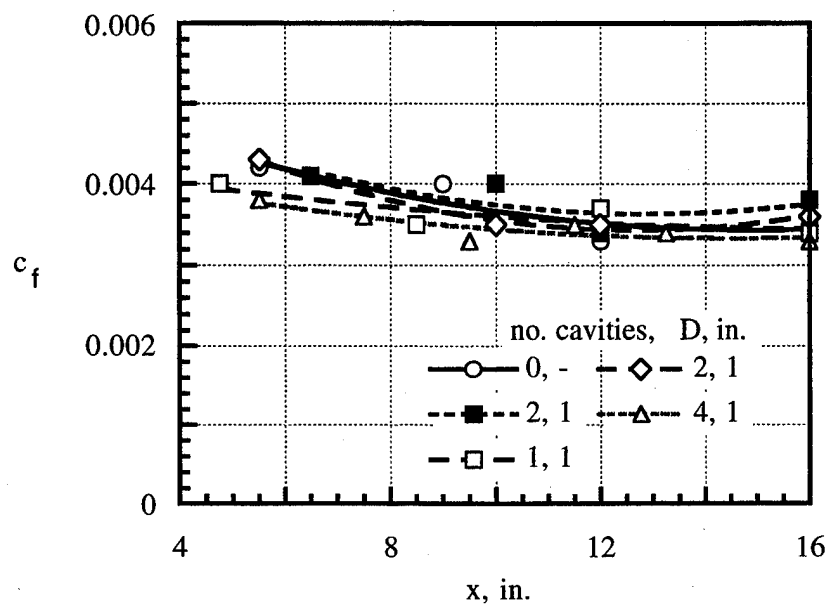
Figure 48. Continued.



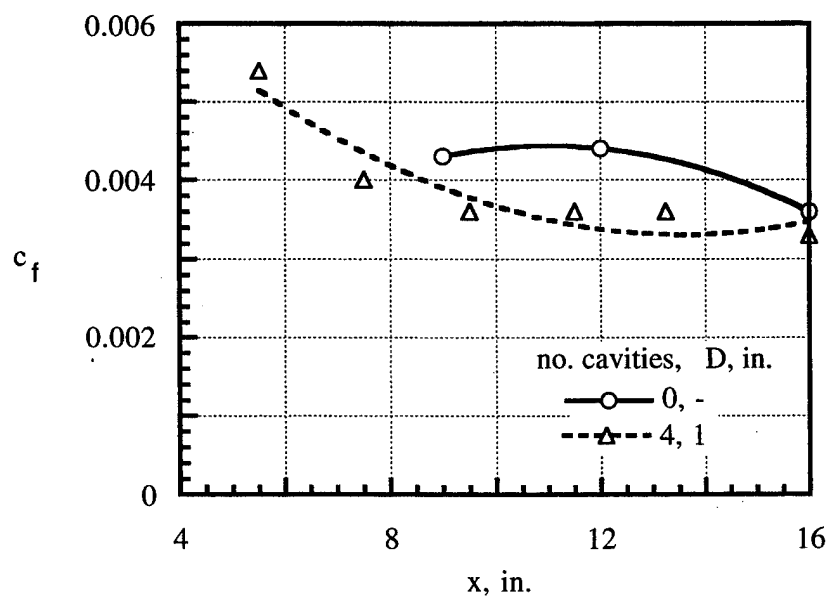
(c) 120" test section with the 7° test-section diffuser.
Figure 48. Continued.



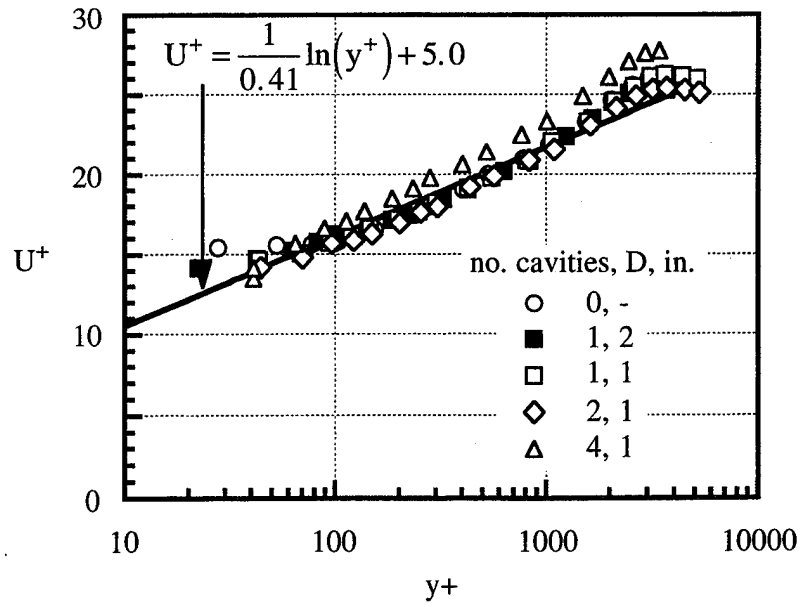
(d) 24" test section
Figure 48. Continued.



(e) 24" test section with the 14° test-section diffuser.
Figure 48. Continued.

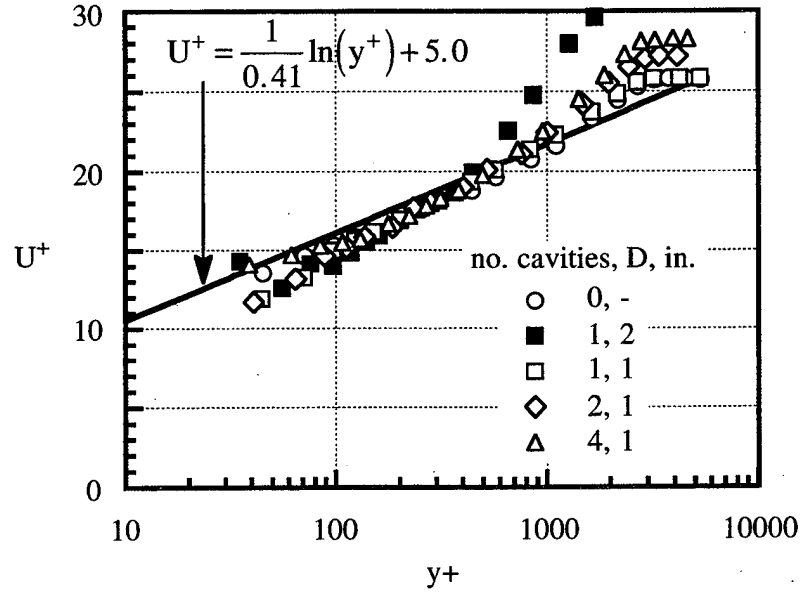


(f) 24" test section with the 7° test-section diffuser.
Figure 48. Concluded.



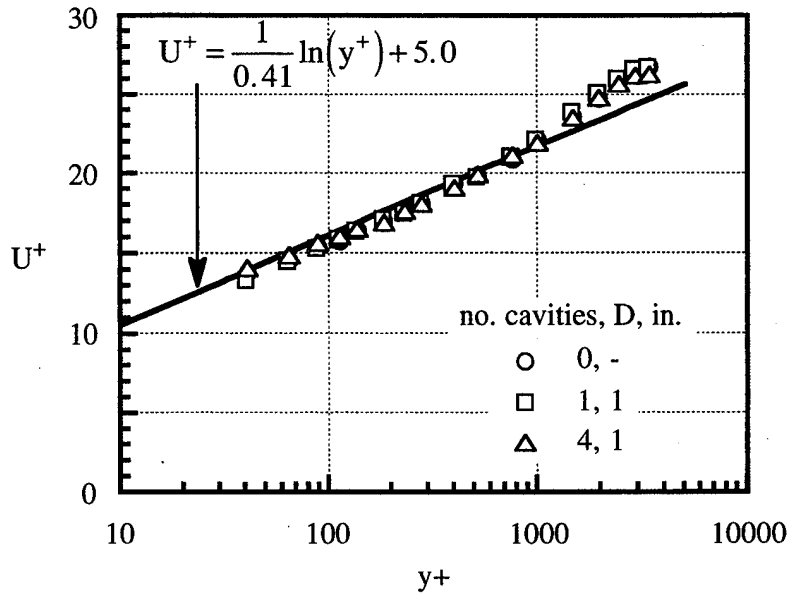
(a) 120" test section at $x \approx 101"$.

Figure 49. Effect of the cavity geometry on the boundary-layer log-law profile.

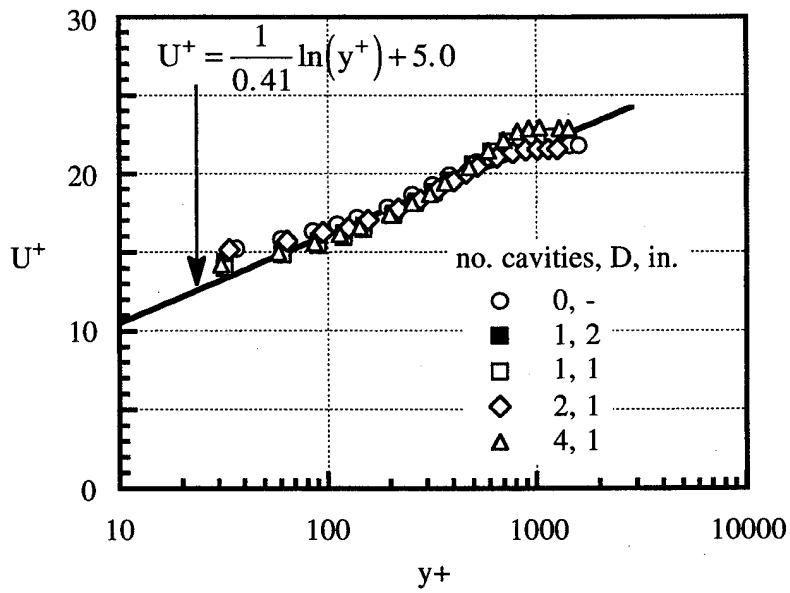


(b) 120" test section at $x \approx 101"$ with the 14° test-section diffuser.

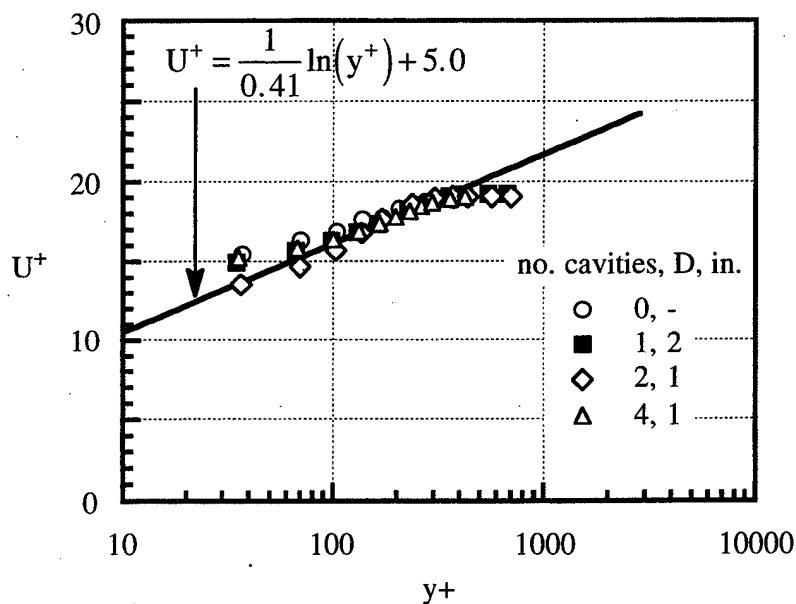
Figure 49. Continued.



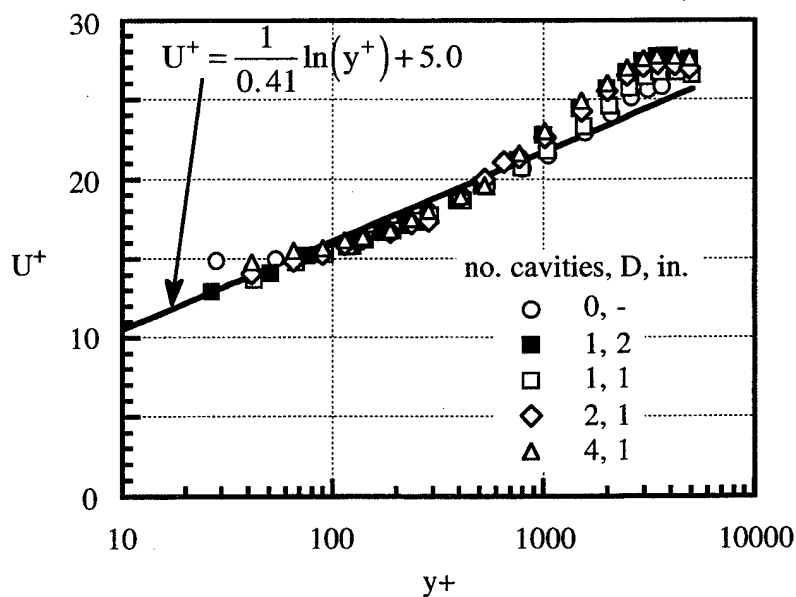
(c) 120" test section at $x \approx 101$ " with the 7° test-section diffuser.
Figure 49. Continued.



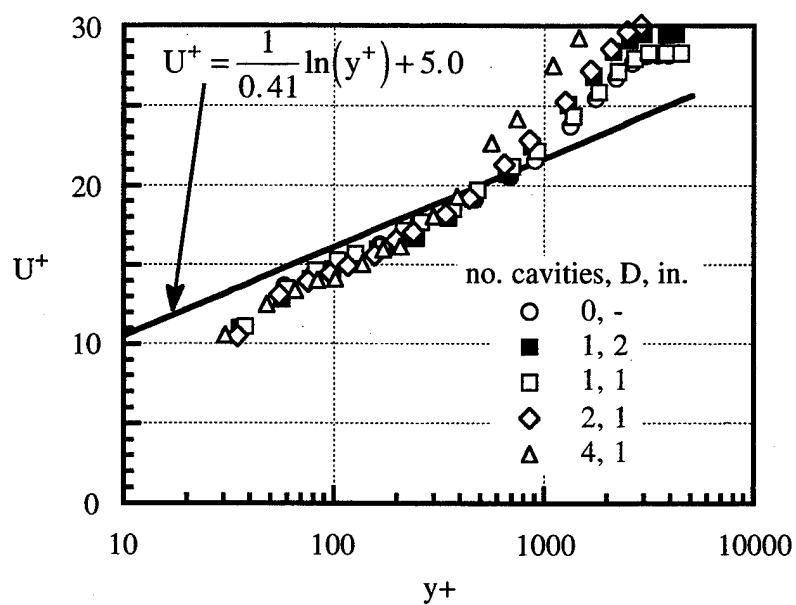
(d) 24" test section at $x \approx 5$ ".
Figure 49. Continued.



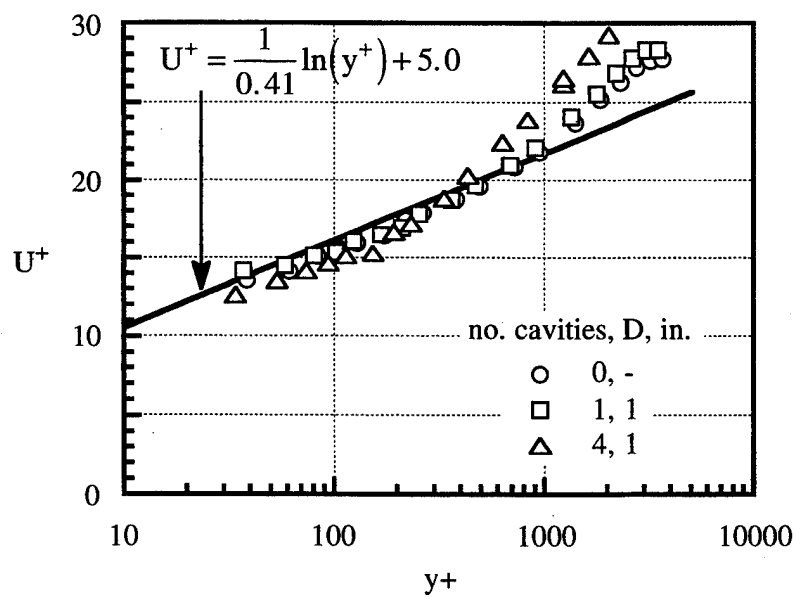
(e) 24" test section at $x \approx 5"$ with the 14° test-section diffuser.
Figure 49. Concluded.



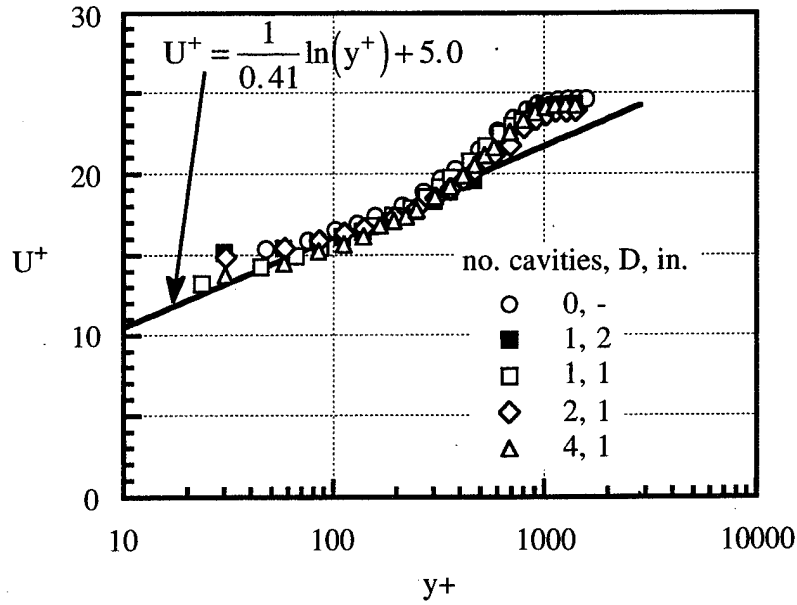
(a) 120" test section at $x \approx 108"$.
Figure 50. Effect of the cavity geometry on the boundary-layer log-law profile.



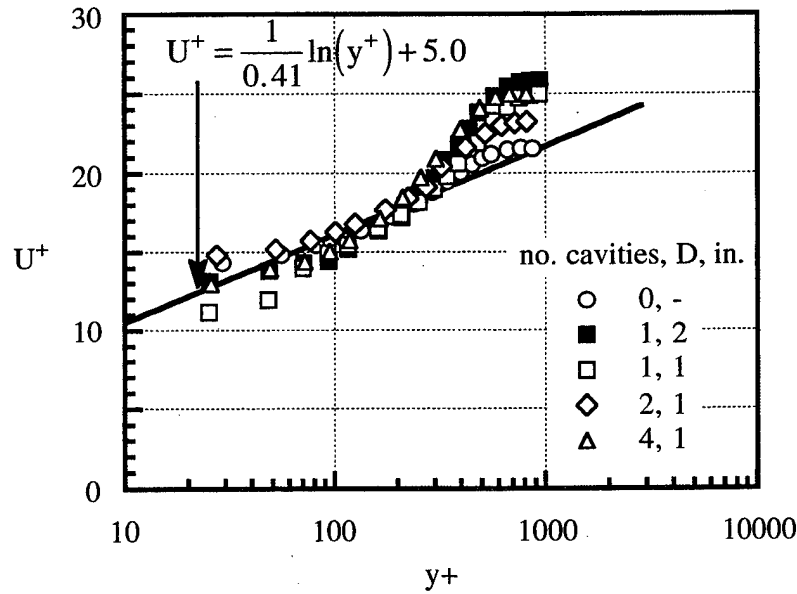
(b) 120" test section at $x \approx 108"$ with the 14° test-section diffuser.
Figure 50. Continued.



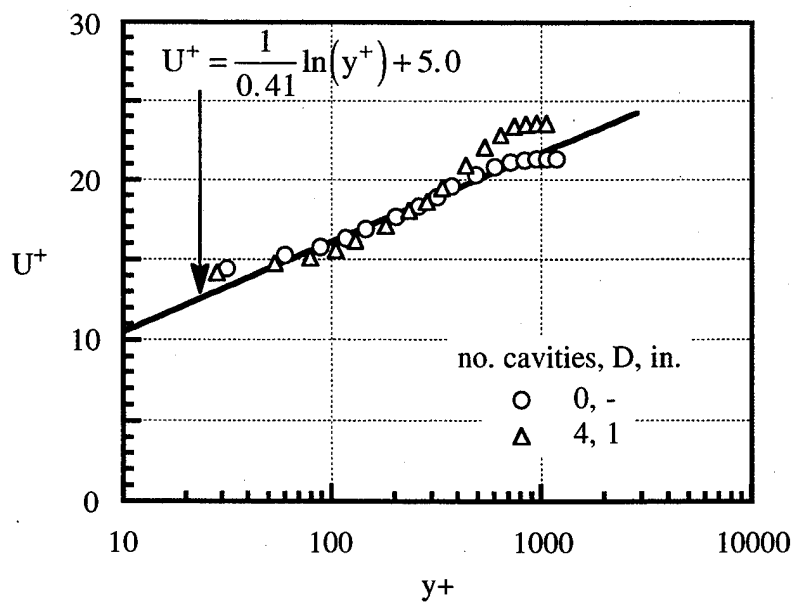
(c) 120" test section at $x \approx 108"$ with the 7° test-section diffuser.
Figure 50. Continued.



(d) 24" test section at $x \approx 12"$.
Figure 50. Continued.

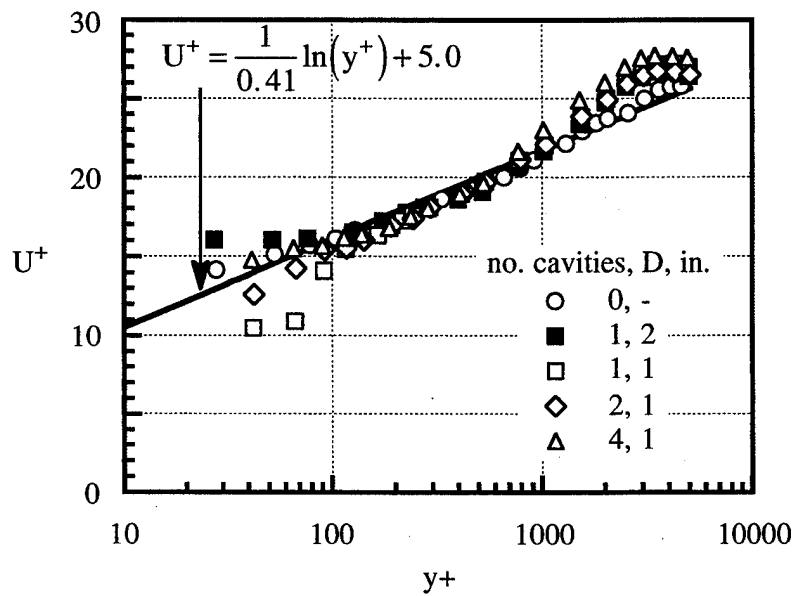


(e) 24" test section at $x \approx 12"$ with the 14° test-section diffuser.
Figure 50. Continued.



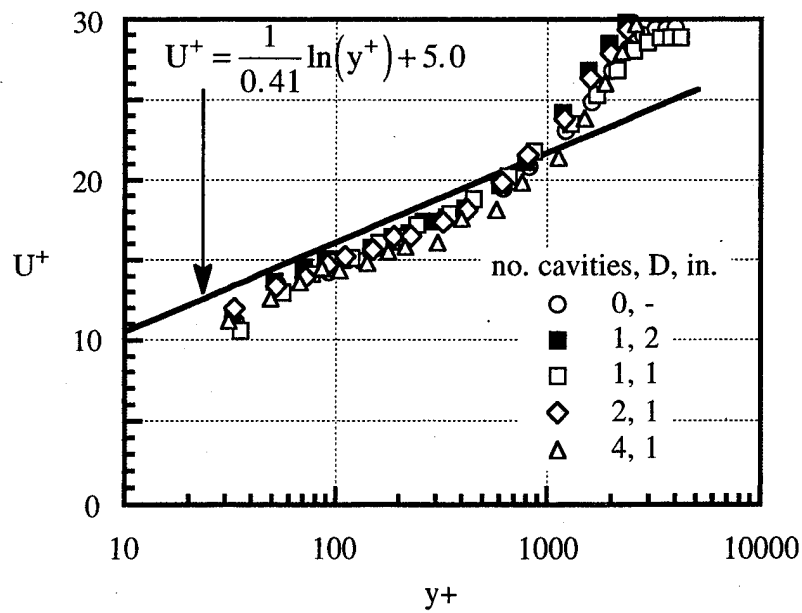
(f) 24" test section at $x \approx 12''$ with the 7° test-section diffuser.

Figure 50. Concluded.

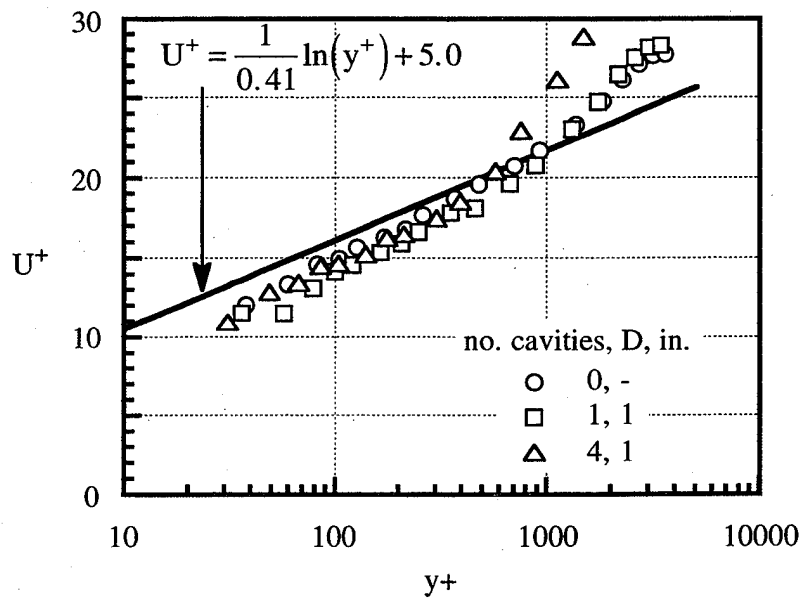


(a) 120" test section at $x = 112''$.

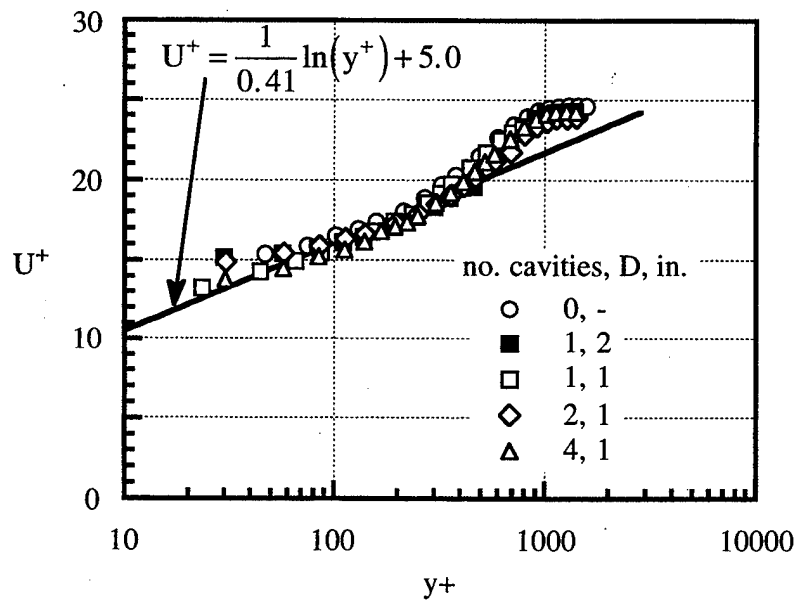
Figure 51. Effect of the cavity geometry on the boundary-layer log-law profile.



(b) 120" test section at $x = 112"$ with the 14° test-section diffuser.
Figure 51. Continued.

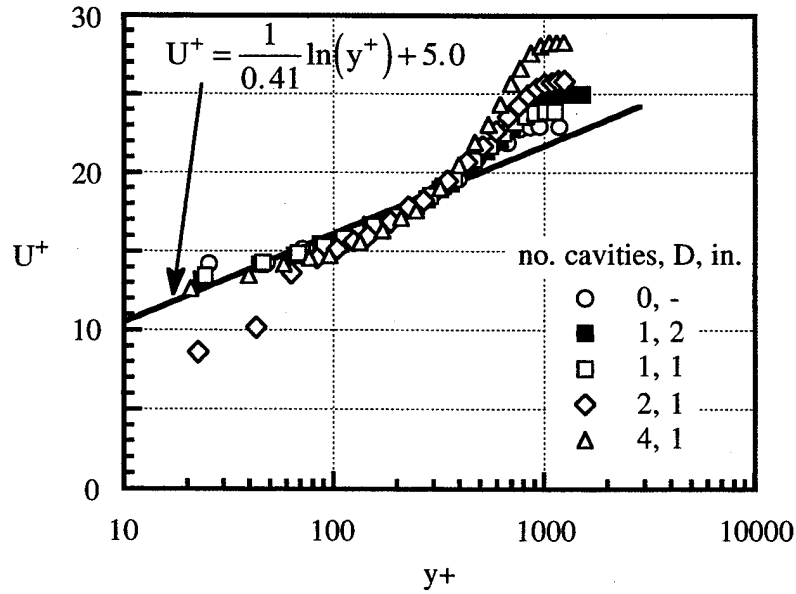


(c) 120" test section at $x = 112"$ with the 7° test-section diffuser.
Figure 51. Continued.



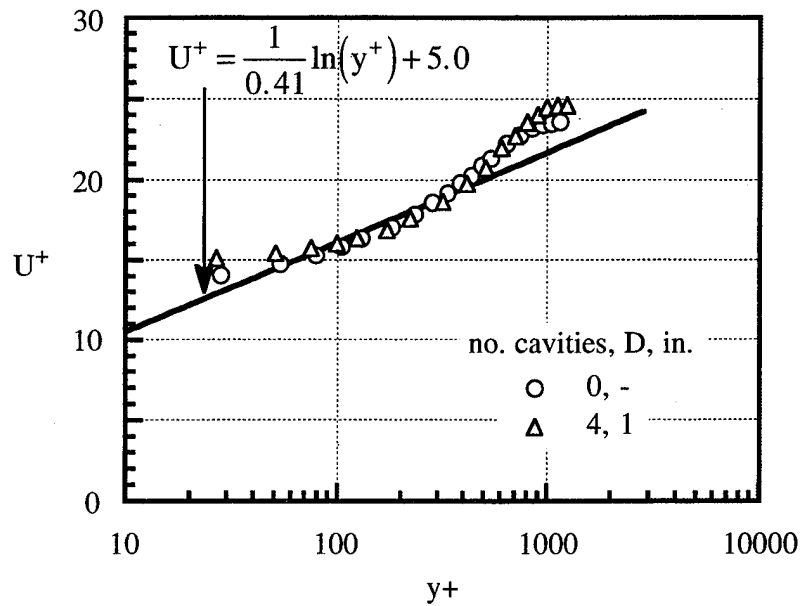
(d) 24" test section at $x = 16"$.

Figure 51. Continued.

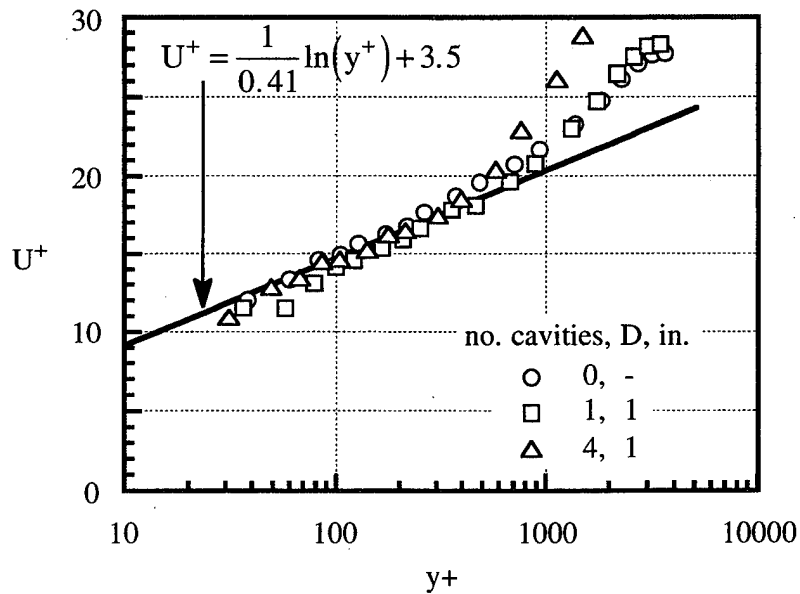


(e) 24" test section at $x = 16"$ with the 14° test-section diffuser.

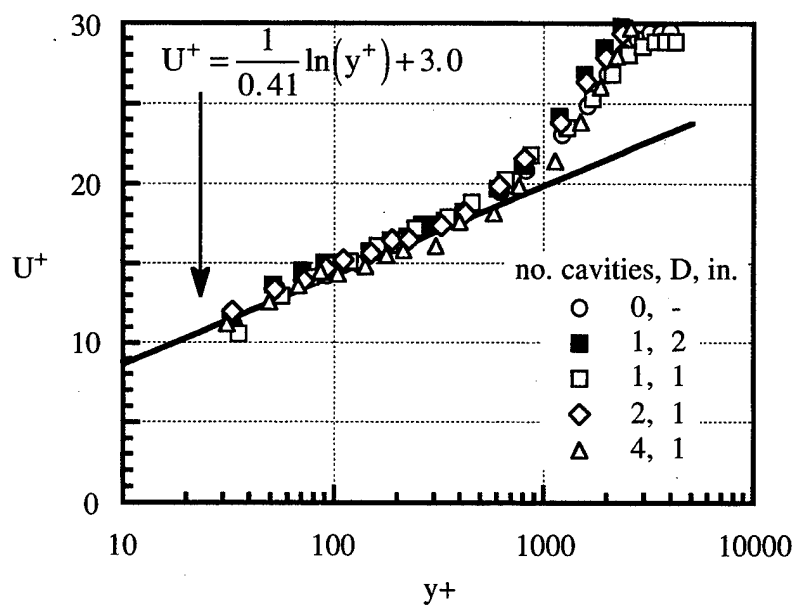
Figure 51. Continued.



(f) 24" test section at $x = 16"$ with the 7° test-section diffuser.
Figure 51. Concluded.

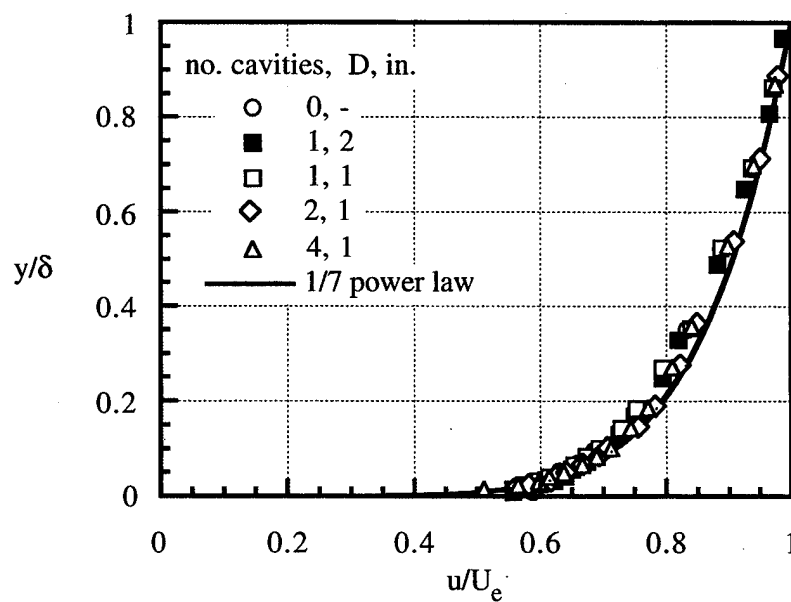


(a) 7° test-section diffuser data compared with log-law equation using $C_1 = 3.5$.
Figure 52. Comparison of 120" test-section experimental data at $x = 112"$ with the log-law equation with C_1 changed from 5.0.



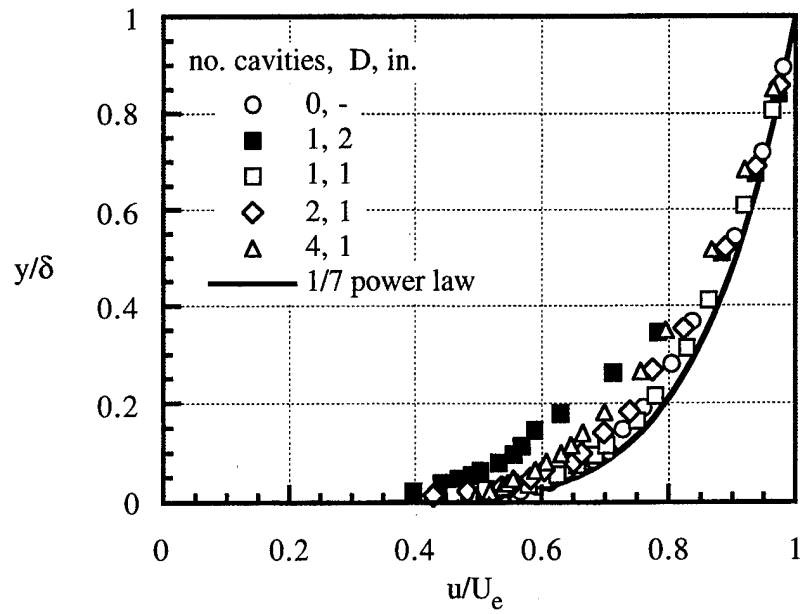
(b) 14° test-section diffuser data compared with log-law equation using $C_1 = 3.0$.

Figure 52. Concluded

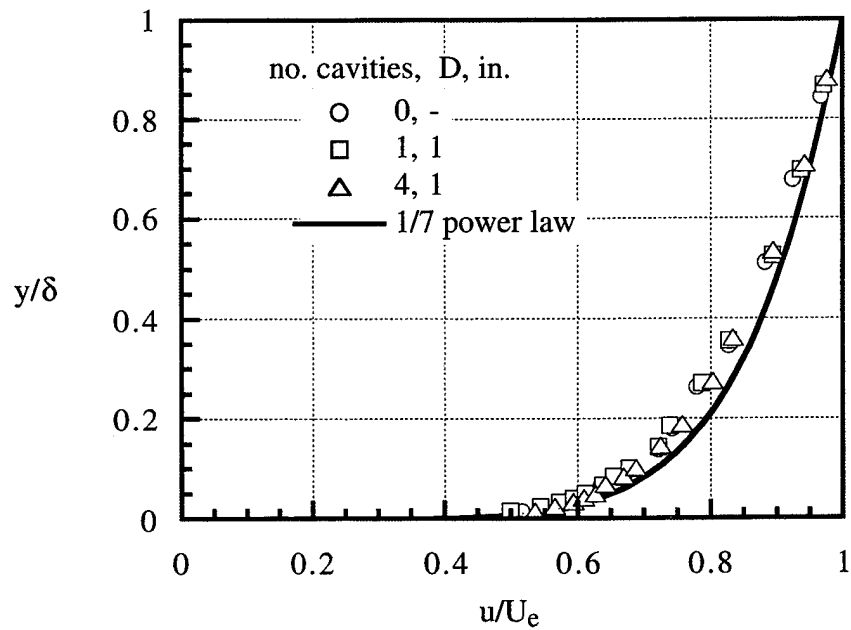


(a) 120" test section at $x \approx 101"$.

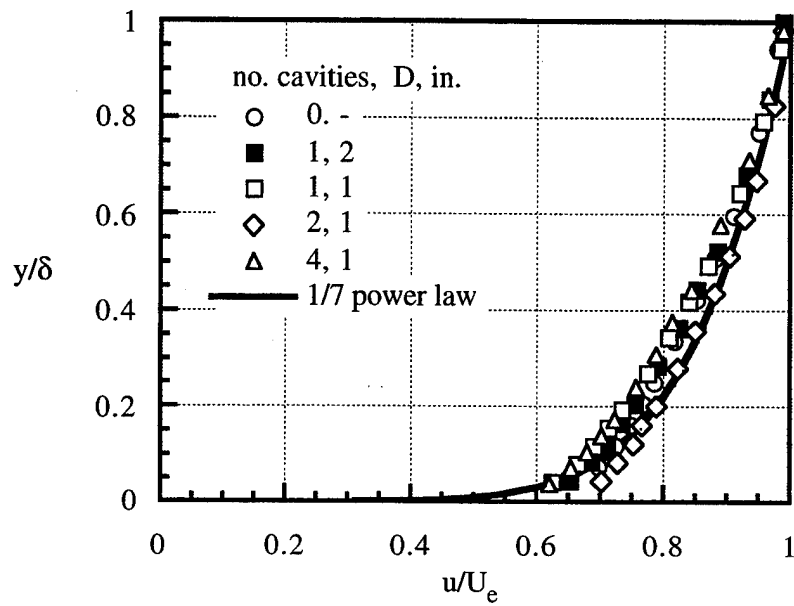
Figure 53. Effect of the cavity configuration on the boundary-layer profile.



(b) 120" test section at $x \approx 101"$ with the 14° test-section diffuser.
Figure 53. Continued.

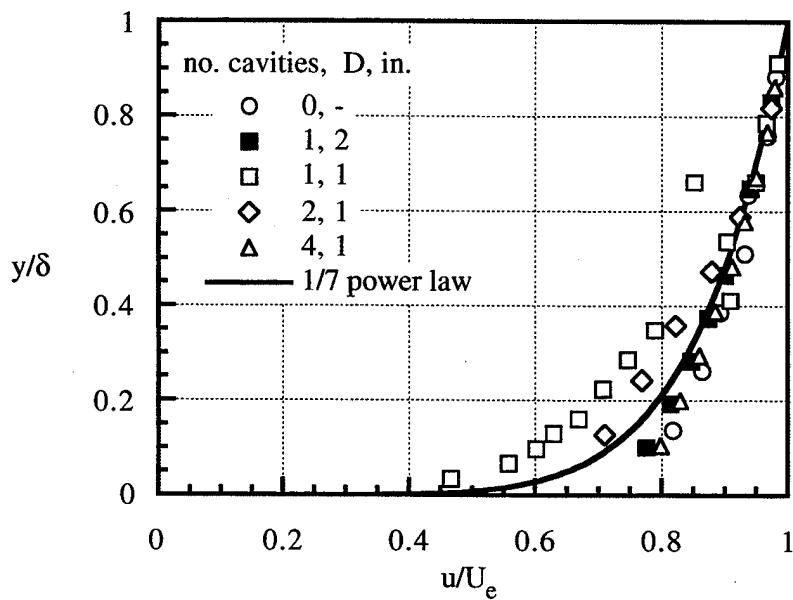


(c) 120" test section at $x \approx 101"$ with the 7° test-section diffuser.
Figure 53. Continued.



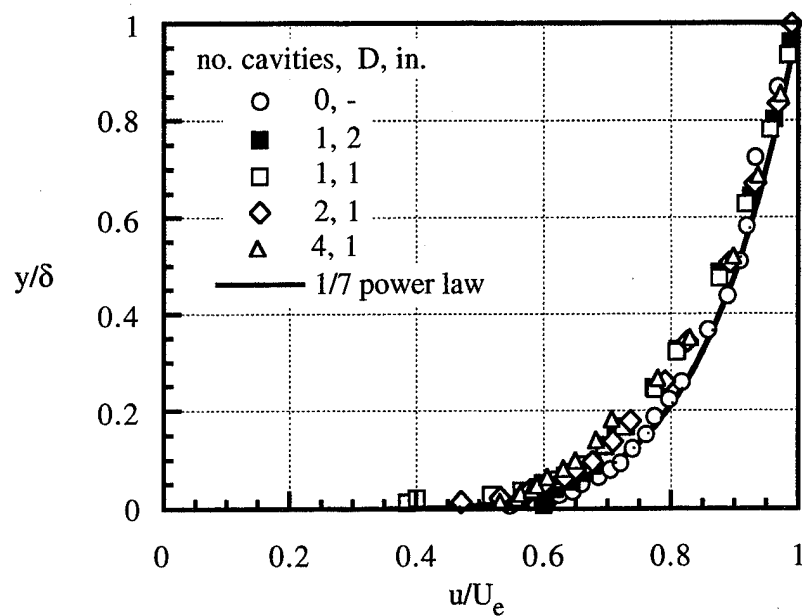
(d) 24" test section at $x \approx 5"$.

Figure 53. Continued.



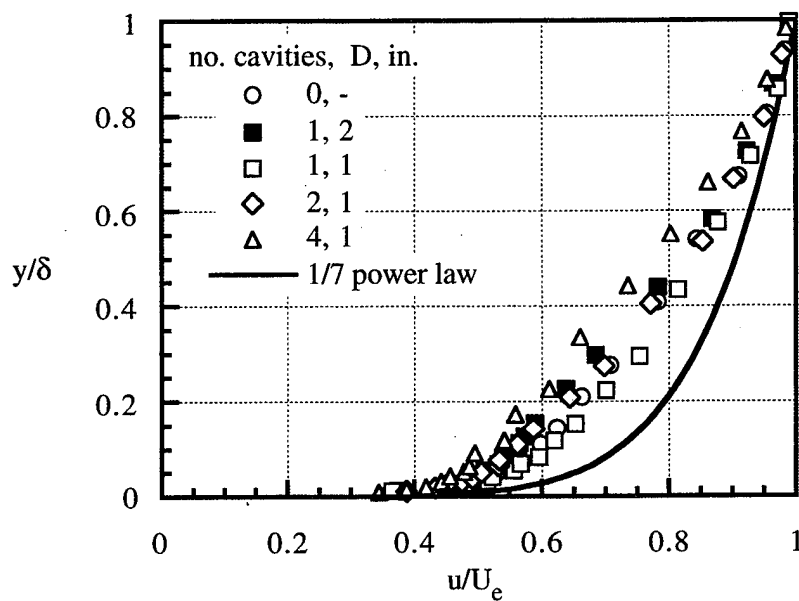
(e) 24" test section at $x \approx 5"$ with the 14° test-section diffuser.

Figure 53. Concluded.



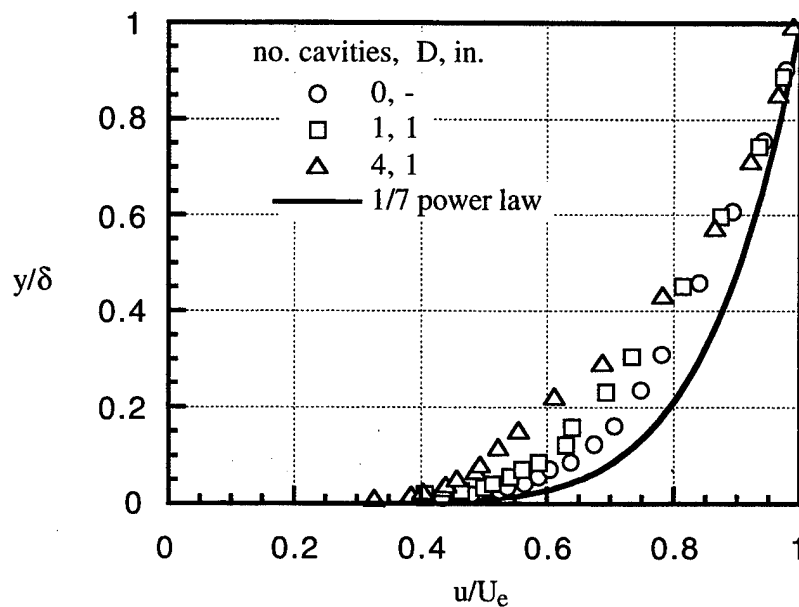
(a) 120" test section at $x = 112"$.

Figure 54. Effect of the cavity configuration on the boundary-layer profile.



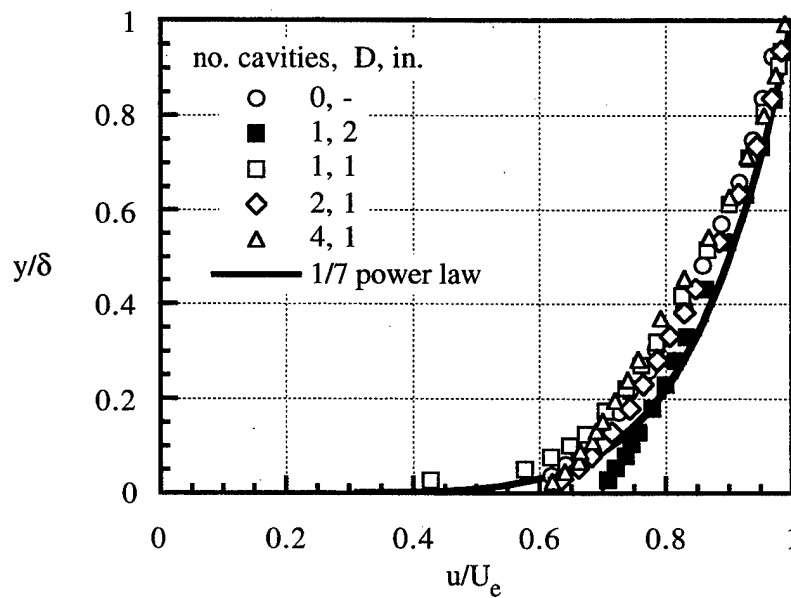
(b) 120" test section at $x = 112"$ with the 14° test-section diffuser.

Figure 54. Continued.



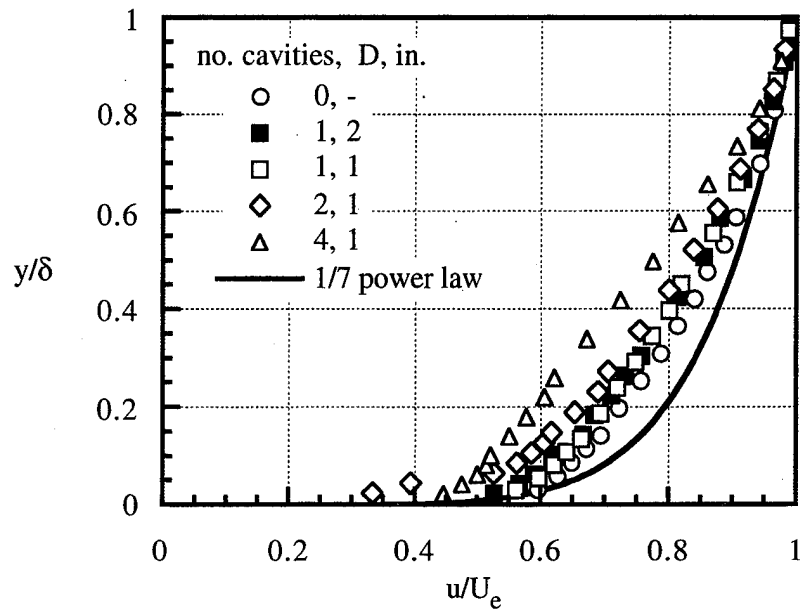
(c) 120" test section at $x = 112$ " with the 7° test-section diffuser.

Figure 54. Continued.

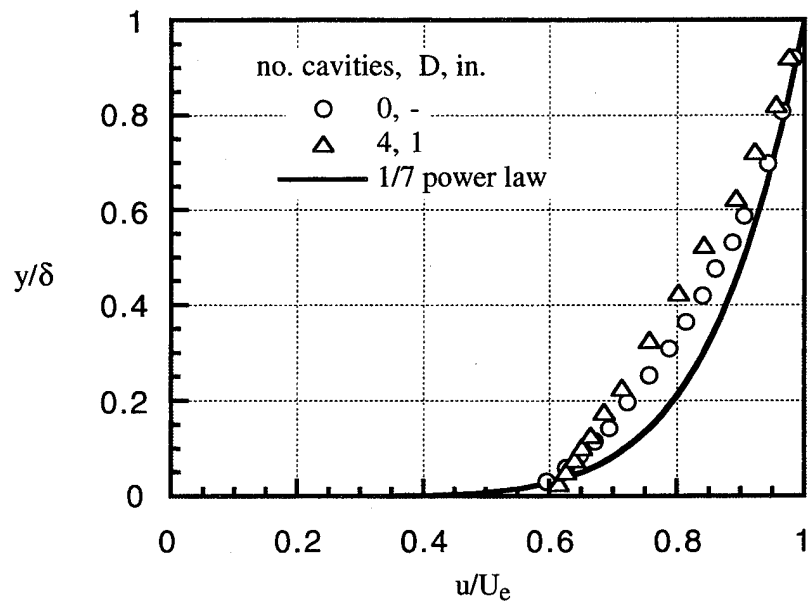


(d) 24" test section at $x = 16$ ".

Figure 54. Continued.



(e) 24" test section at $x = 16"$ with the 14° test-section diffuser.
Figure 54. Continued.



(f) 24" test section at $x = 16"$ with the 7° test-section diffuser.
Figure 54. Concluded.

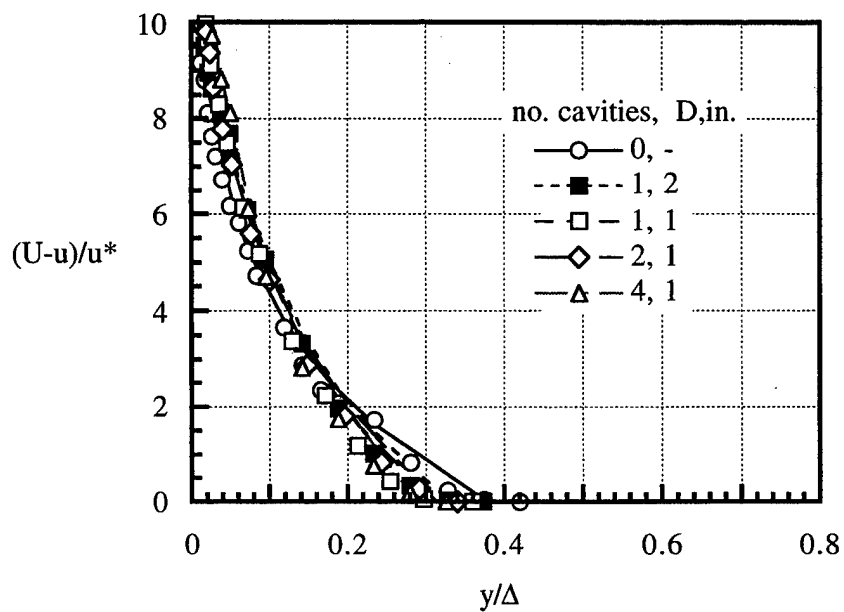


Figure 55. Effect of the cavity configuration on the universal velocity profile.

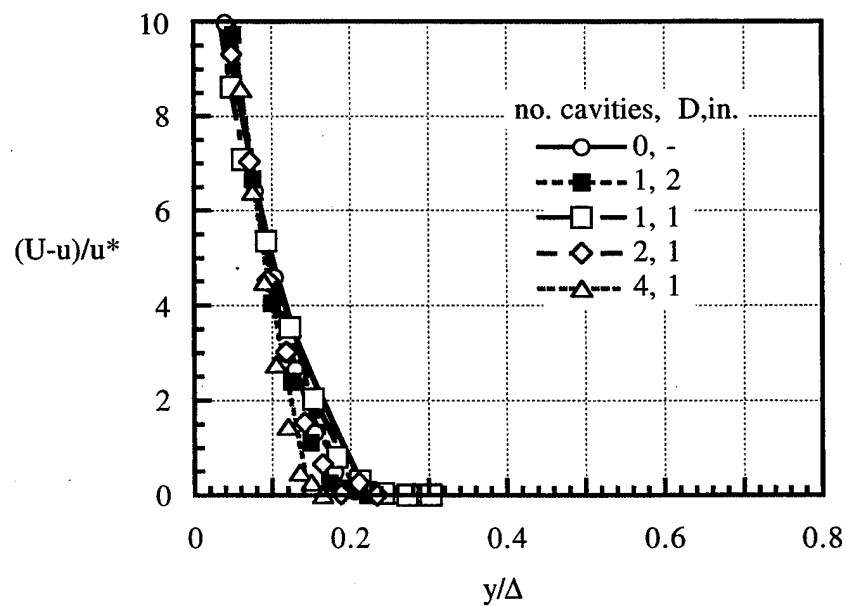
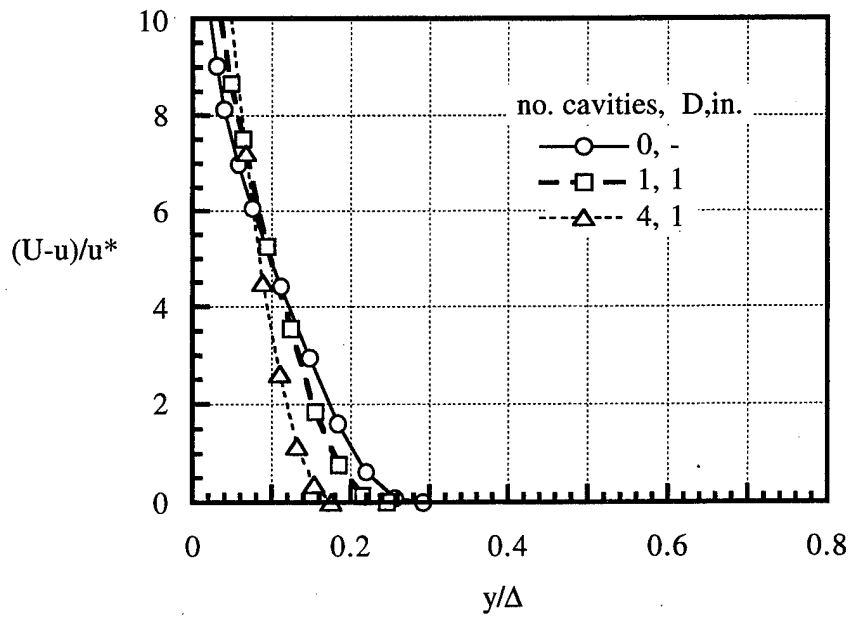
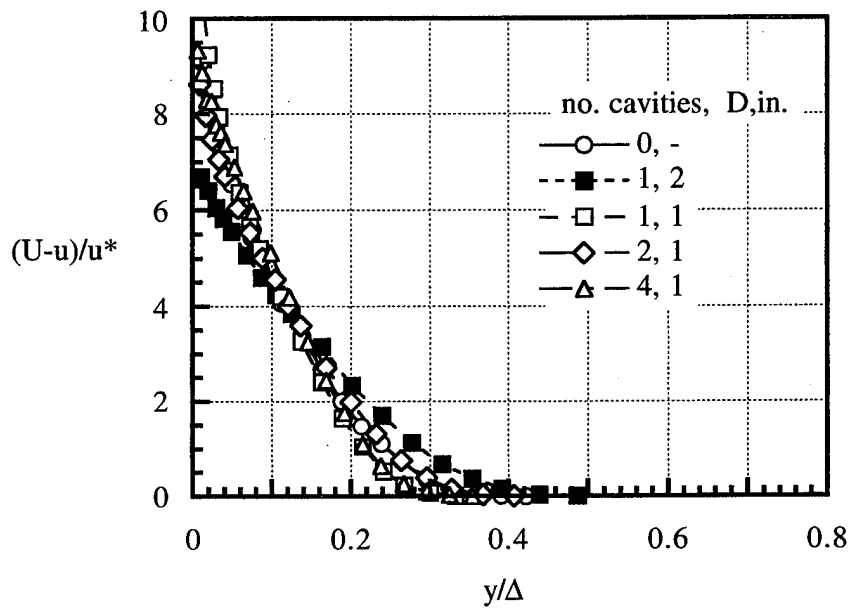


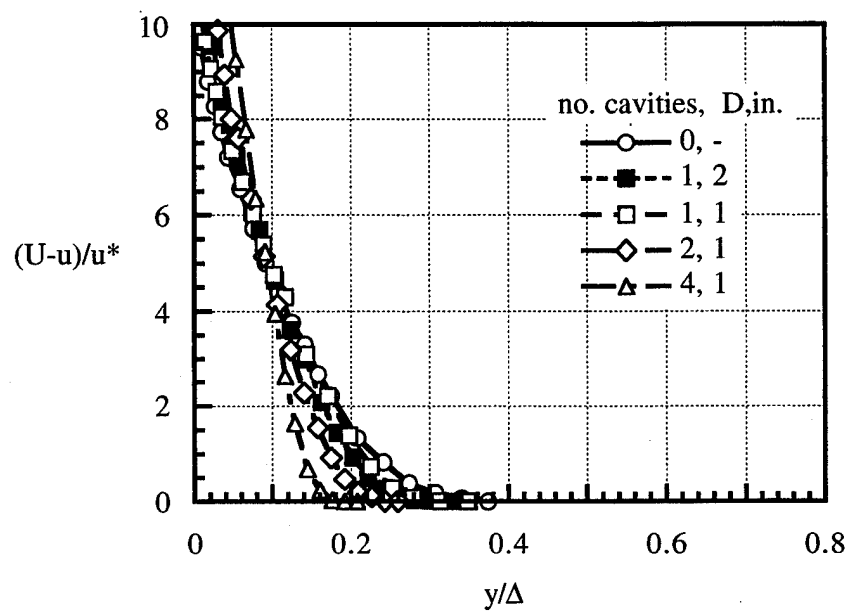
Figure 55. Continued.



(c) 120" test section at $x = 112$ with the 7° test-section diffuser.
Figure 55. Continued.

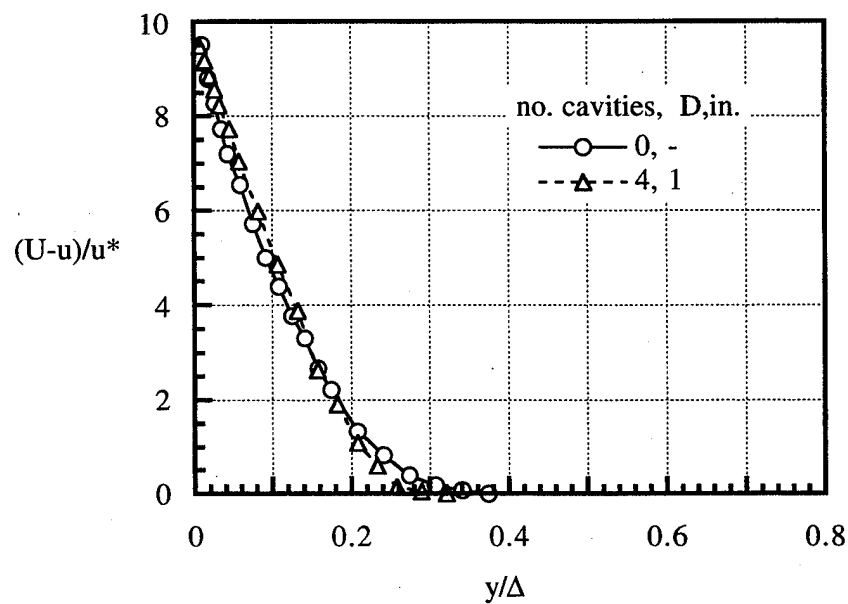


(d) 24" test section at $x = 16$.
Figure 55. Continued.



(e) 24" test section at $x = 16"$ with the 14° test-section diffuser.

Figure 55. Continued.



(f) 24" test section at $x = 16"$ with the 7° test-section diffuser.

Figure 55. Concluded.

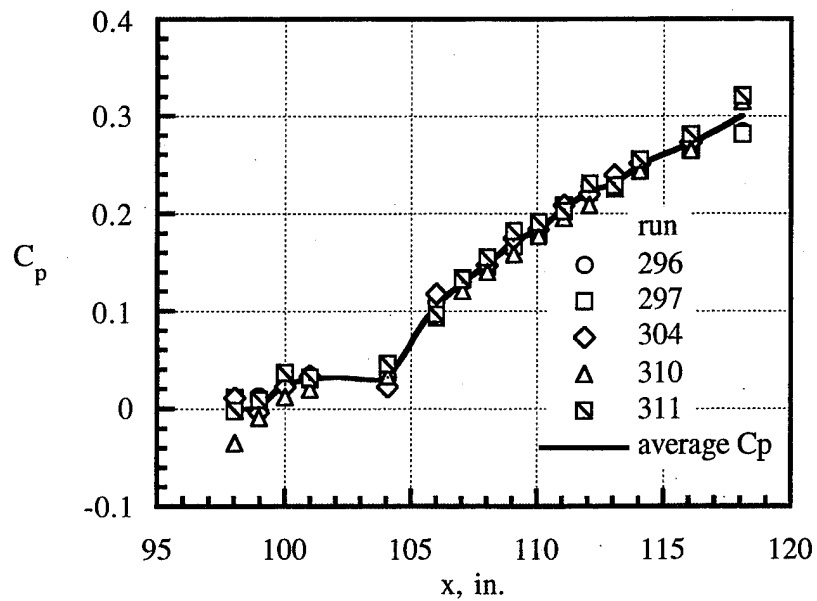


Figure 56. An example of pressure-data repeatability using the tunnel ceiling measurements for configuration 8431c (120" test section and $D = 2"$ with the door closed).

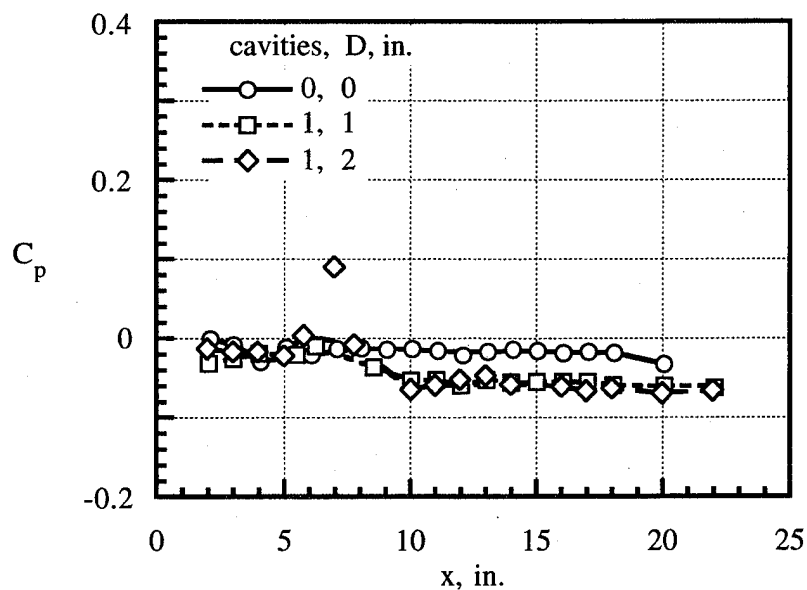


Figure 57. Effect of the single cavity size on the ceiling pressure distribution (24" test section with $D = 1"$ or $2"$).

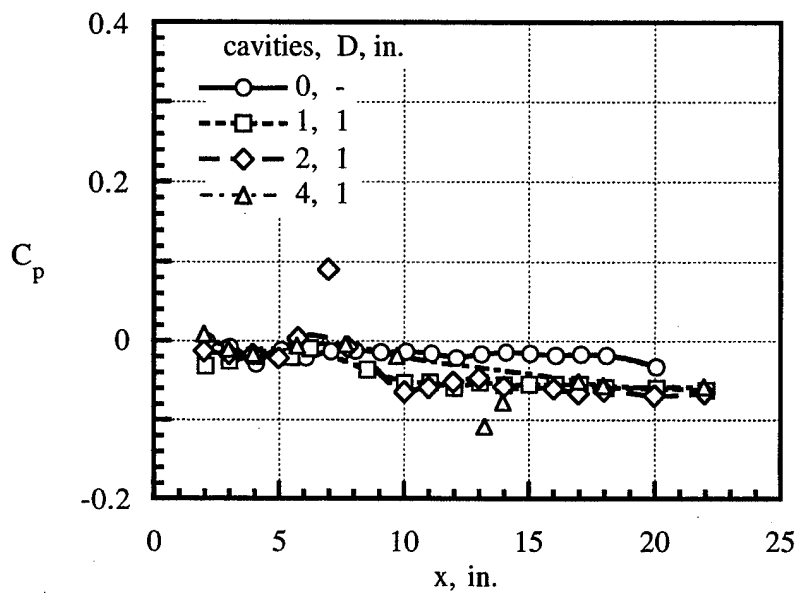


Figure 58. Effect of the multiple cavities on the ceiling pressure distribution (24" test section with $D = 1$ ").

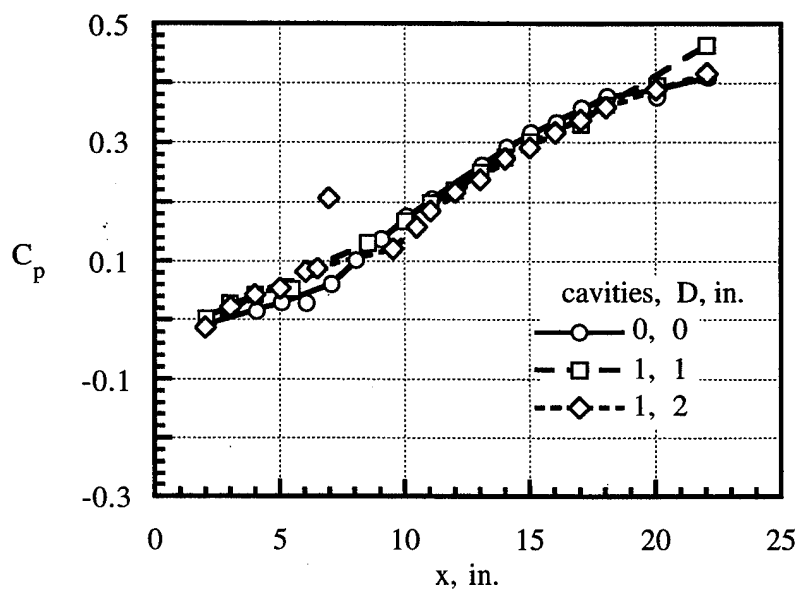


Figure 59. Effect of the single cavity size on the ceiling pressure distribution (24" test section, 14° test-section diffuser with $D = 1$ " or 2").

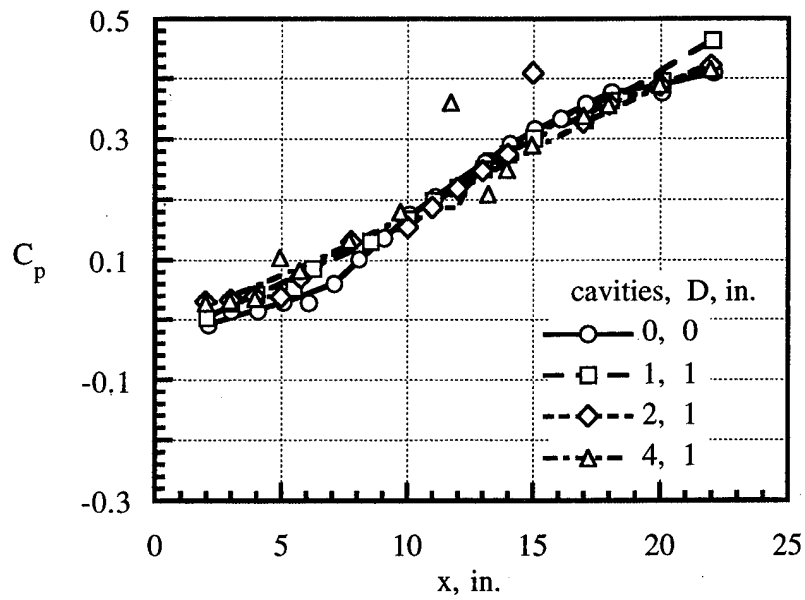


Figure 60. Effect of the multiple cavities on the ceiling pressure distribution (24" test section, 14° test-section diffuser with $D = 1$ ").

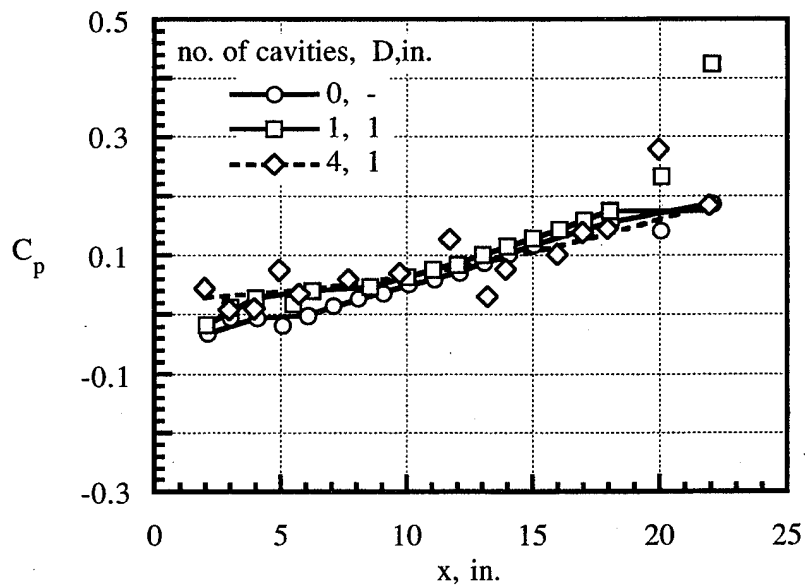


Figure 61. Effect of the multiple cavities on the ceiling pressure distribution (24" test section, 7° test-section diffuser with $D = 1$ ").

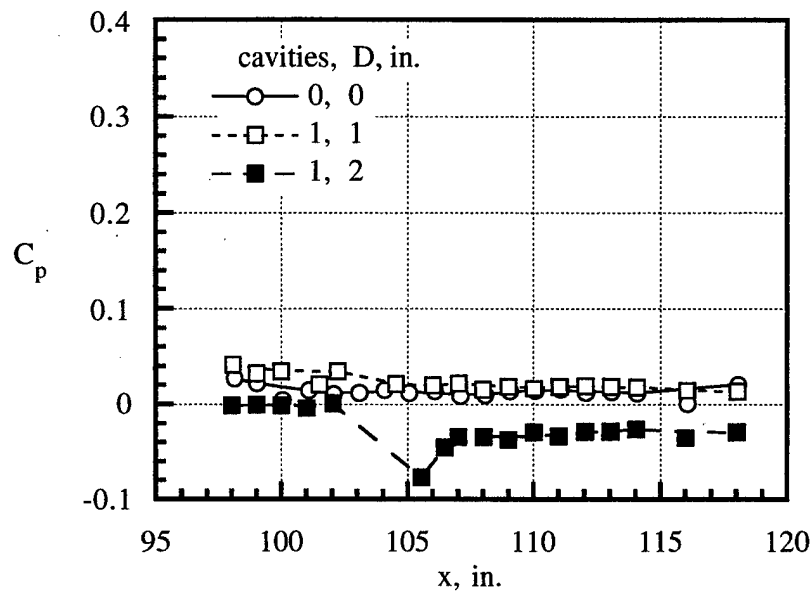


Figure 62. Effect of the single cavity size on the ceiling pressure distribution (120" test section with $D = 1$ " or 2 ").

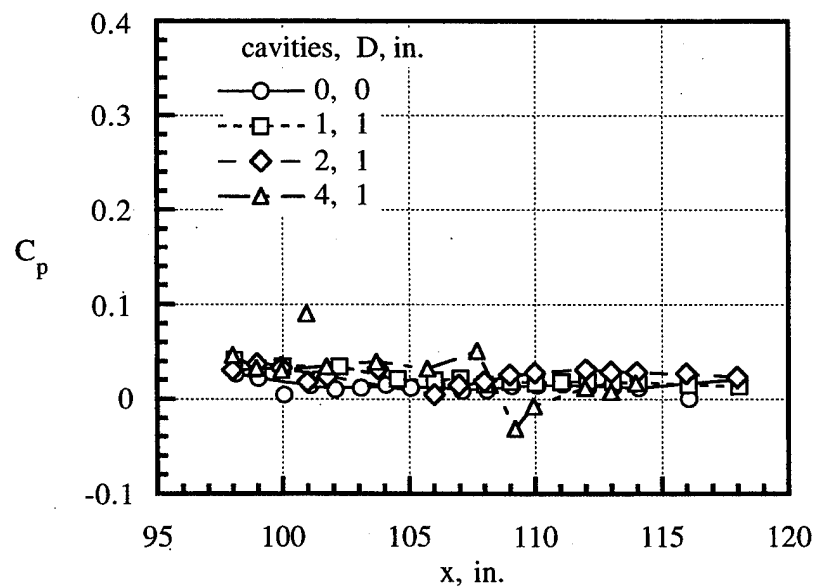


Figure 63. Effect of the multiple cavities on the ceiling pressure distribution (120" test section with $D = 1$ ").

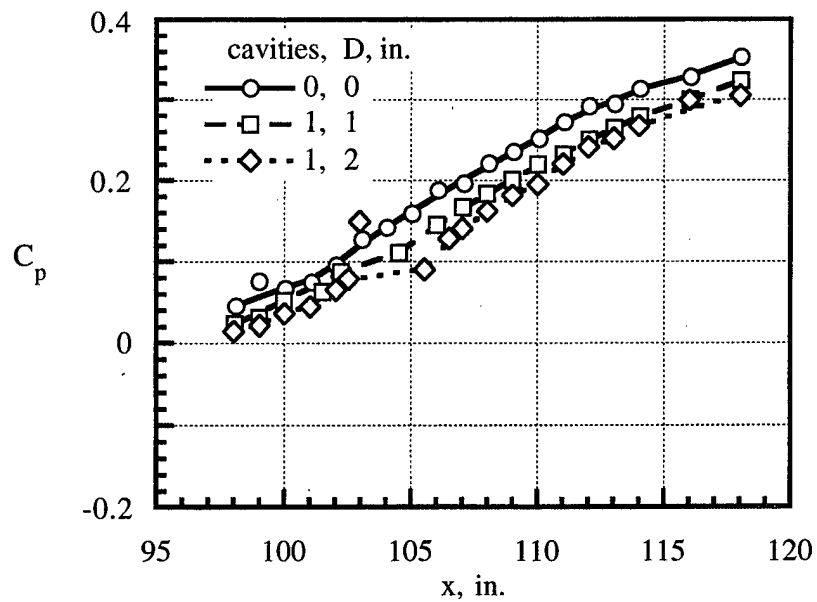


Figure 64. Effect of the single cavity size on the ceiling pressure distribution (120" test section, 14° test-section diffuser with $D = 1$ " or 2").

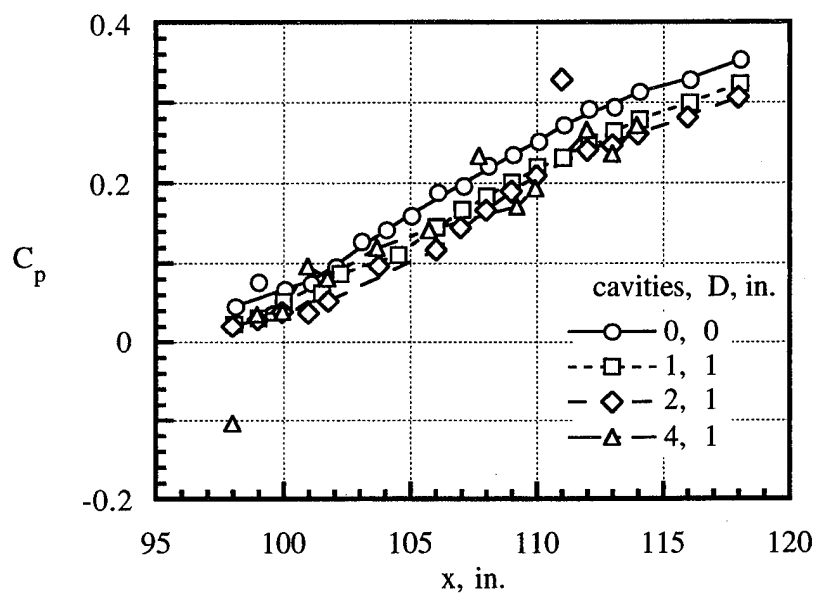


Figure 65. Effect of the multiple cavities on the ceiling pressure distribution (120" test section, 14° test-section diffuser with $D = 1$ ").

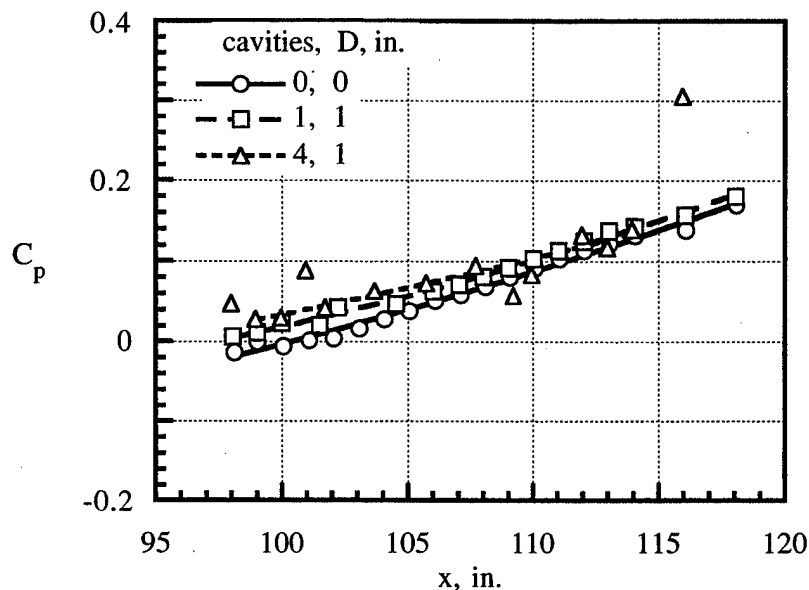


Figure 66. Effect of the multiple cavities on the ceiling pressure distribution (120" test section, 7° test-section diffuser with $D = 1$ ").

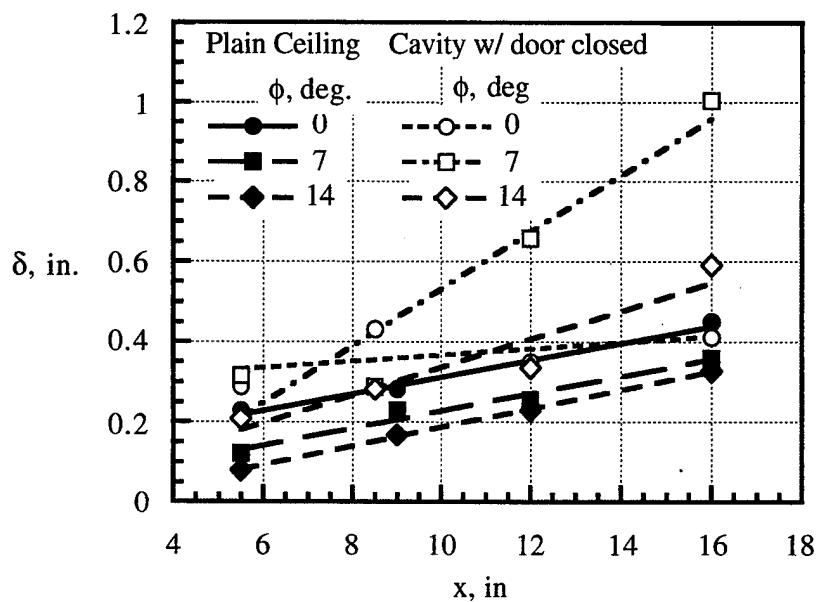
3. Cavity With a Door

As described in the introduction, the effect of cavities are being studied as a means for increasing airfoil camber to provide a new high lift device. One aspect of this application is the effect of surface non-uniformities (which could be caused by cavity doors) on the boundary layer and on the surface pressure distribution. Tests were conducted which compared a plain, smooth ceiling with a ceiling which had a two-inch square cavity which was closed by a flush door. The door was mounted by a pivot at its upstream end. When the wind tunnel was not operating, the closed door was adjusted to be flush with the adjacent tunnel ceiling. When the tunnel was turned on and operated at a freestream velocity of 120 feet per second, it was noted that the door deflected into the flow

approximately 1/16 to 1/8 inch at its downstream edge. The larger deflections occurred when one of the test-section diffusers was present ($\phi = 7^\circ$ or 14°).

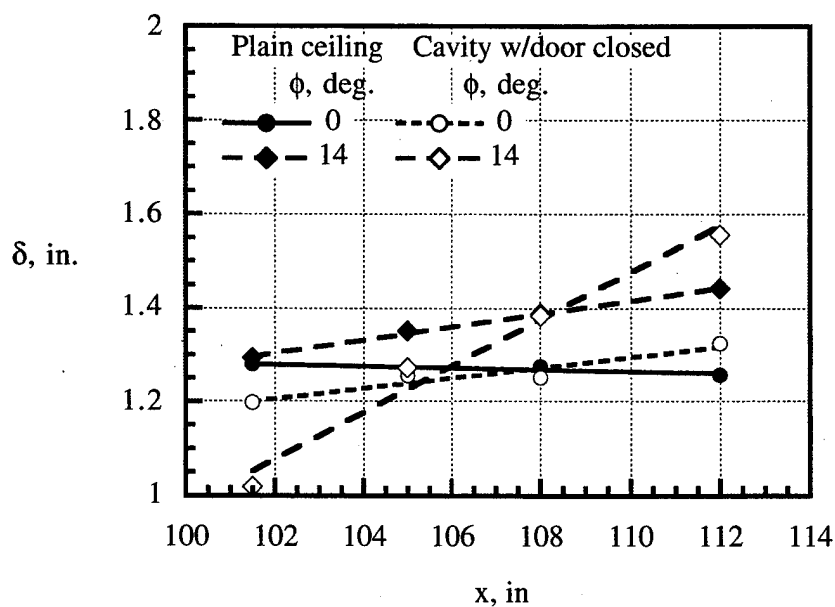
For these tunnel geometries, the measured boundary-layer thicknesses are presented in Figure 67 and the pressure distributions are presented in Figure 68. In each figure, part (a) presents data from the 24" test section and part (b) has data from the 120" test section. The data for the plain ceiling are presented by the solid symbols and the data for the cavity with a door are presented by open symbols. The boundary-layer thicknesses for the 24" test section cavity with a diffuser and a cavity with a closed door (Figure 67(a)) are thicker than those for the plain ceiling. The boundary layer thickness for the closed cavity with the 7° test-section diffuser increased much more rapidly than any of the other configurations. This difference is probably due to the increased projection of the cavity door trailing edge into the freestream, which was a significant fraction of the δ of 0.25 to 0.45 inch in this test section. The data for the 120" test section (Figure 67(b)) show a more noticeable effect of the cavity door projection even though the door projection was a small fraction of the measured δ , which was greater than an inch. This indicates that poor fit of a cavity door could increase skin friction drag. It is seen in Figure 68 that there were differences in the longitudinal pressure distribution for both test sections. This indicates that the surface non-uniformity had an effect on the inviscid freestream which determines the surface pressure distribution.

A second set of tests was conducted which compared the flow in the presence of a two-inch square open cavity with a similar two inch cavity (the closed cavity used in Figures 67 and 68) where a door was opened into the cavity to form a front cavity wall of an open-door cavity. The open cavity without a door had a smooth surface upstream of the cavity. In contrast, the open cavity door had a small gap of about 1/16 inch from the upstream end of the ceiling surface. These results are presented in Figure 69 (boundary layer thicknesses) and Figure 70 (longitudinal pressure distribution). While these results appear to be similar to those presented for the closed cavity in Figures 67 and 68, there are notable differences. The boundary-layer thicknesses for all of the open-door cavity configurations showed an increase with longitudinal distance similar to the increase of the closed cavity which had the largest increase, the 7° test-section

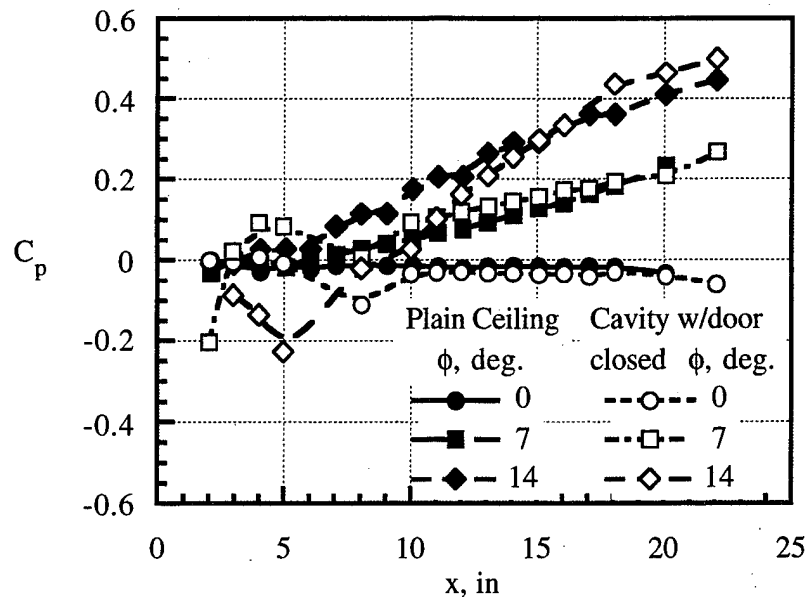


(a) 24" test section

Figure 67. Effects of closed cavity door and test-section diffusers on the variation of boundary-layer thickness as a function of longitudinal location.

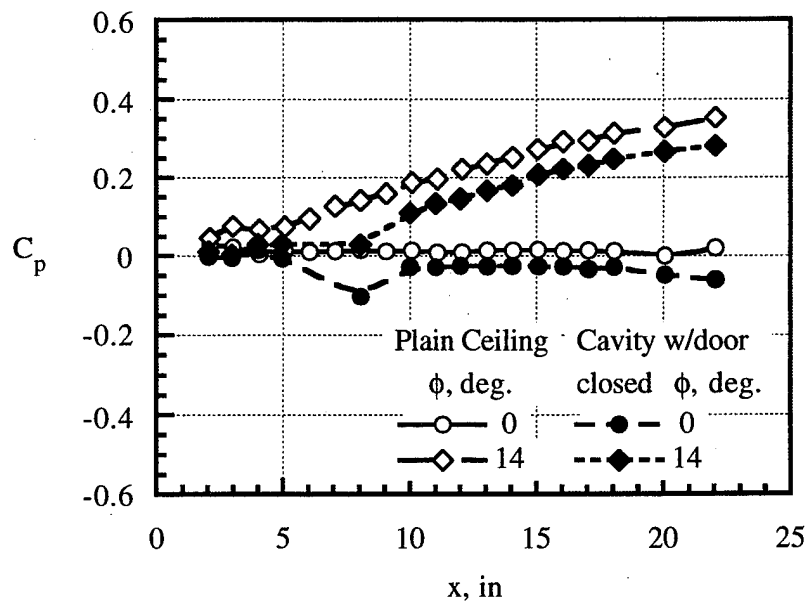


(b) 120" test section
Figure 67. Concluded

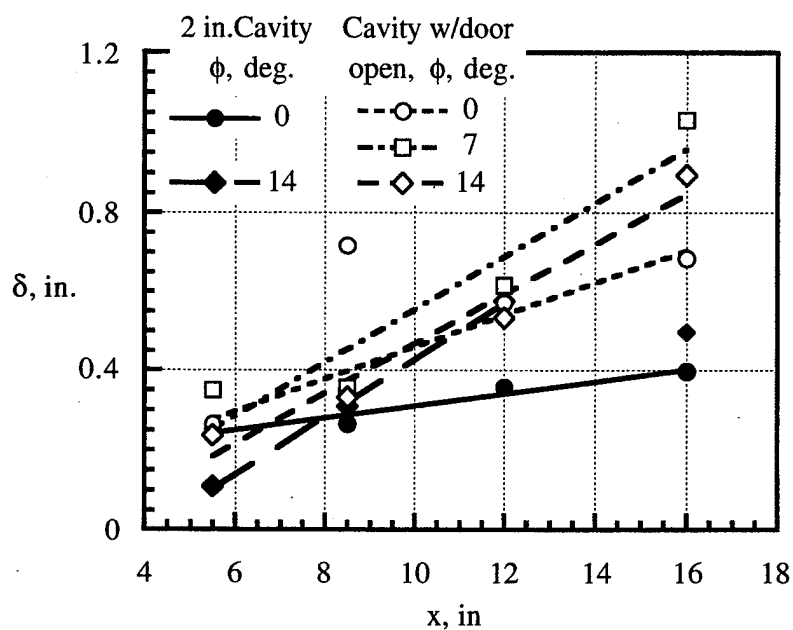


(a) 24" test section

Figure 68. Effects of closed cavity door and test-section diffusers on the variation of ceiling pressure distribution.

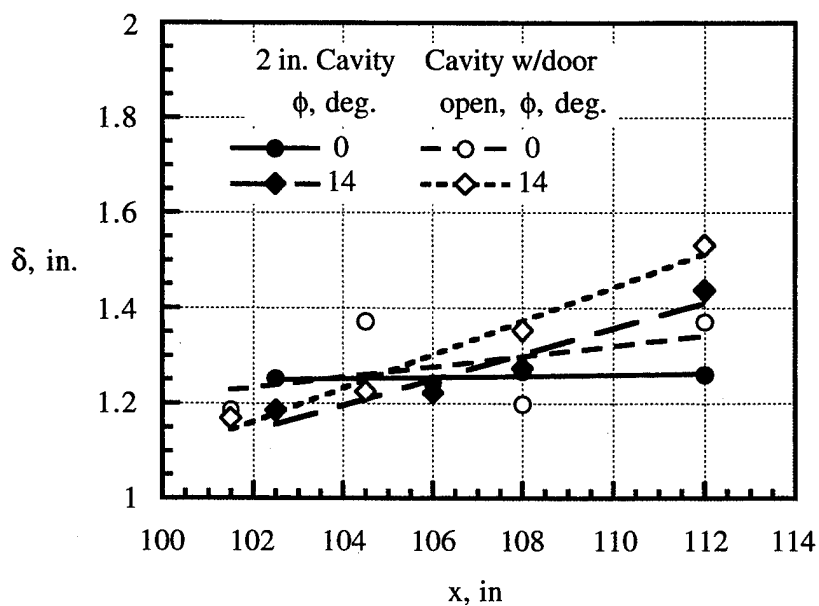


(b) 120" test section
Figure 68. Concluded

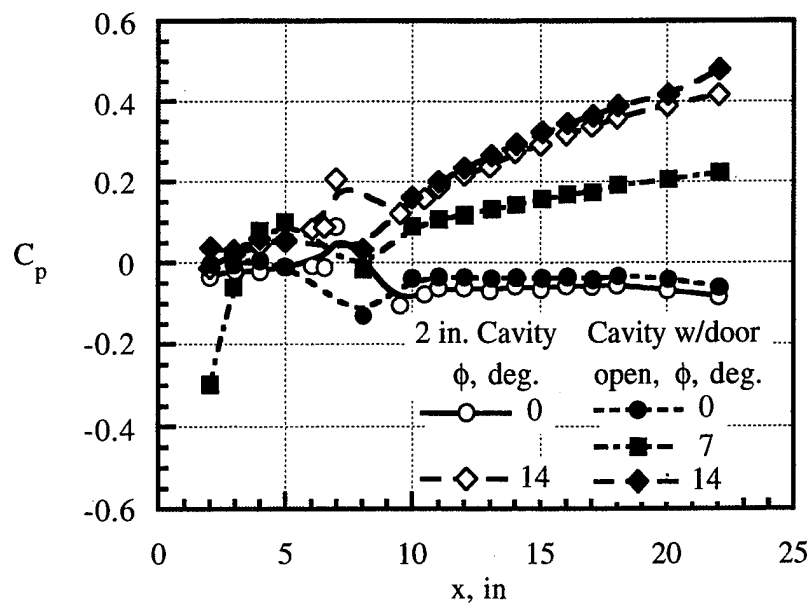


(a) 24" test section

Figure 69. Effect of open cavity door and test-section diffuser angle on the ceiling boundary-layer thickness as a function of longitudinal location.

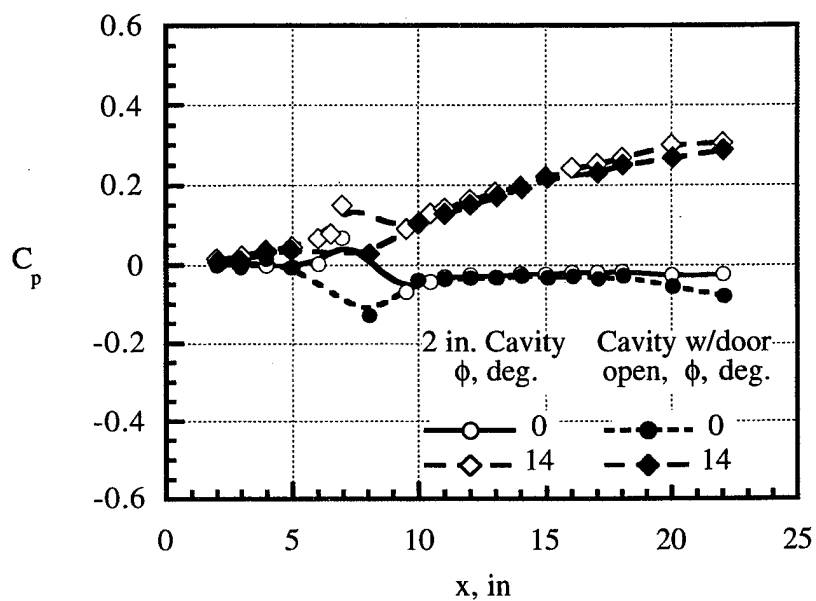


(b) 120" test section
Figure 69. Concluded



(a) 24" test section

Figure 70. Effect of open cavity configuration and test-section diffuser angle on the ceiling longitudinal pressure distribution.



(b) 120" test section

Figure 70. Concluded

configuration. The reasons for this result have not been identified. In contrast, it is seen that with the open cavities (Figure 70) there were smaller differences in the longitudinal pressure distribution for either test section length than that shown by the closed cavity and plain ceiling. These results suggest that the open cavities produce less change in the surface pressure distributions than do surface non-uniformities in an otherwise plain ceiling.

IV. INCOMPRESSIBLE NAVIER-STOKES COMPUTATIONS

There are some simple flows related to the present investigation which may be represented by empirical correlations. One example is a two-dimensional, turbulent boundary-layer profiles using the 1/7 power law ($u/U_\infty = (y/\delta)^{(1/7)}$). More complete flow solutions require more complete sets of equations. There is a range of equation sets of increasing complexity available for the solution of fluid flows. All of these equation sets may be obtained as simplifications of the Navier-Stokes equations. The particular equations selected for a problem of interest depends on the characteristics of that flow. The simplest of these equations is the linear potential Laplace equation which assumes inviscid, incompressible, irrotational flow.

$$\nabla^2 \Phi = 0 \quad (26)$$

When there are viscous effects more complex equation sets are needed. Two-dimensional, viscous flows in a conventional, subsonic wind tunnel test section may usually be accurately computed using the boundary-layer equations (Equations 11 through 13). These equations describe the attached boundary layer near the walls which develops adjacent to the inviscid outer flow, which is representative of the bulk of the freestream flow.

The boundary-layer concept of Prandtl assumes that the viscous layer is small (thin boundary layer) relative to the streamwise flow distance ($\delta/L \ll 1$). As a consequence, the Navier-Stokes equations may be simplified to obtain the boundary layer approximation for steady, two-dimensional, incompressible, constant fluid-property flow [Ref. 90]. The present experimental investigation adds an adverse pressure gradient and one or more cavities to produce a flow which is more complicated than those which can be resolved by the boundary-layer equations. Especially difficult is the resolution of the recirculating flow in a cavity and its interaction with the freestream in an adverse pressure gradient. For example, in the 120-inch test section in the present investigation, the cavity flow had a viscous layer whose thickness was nearly the same as the cavity depth. In

contrast, for the 24 inch test section the viscous boundary layer thickness was much less than the cavity depth.

Based on the present literature survey, neither experimental nor computational data have been obtained for these flows prior to the present investigation. The present experiment measured the flow in the vicinity of several cavity configurations with a freestream Mach number of the order of 0.10. For flows such as these, the incompressible Navier-Stokes equations are a more suitable representation than the boundary layer equations. The incompressible Navier-Stokes equations are derived from the Reynolds-averaged Navier-Stokes equations by assuming an incompressible flow (i.e., $M = 0$ and $a = \infty$).

Since the temperature was essentially constant in the present experimental investigation the energy equation is not required. The two-dimensional, incompressible Navier-Stokes equations in Cartesian coordinates become the following:

$$\text{continuity equation,} \quad \frac{\partial u}{\partial x} + \frac{\partial v}{\partial y} = 0 \quad (27)$$

$$\text{x momentum equation,} \quad \frac{\partial u}{\partial t} + u \frac{\partial u}{\partial x} + v \frac{\partial u}{\partial y} = -\frac{1}{\rho} \frac{\partial p}{\partial x} + \nu \left(\frac{\partial^2 u}{\partial x^2} + \frac{\partial^2 u}{\partial y^2} \right) \quad (28)$$

$$\text{y-momentum equation,} \quad \frac{\partial v}{\partial t} + u \frac{\partial v}{\partial x} + v \frac{\partial v}{\partial y} = -\frac{1}{\rho} \frac{\partial p}{\partial y} + \nu \left(\frac{\partial^2 v}{\partial x^2} + \frac{\partial^2 v}{\partial y^2} \right) \quad (29)$$

A numerical solution of these equations may be obtained for example using either a finite-element or finite-difference scheme, a suitable grid, and the definition of appropriate boundary conditions.

A. INCOMPRESSIBLE NAVIER-STOKES CODE (ins2d)

The ins2d computer code [Ref. 91 and 92] numerically solves the two-dimensional, incompressible Navier-Stokes equations in a time-accurate manner. In a pseudocompressibility formulation, a time derivative of pressure is added to the continuity equation,

$$\frac{\partial p}{\partial \tau} + \beta \left(\frac{\partial u}{\partial x} + \frac{\partial v}{\partial y} \right) = 0 \quad (30)$$

Note that β is the pseudocompressibility constant and τ represents a pseudotime which is not related in any way to physical time. Equation 30 is then combined with the momentum equations to obtain the following equations in two-dimensional Cartesian coordinates.

$$\frac{\partial}{\partial \tau} D + \frac{\partial}{\partial x} (E - E_v) + \frac{\partial}{\partial y} (F - F_v) = 0 \quad (31)$$

where

$$D = \begin{bmatrix} p \\ u \\ v \end{bmatrix} \quad E = \begin{bmatrix} \beta u \\ u^2 + p \\ uv \end{bmatrix} \quad F = \begin{bmatrix} \beta v \\ uv \\ v^2 + p \end{bmatrix}$$
$$E_v = \begin{bmatrix} 0 \\ \tau_{xx} \\ \tau_{xy} \end{bmatrix} \quad F_v = \begin{bmatrix} 0 \\ \tau_{yx} \\ \tau_{yy} \end{bmatrix}$$

$$\tau_{xx} = 2\nu \frac{\partial u}{\partial x} \quad \tau_{yy} = 2\nu \frac{\partial v}{\partial y}$$

$$\tau_{xy} = \tau_{yx} = \nu \left(\frac{\partial u}{\partial y} + \frac{\partial v}{\partial x} \right)$$

The convective terms are upwind-differenced using a Roe [Ref. 93] flux-difference split approach that has uniformly high accuracy throughout the interior grid points. This scheme was derived as an approximate Riemann solver for the compressible flow equations. In this formulation the Reynolds stress has been approximated as a function of the strain-rate tensor, and thus represents a sum of the kinematic viscosity and the turbulent eddy viscosity. Constant kinematic viscosity is assumed for simplicity. The viscous fluxes are differenced using second-order accurate central differences.

The system of equations (equations 31) is solved numerically using an implicit line-relaxation scheme. Application of a first-order backward Euler formula to equations 31 yields the delta-form equation

$$\left[\frac{1}{J\Delta\tau} I + \left(\frac{\partial R}{\partial D} \right)^n \right] (D^{n+1} - D^n) = -R^n \quad (32)$$

Here the superscript n is the pseudotime iteration count and R is the residual vector. Unsteady problems are solved with the use of subiterations in pseudotime at each physical time step.

At the inflow boundary there is one characteristic wave traveling out of the computational domain the since fluid is traveling into the domain. When the inflow velocity profile is not known, there is a vector of variables which is held constant and defined as

$$\Omega = \begin{bmatrix} p + \frac{1}{2}(u^2 + v^2) \\ 0 \\ v \end{bmatrix} \quad \frac{\partial \Omega}{\partial D} = \begin{bmatrix} 1 & u & v \\ 0 & 0 & 0 \\ 0 & 0 & 1 \end{bmatrix} \quad (33)$$

For the present calculation the vertical inflow velocity component v was set to zero and the horizontal inflow velocity u was set to unity at all of the inflow plane grid points except at the floor and ceiling grid points where both were zero.

At the outflow boundary there are two characteristic waves traveling out of the computational domain since fluid is also leaving the domain. This computation used a specified static pressure at the outflow plane which was defined as

$$\Omega = \begin{bmatrix} p \\ 0 \\ 0 \end{bmatrix} \quad \frac{\partial \Omega}{\partial D} = \begin{bmatrix} 1 & 0 & 0 \\ 0 & 0 & 0 \\ 0 & 0 & 0 \end{bmatrix} \quad (34)$$

The tangential flow boundary conditions on the tunnel floor and ceiling were obtained by setting both the u and v velocity components to zero.

B. GRID GENERATION

The grid was generated using several computers and codes. Several FORTRAN codes were written to generate both the freestream flow grid between the wind tunnel ceiling and the floor (sjtgg.f and rtgg.f) and the cavity grid (cgg.f and cgga.f). Then these grids were coupled by the PEGSUS code [Ref. 94] which uses an overset scheme. Typically these codes were run interactively. For the basic wind tunnel flow computations the grid from code sjtgg.f was used directly in the ins2d code. These FORTRAN programs were solved using a Silicon Graphics (SGI) Challenger L workstation. This computer has 4 processors, a MIPS R4400 microprocessors with a clock speed of 150 MHz, 256 MB random-access memory and 2GB random-access disk storage.

For a boundary layer flow, the largest velocity gradient occurs adjacent to the walls and normal to the flow direction. For the present ins2d Navier-Stokes flow solver, it is recommended that the finest spacing near the wall lead to a minimum non-dimensional inner layer distance normal to the wall y^+ of approximately 1. The y^+ is reduced by reducing the grid spacing near the tunnel wall. In Anderson, Tannehill, and Pletcher [Ref. 90] several simple transformations are presented which can be used to cluster the grid in regions of large gradients such as boundary layers. These transformations are part of a general family proposed by Roberts [see Ref. 90, pp. 247-250]. One transformation was developed to refine the mesh near the walls of a two-dimensional tunnel using equations

$$x = \bar{x}$$

and

$$y = h \frac{(\beta + 2\alpha)[(\beta + 1)/(\beta - 1)]^{(\bar{y}-\alpha)/(1-\alpha)} - \beta + 2\alpha}{(2\alpha + 1) \left\{ 1 + [(\beta + 1)/(\beta - 1)]^{(\bar{y}-\alpha)/(1-\alpha)} \right\}} \quad (35)$$

where h is tunnel height, $\alpha = 1/2$ refines the grid equally near $y = 0$ and $y = h$, and

$$\beta = \left(1 - \frac{\delta}{h}\right)^{-1/2} \quad \text{for} \quad 0 < \frac{\delta}{h} < 1 \quad (36)$$

Coordinates \bar{x} and \bar{y} represent a uniform Cartesian grid and coordinates x and y represent a clustered grid. A computer program (rtgg.f) was written to generate the grid for the wind tunnel used in the experimental investigation.

An example of Roberts' transformation grid clustering is shown in Figure 71(a) for the region between the tunnel floor and the tunnel centerline. The region from the tunnel centerline to the tunnel ceiling is the reflection of the clustering shown in Figure 71. The horizontal scale is a uniformly-spaced coordinate η_i non-dimensionalized by the scale factor SF , and the vertical scale is clustered grid scale y_i norm which is then converted from the 0 to 1 scale to the dimensions of the tunnel half height. The grid clustering is determined by the value of β which is shown to range from 2, for the least clustering, to 1.001, for the greatest clustering.

The largest two values, 2 and 1.2, provide only a limited clustering. In the next section results from the ins2d code will be presented for the three finest scale factors shown in Figure 71(a): 1.05, 1.01, and 1.001. These results will be used to evaluate the usefulness of the Roberts grid-transformation scheme for representing these boundary-layer flows.

An alternative to Roberts' transformation-clustering scheme was developed by the author using a tangential grid-spacing scheme. This transcendental function was used to transform a uniform spacing to a variable grid spacing. The fineness of the grid spacing was determined by a tangential grid-spacing scale factor SF. Initially the scheme divided a distance into a uniform spacing where

$$\delta\eta = \frac{\eta_{\max} - \eta_l}{NC - 1} \quad (37)$$

using

$$\eta_l = \tan^{-1}(-SF) \quad \text{and} \quad \eta_{\max} = \tan^{-1}(SF) \quad (38)$$

The value of the scale factor is increased when a finer grid is desired at the outer grid edges. For the present investigation, SF was typically 2 in the streamwise direction and ranged from 16 to 72 normal to the freestream direction.

As an illustration of the final steps only the y coordinate equations are used. Similar calculations are done in the x direction. For the next step, a normalized spacing from -1 to 1 was computed as

$$\bar{y}_i = \frac{\tan^{-1} \eta_i}{\tan^{-1} \eta_{\max}} \quad (39)$$

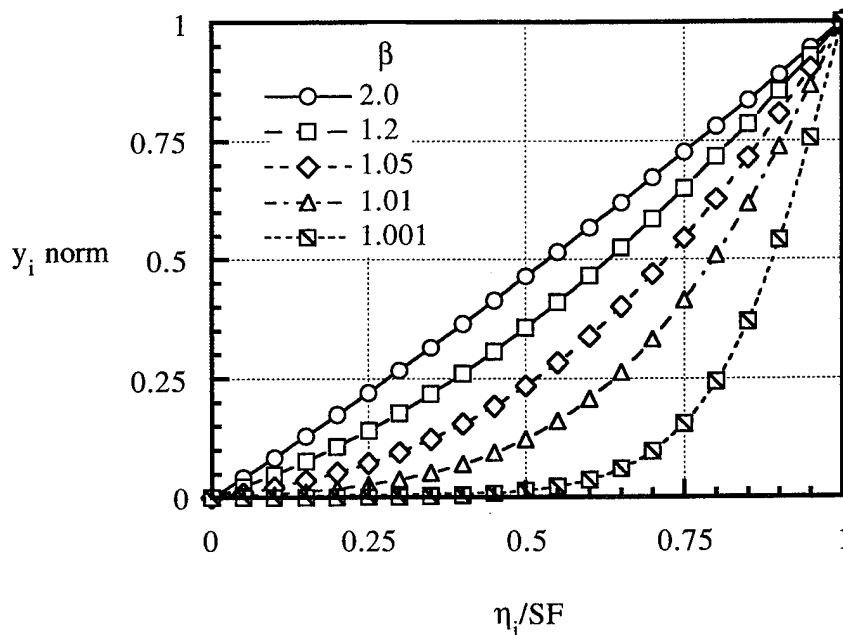
Finally the physical coordinates were computed as

$$y_i = y_{\text{org}} + \frac{\bar{y}_i + 1}{2} L \quad (40)$$

The fraction in the second term scales length from \bar{y}_i to a range from 0 to 1. Since y_{org} is the minimum physical dimension and L is the dimension length, the y_i values cover the entire length of this direction. Program sjtgg.f was used

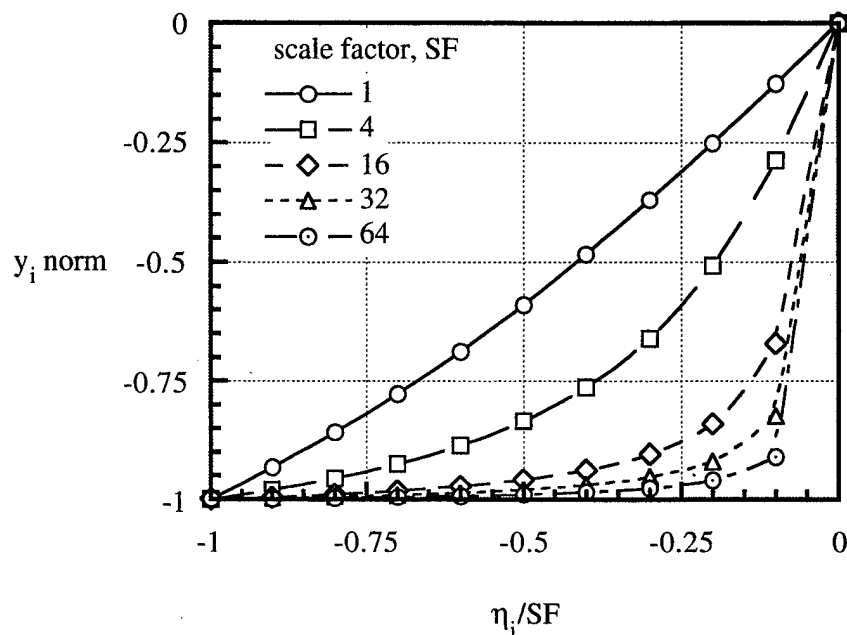
to algebraically calculate a two-dimensional grid for the wind tunnel freestream including the tunnel ceiling and floor, with or without the test section diffuser. Program `cgg.f` was used to generate each cavity grid. Both calculations clustered the grid using a tangential spacing scheme.

The normalized spacings obtained from this procedure is illustrated for several scale factors in Figure 71 (b). The increased clustering near the walls is readily apparent. At the highest scale factors the grid tends to be sparse near the center of the physical space. For the streamwise direction the flow tends to a zero gradient in the potential flow region away from the boundary layer. As a consequence the coarser spacing is adequate near the tunnel centerline. The grid size variation is well behaved for the present calculations because it changes by less than 1.2 between adjacent grid cells. This grid clustering scheme is evaluated in the next section to determine its suitability for the present investigation.



(a) Roberts grid transformation.

Figure 71. Clustered grid spacing as a function of a uniform spacing for several scale factors.



(b) Tangential grid transformation.
Figure 71. Concluded

The tangential grid spacing is used for both directions in each cavity and for both tunnel directions. When the tunnel has one or more cavities, the tangential grid spacing in the streamwise direction must be modified to satisfy an adjacent grid spacing variation of 1.2 or less. This requirement was satisfied as part of the program `cgga.f`. First this program generates the grid for the specified cavity. Then the tunnel grid generated in `sjtgg.f` is read and modified. In the streamwise direction the grid spacing is reduced immediately upstream and downstream of the cavity. Generally the two grids, freestream and cavity, are compatibly spaced in the vertical direction and require no modification. If modification is needed to satisfy the 1.2 adjacent spacing criterion the program `cgga.f` accomplishes this change in the freestream grid. If more than one cavity is present then `cgga.f` continues on to add these cavities to complete the grid.

C. CFD RESULTS

After the grid generation was completed, the CFD code computed the fluid flow solution and analysis of the results. After the grids were prepared, two additional input files were prepared which provided: (1) the boundary conditions and (2) the ins2d input data for the desired code options. The present input boundary conditions were (a) an inflow boundary with a constant velocity and characteristic relation for pressure, (b) an outflow boundary using characteristic relations for velocity and constant static pressure, (c) the ceiling with a no-slip wall with the wall normal vector pointing in the negative computational direction, and (d) the floor with a no-slip wall with the wall normal vector pointing in the positive computational direction. About 40 items of data make up the ins2d.in file. These data are defined in a user file described by the ins2d code and will not be discussed in detail in this paper.

The ins2d code was run on a Cray C-90 supercomputer with 8 processors, 256 Mw of random access memory (ram), 8 Gw of disk storage. The floating-point processor speed was 1 GFLOP which is about 20 faster than the Challenge L workstation used for grid generation. A typical case with a 201 by 321 grid used about 7.75 Mw of ram and required about 2.2 seconds/iteration or 345×10^{-7} seconds/iteration/grid point. The convergence criterion is based on the magnitude of the change in the residual term from the previous iteration. It was found that if a case converged it took 40 to 150 iterations. If a case took more iterations it did not converge. Some cases were run for as many as 20,000 iterations without convergence.

For data analysis, the desired ins2d results were then selected from the solution file using a postprocessing program called plot3d on the Cray C-90. These results were then transferred as a group of ASCII data files using a file transfer protocol to an Apple Macintosh IIfx personal computer. This computer used a Motorola 68030 microprocessor which had a clock speed of 40 MHz and an 8 MB random-access memory and an 80 MB hard disk. In most cases these data were read by a plotting program called Kaleidagraph.

1. Wind Tunnel Flow Computation

Several grid geometries were examined for the basic 24" test section (identified as C0000) and for the 120" test section (identified as C8000) used in the experimental investigation. For this phase of the computational investigation both the Robert's transformation and the tangential transformation were used to generate grids to represent the flow in the wind tunnel for both the 24-inch test section and the 120-inch test section. Also examined for both test section lengths were the number of grid points in the y direction, normal to the freestream. For the 24-inch test section, the effect of the longitudinal length of the x grid was varied.

a. 24 Inch Test Section

The grid was used to represent the 24 inch wind tunnel test section (C0000) from the floor to the ceiling and between the longitudinal stations of -16 to 24 inches. A few preliminary cases were run for a shorter longitudinal grid which ran from 0 to 24 inches. It was found that this provided boundary layer thicknesses which were too thin in relation to the experimental data. The grid clustering for Roberts' transformation is determined by the value used for the stretching parameter β (equation 36). For the 24" test section the boundary layer thickness δ ranged from 0.22 to 0.45 inch depending on the longitudinal survey location. This lead to a recommended stretching parameter of about 1.01. In the ins2d code the resultant grid resulted in a minimum y^+ value of 10.0 which is larger than the recommended value of about 1.

Using 201 grid points in the y direction, normal to the freestream, three values of β were used which resulted in a reduction in the minimum y^+ from 14.0 to 1.8. An additional grid with 401 y grid points was also used to obtain a y^+

value near the desired value of 1. The following table outlines the Robert's transformation cases which were used to evaluate these grids.

C0000 y grid points	Robert's grid β	min. y^+
201	1.05	14.0
201	1.01	10.0
201	1.001	1.8
401	1.001	0.9

The ins2d code iterates until either the maximum number of iterations are completed or the computation converges. None of these cases converged within 5000 iterations. This undesirable result indicates Lax's equilibrium theorem [Ref. 90] is not being satisfied. This theorem states that given a properly-posed initial-value problem and a finite-difference approximation that satisfies the consistency condition, stability is the necessary and sufficient condition for convergence.

The computed boundary-layer thicknesses (δ) are presented in Figure 72 along with the experimental data and the 1/7 power law result. The latter two values are shown to be in good agreement. The computational result from the coarsest grids produced thicknesses greater than experimental data. The computational result from the two finest grids where y^+ is near 1 show thicknesses which are less than the experimental data. These inadequate results reflect the lack of convergence in these computations and suggest that Roberts' transformation grids do not provide a satisfactory grid for the present problem. Even though the thicknesses do not show good agreement with the experimental data, the boundary-layer profiles at longitudinal locations 5.5 (Figure 73(a)) and 16 inches (Figure 73(b)) show agreement between the experimental and the computational results. This suggests that the profile is a less useful parameter for evaluating the adequacy of the computational results.

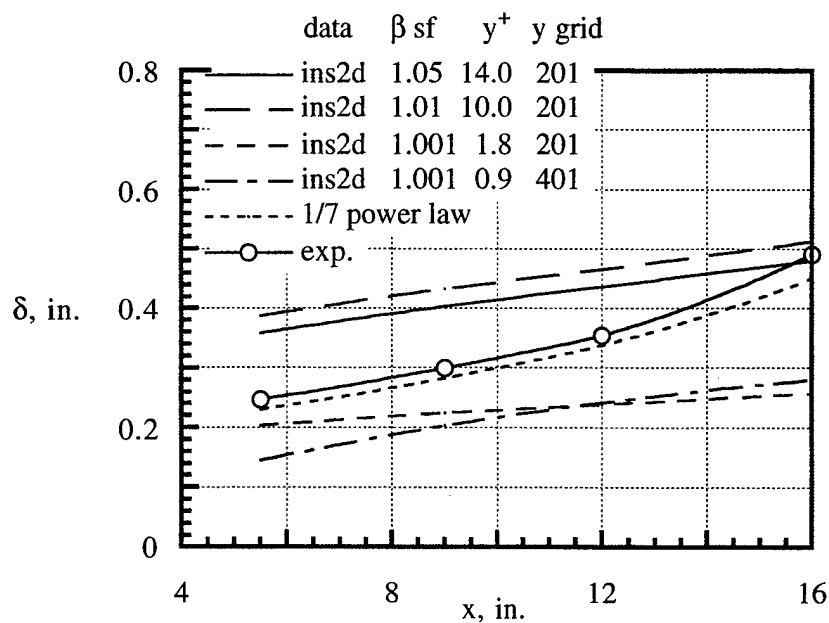
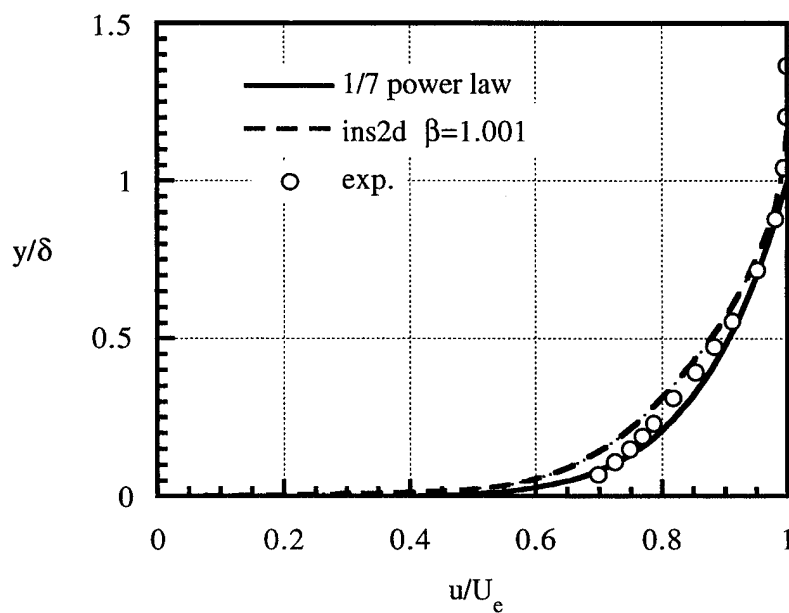
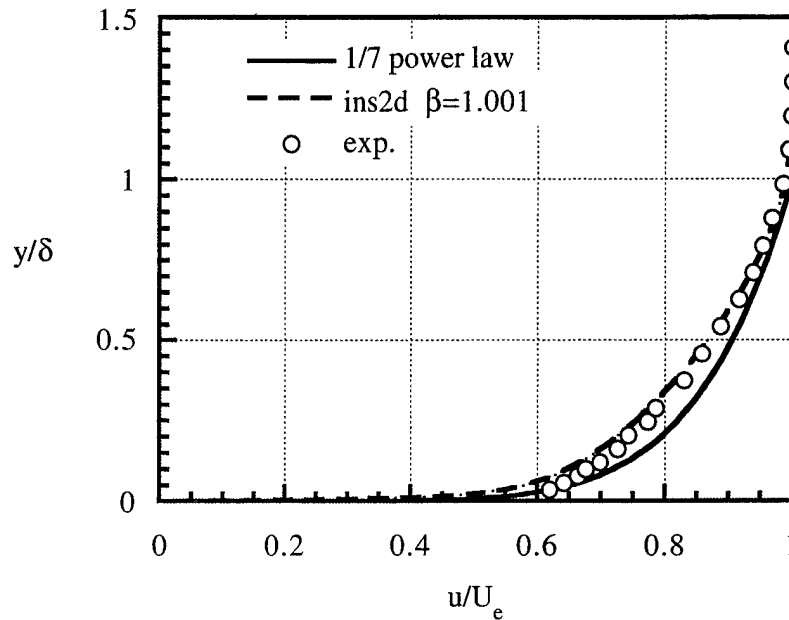


Figure 72. Boundary-layer thickness as a function of longitudinal tunnel location computed by the ins2d for 24" tunnel using Roberts' transformation grid.



(a) $x = 5.5"$.

Figure 73. Boundary-layer profile computed by the ins2d for 24" tunnel using Roberts' transformation grid.



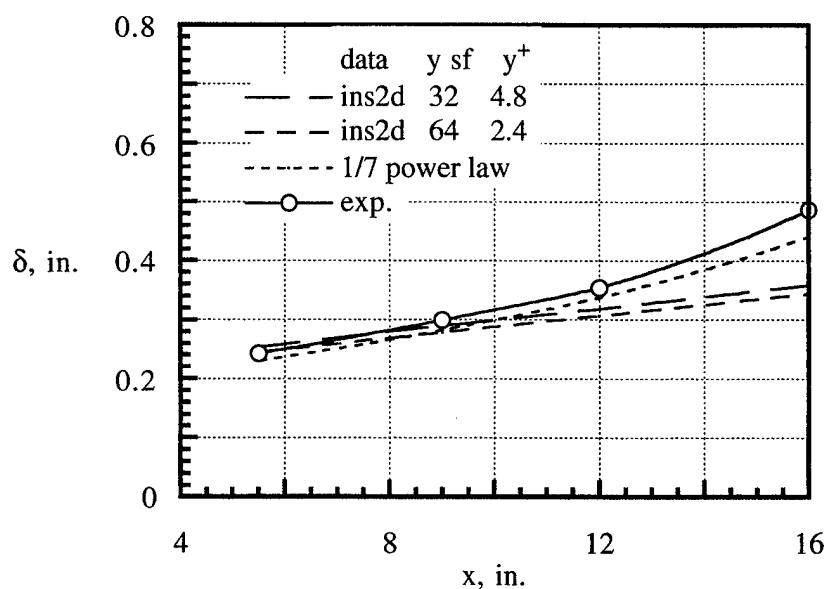
(b) $x = 16''$.

Figure 73. Concluded.

The tangential-grid scheme was also used for the 24 inch test section tunnel (C0000). Scale factors of 32 and 64 were selected to achieve y^+ values which approached 1. The number of y grid points was increased from 201 to 401 to obtain a minimum value of 1.2. In contrast to the Robert's transformation all of these cases converged in from 48 to 76 iterations. These rapid solutions enabled the cases to be run in the debug queue on the Cray C-90 computer in less than three minutes. This rapid convergence provides confidence that these grids provide consistent, stable computational results.

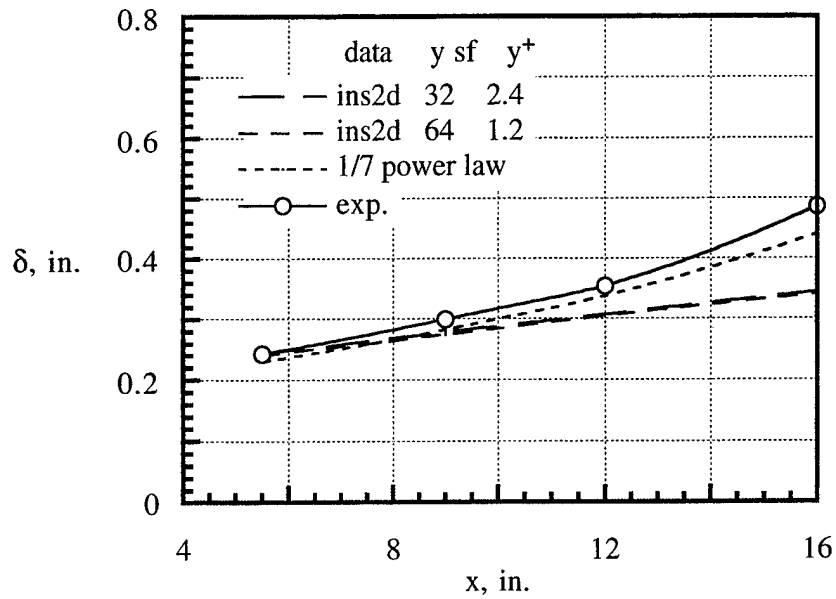
Tangential grid scale factor	C0000 y grid points	
	$y^+ /$ (iterations for convergence)	
	201	401
32	4.8 / 53	2.4 / 76
64	2.4 / 48	1.2 / 75

Examples of the computed boundary layer thicknesses using the tangential-grid scheme are presented in Figures 74(a) for 201 y grid-points and in Figure 74(b) for 401 y grid-points. Both figures present data for scale factors of 32 and 64. In both figures there is excellent agreement between the computational results, the experimental data, and the 1/7 power law at longitudinal locations at 5.5 inches and 12 inches. The reasons for the disagreement at the 16 inch station is unknown. It is possible there may be an influence of the diffuser downstream of the test section on the downstream end of the test section. This diffuser was not modelled in these calculations. Figure 75 presents comparisons of computational results, the 1/7 power law, and the experimental data for the boundary layer profiles. All of these results show agreement. These comparisons for the 24 inch test section indicate that the tangential grid scheme provides a useful grid which is validated by the experimental data. It should be noted that even though both of the grid schemes tried here satisfied the minimum desired y^+ value of 1 only the tangential grid scheme provided good agreement with experimental data. In this case there was little difference among grids which had y^+ values less than 5.

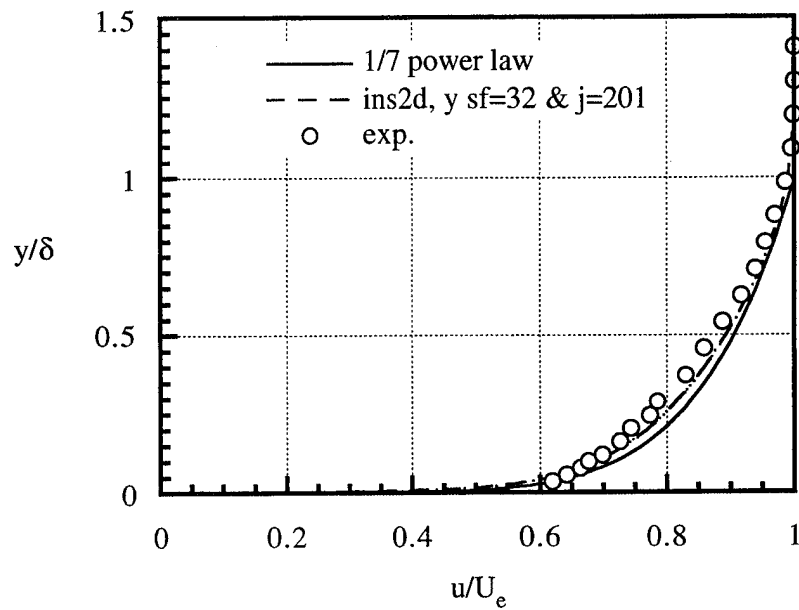


(a) 201 grid points in y direction.

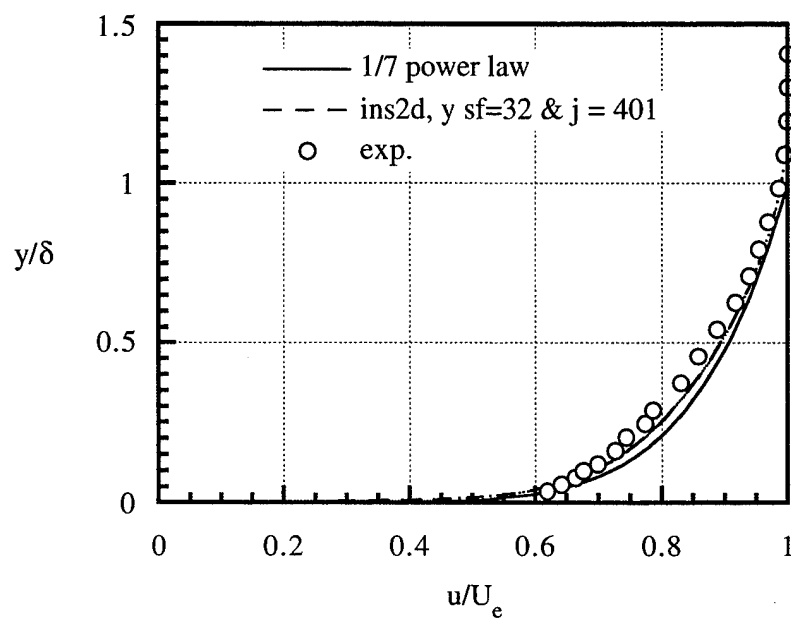
Figure 74. Boundary-layer thickness as a function of longitudinal tunnel location computed by the ins2d for 24" tunnel at $x = 16$ " using the tangential grid.



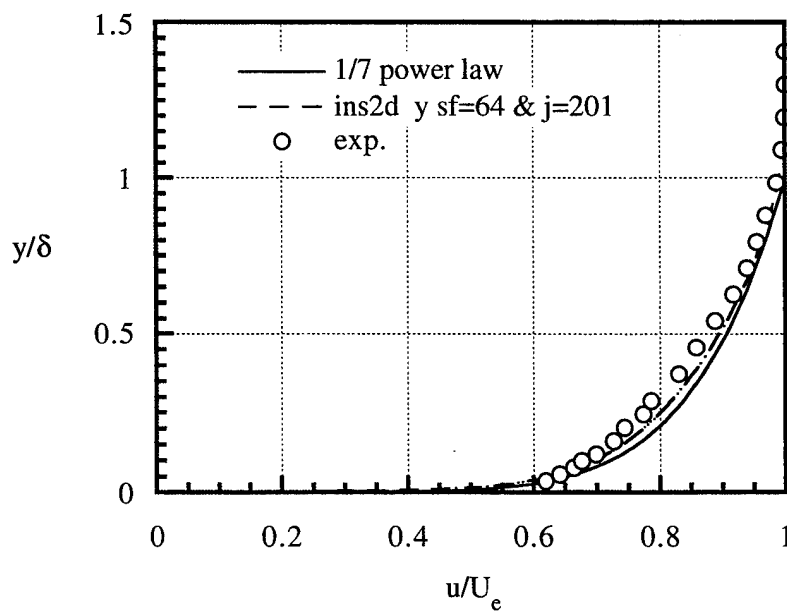
(b) 401 grid points in y direction.
Figure 74. Concluded.



(a) Tangential scale factor of 32 and 201 grid lines vertically.
Figure 75. Boundary-layer profile computed by the ins2d for 24" tunnel at $x = 16$ " using the tangential-transformation grid.



(b) Tangential scale factor of 32 and 401 grid lines vertically.
Figure 75. Continued.



(c) Tangential scale factor of 64 and 201 grid lines vertically.
Figure 75. Concluded.

b. 120 Inch Test Section

The grid was used to represent the 120 inch wind tunnel test section (C8000) from the floor to the ceiling and between the longitudinal stations from 0 to 120 inches. The grid clustering for Roberts' transformation is determined by the value used for the stretching parameter β (equation 36). For the 120" test section, the boundary layer thickness (δ) ranged from 1.1 to 1.5 inches depending on the longitudinal survey location. This leads to a recommended stretching parameter of about 1.05. In the ins2d code the resultant grid yields a minimum y^+ value of 7.0, which is larger than the recommended value of about 1. Using 201 grid points in the y direction, normal to the freestream, three values of β were used which resulted in a reduction in the minimum y^+ from 8.6 to 0.7. None of these cases resulted in converged calculations even after 10,000 or more iterations. As discussed earlier, this is an undesirable feature of these grids. The following table outlines Roberts' transformation cases which were used to evaluate these grids.

C8000 Robert's grid β	min. y^+	iterations
1.01	8.6	17,628
1.001	1.3	10,126
1.0005	0.7	10,000

The computed boundary layer thicknesses (δ) are presented in Figure 76 along with the experimental data and the 1/7 power law result. The experimental values are much less than those from the 1/7 power law, as noted earlier in the discussion of the experimental data. The computational result from the coarsest grid produced thicknesses which were less than one-half of that measured in the experiment. The computational result from the two finest grids where y^+ is near 1 provide thicknesses which are less than one-third of that measured in the experiment. These inadequate results reflect the lack of convergence in these computations and suggest that the Robert's transformation grids are not satisfactory for the 120 inch test section.

The tangential-grid scheme was also used for the 120-inch test-section tunnel (C8000). Scale factors from 8 to 72 were selected to achieve a range of y^+ values which approached 1. The number of y grid points ranged from 201 to 601 to evaluate grid-density effects. In contrast to the tangential grid transformation for the 24 inch test section, not all of these cases converged in less than 100 iterations. The y^+ and iterations associated with the tangential-grid scheme are presented in the following table:

Tangential grid scale factor	C8000 y grid points y^+ / iterations		
	201	401	601
8	8.3 / 8,600 nc	6.2 / 10,115 nc	---
16	6.5 / 10,249 nc	3.5 / 7,859 nc	---
32	3.1 / 65 c	1.7 / 9,334 nc	---
64	1.5 / 48 c	0.8 / 91 c	0.6 / 11,271 nc
72	1.4 / 46 c	0.7 / 86 c	---

Here nc means 'not converged solution' and c means 'converged solution'. It is noted that while all of the converged cases required less than 100 iterations, the unconverged cases were run for about 8000 or more iterations. It is noted that with grids using scale factors of 8 and 16, the solutions did not converge. Increasing the grids from 401 to 601 y grid points (using a scale factor of 64) caused the calculations to diverge even though the y^+ value was reduced from 0.8 to 0.6.

Calculated boundary-layer thicknesses are compared in Figure 77. Figure 77(a) presents the results for 201 y grid points. Only the unconverged scale factor of 8 results differ significantly from the experimental data. Even the

unconverged scale factor 16 results provide good agreement with the experimental data. As a result, good agreement is achieved with y^+ of 6.5 down to 1.4. Figure 77(b) presents the results for 401 y grid points. None of the unconverged results agree with the experimental data. The scale factor 8 result overestimates the boundary layer thickness and the scale factors of 16 and 32 underestimate the experimental data. Only the two converged results for scale factors of 64 and 72 achieve reasonable agreement with the experimental data. In this y grid size convergence was achieved for y^+ of 1.7 or less. The final comparison in Figure

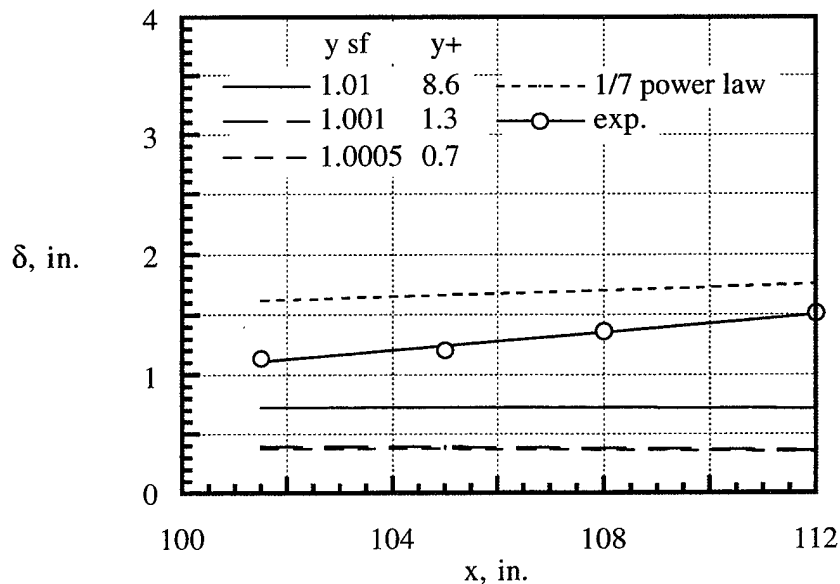
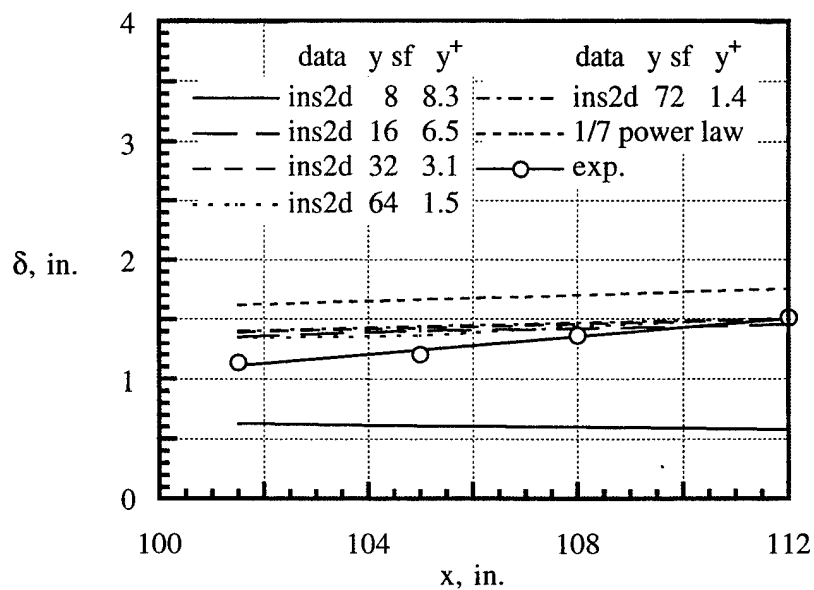
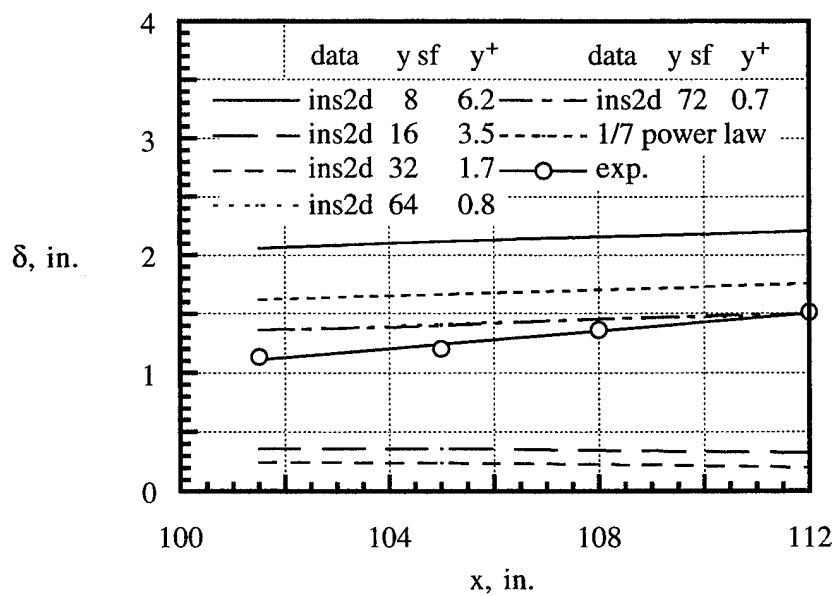


Figure 76. Boundary-layer thickness computed by the ins2d for 120" tunnel using Roberts' transformation grid, 201 y points.



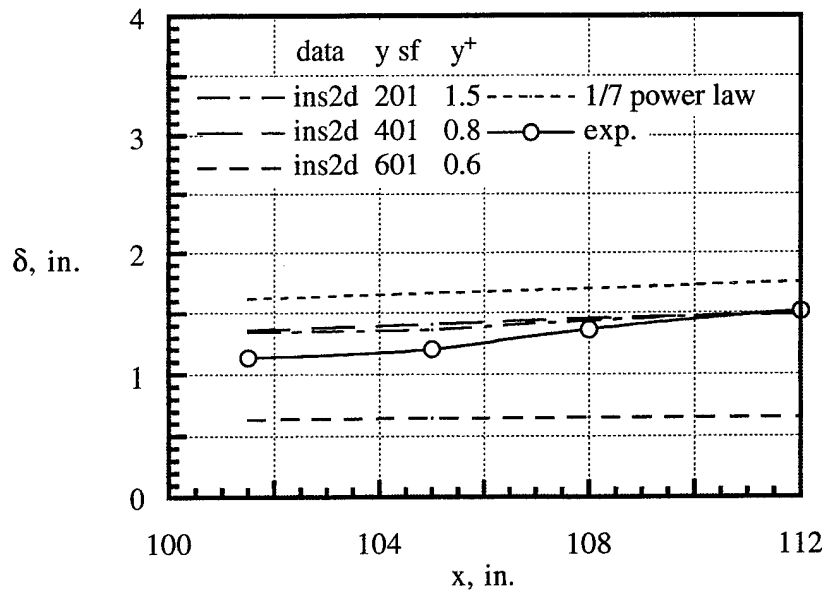
(a) 201 grid lines vertically.

Figure 77. Boundary-layer profile computed by the ins2d for 120" tunnel using the tangential-transformation grid.



(b) 401 grid lines vertically.

Figure 77. Continued.



(c) Tangential scale factor of 64.
Figure 77. Concluded.

77(c) for scale factor 64 grids show that increasing the number of y grid points from 201 to 401 to 601 reduces the y^+ from 1.5 to 0.8 to 0.6 for the finest grid. Yet the worst result was from the finest grid, which is also the only unconverged result shown in this plot.

In summary, the computational results from both of the test section lengths used in the experimental investigation, show that, first, a grid which provides a converged solution is needed before a reasonable comparison with experimental data can be expected. The value of y^+ is of less importance as shown by the Robert's grid where a y^+ of 0.7 gave poor results; yet a tangential grid with a y^+ of 7 gave good results. The appropriate grid clustering, size, and density are not always apparent before comparing results with experimental data.

2. Driven Cavity Computations

A frequently used model problem for cavity flow is the driven cavity. This cavity has three stationary walls and one wall which moves at a constant velocity. The velocity magnitude is determined by the Reynolds number of the calculation. Ghia et al [Ref. 67] conducted a very detailed analysis using a vorticity-stream-function formulation for the incompressible Navier-Stokes equations. Uniform grids were used in these calculations. For Reynolds numbers from 100 to 3200 the grid was 129 by 129; and for Reynolds numbers of 5000 or greater the grid was 257 by 257. An example of their streamline flow pattern was presented in Figure 10 for a Reynolds number of 10,000. In this paper, flows were computed for Reynolds numbers from 1000 to 10,000 and then the results were compared with those from several other investigators [Ref. 68, 95, and 96]. The Ghia u velocity results along a vertical line which passes through the center of the cavity compared with the other computations in Figure 78. The origins in Figure 78 are displaced to separate the various curves. At low Reynolds numbers the boundary layers are very thick. As Reynolds number reaches and exceeds 5000, δ asymptotes toward a converged magnitude. Away from the cavity walls, the velocities tend toward a linear variation especially for the high Reynolds number cases where the boundary layer thickness is a small fraction of the cavity depth. In most of these comparisons, the Ghia results are very consistent with those of the other three investigators. The most notable difference occurs when the Ghia results are compared with those from Ref. 95, which used the coarsest grid (50 x 50) of the four sets of results shown.

Comparable calculations done using the ins2d incompressible Navier-Stokes code [Ref. 91 and 92] for Reynolds numbers of 1000 and 10,000 are presented in Figure 79 with the results from Ghia et al [Ref. 67]. In Reference 91 it was found that a clustered 81 by 81 grid agreed with the Ghia et al [Ref. 67] results. For the present investigation, an ins2d calculation was made using an 81 by 81 grid with tangential spacing. The grid was generated using the cavity grid

Ref.	Re	100	400	1000	3200	5000	7500	10000
		a	b	c	d	e	f	g
75	Ghia et al	—	—	—	—	—	—	—
76	Rubin and Khosla [1977]	△		▲				
96	Nallasamy & Prasad [1977]	□		■				□
97	Agarwal [1981]	○	●	●	○		○	

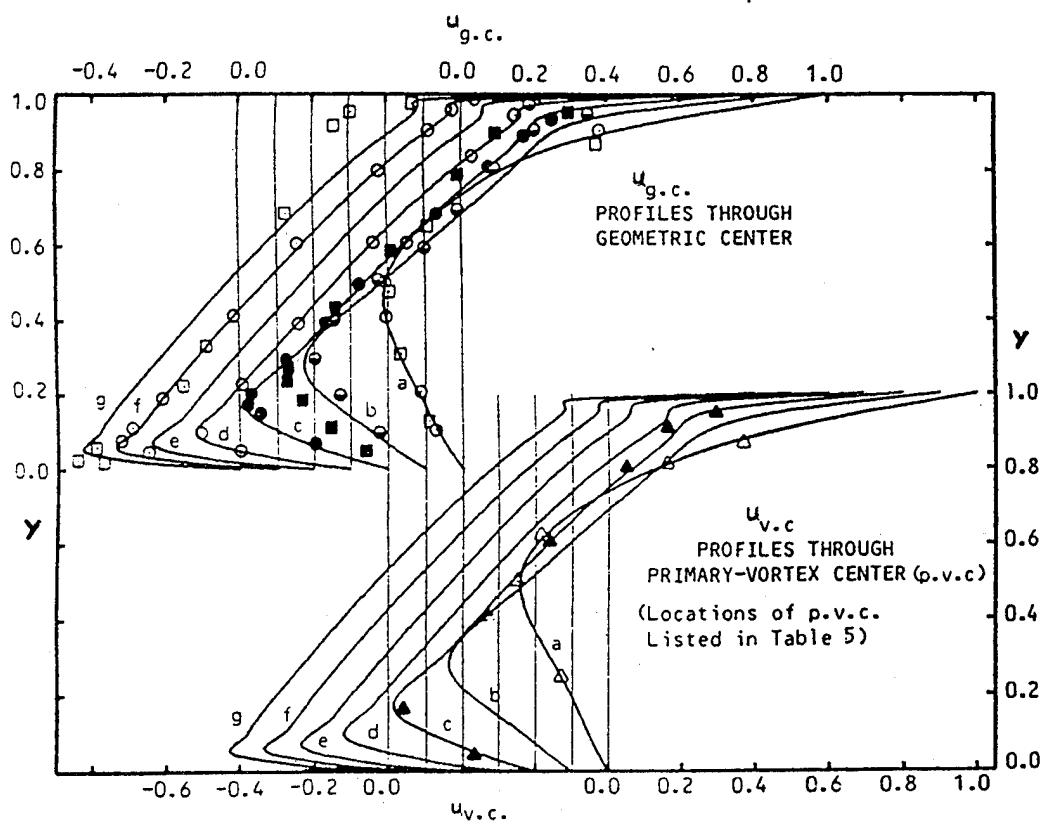
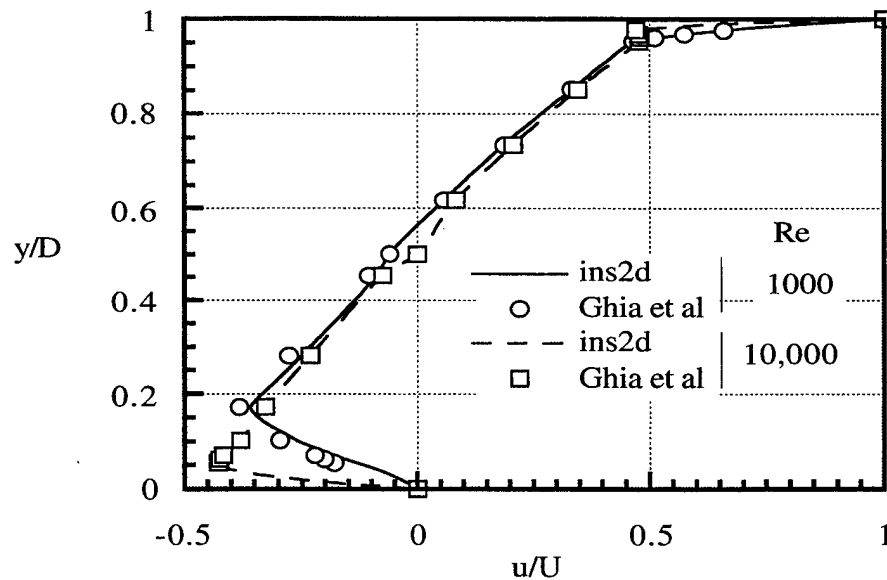


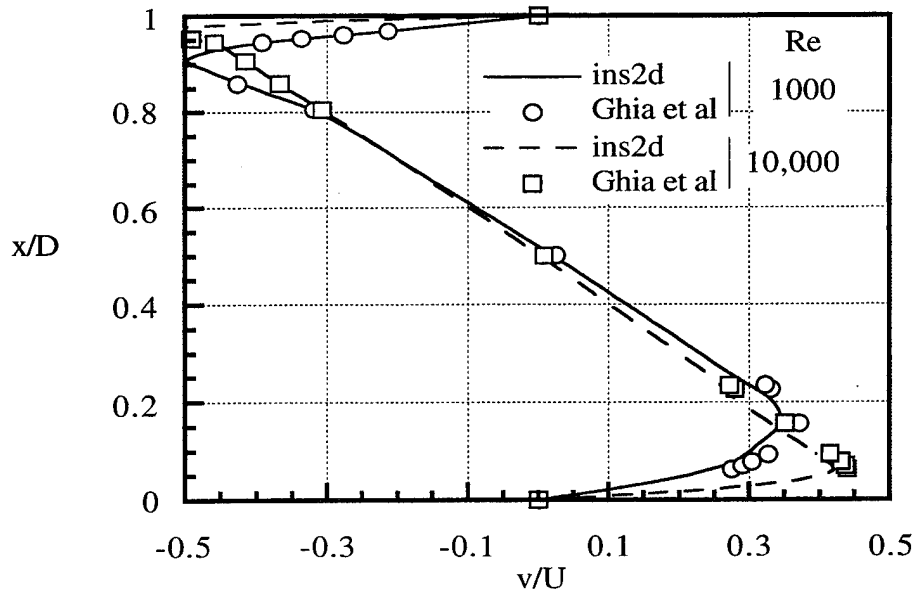
Figure 78. Comparison of u velocity along vertical lines through the geometric center of the cavity [Ref. 67].

generation code `cgg.f` as described previously. The u (Fig. 79(a)) and v (Fig. 79(b)) velocity components on vertical or horizontal lines, respectively, are non-dimensionalized by the moving wall velocity. These comparisons show very good agreement for both velocity components. This calculation is consistent with previous `ins2d` results and confirms that consistent grids and boundary conditions are being used in the present investigation.



(a) u velocities.

Figure 79. Comparison between `ins2d`[Ref. 91 and 92] and Ghia et al [Ref. 67] Navier-Stokes computational results for Re of 1000 and 10,000.



(b) v velocities.

Figure 79. Concluded.

3. Open Cavity Flow Computations

The ins2d results of the previous two sections provided consistent results for the two SJSU tunnel test section configuration's (24" and 120") boundary layers and for a driven cavity problem. These data provided the confidence needed to progress to the computations of the wind tunnel with a cavity and with a test section diffuser.

Initial computational efforts focused on the 24" test section with one cavity ($D = 1"$). The tunnel grid from the tunnel grid generation program `stgg.f` was used as a starting point. The single cavity was added using the cavity grid generation program `cgga.f`. This program used an 81 by 81 cavity grid with tangential spacing, using a scale factor of 16. Then the tunnel grid with a scale

factor of 32 vertically was augmented from 201 high by 495 long to satisfy the longitudinal spacing criteria after the cavity grid was introduced. This criteria uses a maximum grid spacing increase of no more than 20 percent between adjacent grid cells. The augmentation increased the grid to 201 high by 495 long for the basic 24" test section. The resultant experimental and computational boundary layer thicknesses are presented in Figure 80 for both the tunnel without a cavity and the tunnel with the 1" cavity. These results show a small increase (≈ 0.03 ") in δ when the cavity was present. In contrast the experimental data show a crossover in δ , so that at $x \approx 5$ the basic tunnel has a slightly thinner δ , while at $x = 16$ the basic tunnel has an increased δ . In the region immediately downstream of the cavity there is only a small difference in the δ for these two configurations. The boundary layer profiles were very similar to the one shown in Figure 75(a).

Similar computations were done for the 120" test section both with and without the 7° test section diffuser. In this case the same 81 by 81 tangentially-spaced cavity grid was used. The freestream grid was increased from 321 to 561 by cgg.f to satisfy grid spacing change rate requirements. The ins2d code did not converge to a solution for this case. The freestream grid was split into two grids (201 by 321 each) and merged using the PEGSUS overset scheme [Ref. 94]. The first grid extended from $x = 0$ " to 96" and the second grid from $x = 96$ " to 120". This provided a denser grid in the test section region where the boundary layer thicknesses were measured and where the cavity and test section diffuser were located. For the cavity cases, the cavity grid was overset as a third grid using PEGSUS. These computations converged in about 200 to 240 iterations depending on the specific configuration.

The experimental and computational boundary layer thickness results are presented for the test section region in Figure 81. The experimental boundary-layer thickness was slightly greater with the 1" cavity than without the cavity. The computed δ 's are nearly the same as the cavity case where the experimental data are a small increment (≈ 0.09 ") thicker. For the case with the test section diffuser (Figure 82) the experimental data for the cavity case has a slightly thinner δ ($\Delta\delta \approx 0.03$ ") while the computational data has a little larger difference ($\Delta\delta \approx 0.05$ ").

While the computational results shown in Figure 80 through 82 have some disagreement with a few experimental data points, the trends tend to be consistent with the experimental data trends for the zero pressure gradient in both test sections; the presence of the cavity slightly increases the boundary layer thickness. For the 120" test-section case with the 7° test-section diffuser, the cavity slightly decreases the boundary-layer thickness δ . Overall, both experimental and computational results show only small changes in the boundary layer characteristics due to the presence of a 1" cavity.

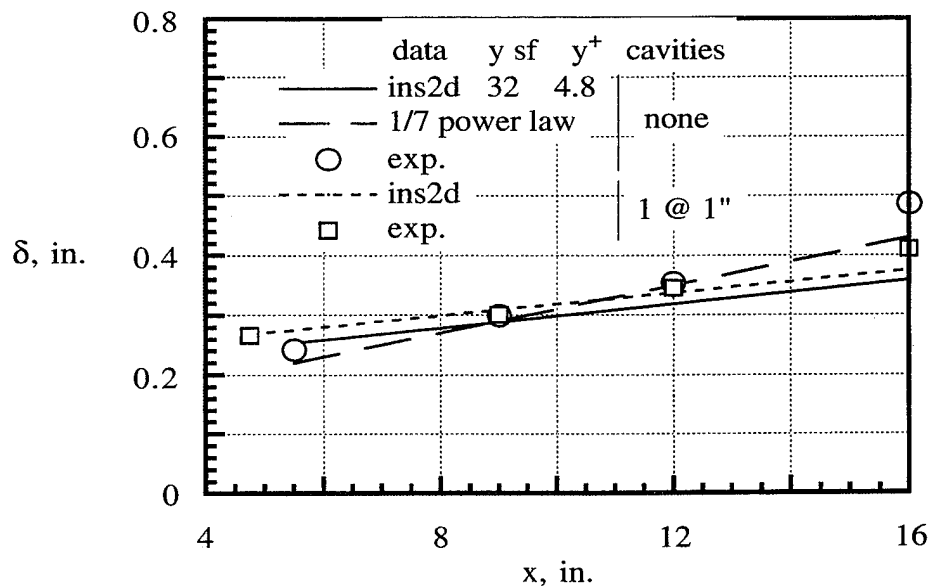


Figure 80. Boundary-layer thickness as a function of longitudinal tunnel location computed by ins2d for 24" tunnel.

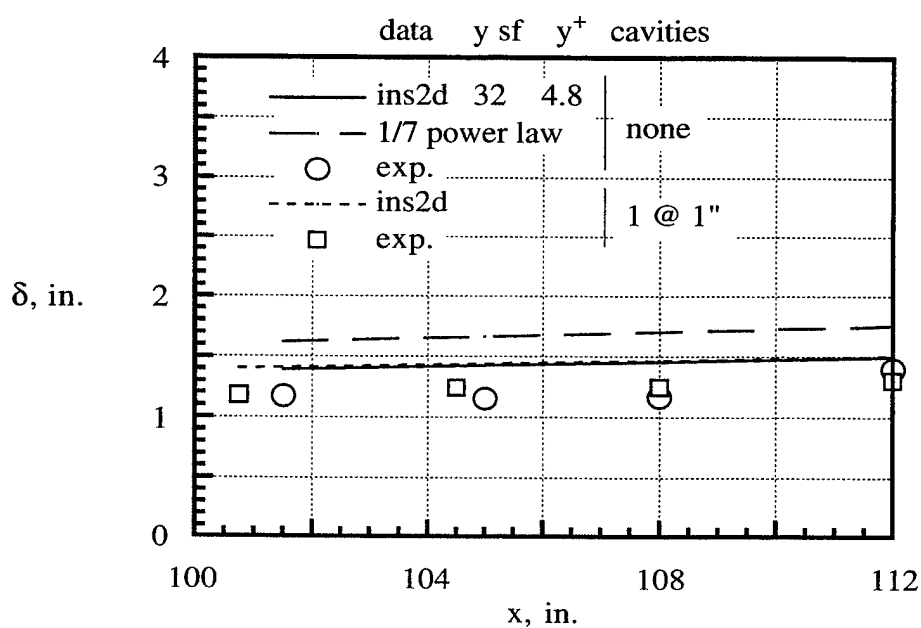


Figure 81. Boundary-layer thickness as a function of longitudinal tunnel location computed by ins2d for 120" tunnel.

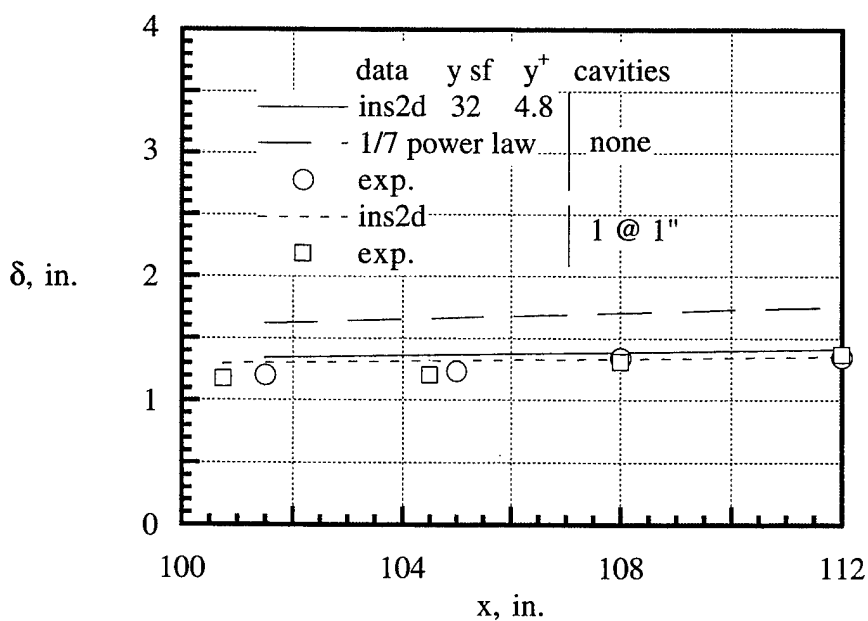


Figure 82. Boundary-layer thickness as a function of longitudinal tunnel location computed by ins2d for 120" tunnel with the 7° test section diffuser.

V. CONCLUSIONS AND RECOMMENDATIONS

One airfoil high-lift concept uses multiple cavities on its upper surface to increase camber. The usefulness of cavities in an adverse pressure gradient is determined by their effect on the viscous flow in the boundary layer downstream of the cavities. Maintenance of attached flow requires that the flow over the cavities and downstream of them retains enough momentum to overcome the kinetic energy loss due to an adverse pressure gradient, shear-layer flow gradients, and viscous dissipation. For this concept's feasibility to be demonstrated the effect of cavities on boundary-layer characteristics especially in an adverse pressure gradient must be determined. The present investigation concentrated on the effect of cavity flow on the attached surface boundary-layer characteristics in adverse pressure gradients.

The purpose of the present investigation was to experimentally and computationally determine the effect of 1, 2, or 4 two-dimensional spanwise cavities with square cross-sections on the boundary-layer characteristics in both a constant-pressure flow and for two adverse pressure-gradient flows. The experimental investigation was conducted in the San Jose State University (SJSU) 12" by 12" low-speed tunnel. Two test-section lengths, 24" and 120", were used to obtain a boundary-layer thickness relative to the cavity depth δ/D which was either less than 0.5 ($\delta/D < 0.5$), where unsteady flow oscillations may exist in the cavity (or cavities), or greater than 1.0 ($\delta/D > 1.0$) where there is predominately a steady, standing vortex flow in the cavity (or cavities). Adverse pressure gradients ($dp/dx > 0$) were obtained using 7° and 14° inserts on the floor of the test section. Total pressure profiles in the boundary layer were measured at several longitudinal locations both upstream and downstream of the cavities. Computational results were obtained using a numerical solution to the incompressible Navier-Stokes equations. Additional tests were conducted with a single cavity which was either open or closed to determine the effects of surface discontinuities on the boundary-layer development.

The measured profiles demonstrated boundary layer similarity for the basic test section and for the 7° test-section diffuser. There was a significant boundary-

layer profile variation from the $1/7$ power law for the 14° test-section diffuser which was typical of an adverse pressure gradient. The single and double cavities showed only a small deviation from the profile measured with no cavity. The four-cavity configuration profile, in most cases, represented a boundary layer profile similar to those found in an adverse pressure gradient. All of the surface pressure data suggest that the presence of the cavities had no noticeable effect. It may be concluded that cavities may be deployed with only a small change to the boundary-layer profile and without significantly modifying the resultant pressure distribution. This important conclusion shows that this high-lift concept may be feasible because the multiple cavities make only small changes in the boundary-layer characteristics.

Another aspect of this application is the effect of surface non-uniformities which could be caused by cavity doors on the boundary layer and on the surface pressure distribution. As expected, a poor fit of a cavity door could increase boundary-layer thickness and the skin-friction drag. There were differences in the longitudinal pressure distribution for both test sections. These results indicated that the surface uniformity for a closed cavity had an effect on the freestream characteristics, which determine the surface pressure distribution. It was also found that the open cavities produced less change in the surface pressure distribution than did surface non-uniformity in an otherwise plain ceiling. This is a further indication of the feasibility of the use of cavities.

In summary, the computational results for both of the test-section lengths used in the experimental investigation, show that a grid which provides a converged solution is needed before a reasonable comparison with experimental data can be expected. A small value of y^+ is of less importance than convergence. This was shown by the unconverged Roberts' transformation grid with a y^+ of 0.9 which gave poor results, while a converged tangential grid with a y^+ of 7 gave good results. Computations for the 120" test section with either a one inch cavity and/or with a 7° test-section diffuser showed only small changes in the boundary-layer characteristics. The appropriate grid clustering, size, and density were not always apparent before comparing computational results with experimental data.

Stated another way, it was found that the experimental data were needed to guide the computational effort.

This experimental and computational investigation has shown that multiple open cavities in either zero or adverse pressure gradients make only small changes in the boundary-layer characteristics. It was also found that a small backward-facing step made larger, adverse changes to the boundary layer than those made by the cavities. It is concluded that multiple cavities may be a feasible high-lift concept. It is recommended that the cavity concept be implemented in an airfoil and that it be tested in a wind tunnel to quantify its high-lift and drag characteristics.

REFERENCES

1. Smith, A. M. O., High-Lift Aerodynamics, *J. Aircraft*, v. 12, no. 6, pp. 501-530, June 1975.
2. Conversation with Prof. M. Platzer, NPS, Monterey, CA, 8 April 1991.
3. Ligrani, Phillip M., Structure of Turbulent Boundary Layers, *Aerodynamics and Compressible Flows, Encyclopedia of Fluid Mechanics* (Editor: N. Cheremisinoff), v. 3, pp.111-189, Gulf Publishing, Oct. 1988.
4. Schlichting, H., *Boundary-Layer Theory*, McGraw-Hill Book Co.,1968.
5. White, F. M., *Viscous Fluid Flow*, McGraw-Hill Publishing Co., 1974.
6. Cebeci,T. and Smith, A. M. O., *Analysis of Turbulent Boundary Layers*, Academic Press, New York, 1974.
7. Blasius, H., *The Boundary Layers in Fluids with Little Friction*, NACA TM 1256, 1950 (English translation of *Grenzschichten in Flüssigkeiten mit kleiner Reibung*, Zeitschrift für Mathematik und Physik, Band 56, Heft 1, pp. 1-37, 1908)
8. Clauser, Francis H., Turbulent Boundary Layers in Adverse Pressure Gradients, *J. Aeronautical Sciences*, v. 21, Feb. 1954, pp.91-108.
9. Kline, S. J., Morkovin, M. V., Sovran, G., and Cockrell, D. J. (editors), *Proceedings Computation of Turbulent Boundary Layers-1968 AFSOR-IFP-Stanford Conference*, Thermosciences Division, Department of Mechanical Engineering, Stanford University, 1968.
10. Kline, S. J., Cantwell, B. J., and Lilley, G. M. (editors), *Proceedings 1980-81 AFSOR-HTIM-Stanford Conference on Computation of Complex Turbulent Flows*, Thermosciences Division, Department of Mechanical Engineering, Stanford University, 1982.

11. von Kármán, Theodore, *Mechanical Similitude and Turbulence* , NACA TM 611, 1031 (English translation of *Mechanische Ähnlichkeit und Turbulenz*, Nachrichten von der Gesellschaft der Wissenschaften zu Göttingen, Fachgruppe I (Mathematik), No. 5, 1930, pp.58-76, also available in Proc. 3rd. International Congress of Applied Mechanics, Stockholm, part I, paper 85, 1930).
12. Rotta, J., *On the Theory of the Turbulent Boundary Layer*, NACA TM 1344, Feb. 1953 (English translation of *Über die Theorie der turbulenten Grenzschichten*, Mitteilungen aus dem Max-Planck-Institut für Strömungsforschung (Göttingen), No. 1, 1950).
13. Hoerner, S. F., *Fluid-Dynamic Drag*, Hoerner Fluid Dynamics, Albuquerque, NM, 1965.
14. Winter, K. G., *An Outline of the Techniques Available for the Measurement of Skin Friction in Turbulent Boundary Layers*, RAE Tech. Memo Aero 1656, Dec. 1975.
15. Elfstrom, Gary M., *Indirect Measurement of Turbulent Skin Friction*, DME/NAE Quarterly Bulletin No. 1979(1), Apr. 1979, pp. 21-48.
16. Ludwig, H., *Instrument for Measuring the Wall Shearing Stress of Turbulent Boundary Layers* (Translation of *Ein Gerät zur Messung der Wandschubspannung turbulenter Reibungsschichten*), NACA TM 1284, May 1950.
17. Ludwig, H. and Tillmann, W., *Investigations of the Wall-Shearing Stress in Turbulent Boundary Layers* (Translation of *Untersuchungen über die Wandschubspannung in turbulenten Reibungsschichten* , Ing.-Arch. 17, pg. 288-299, 1949), NACA TM 1285, May 1950.

18. Patel, V. C., Calibration of the Preston Tube and Limitations on its Use in Pressure Gradients, *J. Fluid Mechanics*, vol. 23, part 1, July 1965, pp. 185-208.
19. Schultz-Grunow, F, *New Frictional Resistance Law for Smooth Plates* (translation of *Neues Reibungswiderstandsgesetz für glatte Platten*, *Luftfahrtforschung*, vol. 17, no. 8, Aug. 1940, pp. 239-246., NACA TM 986, Sept. 1941.
20. Coles, Donald, The Law of the Wake in the Turbulent Boundary Layer, *J. Fluid Mechanics*, vol. 1, part 2, July 1956, pp. 191-226.
21. Falkner, V. M. and Skan, S. W., *Some Approximate Solutions of the Boundary Layer Equations*, A.R.C. Reports & Memoranda No. 1314, 1930.
22. Wieghardt, K. and Tillmann, W., *On the Turbulent Friction Layer for Rising Pressure* (translation of *Zur turbulenten Reibungsschicht bei Druckanstieg*, ZWB Untersuchungen und Mitteilungen, Nr. 6617, Nov. 20, 1944.
23. von Doenhoff, A. E., and Tetervin, N., *Determination of General Relations for the Behavior of Turbulent Boundary Layers*, NACA Rept. No. 772, 1943.
24. Mellor, G. L., and Gibson, D. M., Equilibrium Turbulent Boundary Layers, *J. Fluid Mech.*, vol. 24, part 2, pp. 225-253, 1966.
25. Townes, Harry W. and Sabersky, Rolf H., Experiments on the Flow Over a Rough Surface, *Int. J. Heat Mass Transfer*, vol. 9, pp. 729-738, 1966.
26. Perry, A. E., Schofield, W. H., and Joubert, P. N., Rough Wall Turbulent Boundary Layers, *J. Fluid Mech.*, vol. 37, part 2, pp. 383-413, 1969.
27. Bradshaw, P. and Wong, F. Y. F., The Reattachment and Relaxation of a Turbulent Shear Layer, *J. Fluid Mech.*, vol. 52, part 1, 1972, pp. 113-135.

28. Roshko, Anatol, Structure of Turbulent Shear Flows: A New Look, *AIAA J.*, vol. 14, no. 10, Oct. 1975.
29. Thomas, F. O., Structure of Mixing ZLayers and Jets, *Appl. Mech. Rev.*, vol. 44, no. 3, March 1991, pp. 119-153.
30. Ho, Chih-Ming and Huerre, Patrick, Perturbed Free Shear Layers, *Ann. Rev. Mech.*, vol. 16, 1984, pp. 365-424.
31. Schneider, W., Boundary-layer Theory of Free Turbulent Shear Flows, *Z. Flugwiss. Weltraumforsch.*, vol. 15, 1991, pp. 143-158.
32. Roshko, Anatol, *Some Measurements of Flow in a Rectangular Cutout*, NACA TN 3488, Aug. 1955.
33. Krishnamurty, K., *Acoustic Radiation from Two-Dimensional Rectangular Cutouts in Aerodynamic Surfaces*, NACA TN 3487, Aug. 1955.
34. Maull, D. J. and East, L. F., Three-Dimensional Flow in Cavities, *J. Fluid Mech.*, vol.16, part 4, Aug. 1963, pp.620-632.
35. Rossiter, J. E., *Wind-Tunnel Experiments on the Flow over Rectangular Cavities at Subsonic and Transonic Speeds*, R.A.E. R and M No. 3438, Oct. 1964.
36. Charwat, A. F., Roos, J. N., Dewey, F. C., Jr., and Hitz, J. A., An Investigation of Separated Flows - Part I: The Pressure Field, *J. Aerospace Sciences*, vol. 28, no. 6, June 1961, pp.457-470.
37. Charwat, A. F., Roos, J. N., Dewey, F. C., Jr., and Hitz, J. A., An Investigation of Separated Flows - Part II: Flow in the Cavity and Heat Transfer, *J. Aerospace Sciences*, vol. 28, no. 7, July 1961, pp. 513-527.
38. Plentovich, E. B., *Three-Dimensional Cavity Flow Fields at Subsonic and Transonic Speeds*, NASA TM 4209, Sept. 1990.
39. Buell, Donald A., *An Experimental Investigation of the Airflow over a Cavity with Antiresonance Devices*, NASA TN D-6205, Mar. 1971.

40. Rockwell, D. and Naudascher, E., Review-Self-Sustaining Oscillations of Flow Past Cavities, *Trans. of the ASME*, vol. 100, June 1978, pp. 152-165.
41. Komerath, N. M., Ahuja, K. K., and Chambers, F. W., *Prediction and Measurement of Flows Over Cavities - A Survey*, AIAA Paper No. 87-0166 presented at the AIAA 25th Aerospace Sciences Meeting, 12-15 Jan. 1987.
42. East, L. F., Aerodynamically Induced Resonance in Rectangular Cavities, *J. Sound Vib.*, vol. 3, Mar. 1966, pp.277-287.
43. Heller, H. H., Holmes, D. G., and Covert, E. E., Flow-Induced Pressure Oscillations in Shallow Cavities, *J. Sound Vib.*, vol. 18, Apr. 1971, pp.545-553.
44. Bilanin, Alan J. and Covert, Eugene E., Estimation of Possible Frequencies for Shallow Rectangular Cavities, *AIAA J.*, vol. 11, no. 3, March 1973, pp. 347-351.
45. Miles, J. W., On the Disturbed Motion of a Plane Vortex Sheet, *J. Fluid Mech.*, vol. 4, 1958, pp. 538-552.
46. Block, Patricia J. W., *Noise Response of Cavities of Varying Dimensions at Subsonic Speeds*, NASA TN D-8351, Dec. 1976.
47. Sarohia, Virendra, Experimental Investigation of Oscillations in Flows Over Shallow Cavities, *AIAA J.*, vol. 15, no. 7, July 1977, pp. 984-991.
48. Yu, Yung H., *Measurements of Sound Radiation from Cavities at Subsonic Speeds*, AIAA Paper No. 76-529, July 1976.
49. Gharib, M. and Roshko, A., The Effect of Flow Oscillations on Cavity Drag, *J. Fluid Mech.*, vol. 177, Apr. 1987, pp. 501-530.
50. Tam, Christopher K. W. and Block, Patricia J. W., On the Tones and Pressure Oscillations Induced by Flow Over Rectangular Cavities, *J. Fluid Mech.*, vol. 89, part 2, 1978, pp. 373-399.

51. Heller and Bliss, Donald B., The Physical Mechanism of Flow-Induced Pressure Fluctuations in Cavities and Concepts for Their Suppression, AIAA Paper No. 75-491, March 1975.
52. Ziada, Samir and Rockwell, Donald, Generation of Higher Harmonics in a Self-Oscillating Mixing Layer-Wedge System, *AIAA J.*, vol. 20, no. 2, Feb. 1982, pp. 196-202.
53. Rockwell, D. and Knisely, C., The Organized Nature of Flow Impingement Upon a Corner, *J. Fluid Mech.*, vol. 93, part 3, 1979, pp. 413-432.
54. Franke, M. E. and Carr, D. L., *Effect of Geometry on Open Cavity Flow-Induced Pressure Oscillations*, AIAA Paper No. 75-492, March 1975.
55. Zhang, Xin and Edwards, John A., Experimental Investigation of Supersonic Flow over Two Cavities in Tandem, *AIAA J.*, vol. 30, no. 5, May 1992, pp. 1182-1190.
56. Betts, P. L., Self-Induced Oscillations in an Open Water-Channel with Slotted Walls, *J. Fluid Mech.*, vol. 55, part 3, 1972, pp. 401-417.
57. Sarno, R. L. and Franke, M. E., Suppression of Flow-Induced Pressure Oscillations in Cavities, *J. Aircraft*, vol. 31, no. 1, Jan.-Feb. 1994, pp. 90-96.
58. Liepmann, H. W. and Laufer, J., *Investigations of Free Turbulent Mixing*, NACA TN 1257, Aug. 1947.
59. Kistler, Alan L. and Tan, Felix C., Some Properties of Turbulent Separated Flows, Boundary Layers and Turbulence, *Phys. Fluids Suppl.*, 1967, pp. S165-S173..
60. Koenig, Keith and Roshko, Anatol, An Experimental Study of Geometrical Effects on the Drag and Flow Field of Two Bluff Bodies Separated by a Gap, *J. Fluid Mech.*, vol. 156, July 1985, pp. 167-204.

61. Burggraf, O. R., Analytical and Numerical Studies of the Structure of Steady Separated Flows , *J.Fluid Mech.*, vol. 24, part 1, Jan. 1966, pp. 113-152.
62. Rossow, Vernon J., Aerodynamics of Airfoils with Vortex Trapped by Two Spanwise Fences, *J. Aircraft*, v. 31, no. 1, pp. 146-153, Jan.-Feb. 1994.
63. Pan, Frank and Acrivos, Andreas, Steady Flows in Rectangular Cavities, *J. Fluid Mech.*, vol. 28, part 4, June 1967, pp. 643-655.
64. Mehta, Unmeel B. and Lavan, Zalman, *Flow in a Two-Dimensional Channel with a Rectangular Cavity*, NASA CR-1245, Jan. 1969.
65. Borland, Christopher J., *Numerical Prediction of the Unsteady Flow Field in an Open Cavity*, AIAA Paper No. 77-673, AIAA Aerospace Sciences Meeting, Jan. 1977.
66. Hankey, W. L. and Shang, J. S., Analysis of Pressure Oscillations in an Open Cavity, *AIAA J.*, vol. 18, no. 8, Aug. 1980, pp. 892-898.
67. Ghia, U., Ghia, K. N., and Shin, C. T., High-Re Solutions for Incompressible Flow Using the Navier-Stokes Equations and a Multigrid Method, *J. Comp. Physics*, vol. 48, no. 3, Dec. 1982, pp. 387-411.
68. Rubin, S. G. and Khosla, P. K., A Conjugate Gradient Iterative Method , *Comput. Fluids*, vol. 9, no. 2, June 1981, pp. 109-121.
69. Gatski, T. B. and Grosch, C. E., Embedded Cavity Drag in Steady Laminar Flow, *AIAA J.*, vol. 23, no. 7, July 1985, pp. 1028-1037.
70. Gustafson, K. and Halaski, K., Vortex Dynamics of Cavity Flows, *J. Comput. Physics*, vol. 64, no. 2, June 1986, pp. 279-319.
71. Venkatapathy, E., Lombard, C. K., and Nagaraj, N., *Numerical Simulation of Compressible Flow Around Complex Two-Dimensional Cavities*, AIAA Paper No. 87-0116, Jan. 1987.

72. Neary, M. D., *Time-Dependent Self-Sustaining Oscillations of Cavity Flow*, AIAA Paper No. 87-0142, Jan. 1987.
73. Om, D., Navier-Stokes Simulation for Flow Past an Open Cavity, *J. Aircraft*, vol. 25, no. 9, Sept. 1988, pp. 842-848.
74. Khorrami, Mehdi R., A Study of the Temporal Stability of Multiple Cell Vortices, NASA CR-4261, Nov. 1969.
75. Estivalezes, J. L. and Boisson, H. C., Oscillatory Flows in Rectangular Cavities with Steady Boundary Conditions, *International Congress of Fluid Mechanics Proceedings*, vol. 3, 1990, pp.947-950.
76. Emerson, D. R. and Poll, D. I. A., Computation of Laminar Flow Over Cavities, Aero. Rept.-9013, Manchester University (England) Aeronautical Engineering Group, 1990.
77. Dougherty, N. S., Holt, J. B., Nesman, T. E., and Farr, R. A., *Time-Accurate Navier-Stokes Computations of Self-Excited Two-Dimensional Unsteady Cavity Flows*, AIAA Paper No. 90-0691, Jan. 1990.
78. Atwood, Christopher A. and VanDalsem, William R., Flowfield Simulation About the Stratospheric Observatory for Infrared Astronomy, *J. Aircraft*, vol. 30, no. 5, Sept.-Oct. 1993, pp. 719-727.
79. Rossow, Vernon J. and Ross, James, unpublished investigation of trapped vortex for a high aspect ratio, swept back wing, Oct. 1993.
80. Migay, V. K., The Efficiency of a Cross-Ribbed Curvilinear Diffuser, *Energomashinosrtoeyeniye*, No. 1, 1962, pp. 45-46 (English translation FTD-TT-62-1151).
81. Lin, J. C. and Howard, F. G., *Turbulent Flow Separation Control Through Passive Techniques*, AIAA Paper No. 89-0976 presented at AIAA 2nd Shear Flow Conference, 13-16 March 1989.

82. Lin, J. C., Howard, F. G., Bushnell, D. M., and Selby, G. V., *Investigation of Several Passive and Active Methods for Turbulent Flow Separation Control*, AIAA Paper No. 90-1598 presented at AIAA 21st Fluid Dynamics, Plasma Dynamics and Laser Conference, 18-20 June 1990.
83. Selvey, G. V., Lin, J. C., and Howard, F. G., *Turbulent Flow Separation Control Over a Backward-Facing Via Transverse and Swept Grooves*, *J. Fluids Eng'r.*, v. 112, June 1990, pp. 238-240.
84. Lin, J. C., Selby, G. V., and Howard, F. G., *Exploratory Study of Vortex-Generating Devices for Turbulent Flow Separation Control*, AIAA Paper No. 91-0042 presented at 29th Aerospace Sciences Meeting, 7-10 Jan. 1991.
85. Lin, J. C., *Control of Low-Speed Turbulent Separated Flow Over a Backward-Facing Ramp*, Ph.D. Dissertation, Old Dominion University, Norfolk, VA, May 1992.
86. Howard, Floyd G. and Goodman, Wesley L., Axisymmetric Bluff-Body Drag Reduction Through Geometrical Modification, *J. Aircraft*, v. 22, no. 6, pp. 516-522, June 1985.
87. Milne-Thompson, L. M., *Theoretical Hydrodynamics*, The Macmillan Company, New York, 1960.
88. Mason, W. H., *Fundamental Issues in Subsonic/Transonic Expansion Corner Aerodynamics*, AIAA Paper No. 93-0649, Jan. 1993.
89. Ashby, D.L., Dudley, M., and Iguchi, S.K., *Development and Validation of an Advanced Low-Order Panel Method*, NASA TM 101024, Oct. 1988.
90. Anderson, D. A., Tannehill, J. C., and Pletcher, R. H., *Computational Fluid Mechanics and Heat Transfer*, Hemisphere Publishing Corp., New York, 1984.

91. Rogers, Stuart E. and Kwak, Dochan, *An Upwind-Differencing Scheme for the Incompressible Navier-Stokes Equations*, NASA TM 101051, Nov. 1988.
92. Rogers, Stuart E. and Kwak, Dochan, Upwind Differencing Scheme for the Time-Accurate Incompressible Navier-Stokes Equations, *AIAA J.*, v. 28, no. 2, Feb. 1990, pp. 253-262.
93. Roe, P. L., Approximate Riemann Solvers, Parameter Vectors, and Difference Schemes, *J. Comp. Phys.*, v. 43, 1981, page 357.
94. Suhs, N.E. and Tramel, R.W., PEGSUS 4.0 User's Manual, AEDC-TR-91-8, June 1991.
95. Nallasamy, M. and Prasad, K. Krishna, On Cavity Flow at High Reynolds Numbers, *J. Fluid Mech.*, vol. 79, part 2, 1977, pp. 391-414.
96. Agrawal, R. K., A Third-Order-Accurate Upwind Scheme for Navier-Stokes Solutions at High Reynolds Numbers, AIAA Paper No. 81-0112, 1981.

APPENDIX A

TEST RUN SCHEDULE

The run schedule for the experimental investigation is presented in this appendix. It lists the following information:

Run	Sequential number assigned to a group of data
Configuration code	<p>A four digit code which describes the tunnel configuration</p> <p>The first digit identifies the test section length:</p> <ul style="list-style-type: none">0 or 1 refers to the 24" long test section8 refers to the 120" long test section <p>The second digit identifies the diffuser angle:</p> <ul style="list-style-type: none">0 means basic test section with no diffuser7 means the 7° test section diffuser14 means the 14° test section diffuser <p>The third digit identifies the cavity depth in inches:</p> <ul style="list-style-type: none">0 means no cavity1 means 1 inch deep cavity(-ies)2 means 2 inch deep cavity3 means 2 inch deep cavity with a movable door which can be used to close the cavity or open the cavity to the freestream flow (i.e., c-closed or o-open). <p>The fourth digit identifies the number of cavities in the streamwise direction as either 0, 1, 2, or 4 cavities.</p>

Run type	This identifies the primary data taken as either CP, surface C_p distribution, or BL, boundary layer profiles.
boundary layer probe position	This identifies the x location of the boundary layer probe tip.
b.l. probe height	This identifies the vertical dimension of the boundary layer probe.
b.l. rake installed	This identifies whether the b.l. rake is installed at the x=16" location.
Notes	Notes related to the run describing unexpected items or information unique to a particular run which is not described in the other columns.

An entry is made in the run schedule only when there is a change in a parameter. If there is no entry then the parameter is unchanged from the previous run.

Run	Configuration code	Run Type	boundary layer probe position	b.l. probe head height	b.l. rake installed	Notes
101	0000	CP	N/A	N/A	yes	
102		BL				void run 102, invalid input code
103			5.5	0.022		
104			9			
105						
106			12			
107			16			
108	0700	CP	N/A	N/A		void run, scanivalve did not step properly
109						repeated run with correct scanivalve stepping
110		BL	16	0.022		pressure sample time increased to 20 sec. to
111						<cont'd> improve scanivalve data repeatability
112		CP	N/A	N/A		
113		BL	16			
114		CP	N/A	N/A		
115						measured Cp with long delay, 12 min./run
116						measured Cp with short delay, 4.5 min./run
117		BL	16	0.022		<cont'd> good data obtained.
118						
119						
120					no	
121	1400	CP	N/A	N/A		:
122						
123		BL	16			
124		CP	N/A			
125		BL	12			
126			9			
127			5.5			
128	0021	CP	16	0.022	no	Bad cavity Cp & p, void run
129						Bad data, void run - switched amplifiers 3 & 4
130						
131		BL	16.19			

Run	Configuration code	Run Type	boundary layer probe position	b.l. probe head height	b.l. rake installed	Notes
132	0021	BL	12	0.022	no	Bad cavity data-used 20 sec. sample time-void run
133		CP				
134		BL	10			
135			6.5			
136	0011		16			
137			12			
138			9			
139			4.75			
140	0012		16			
141			12			
142			10			
143			5.5			
144	0014	CP	16			
145		BL				Scanivalve sample time reduced from 8sec to 2sec
146						
147						Repeated with tape removed from ports 1 & 16
148			13.25			
149			11.5			
150						Repeated with transducers Pt & Pt,bl exchanged
151			9.5			
152			7.5			Pt,bl tube replaced before run. Leak detected.
153			5.5			Ps,bl tube replaced before run. Moisture detected.
154			9.5			Repeated run 151 w/ new Ps,bl tube.
155			11.5			Repeated run 149 w/ new Ps,bl tube.
156			13.25			Repeated run 148 w/ new Ps,bl tube.
157			16			Repeated run 147
158	0014	CP	N/A			
159	0012					Used wrong configuration code - 0014
160						Repeated run 159
161	0011					
162	0021					
163	1421					

Run	Configuration code	Run Type	boundary layer probe position	b.l. probe head height	b.l. rake installed	Notes
164	1421	BL	16.2			
165			12			
166			10			
167			6.5			
168	1411	CP	N/A			Pt,bl leak.
169		BL	16			
170			12			
171			8.5			
172			4.75			
173	1412	CP	16			
174		BL				
175			12			
176			10			
177			5.5			
178	1414	CP	16			
179		BL				
180			13.25			
181			11.5			
182			9.5			
183			7.5			
184			5.5			
185	0014	CP	16			Repeated run 159; lost some Cp data.
186		BL				Repeated run 156; lost data.
187			11.5			Repeat run 186
188						Repeat run 186
189	0714	CP				
190						Repeatability check of run 189.
191		BL	16			
192			13.25			
193			11.5			
194			9.5			
195			7.5			

Run	Configuration code	Run Type	boundary layer probe position	b.l. probe head height	b.l. rake installed	Notes
196	0714	BL	5.5	0.022	no	
197		CP	16			
198		BL				
199			12			
200			8.5			
201			4.75			
202	8000	CP	112			First run with the 120" long test section.
203		BL	112			
204			108			
205			105			
206			101.5			
207	8021	CP	112			Bad data. No seal between wall and ceiling.
208						Repeat run 207 w/ seal in place.
209		BL	112			
210			108			Bad data.
211						Repeat run 210.
212			106			
213			102.5			
214		CP				
215	8011		112			
216						Repeat run 215.
217		BL				
218			108			
219			106.5			
220			100.75			
221		CP				
222	8012		112			
223		BL				
224			108			
225		CP				Repeat of run 222 w/ BL probe @ x=108 in.
226		BL	106			
227			101.5			

Run	Configuration code	Run Type	boundary layer probe position	b.l. probe head height	b.l. rake installed	Notes
228	8014	CP	112	0.022	no	q _∞ started to vary ±0.2 psfg. Void data.
229						Repeat run 222 w/ BL probe @ x=108". Tape
230		BL				<cont'd>obstruction ahead of the probe in run 228
231			109.25			
232			107.5			
233			105.5			
234			103.5			
235						Repeat run 234
236			101.5			
237	N/A	N/A	N/A			This run used to calibrate new Pt,bl probe
238		BL	112			
239			109.25			
240			107.5			
241						Repeat run 240 w/ new Pt,bl probe.
242		CP	112			Repeat run 229 w/ new Pt,bl probe.
243		BL				
244			101.5			
245			105.5			
246			103.5			
247	8000	CP	112			Void run, used the wrong config. code-8014.
248						Repeat run 247 with right config. code-8000
249		BL				
250			108			
251			105			NOTE: Void runs 249-257 due to bad Pt,bl probe.
252			101.5			
253						Repeat run 252 with new Pt,bl probe.
254						Repeat run 253
255				0.034		New Pt,bl probe w/ 0.034" probe height used.
256				0.022		Tried a modified 0.022" probe
257						Tried a second 0.022" probe

Run	Configuration code	Run Type	boundary layer probe position	b.l. probe head height	b.l. rake installed	Notes
258	8014	BL	112	0.022	no	
259			103.5			
260			101.5			
261		CP				
262	8400		112	0.034		Valid data w/ new Pt,bl probe - 0.034" height
263		BL				Void data, probe deflected against the ceiling.
264						Repeat run 263, probe just touching the ceiling.
265			108			
266			105			
267			101.5			
268	8421	CP	112			
269		BL				
270			108			
271			106			
272			102.5			
273	8411	CP	112			
274		BL				
275			108			
276			104.5			
277			100.75			
278	8412	CP	112			
279		BL				
280			108			
281			106			
282			101.5			
283	8414	CP	112			
284		BL				
285			109.25			Void run, delta > 2"
286						Repeated run 285
287						Repeated run 285
288			112			Repeated run 284, checks out o.k.
289			107.5			

Run	Configuration code	Run Type	boundary layer probe position	b.l. probe head height	b.l. rake installed	Notes
290	8414	BL	105.5	0.034	no	
291			103.5			
292			101.5			
293			109.25			Repeated run 285
294						Repeated run 285 again with invalid results
295						Repaired bl probe and obtained valid data
296	8431	CP	112			Void run because of wrong configuration code
297						Repeated run 296
298	door closed	BL				
299	door open	CP				
300		BL				
301			108			
302	door closed					Odd reflex in bl survey for $0.1'' < y < 0.3''$
303						Adjusted the trap door to flush & repeated run 302
304	8431c	CP	112			Repeated run 297
305		BL				Repeated run 298
306			104.5			
307	door open					
308			101.5			
309	door closed					
310		CP	112			Repeated run 297 after repair of tube @ $x=11.03''$
311						Repeated run 310 w/ bl probe flush to ceiling
312	door open					Repeated run 299
313	8700	CP				
314		BL				
315			108			bl profile had odd reflex as seen in run 302
316						Repaired loose tape & repeated run 297
317			105			
318			101.5			
319	8711	CP	112			
320		BL				
321			108			

Run	Configuration code	Run Type	boundary layer probe position	b.l. probe head height	b.l. rake installed	Notes
322	8711	BL	104.5	0.034	no	
323			100.75			
324	8714	CP	112			Invalid data
325						Repeated run 324 after zero values were reset
326		BL				
327			109.25			
328			107.5			
329						Repeated run 328 after changing the sealing tape
330			105.5			
331			103.5			
332			101.5			
333			109.25			Repeat run 327 w/ finer Δy increments for $0 < y < 3$
334	8031c	CP	112			
335	door open					
336		BL				
337	door closed					
338			108			
339	door open					
340			104.5			
341	door closed					
342			101.5			
343	door open					
344	0031o	CP	112			Pitot static tube @ $y=3.5"$
345	door closed	BL				
346						
347	door open					
348			108			
349	door closed					
350			104.5			
351	door open					
352			101.5			
353	door closed					

APPENDIX B

SURFACE PRESSURE TAP LOCATIONS

The ceiling surface and cavity pressure tap locations used to obtain pressure distributions in the present investigation are listed in this appendix. It includes the following tables:

Table	number of ceiling taps	number of cavity taps	Surface
1	16	N/A	7° test section diffuser
2	16	N/A	14° test section diffuser
3	19	N/A	basic ceiling (i.e., no cavities)
4	20	15	one 2" deep cavity and adjacent surfaces
5	16	8	one 2" deep cavity w/ trap door and adjacent surfaces
6	17	11	one 1" deep cavity and adjacent surfaces
7	17	21	two 1" deep cavities and adjacent surfaces
8	16	44	four 1" deep cavities and adjacent surfaces

The basic test section of this wind tunnel uses only the basic ceiling whose pressure tap locations are given in Table 3 and a plain uninstrumented tunnel floor. When an adverse pressure gradient is desired one of the test section diffusers whose pressure tap locations are given in either Table 1 or Table 2 is added on the tunnel floor along with a modified contraction at the test section entrance. When a cavity configuration is desired the basic ceiling is replaced by the appropriate ceiling given in Tables 4 through 8. All of the x station dimensions in these Tables are given for the 24" long test section. The 120" long test section is achieved by adding a 96" insert with a variable floor location upstream of the original test section. As a consequence the x stations for the 120" long test section may be obtained by adding 96" to the x station values given in these Tables.

Table 1. 7° test section diffuser pressure tap locations:

Tap	x, inches	y, inches
1	2.031	-4
2	3.015	-4
3	4.031	-4
4	5.063	-4
5	7.148	-4.128
6	7.985	-4.221
7	8.978	-4.294
8	9.97	-4.441
9	10.947	-4.550
10	11.924	-4.658
11	12.917	-4.769
12	13.909	-4.879
13	15.925	-5.103
14	17.942	-5.327
15	19.927	-5.547
16	21.881	-5.765

Table 2. 14° test section diffuser pressure tap locations:

Tap	x, inches	y, inches
1	2.000	-1.500
2	3.000	-1.500
3	4.015	-1.500
4	5.000	-1.500
5	7.395	-1.849
6	7.910	-1.978
7	8.881	-2.220
8	9.821	-2.455
9	10.791	-2.958
10	11.791	-2.948
11	12.762	-3.191
12	13.732	-3.433
13	15.703	-3.926
14	17.644	-4.411
15	20.524	-5.131
16	21.524	-5.381

Table 3. Basic test section ceiling.

Tap	x, inches	y, inches
1	2.094	6
2	3.01	6
3	4.063	6
4	5.083	6
5	6.063	6
6	7.073	6
7	8.063	6
8	9.063	6
9	10.073	6
10	11.083	6
11	12.083	6
12	13.073	6
13	14.083	6
14	15.063	6
15	16.063	6
16	17.063	6
17	18.073	6
18	20.063	6
19	22.063	6

Table 4. One 2" deep cavity and the adjacent ceiling surface.

Ceiling Tap	x, inches	y, inches	Cavity Tap	x, inches	y, inches
1	2	6	1	7.5	6.5
2	3.015	6	2	7.5	6.97
3	4	6	3	7.5	8
4	5.015	6	4	7.65	8
5	6.041	6	5	8.06	8
6	6.52	6	6	8.35	8
7	6.97	6	7	9.06	8
8	9.5313	6	8	9.31	8
9	9.98	6	9	9.41	8
10	10.48	6	10	9.437	8
11	11.015	6	11	9.437	7.5
12	12.01	6	12	9.437	6.99
13	13.01	6	13	9.437	6.5
14	14.015	6	14	9.437	6.25
15	15.01	6	15	9.437	6.1
16	16.02	6			
17	17.02	6			
18	18.02	6			
19	20.015	6			
20	22.03	6			

Table 5. One 2" deep cavity with a trapdoor and the adjacent ceiling surface.

Ceiling Tap	x, inches	y, inches	Cavity Tap	x, inches	y, inches
1	2.03	6	1	6.13	8.03
2	2.97	6	2	6.53	8.03
3	4	6	3	7.53	8.03
4	4.98	6	4	7.78	8.03
5	8.06	6	5	8	7
6	10	6	6	8	6.46
7	11.03	6	7	8	6.25
8	12.02	6	8	8	6.06
9	13.08	6			
10	14.063	6			
11	15.07	6			
12	16.063	6			
13	17.06	6			
14	18.06	6			
15	20.063	6			
16	22.063	6			

Table 6. One 1" deep cavity and the adjacent ceiling surface.

Ceiling Tap	x, inches	y, inches	Cavity Tap	x, inches	y, inches
1	2.031	6	1	6.5	6.49
2	3	6	2	6.5	6.9
3	4	6	3	6.59	6.938
4	5.5	6	4	6.75	6.938
5	6.24	6	5	7	6.938
6	8.531	6	6	7.24	6.938
7	10.016	6	7	7.4	6.938
8	11.031	6	8	7.5	6.9
9	12	6	9	7.5	6.72
10	13.016	6	10	7.5	6.54
11	14.016	6	11	7.5	6.28
12	15.031	6			
13	16.062	6			
14	17.031	6			
15	18.047	6			
16	20.062	6			
17	22.031	6			

Table 7. Two 1" deep cavities and the adjacent ceiling surface.

Ceiling Tap	x, inches	y, inches	Cavity Tap	x, inches	y, inches	Cavity number
1	1.969	6	1	6	6.47	1
2	2.969	6	2	6	6.85	
3	3.938	6	3	6.09	6.93	
4	4.969	6	4	6.22	6.93	
5	5.75	6	5	6.5	6.94	
6	7.75	6	6	6.74	6.95	
7	10	6	7	6.9	6.95	
8	10.969	6	8	7	6.9	
9	11.969	6	9	7	6.75	
10	12.984	6	10	7	6.53	
11	13.984	6	11	7	6.25	
12	14.984	6	12	8	6.5	2
13	16	6	13	8	6.88	
14	16.969	6	14	8.05	6.93	
15	17.984	6	15	8.25	6.93	
16	19.969	6	16	8.47	6.94	
17	21.969	6	17	8.72	6.95	
			18	8.88	6.95	
			19	9	6.91	
			20	9	6.71	
			21	9	6.49	

Table 8. Four 1" deep cavities and the adjacent ceiling surface.

Ceiling Tap	x, inches	y, inches	Cavity Tap	x, inches	y, inches	Cavity number
1	1.969	6	1	6	6.48	1
2	2.938	6	2	6	6.87	
3	3.95	6	3	6.1	6.95	
4	4.938	6	4	6.25	6.94	
5	5.72	6	5	6.5	6.935	
6	7.67	6	6	6.75	6.93	
7	9.71	6	7	6.91	6.92	
8	11.69	6	8	6.94	6.89	
9	13.2	6	9	6.94	6.75	
10	13.94	6	10	6.94	6.5	
11	14.94	6	11	6.94	6.25	
12	15.97	6	12	7.95	6.46	2
13	16.97	6	13	7.95	6.86	
14	17.95	6	14	8.05	6.93	
15	19.95	6	15	8.2	6.93	
16	21.94	6	16	8.47	6.935	

Ceiling Tap	x, inches	y, inches	Cavity Tap	x, inches	y, inches	Cavity number
			17	8.71	6.94	
			18	8.85	6.94	
			19	8.94	6.9	
			20	8.94	6.75	
			21	8.94	6.5	
			22	8.94	6.25	
			23	9.94	6.5	3
			24	9.94	6.85	
			25	10.04	6.94	
			26	10.19	6.94	
			27	10.46	6.94	
			28	10.68	6.94	
			29	10.84	6.94	
			30	10.94	6.88	
			31	10.94	6.73	
			32	10.94	6.5	
			33	10.94	6.24	
			34	11.95	6.5	4
			35	11.95	6.9	
			36	12.07	6.94	
			37	12.24	6.945	
			38	12.46	6.95	
			39	12.74	6.955	
			40	12.86	6.96	
			41	12.94	6.92	
			42	12.94	6.76	
			43	12.94	6.49	
			44	12.94	6.25	

APPENDIX C

SURFACE PRESSURES

The pressure distributions measured on the wind tunnel surfaces in the cavities and on the adjacent freestream surfaces are presented in this appendix. The data from each cavity are presented in three contiguous plots: (1) front cavity wall; (2) cavity floor; and (3) rear cavity wall. The freestream surface plots are presented for all of the pressures measured on the $y = 6$ inches surface. The data are faired only for the surfaces upstream and downstream of the cavity (or cavities). The following table relates the configurations and their descriptions with the figure numbers:

Config- uration	Test Section Length	Number of Cavities	Cavity Depth	Surface Pressures	Cavity Pressures
0011	24 in.	1	1 in.	C1	C2
0711	24 in.	1	1 in.	C3	C4
1411	24 in.	1	1 in.	C5	C6
8011	120 in.	1	1 in.	C7	C8
8711	120 in.	1	1 in.	C9	C10
8411	120 in.	1	1 in.	C11	C12
0012	24 in.	2	1 in.	C13	C14
0014	24 in.	4	1 in.	C15	C16

Config- uration	Test Section Length	Number of Cavities	Cavity Depth	Surface Pressures	Cavity Pressures
0714	24 in.	4	1 in.	C17	C18
1412	24 in.	2	1 in.	C19	C20
1414	24 in.	4	1 in.	C21	C22
8012	120 in.	2	1 in.	C23	C24
8014	120 in.	4	1 in.	C25	C26
8714	120 in.	4	1 in.	C27	C28
8412	120 in.	2	1 in.	C29	C30
8414	120 in.	4	1 in.	C31	C32
0021	24 in.	1	2 in.	C33	C34
8021	120 in.	1	2 in.	C35	C36
8421	120 in.	1	2 in.	C37	C38
1421	24 in.	1	2 in.	C39	C40
0031	24 in.	1	2 in.	C41	C42
0731	120 in.	1	2 in.	C43	C44
1431	120 in.	1	2 in.	C45	C46
8031	120 in.	1	2 in.	C47	C48
8431	120 in.	1	2 in.	C49	C50

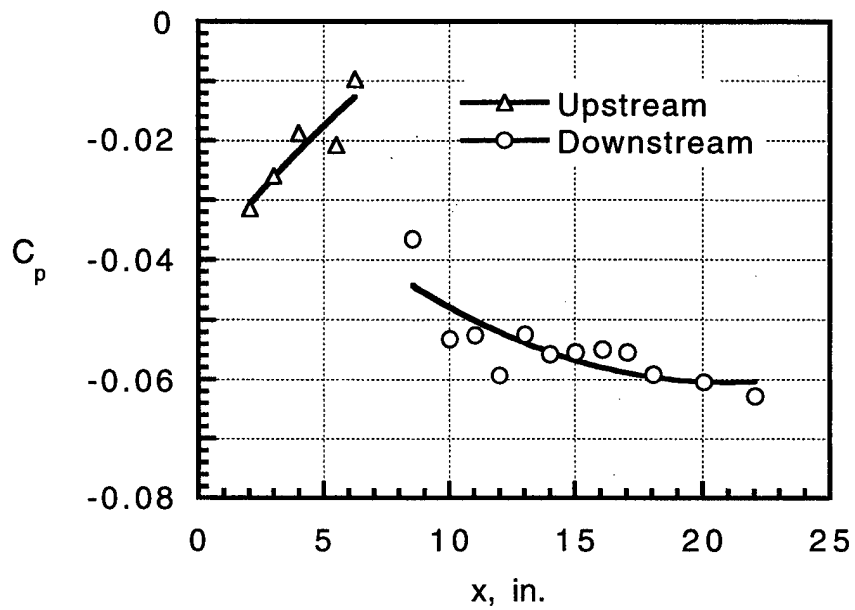


Figure C1. Pressure distribution on the tunnel surfaces adjacent to the 0011 cavity.

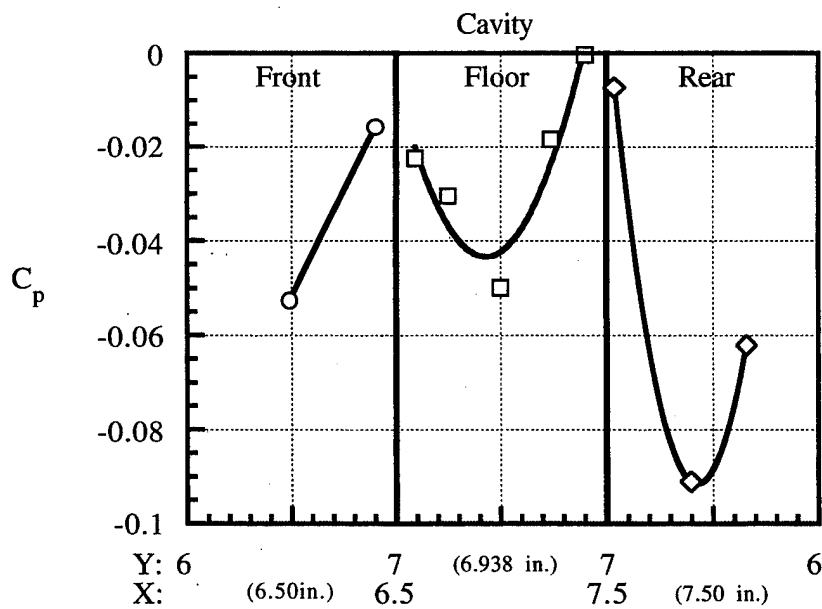


Figure C2. Pressure distribution in the 0011 cavity.

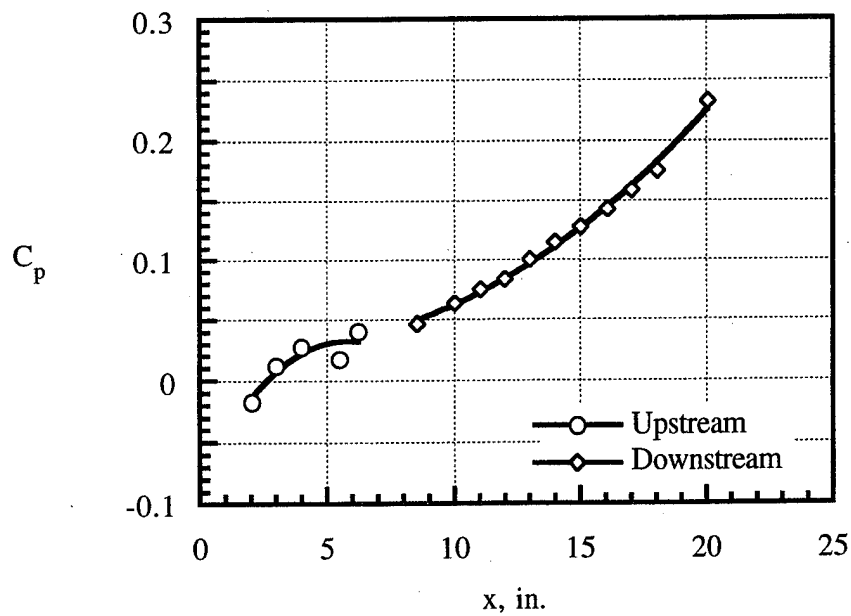


Figure C3. Pressure distribution on the tunnel surfaces adjacent to the 0711 cavity.

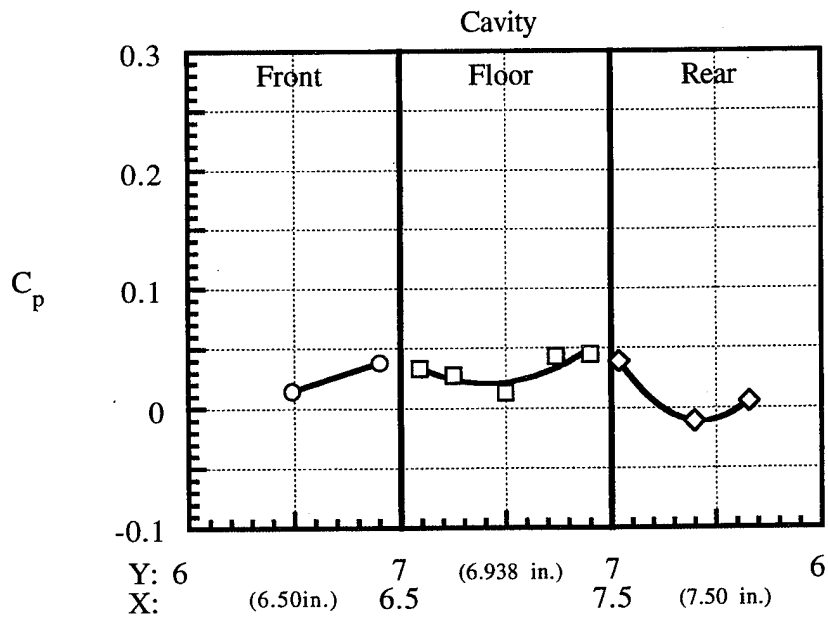


Figure C4. Pressure distribution in the 0711 cavity.

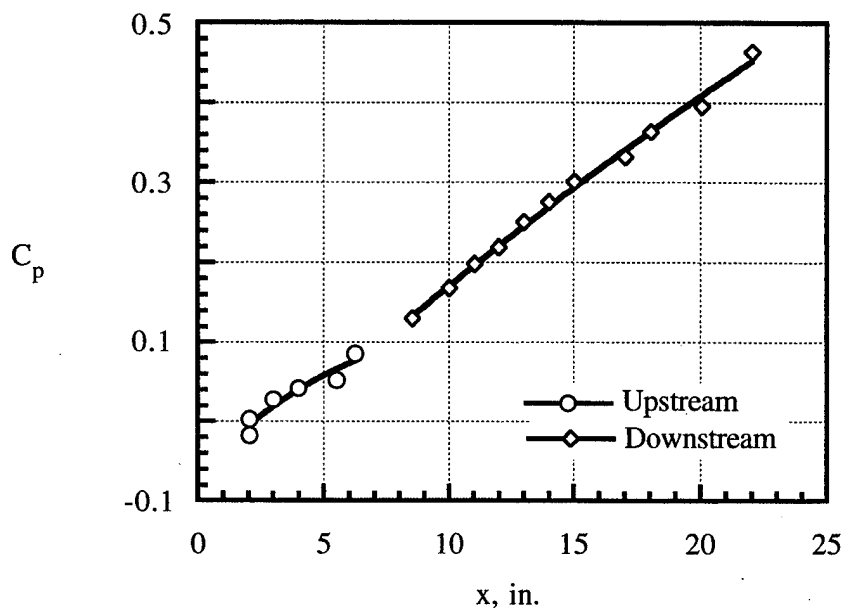


Figure C5. Pressure distribution on the tunnel surfaces adjacent to the 1411 cavity.

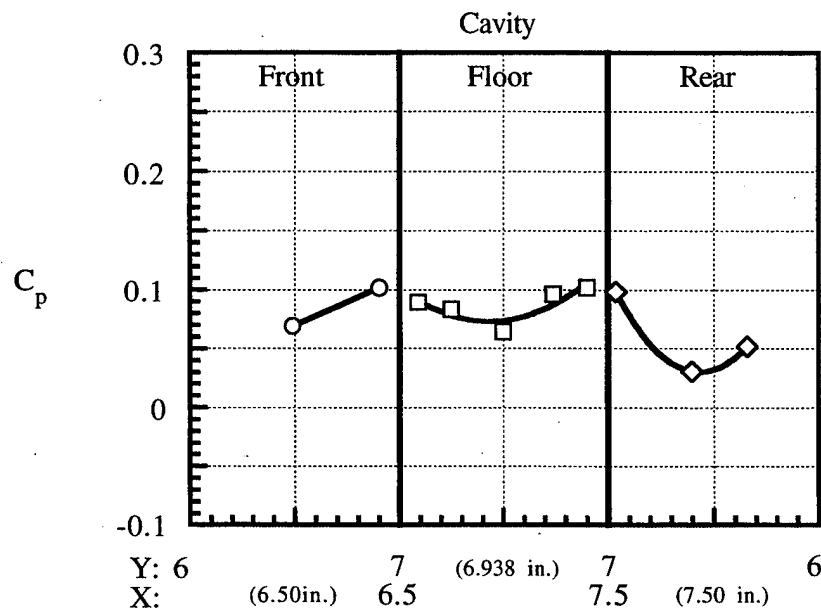


Figure C6. Pressure distribution in the 1411 cavity.

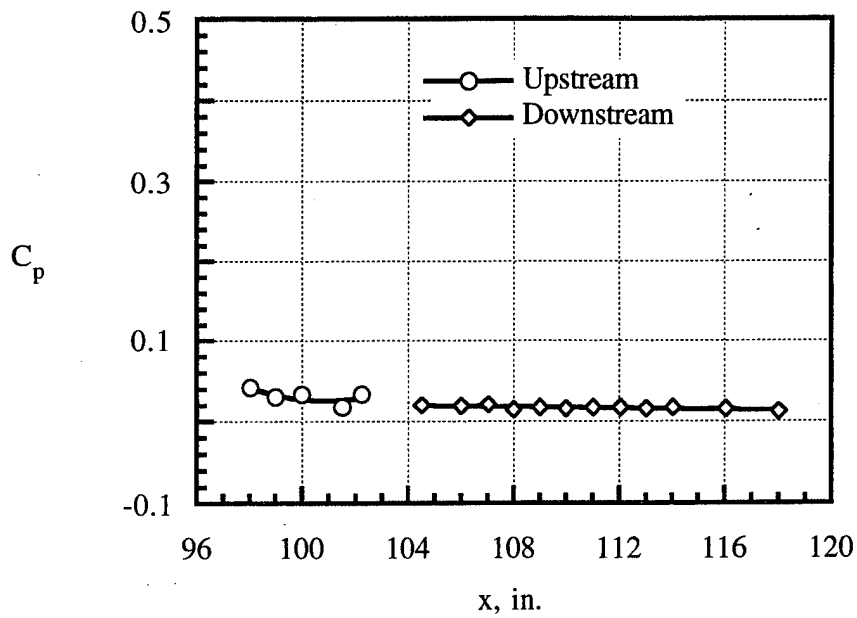


Figure C7. Pressure distribution on the tunnel surfaces adjacent to the 8011 cavity.

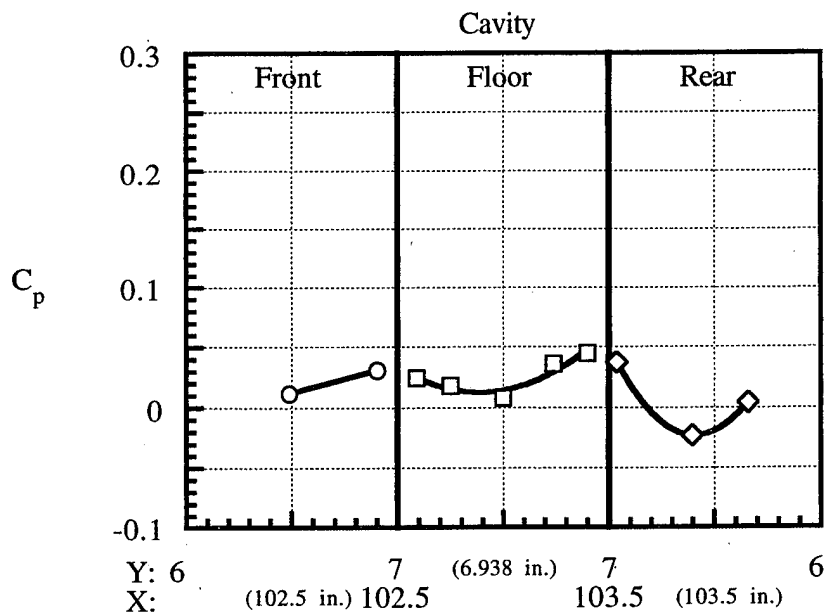


Figure C8. Pressure distribution in the 8011 cavity.

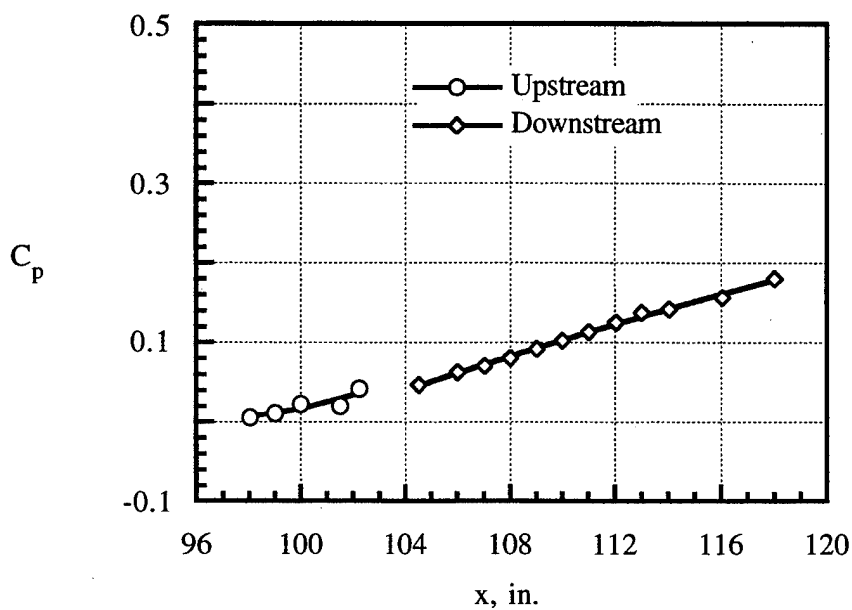


Figure C9. Pressure distribution on the tunnel surfaces adjacent to the 8711 cavity.

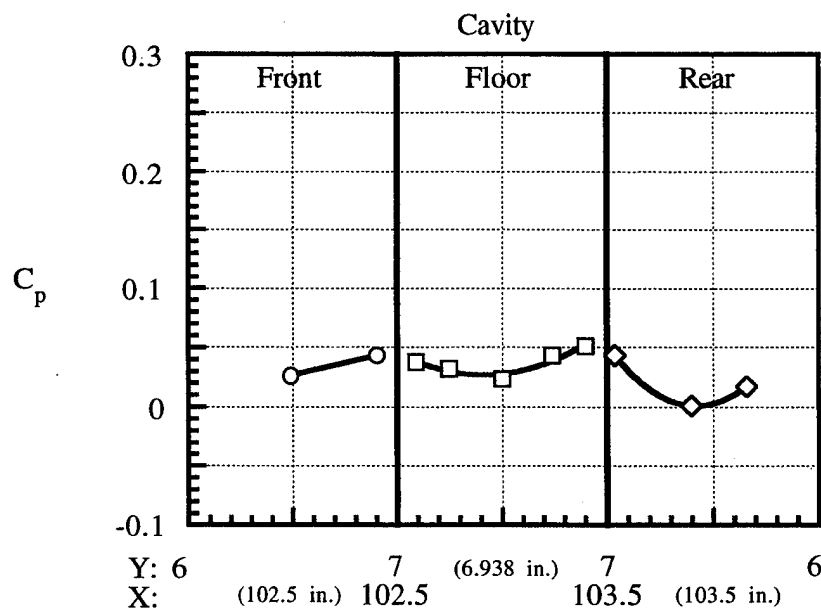


Figure C10. Pressure distribution in the 8711 cavity.

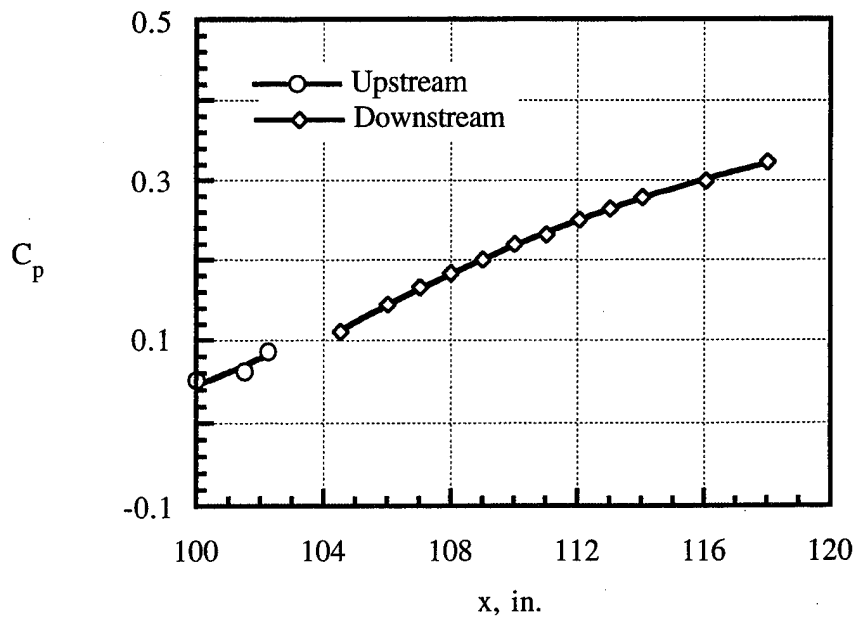


Figure C11. Pressure distribution on the tunnel surfaces adjacent to the 8411 cavity.

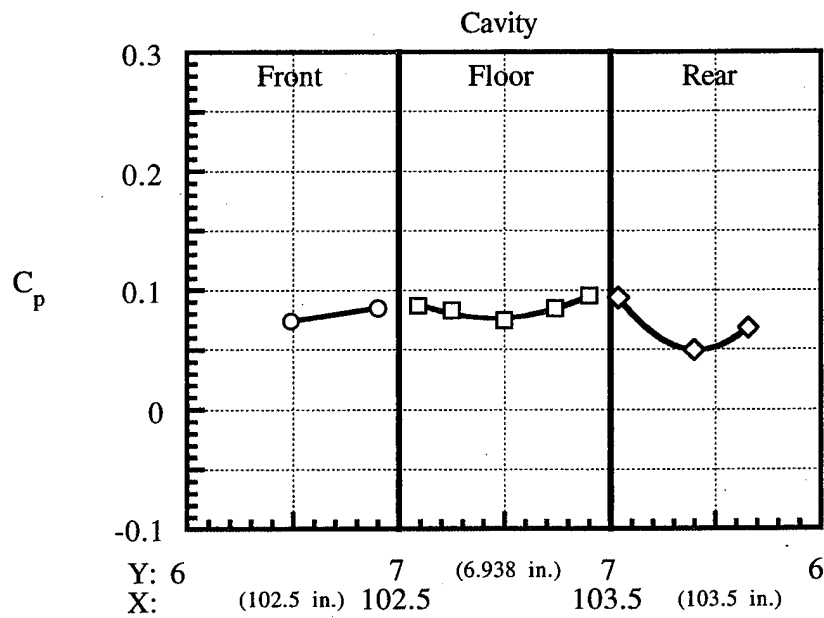


Figure C12. Pressure distribution in the 8411 cavity.

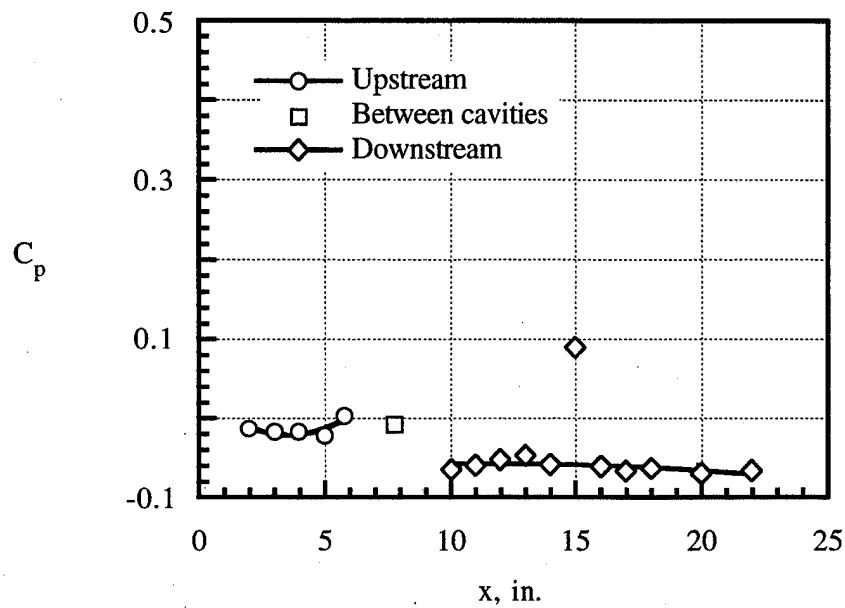


Figure C13. Pressure distribution on the tunnel surfaces adjacent to the 0012 cavities.

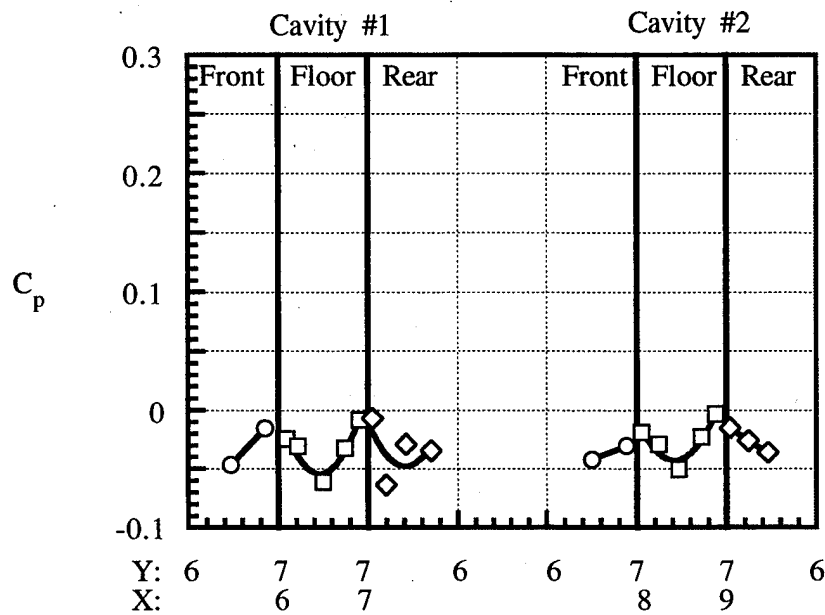


Figure C14. Pressure distribution in the 0012 cavities.

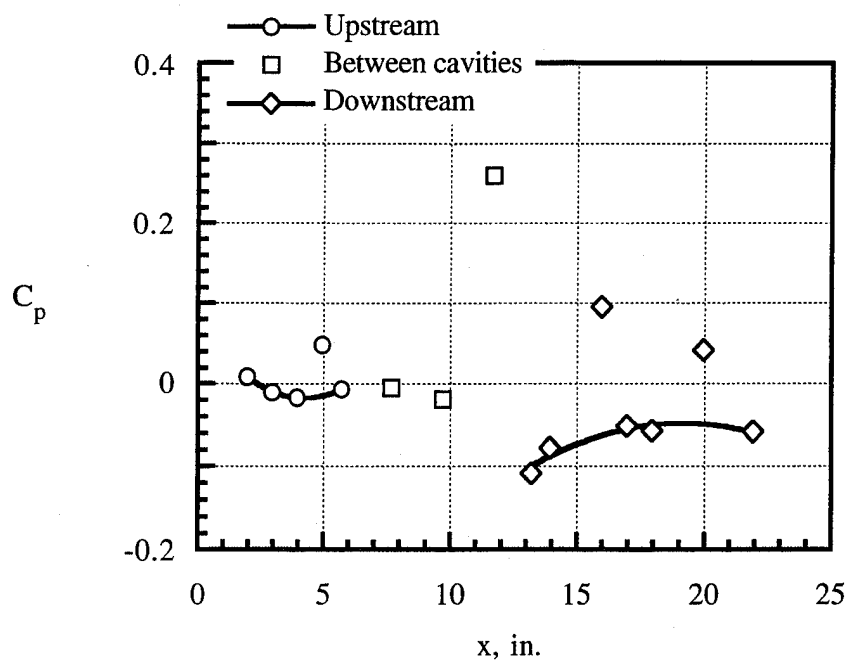
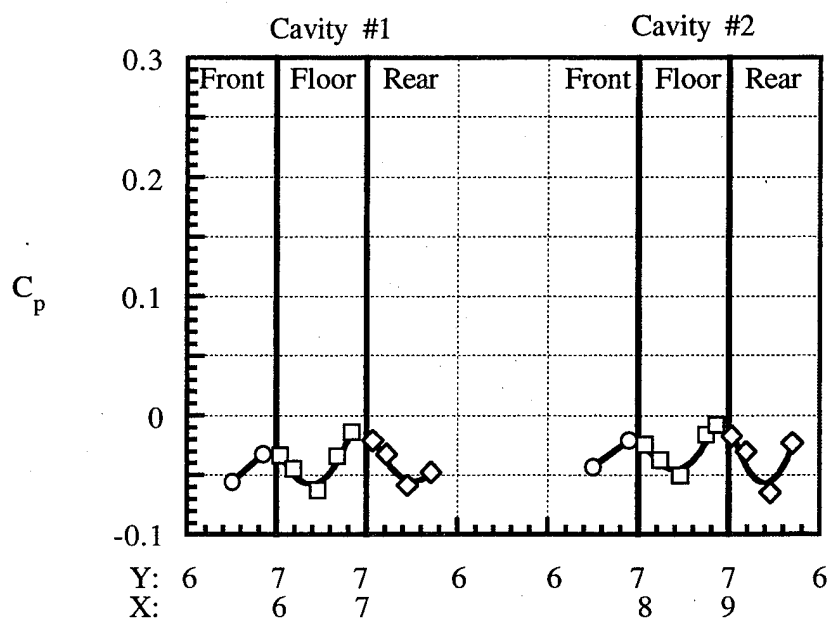
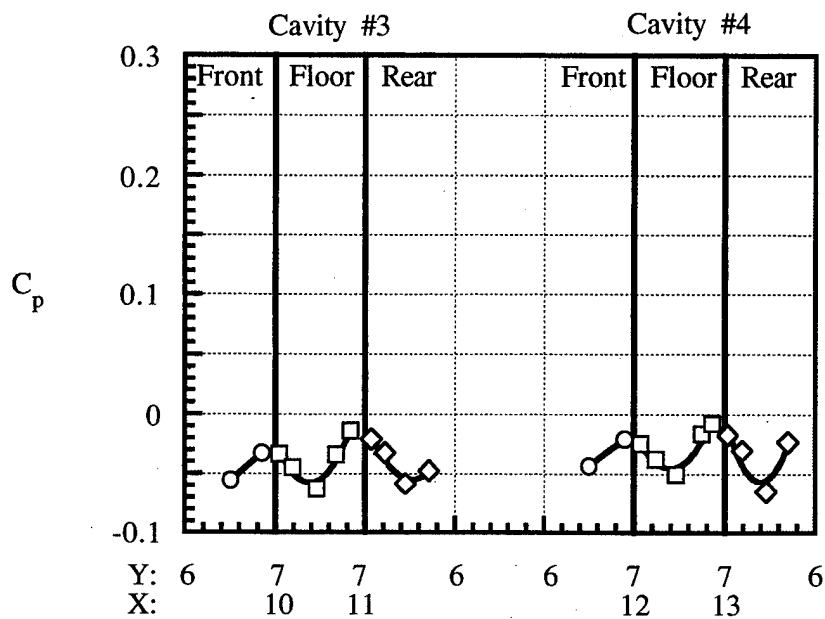


Figure C15. Pressure distribution on the tunnel surfaces adjacent to the 0014 cavities.



(a) Pressure distribution in the first two cavities.

Figure C16. Pressure distribution in the 0014 cavities.



(b) Pressure distribution in the second two cavities.
Figure C16. Concluded.

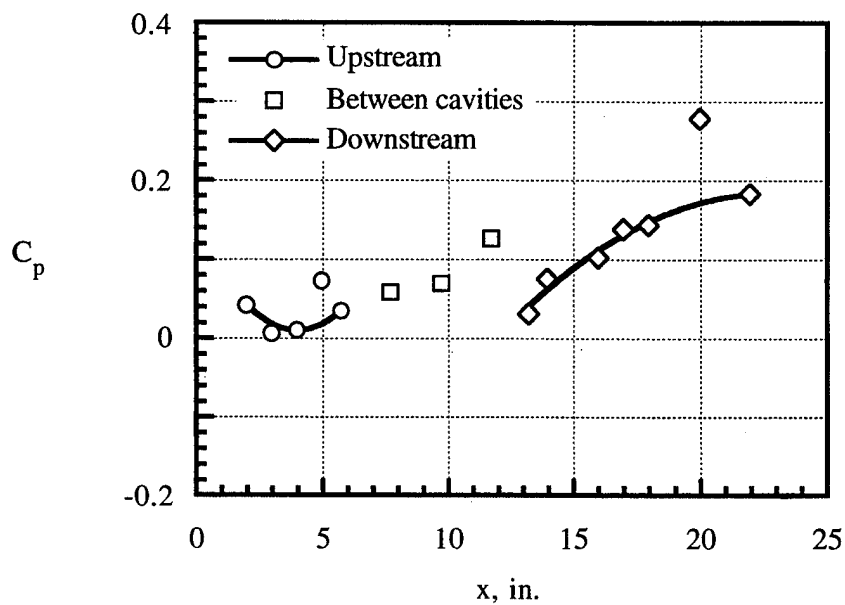
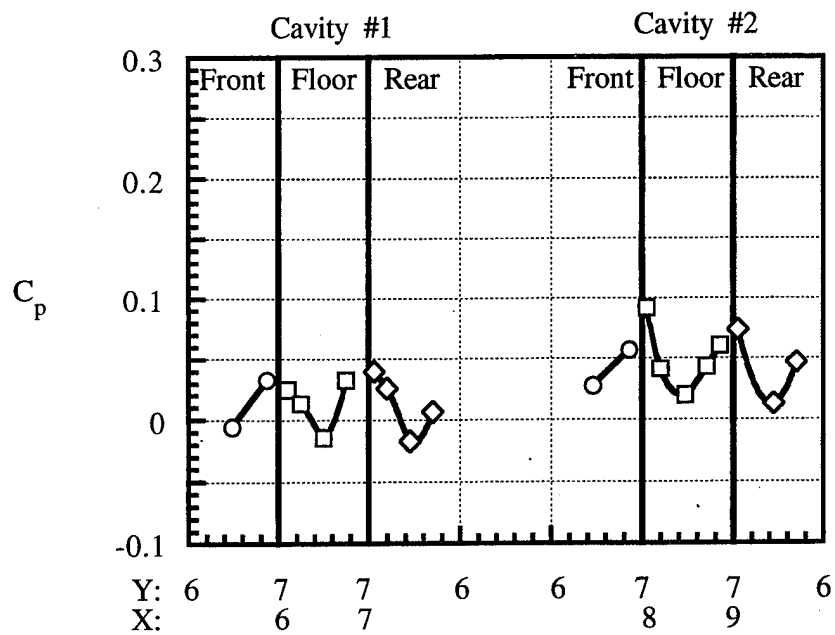
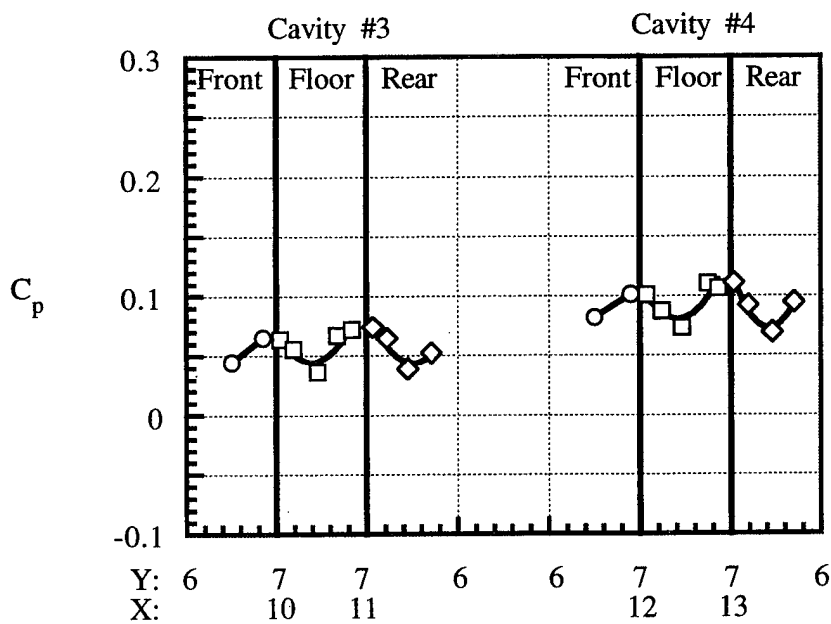


Figure C17. Pressure distribution on the tunnel surfaces adjacent to the 0714 cavities.



(a) Pressure distribution in the first two cavities.
Figure C18. Pressure distribution in the 0714 cavities.



(b) Pressure distribution in the second two cavities.
Figure C18. Concluded.

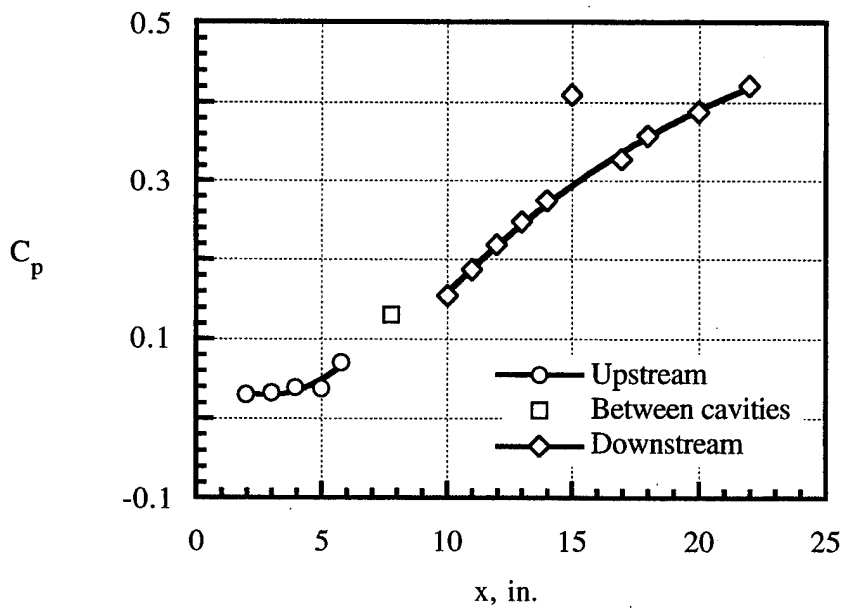


Figure C19. Pressure distribution on the tunnel surfaces adjacent to the 1412 cavities.

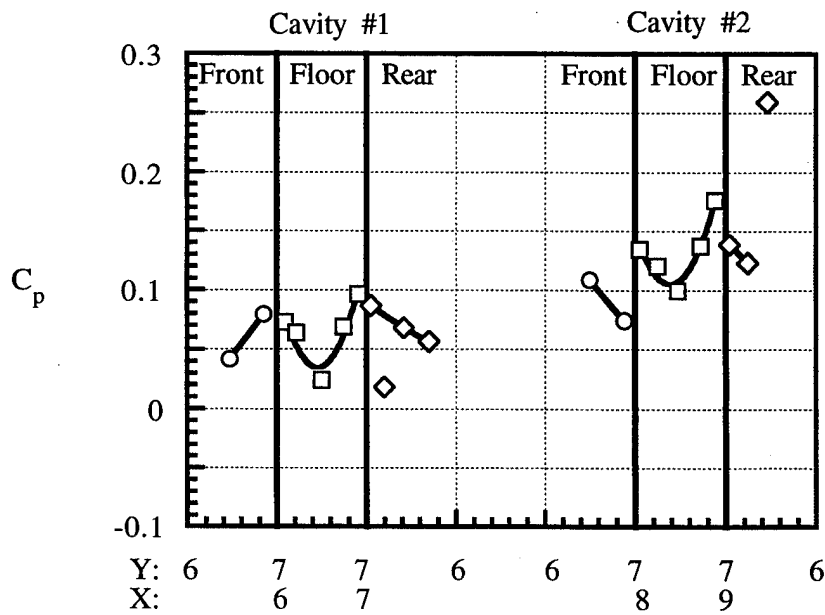


Figure C20. Pressure distribution in the 1412 cavities.

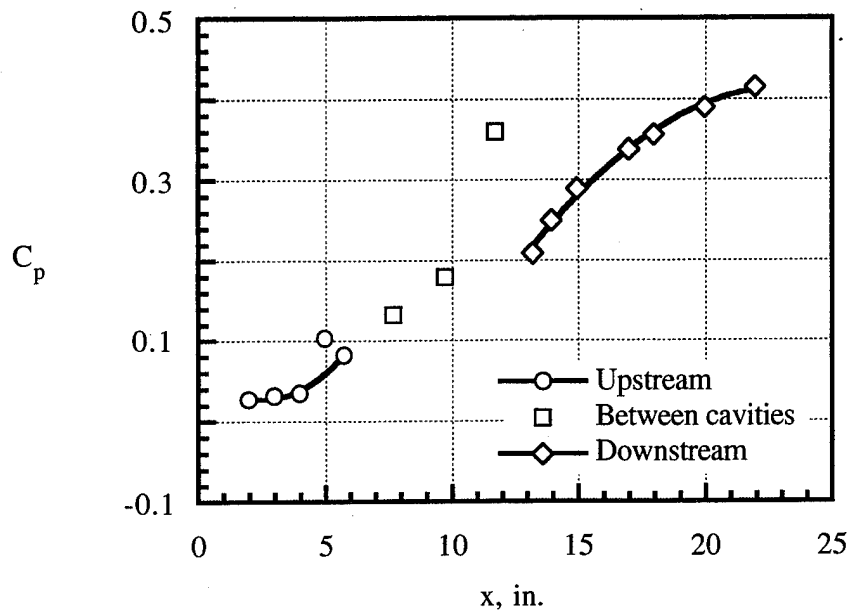
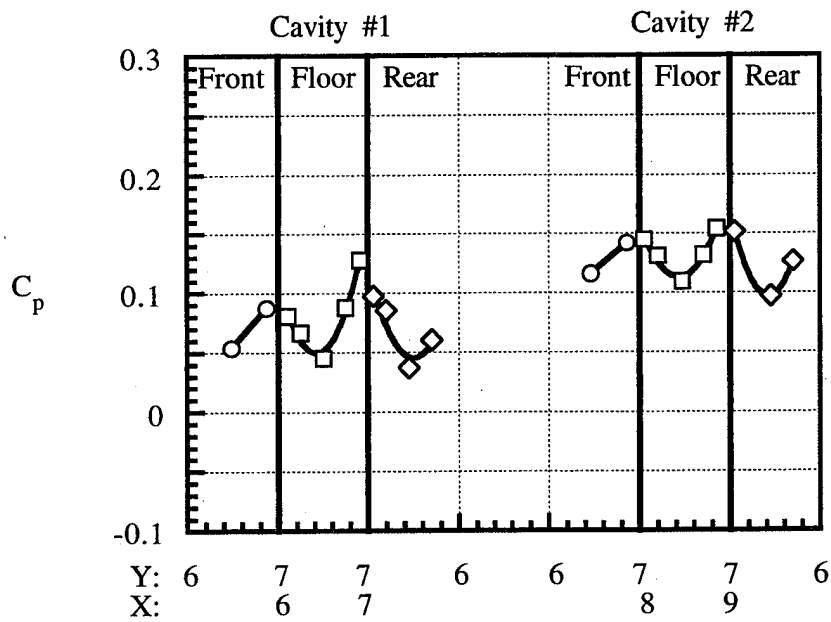
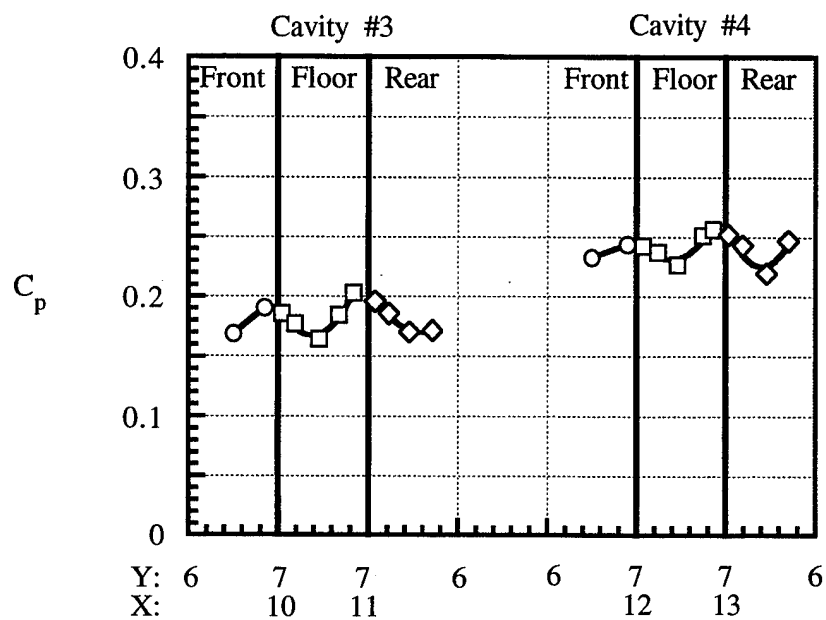


Figure C21. Pressure distribution on the tunnel surfaces adjacent to the 1414 cavities.



(a) Pressure distribution in the first two cavities.

Figure C22. Pressure distribution in the 1414 cavities.



(b) Pressure distribution in the second two cavities.
Figure C22. Concluded.

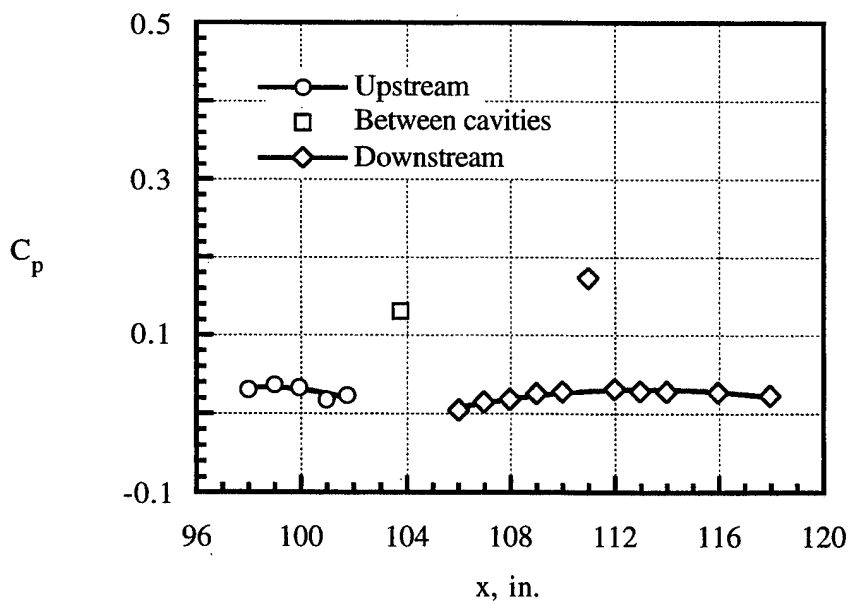


Figure C23. Pressure distribution on the tunnel surfaces adjacent to the 8012 cavities.

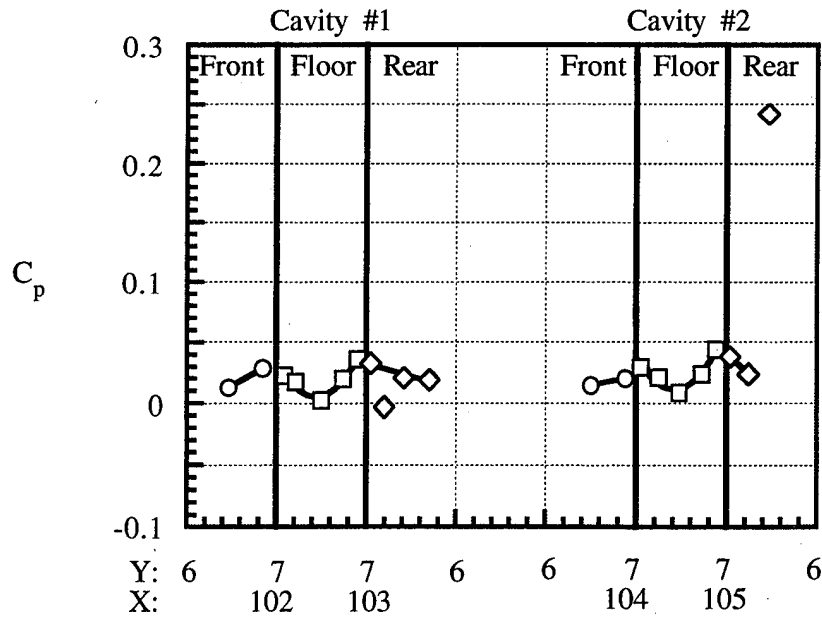


Figure C24. Pressure distribution in the 8012 cavities.

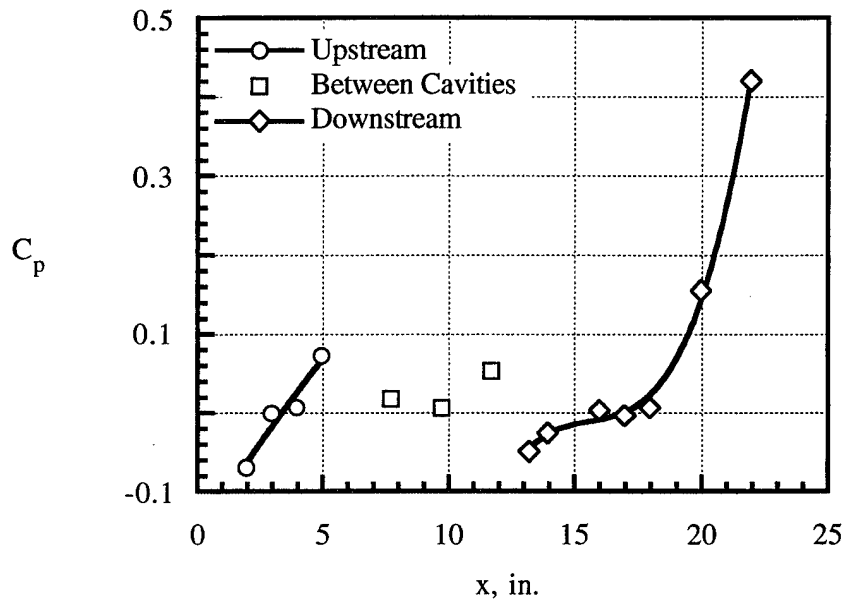
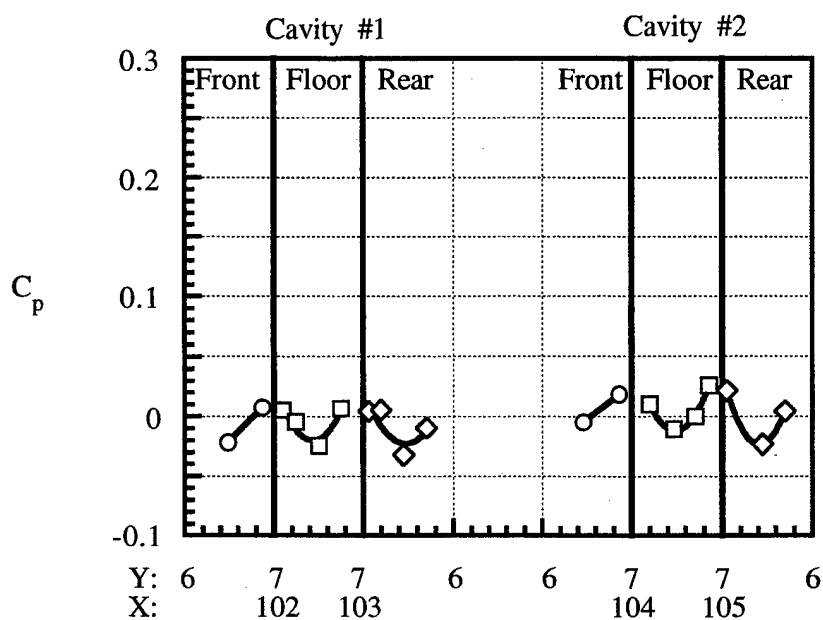
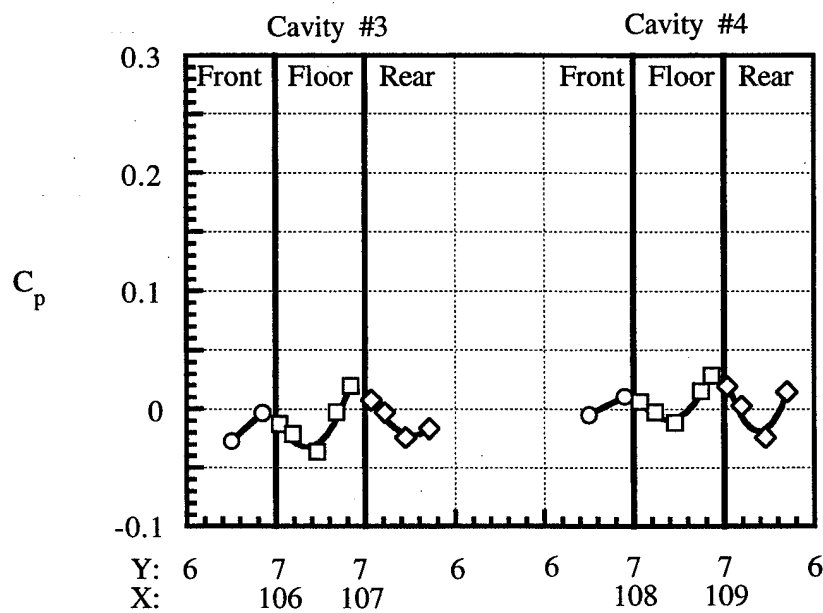


Figure C25. Pressure distribution on the tunnel surfaces adjacent to the 8014 cavities.



(a) Pressure distribution in the first two cavities.
Figure C26. Pressure distribution in the 8014 cavities.



(b) Pressure distribution in the second two cavities.
Figure C26. Concluded.

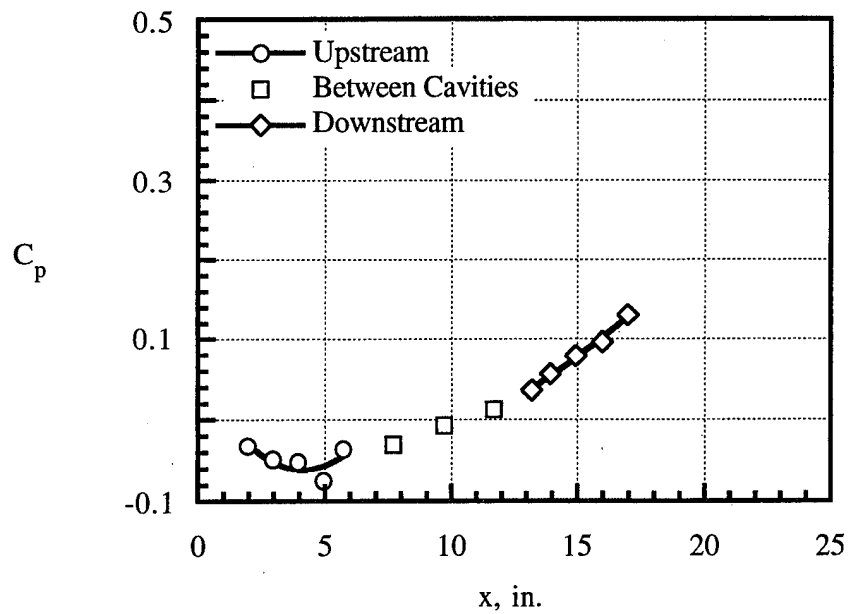
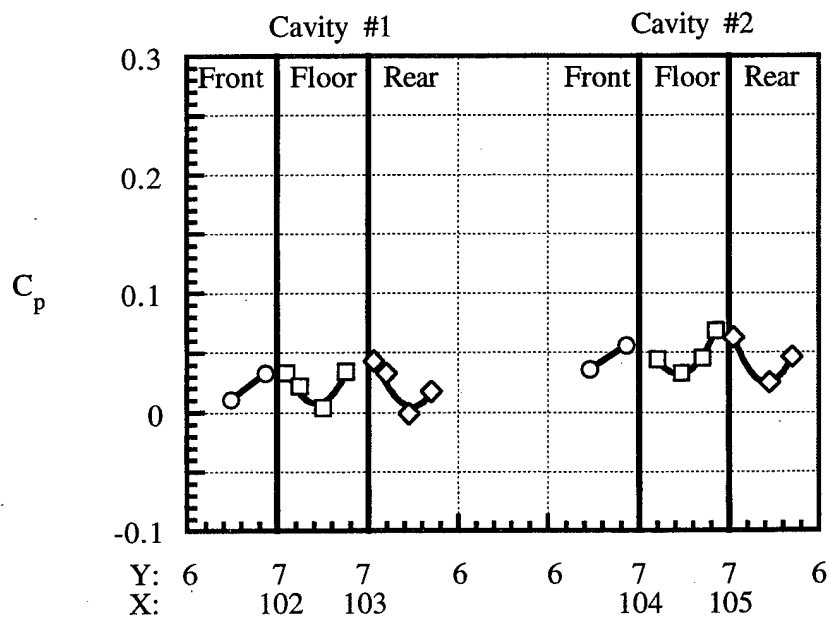
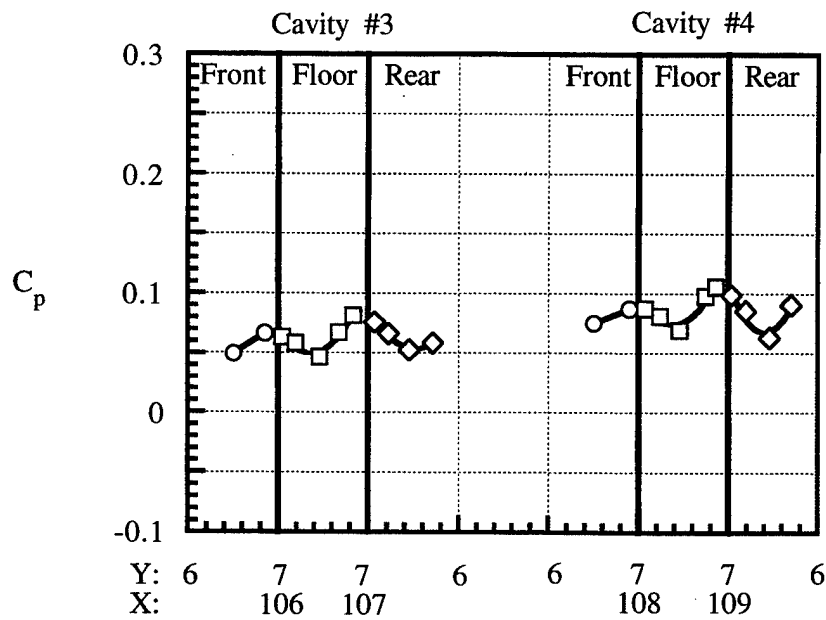


Figure C27. Pressure distribution on the tunnel surfaces adjacent to the 8714 cavities.



(a) Pressure distribution in the first two cavities.

Figure C28. Pressure distribution in the 8714 cavities.



(b) Pressure distribution in the second two cavities.
Figure C28. Concluded.

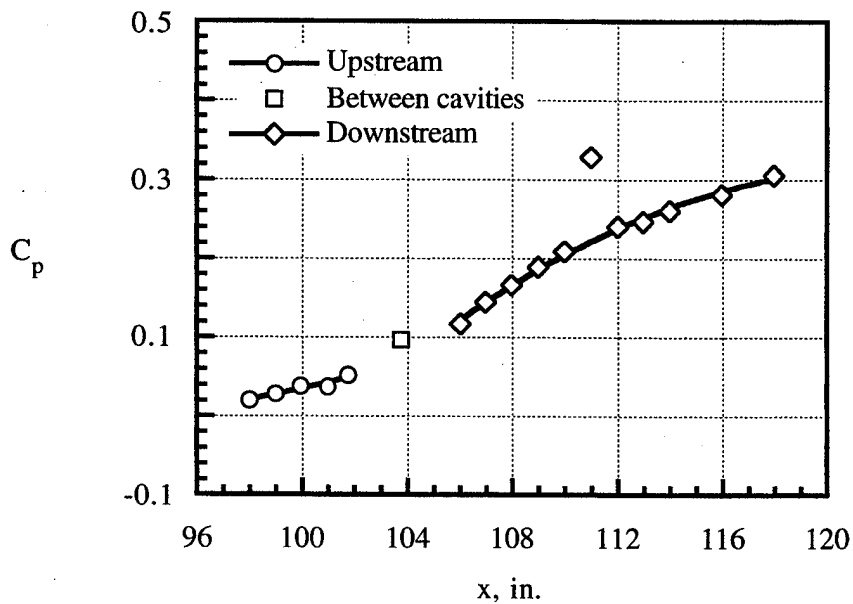


Figure C29. Pressure distribution on the tunnel surfaces adjacent to the 8412 cavities.

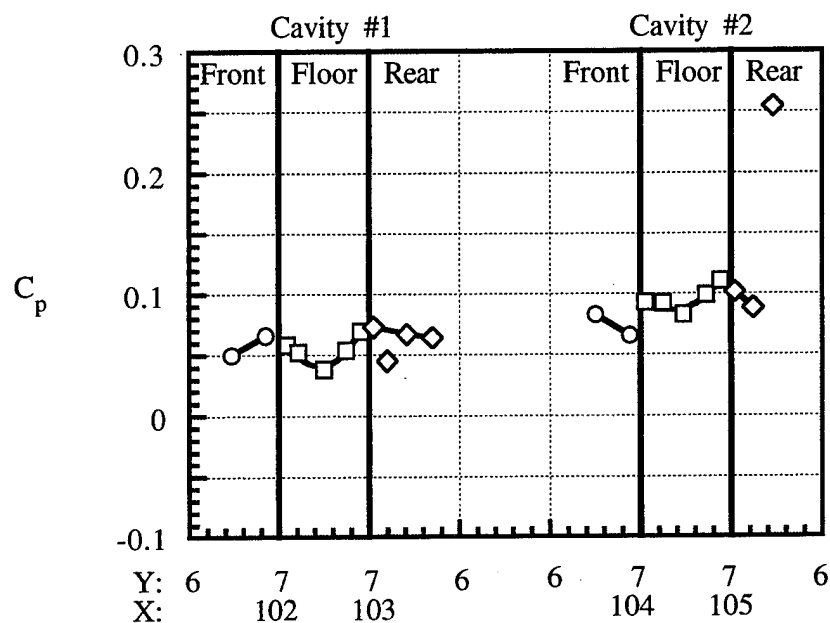


Figure C30. Pressure distribution in the 8412 cavities.

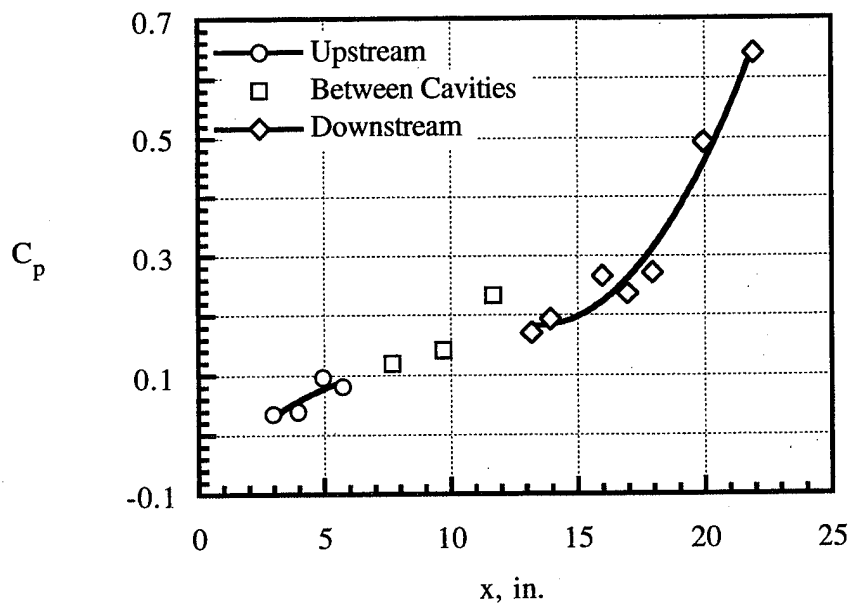
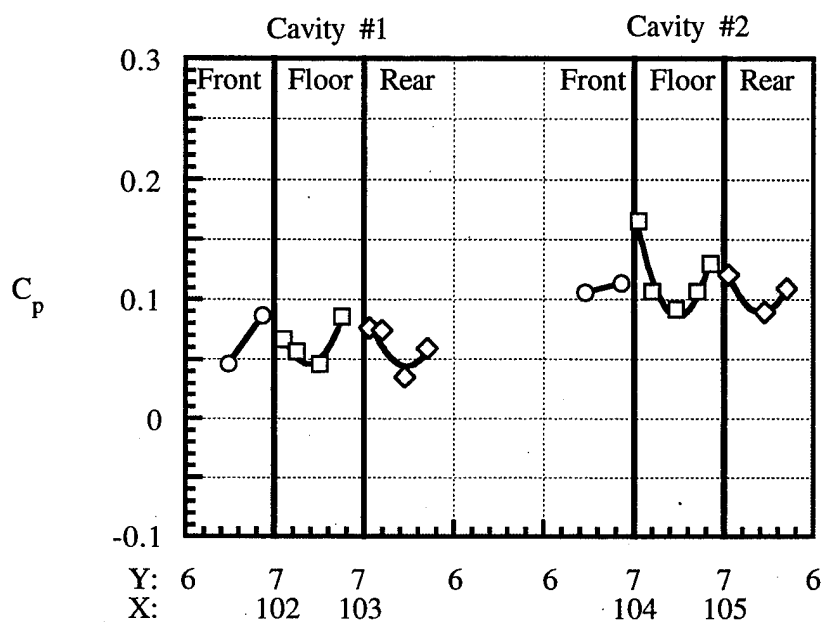
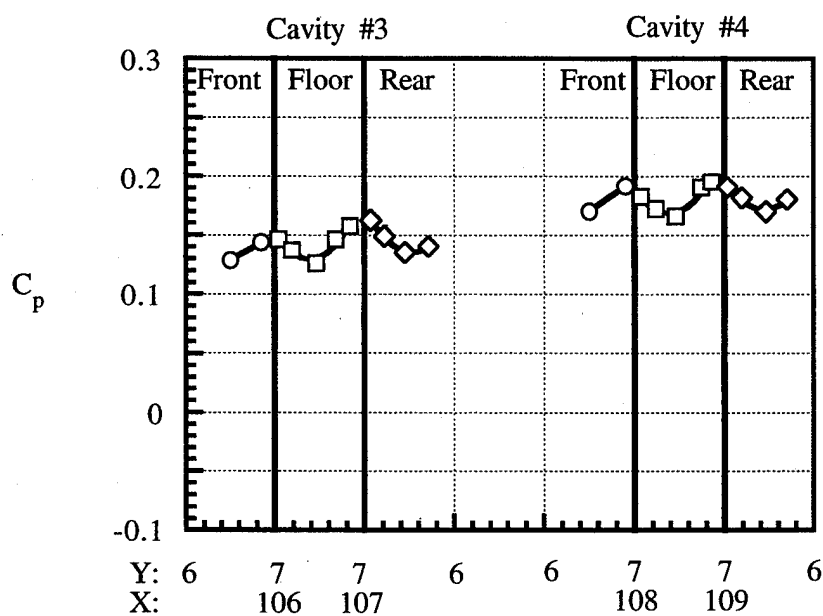


Figure C31. Pressure distribution on the tunnel surfaces adjacent to the 8414 cavities.



(a) Pressure distribution in the first two cavities.
Figure C32. Pressure distribution in the 8414 cavities.



(b) Pressure distribution in the second two cavities.
Figure C32. Concluded.



cavity.



Figure C34. Pressure distribution in the 0021 cavity.

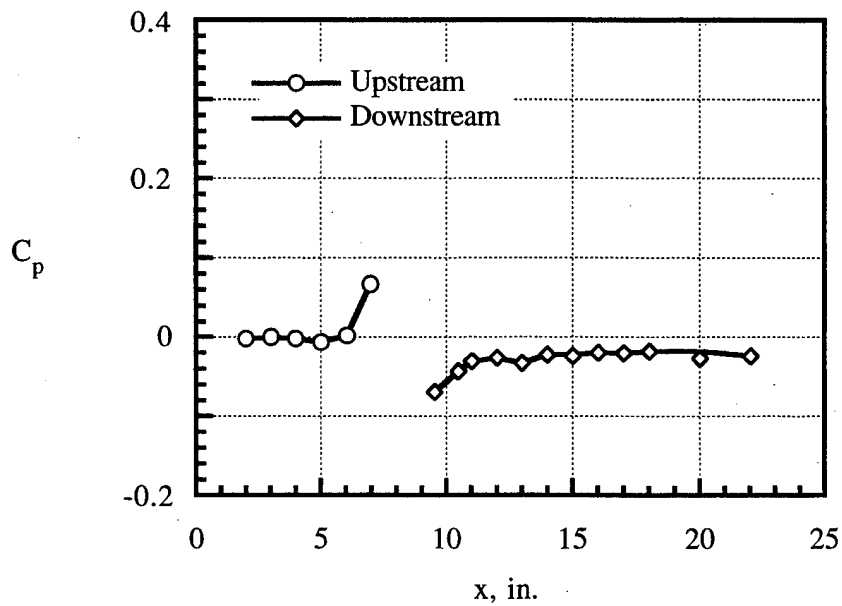


Figure C35. Pressure distribution on the tunnel surfaces adjacent to the 8021 cavity.

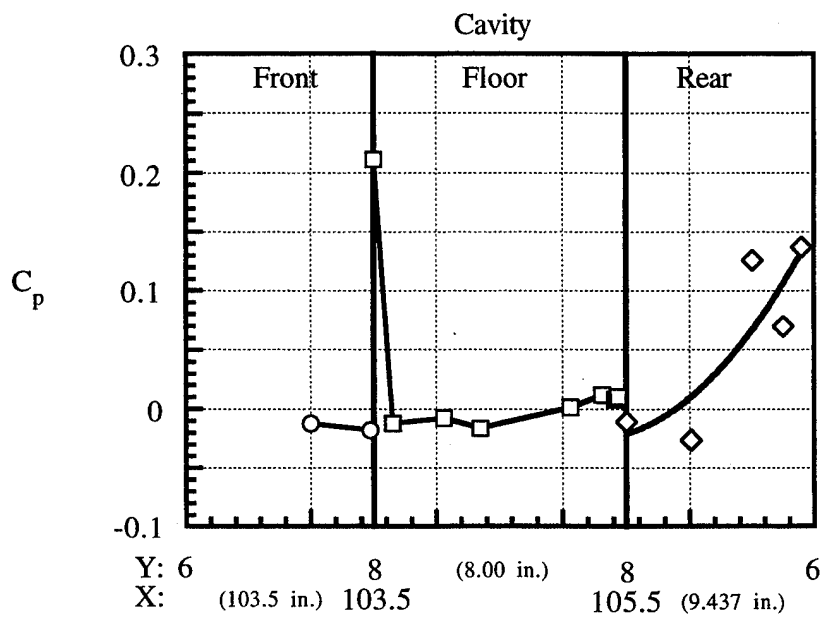


Figure C36. Pressure distribution in the 8021 cavity.

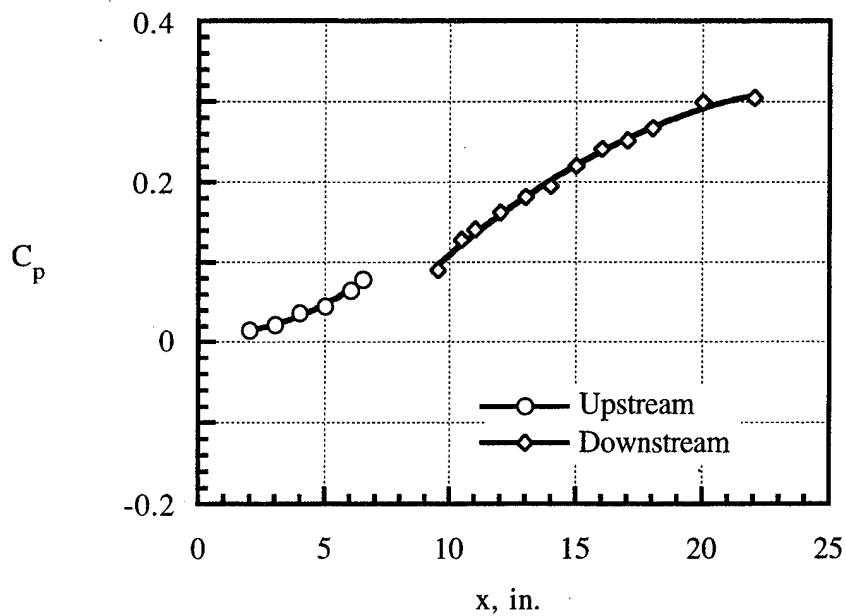


Figure C37. Pressure distribution on the tunnel surfaces adjacent to the 8421 cavity.

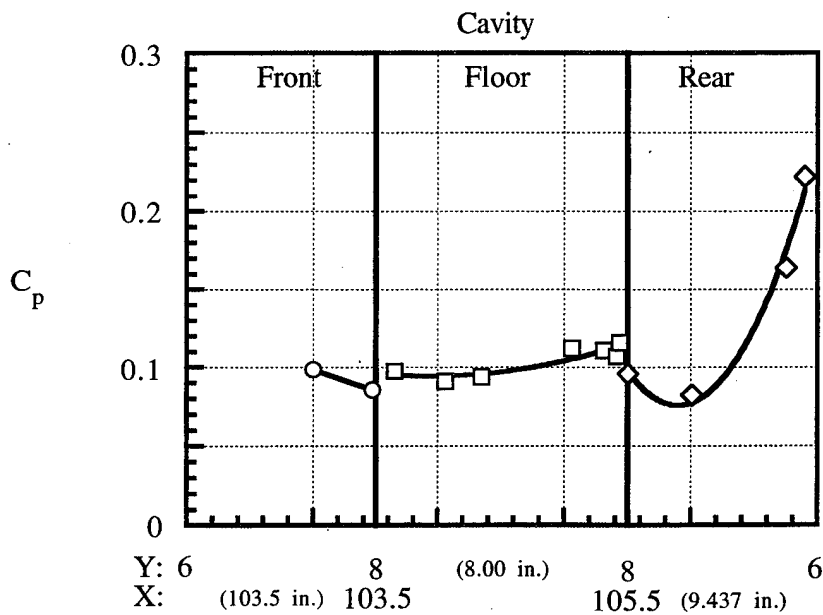


Figure C38. Pressure distribution in the 8421 cavity.

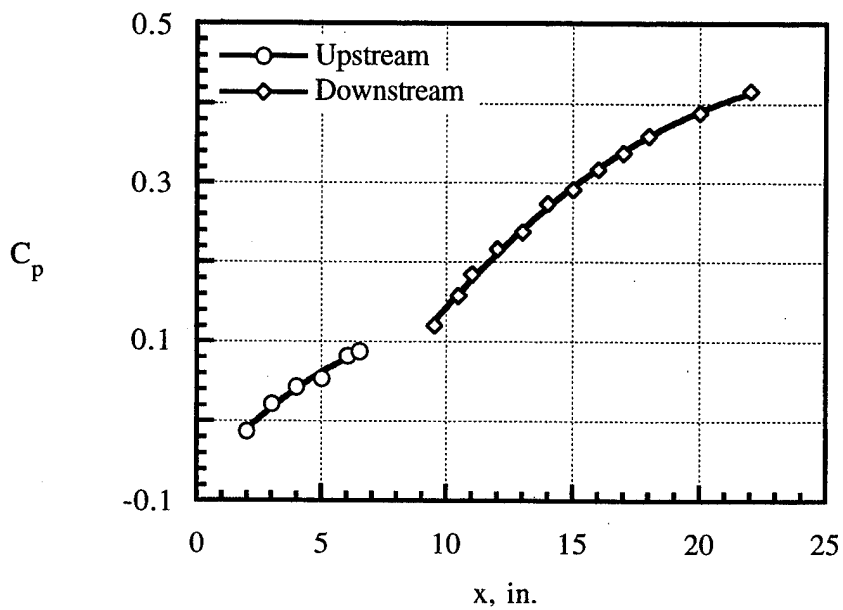


Figure C39. Pressure distribution on the tunnel surfaces adjacent to the 1421 cavity.

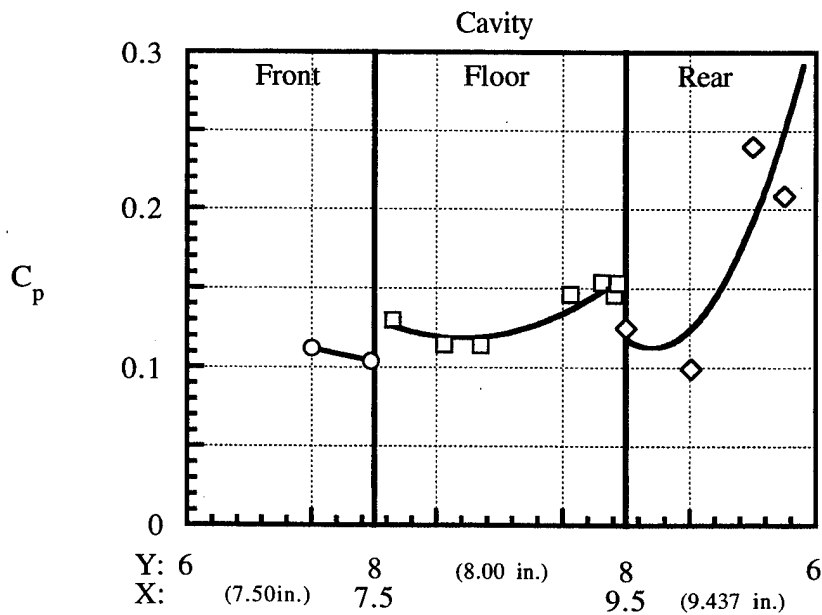


Figure C40. Pressure distribution in the 1421 cavity.

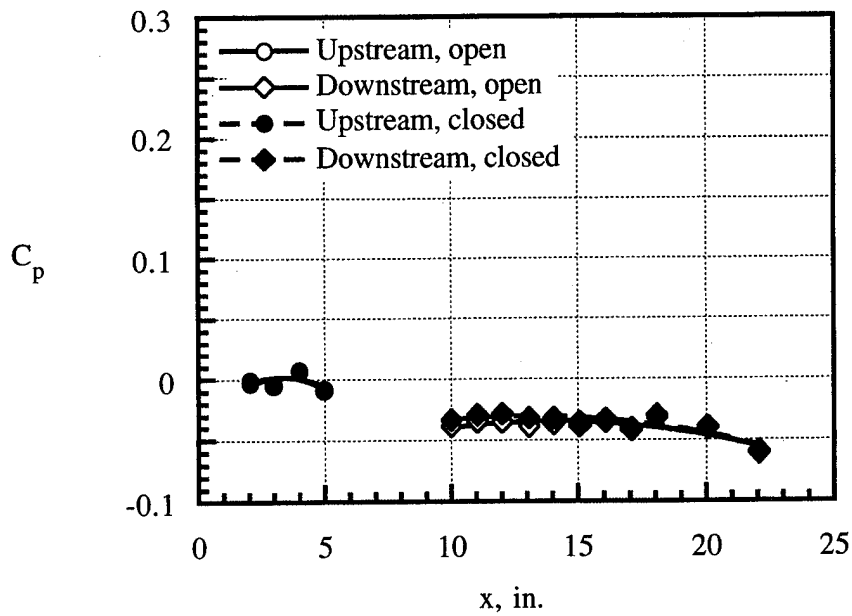


Figure C41. Pressure distribution on the tunnel surfaces adjacent to the 0031 cavity.

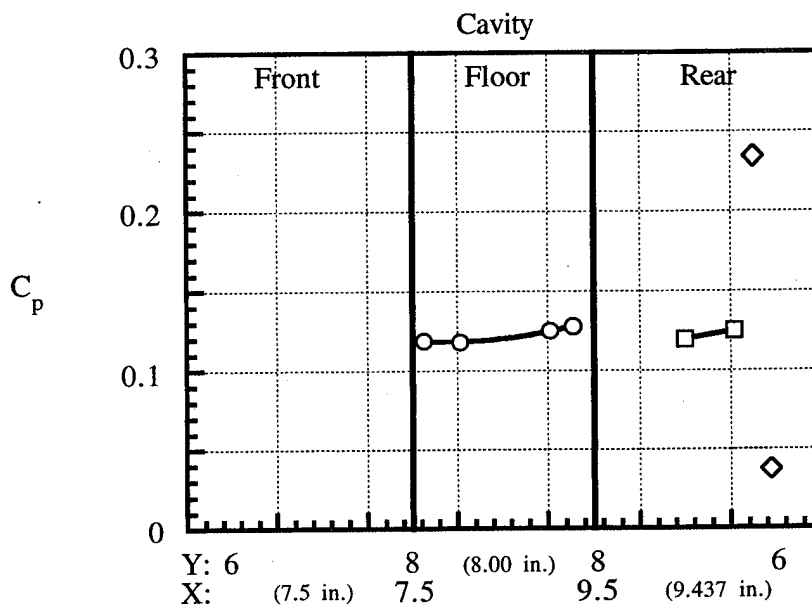


Figure C42. Pressure distribution in the 0031 cavity.

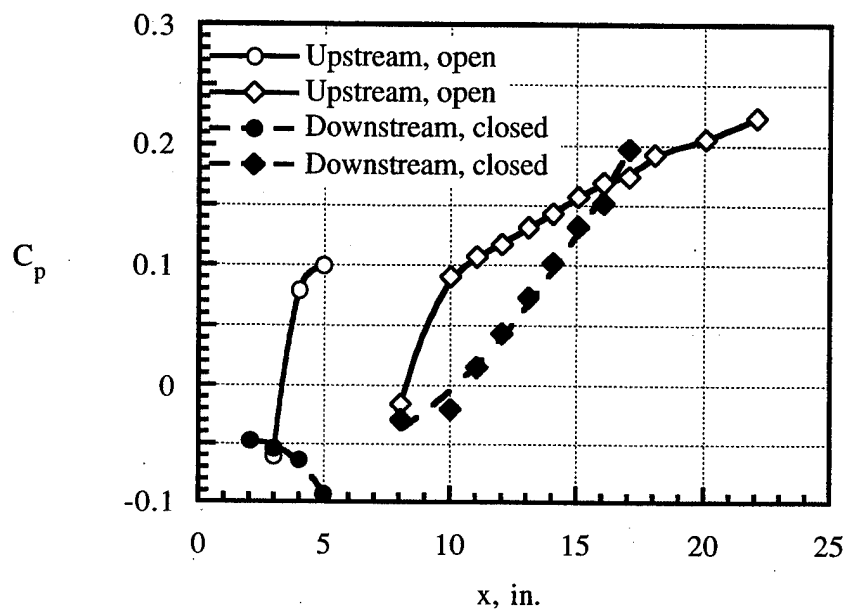


Figure C43. Pressure distribution on the tunnel surfaces adjacent to the 0731 cavity.

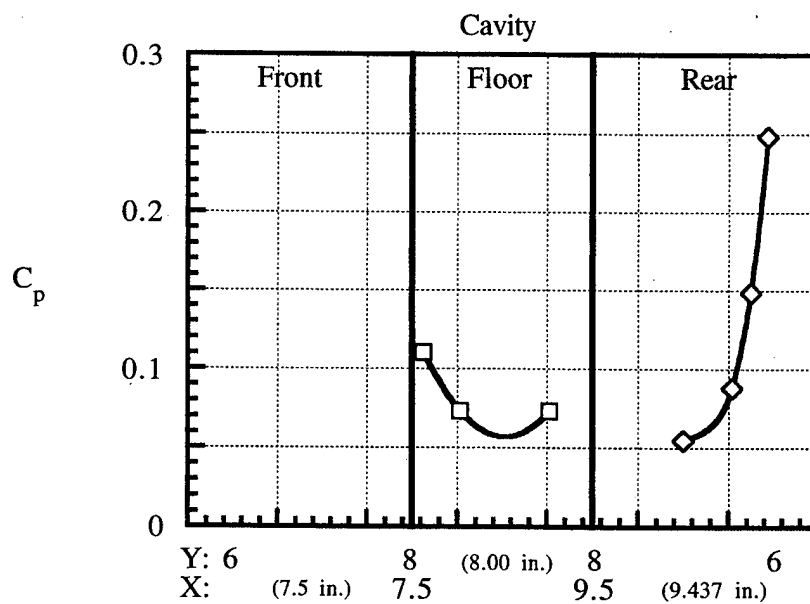


Figure C44. Pressure distribution in the 00731 cavity.

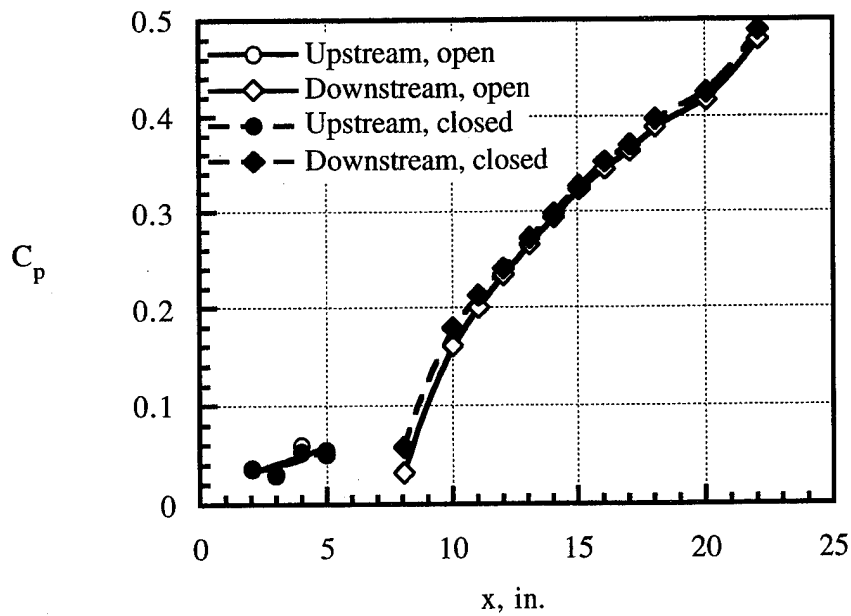


Figure C45. Pressure distribution on the tunnel surfaces adjacent to the 1431 cavity.

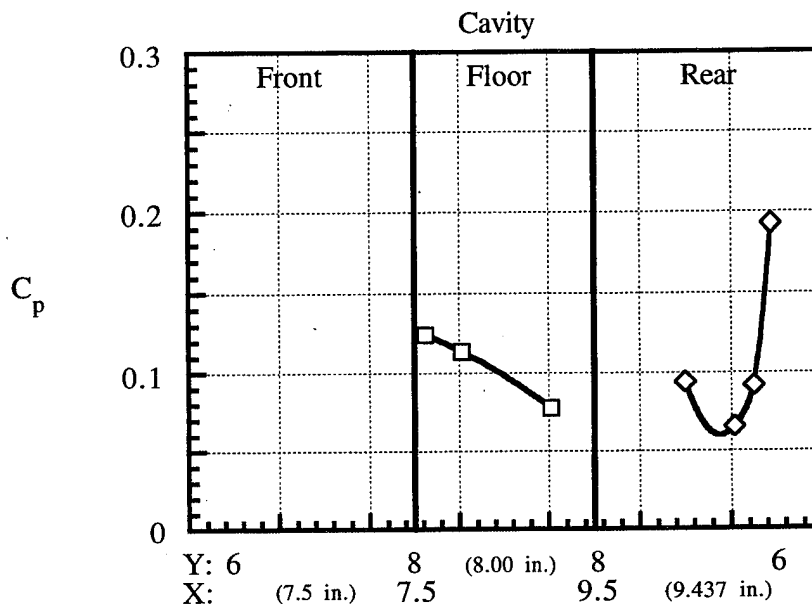


Figure C46. Pressure distribution in the 1431 cavity.

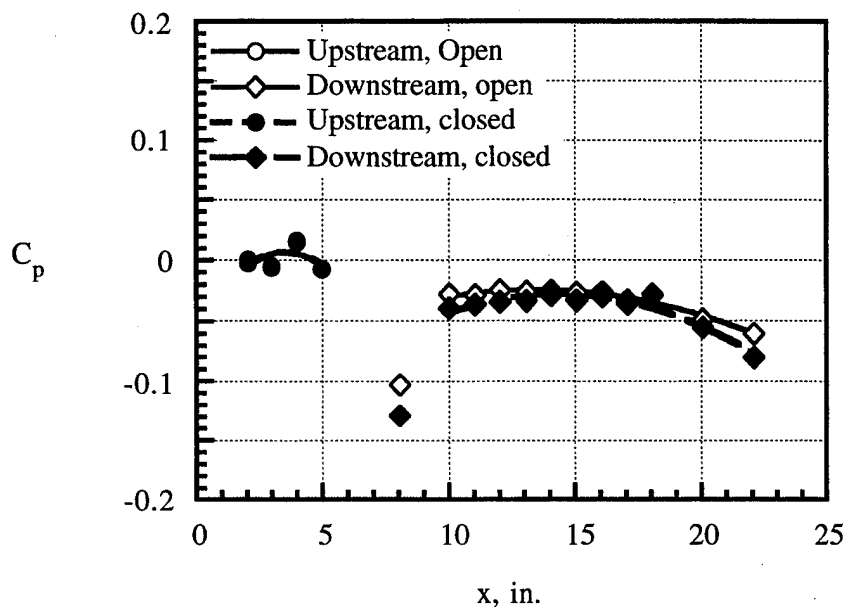


Figure C47. Pressure distribution on the tunnel surfaces adjacent to the 8031 cavity.

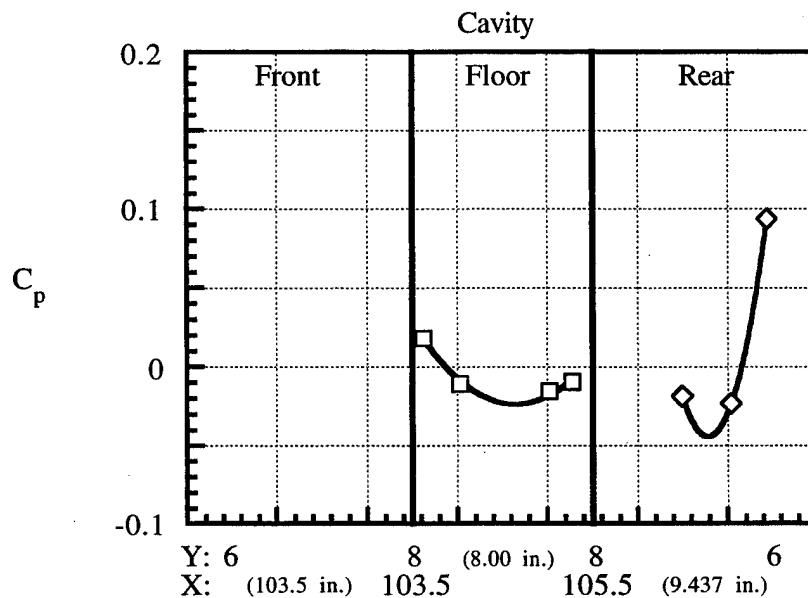


Figure C48. Pressure distribution in the 8031 cavity.

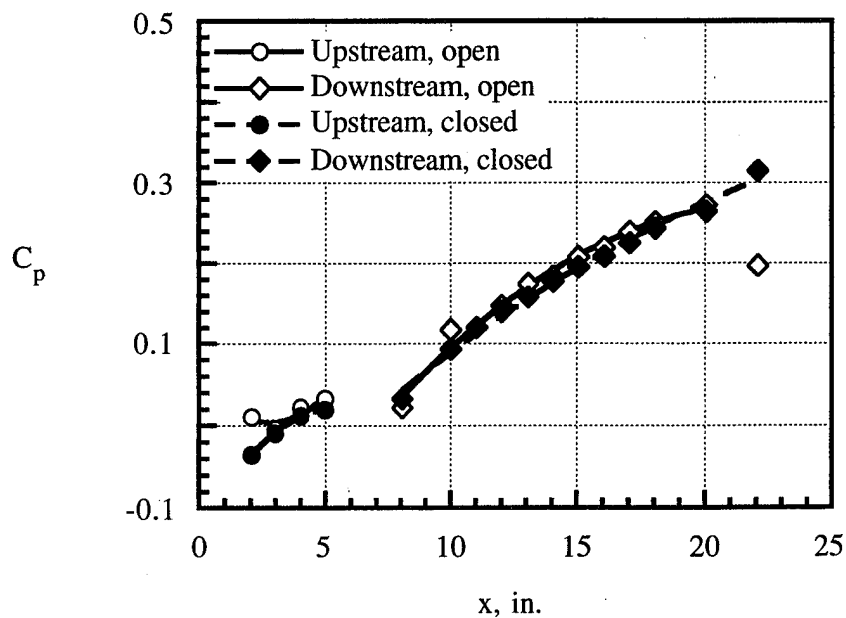


Figure C49. Pressure distribution on the tunnel surfaces adjacent to the 8431 cavity.

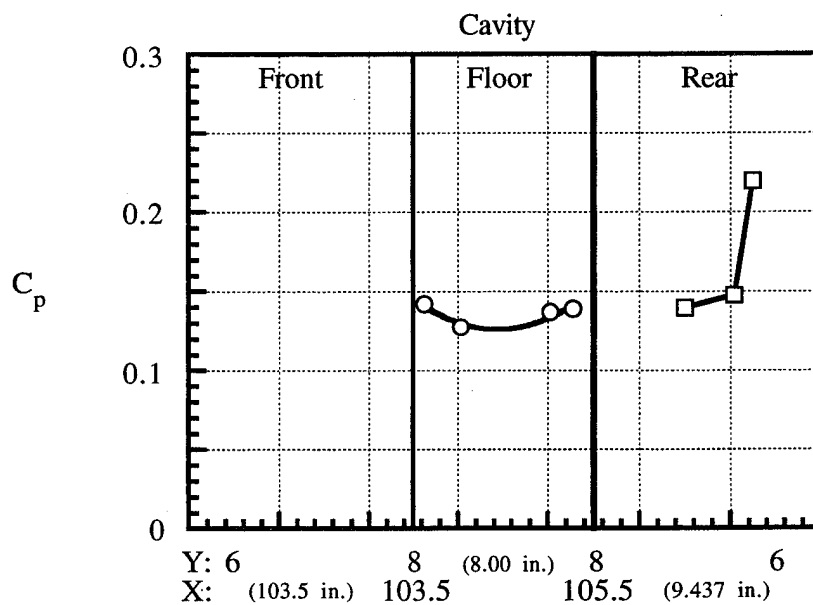


Figure C50. Pressure distribution in the 8431 cavity.

APPENDIX D

BOUNDARY LAYER PROFILES

The boundary layer data from this investigation is presented for each wind tunnel configuration in this appendix. There were four to six longitudinal locations for each configuration where boundary layer profiles were measured. Each figure identifies the x location for the data presented. The displacement thickness was computed from the data and then used to non-dimensionize the distance y which was measured from the wind tunnel ceiling. A pitot probe measured the total-pressure variation and the static pressure was obtained from a port located on the ceiling at the appropriate longitudinal location. As expected, the static pressures were nearly constant and the total pressures varied from a few pounds per square foot greater than the static pressure near the surface to the freestream total pressure at the boundary layer edge. The following table relates the configurations and their description with the figure numbers:

Config- uration	Test Section Length	Number of Cavities	Cavity Depth	Figure Number	Notes
0000	24 in.	0	N/A	D1	
8000	120 in.	0	N/A	D2D	
0700	24 in.	0	N/A	D3	
8700	120 in.	0	N/A	D4D	
1400	24 in.	0	N/A	D5	
8400	120 in.	0	N/A	D6	

Config- uration	T.S. Length	No. of Cavities	Cavity Depth	Figure No.	Notes
0011	24 in.	1	N/A	D7	
0021	24 in.	1	2 in.	D8	
0711	24 in.	1	1 in.	D9	
1411	24 in.	1	1 in.	D10	
1421	24 in.	1	2 in.	D11	
8011	120 in.	1	1 in.	D12	
8021	120 in.	1	2 in.	D13	
8711	120 in.	1	1 in.	D14	
8411	120 in.	1	1 in.	D15	
8421	120 in.	1	2 in.	D16	
0012	24 in.	2	1 in.	D17	
0014	24 in.	4	1 in.	D18	
0714	24 in.	4	1 in.	D19	
1412	24 in.	2	1 in.	D20	
1414	24 in.	4	1 in.	D21	
8012	120 in.	2	1 in.	D22	
8014	120 in.	4	1 in.	D23	
8714	120 in.	4	1 in.	D24	

Config- uration	T.S. Length	No. of Cavities	Cavity Depth	Figure No.	Notes
8412	120 in.	2	1 in.	D25	
8414	120 in.	4	1 in.	D26	
0031c	24 in.	1	2 in.	D27	
0031o	24 in.	1	2 in.	D28	
0731c	24 in.	1	2 in.	D29	
0731o	24 in.	1	2 in.	D30	
1431c	24 in.	1	2 in.	D31	
1431o	24 in.	1	2 in.	D32	
8031c	120 in.	1	2 in.	D33	
8031o	120 in.	1	2 in.	D34	
8431c	120 in.	1	2 in.	D35	
8431o	120 in.	1	2 in.	D36	

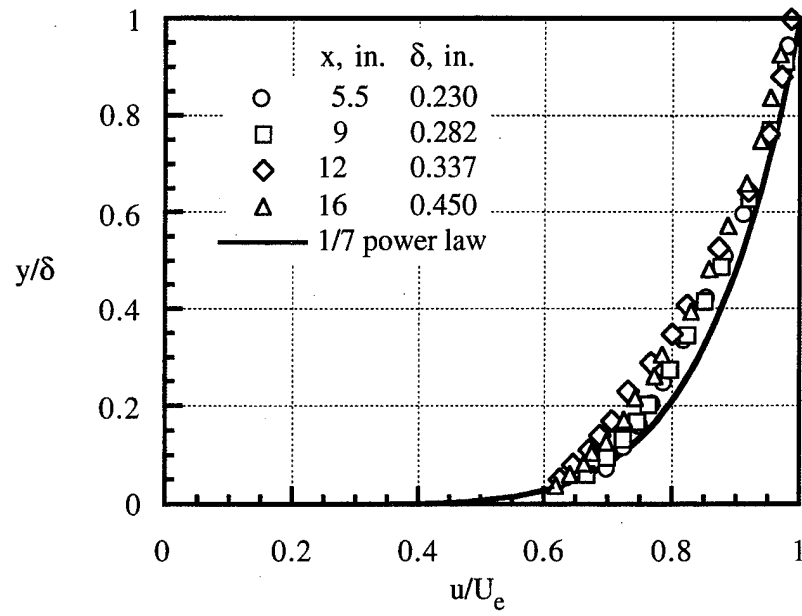


Figure D1. Boundary layer profiles for 0000 configuration.

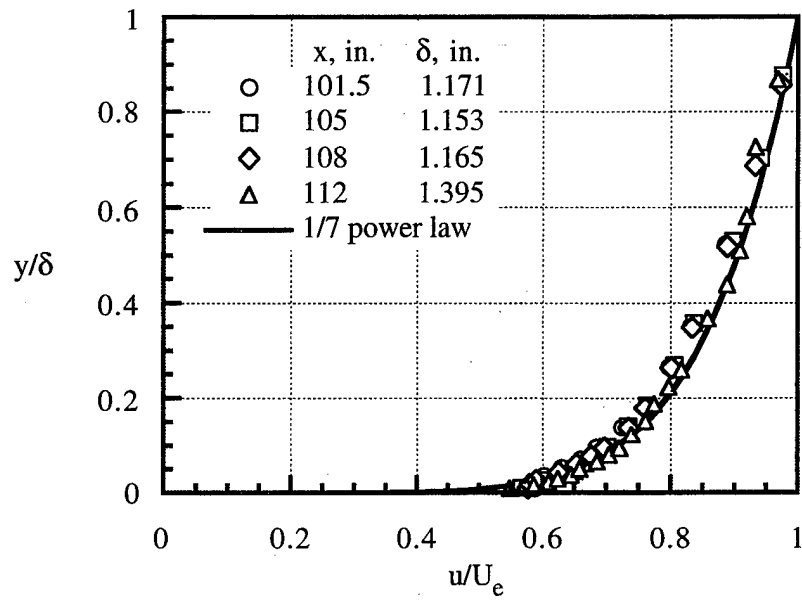


Figure D2. Boundary layer profiles for 8000 configuration.

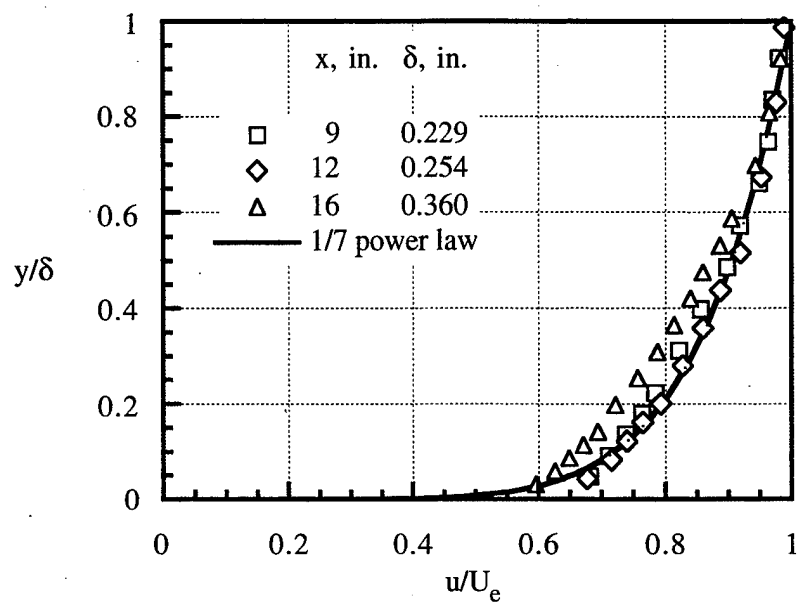


Figure D3. Boundary layer profiles for 0700 configuration.

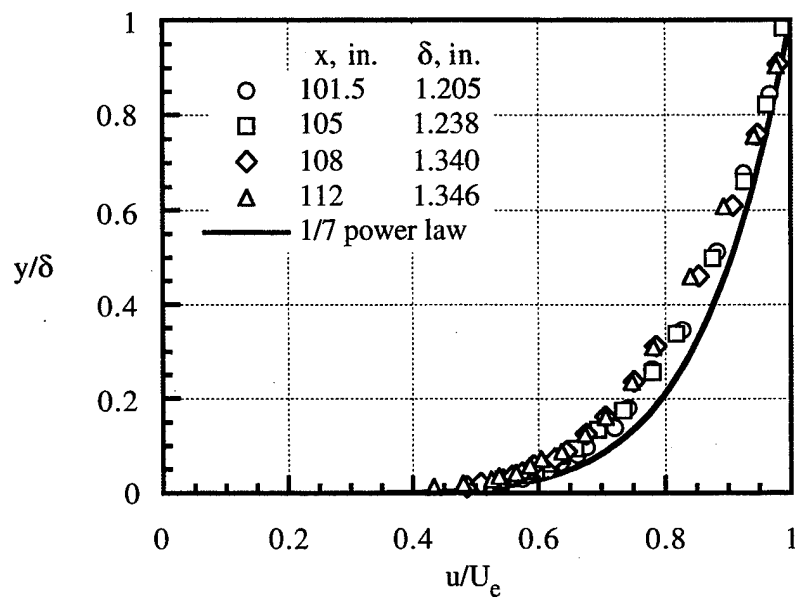


Figure D4. Boundary layer profiles for 8700 configuration.

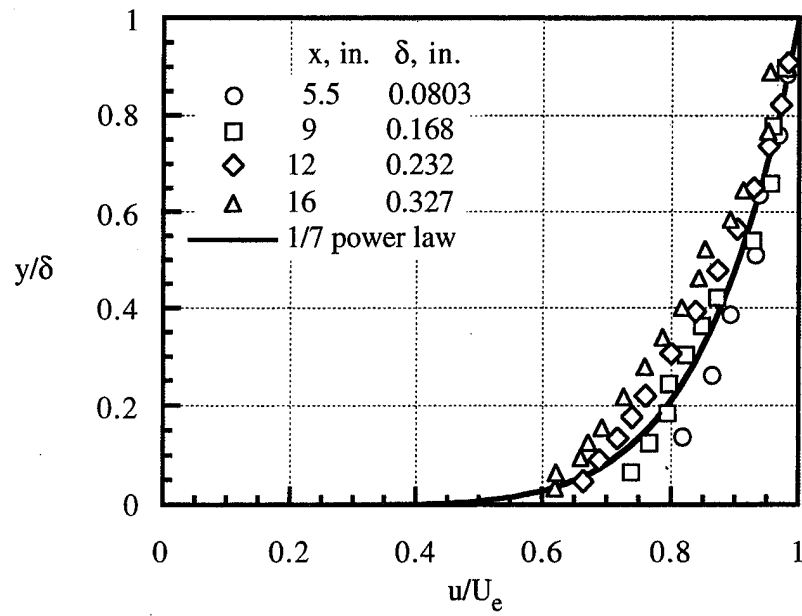


Figure D5. Boundary layer profiles for 1400 configuration.

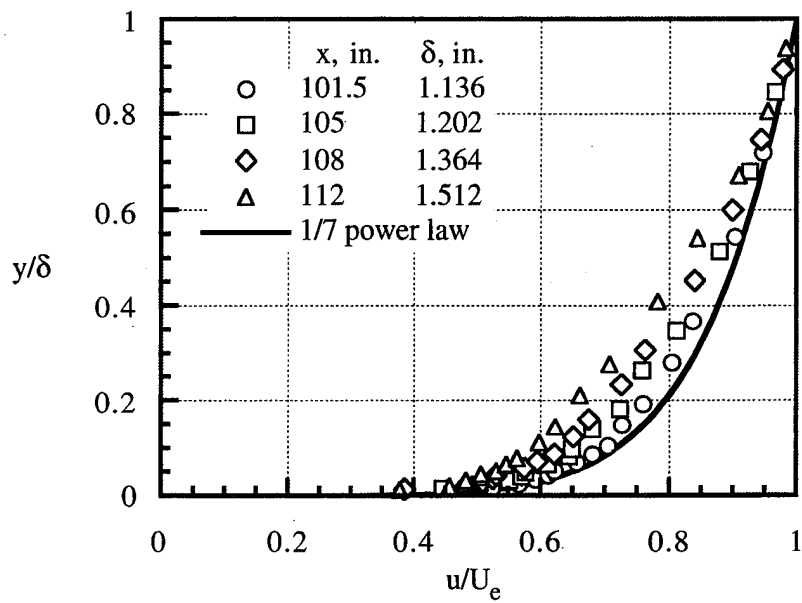


Figure D6. Boundary layer profiles for 8400 configuration.

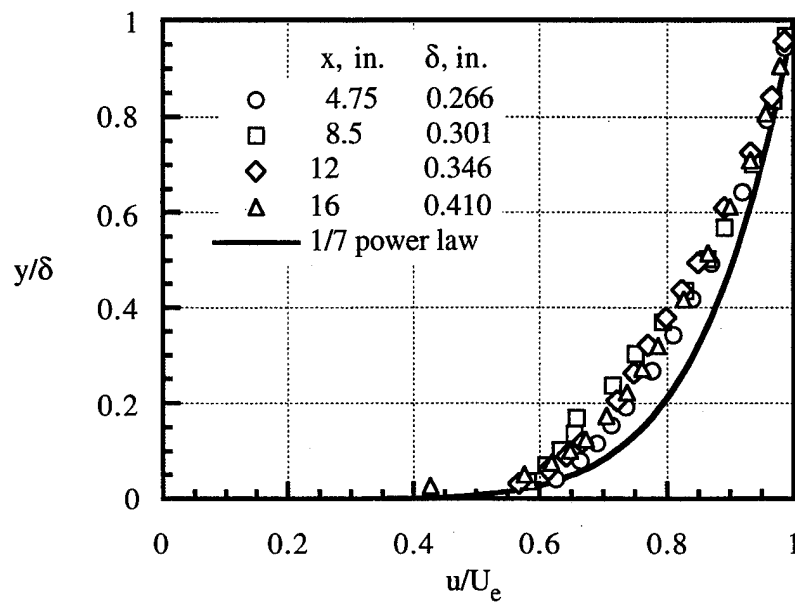


Figure D7. Boundary layer profiles for 0011 configuration.

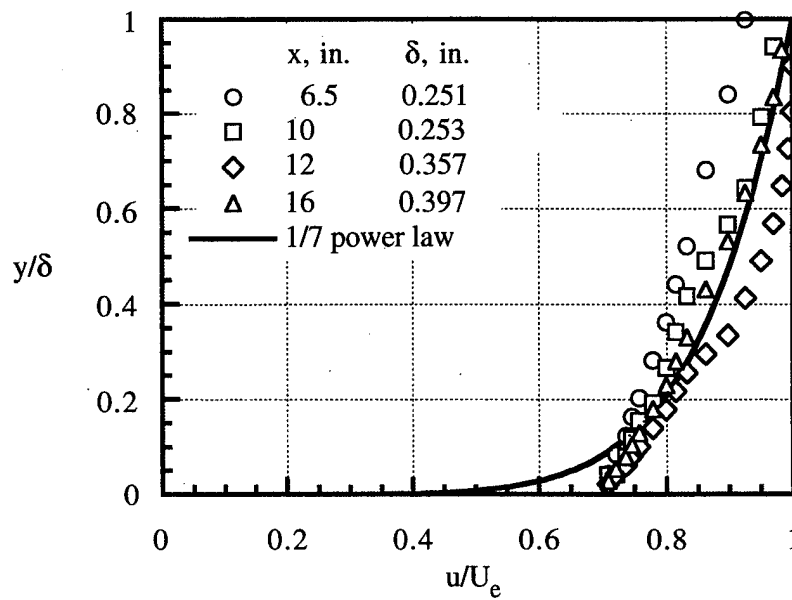


Figure D8. Boundary layer profiles for 0021 configuration.

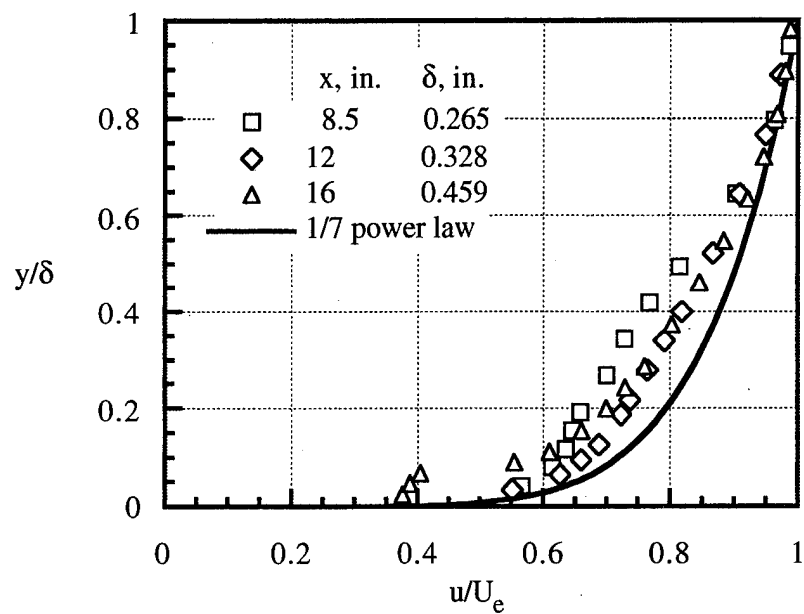


Figure D9. Boundary layer profiles for 0711 configuration.

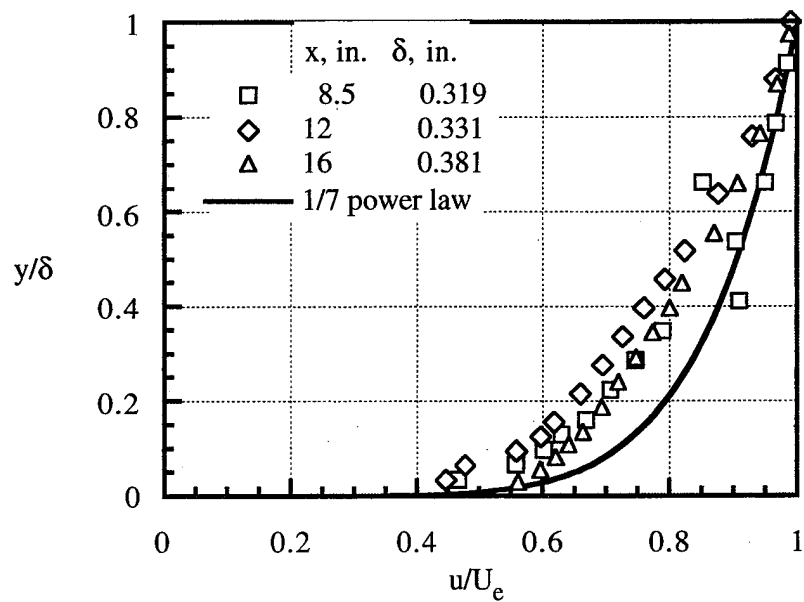


Figure D10. Boundary layer profiles for 1411 configuration.

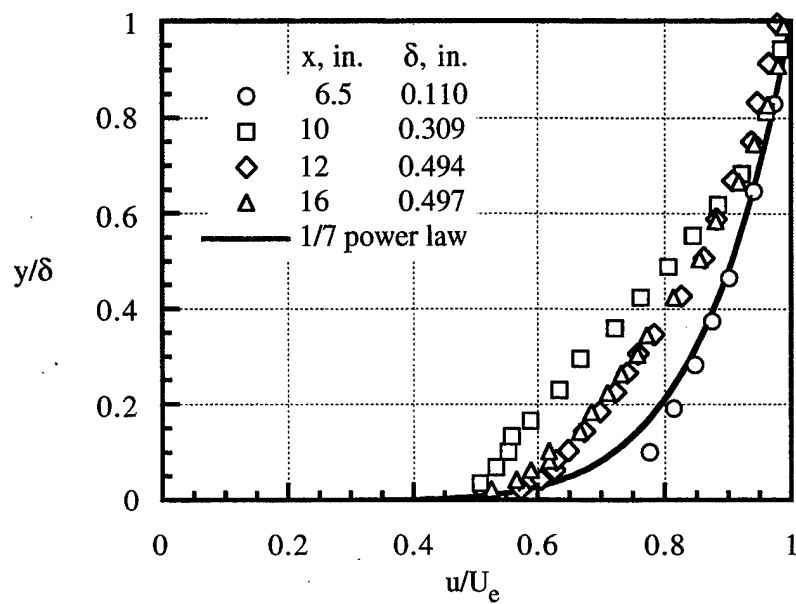


Figure D11. Boundary layer profiles for 1421 configuration.

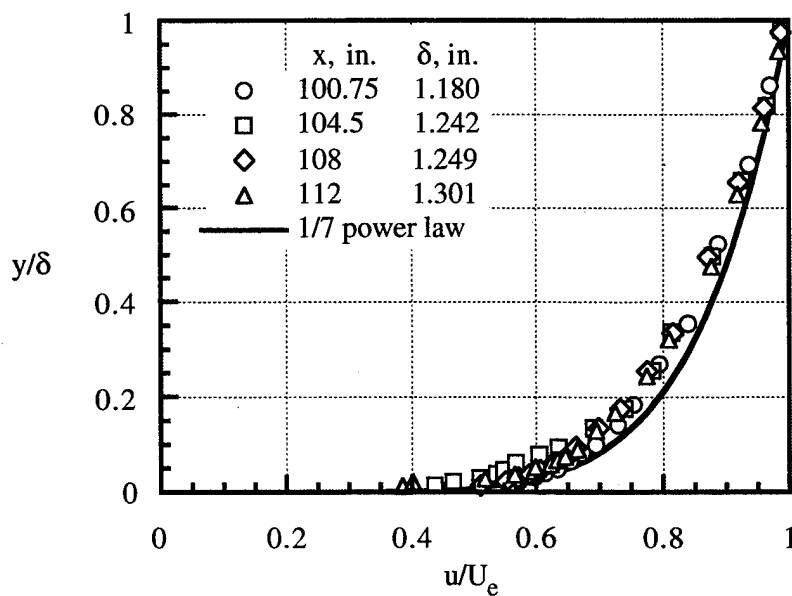


Figure D12. Boundary layer profiles for 8011 configuration.

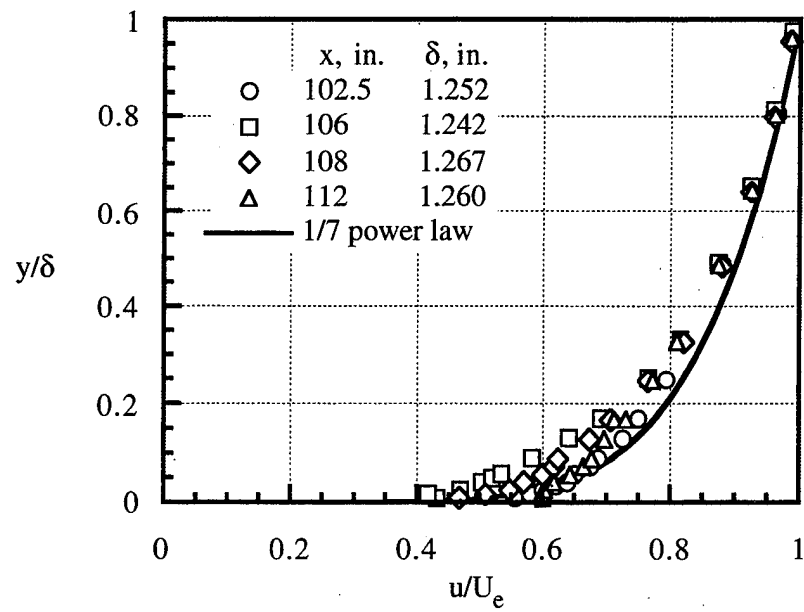


Figure D13. Boundary layer profiles for 8021 configuration.

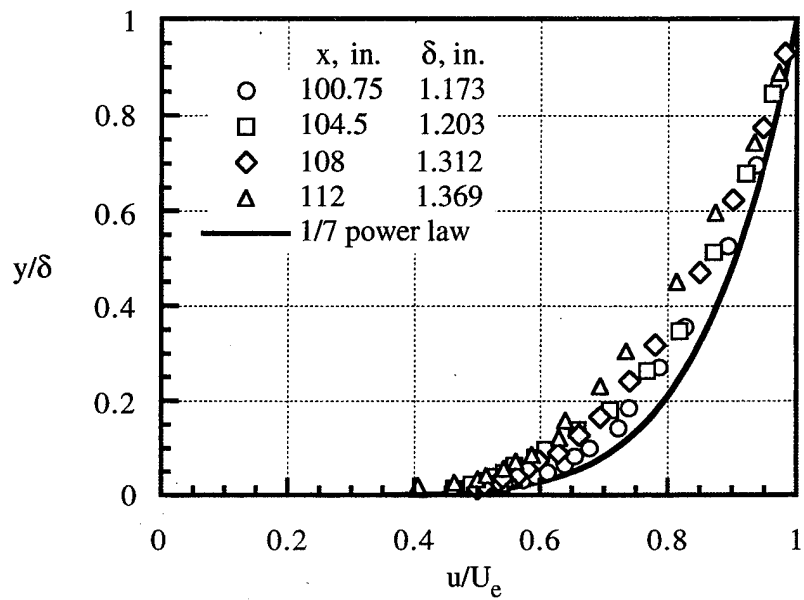


Figure D14. Boundary layer profiles for 8711 configuration.

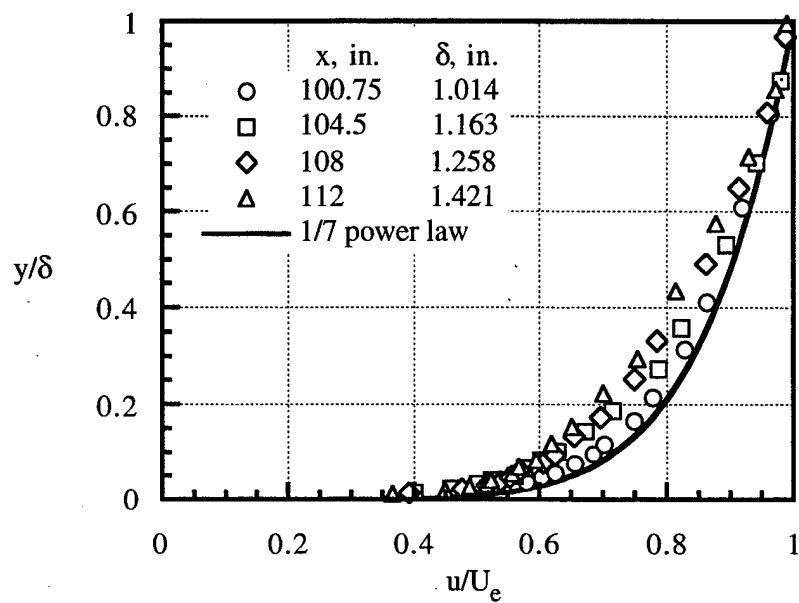


Figure D15. Boundary layer profiles for 8411 configuration.

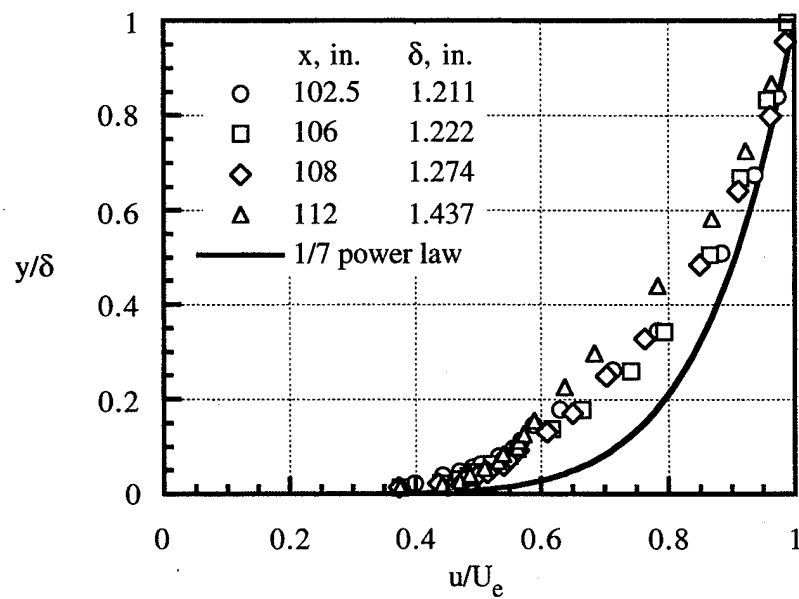


Figure D16. Boundary layer profiles for 8421 configuration.

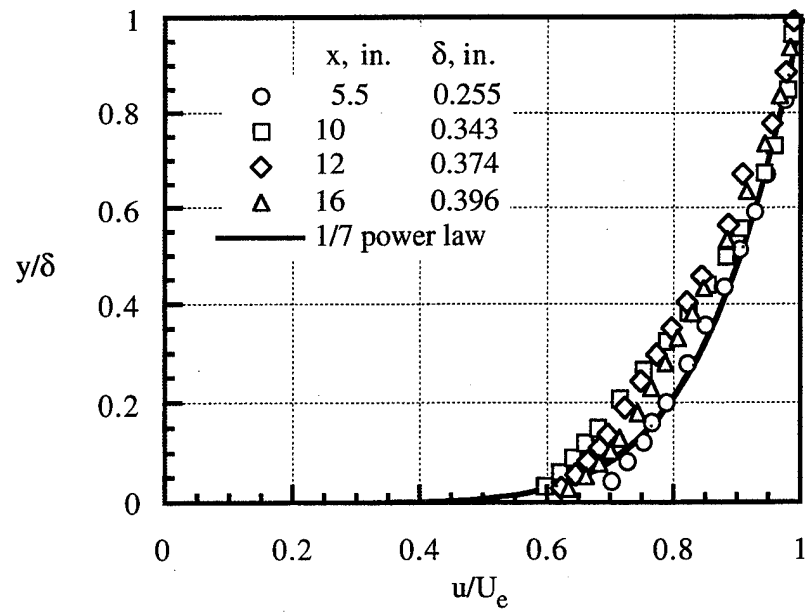


Figure D17. Boundary layer profiles for 0012 configuration.

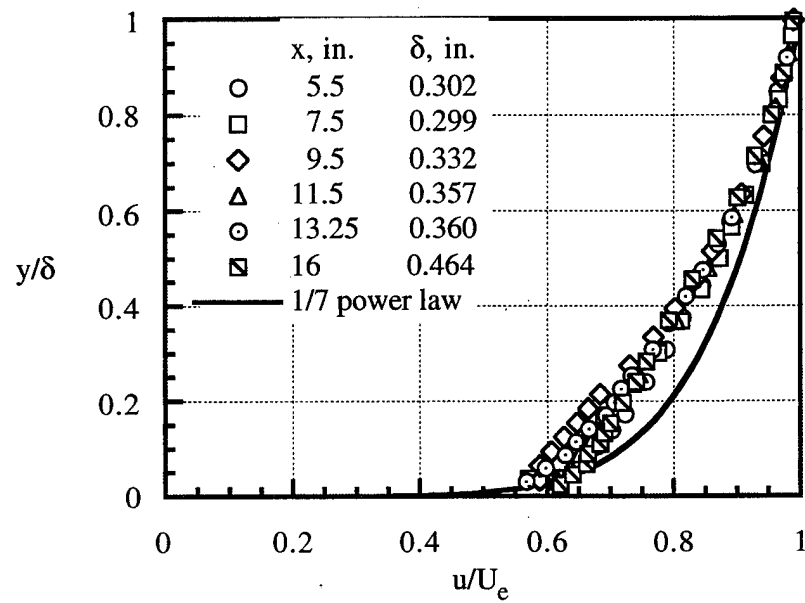


Figure D18. Boundary layer profiles for 0014 configuration.

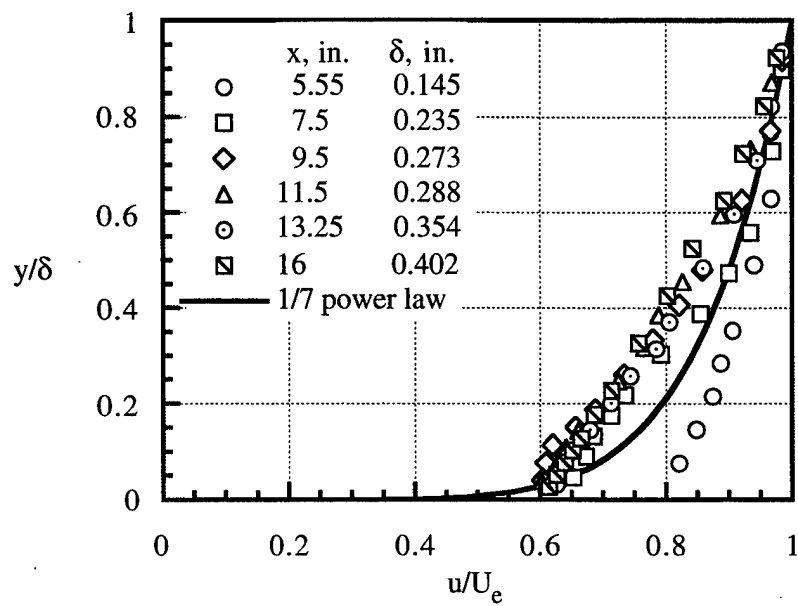


Figure D19. Boundary layer profiles for 0714 configuration.

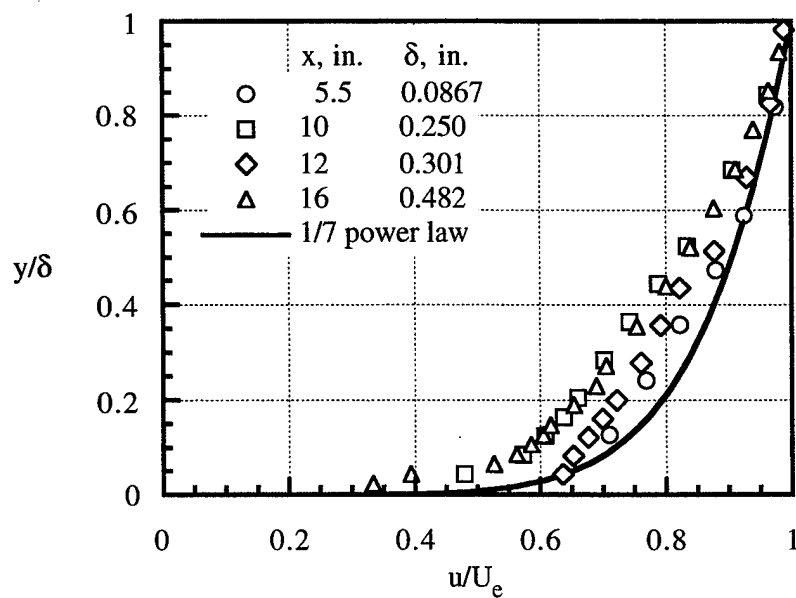


Figure D20. Boundary layer profiles for 1412 configuration.

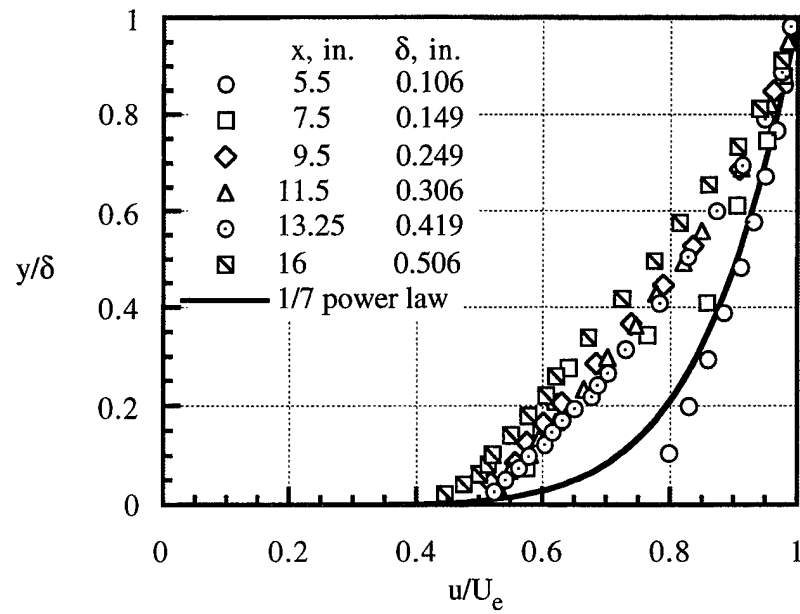


Figure D21. Boundary layer profiles for 1414 configuration.

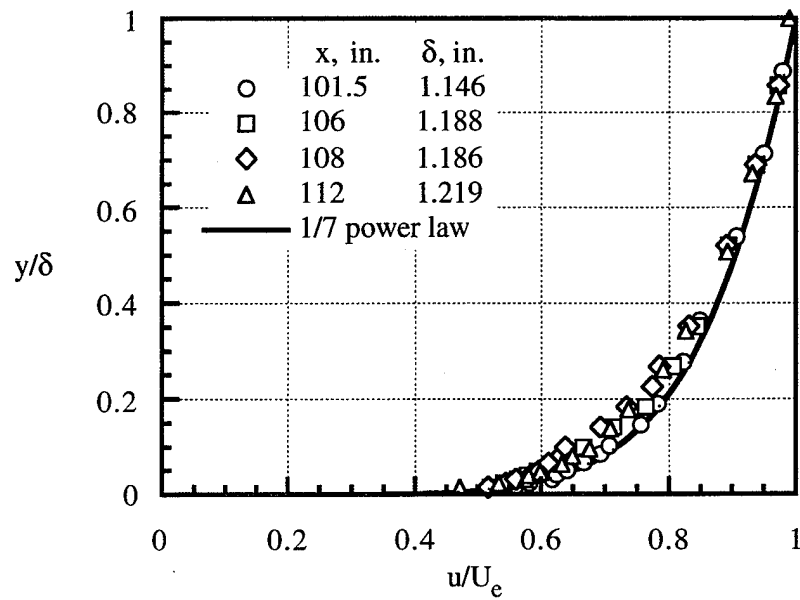


Figure D22. Boundary layer profiles for 8012 configuration.

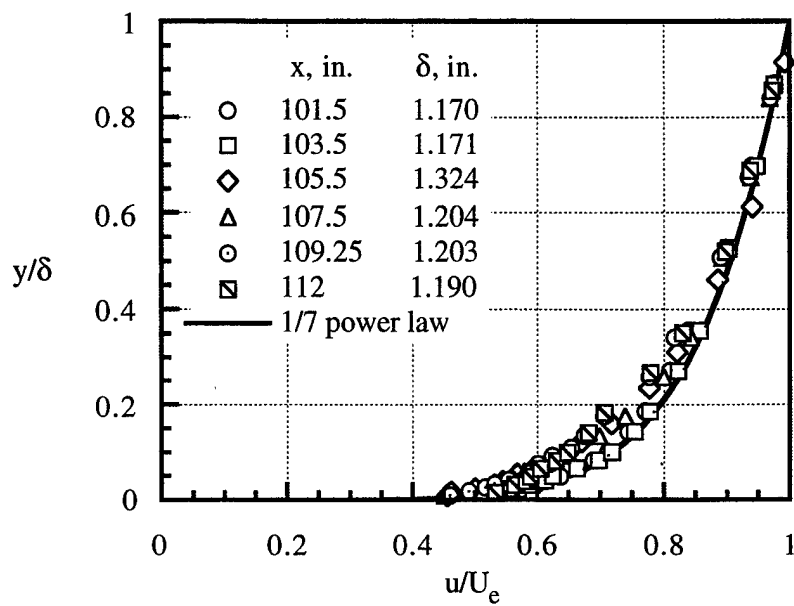


Figure D23. Boundary layer profiles for 8014 configuration.

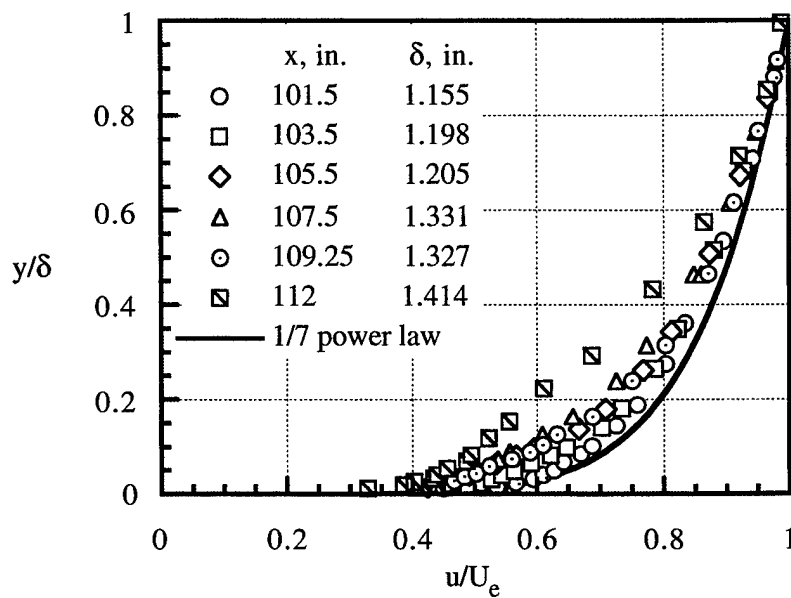


Figure D24. Boundary layer profiles for 8714 configuration.

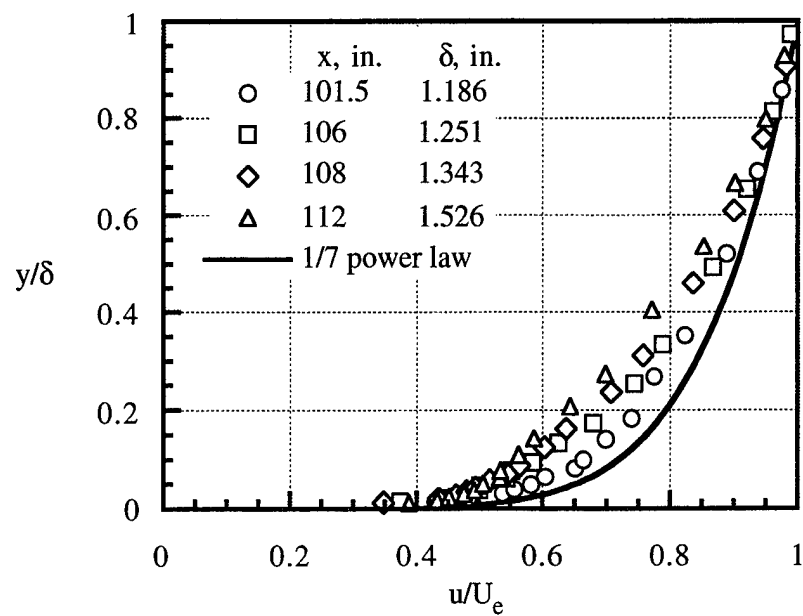


Figure D25. Boundary layer profiles for 8412 configuration.

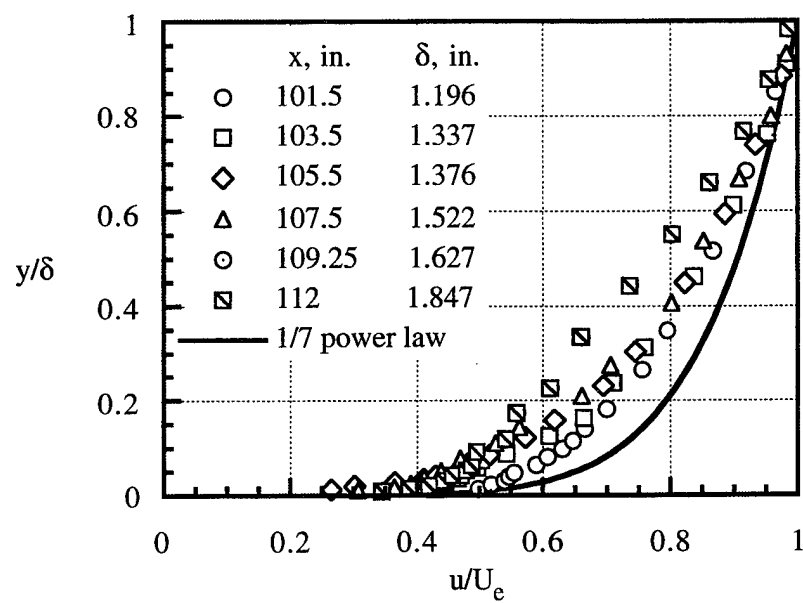


Figure D26. Boundary layer profiles for 8414 configuration.

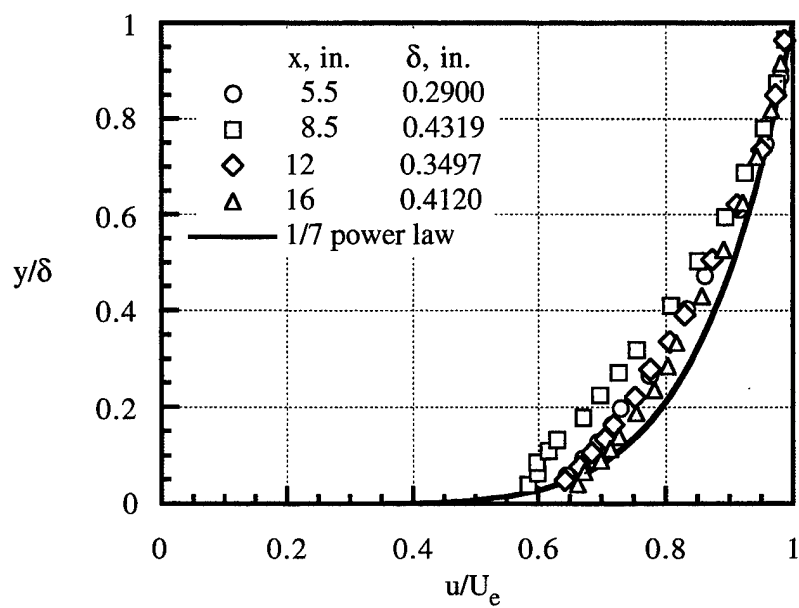


Figure D27. Boundary layer profiles for 0031c configuration.

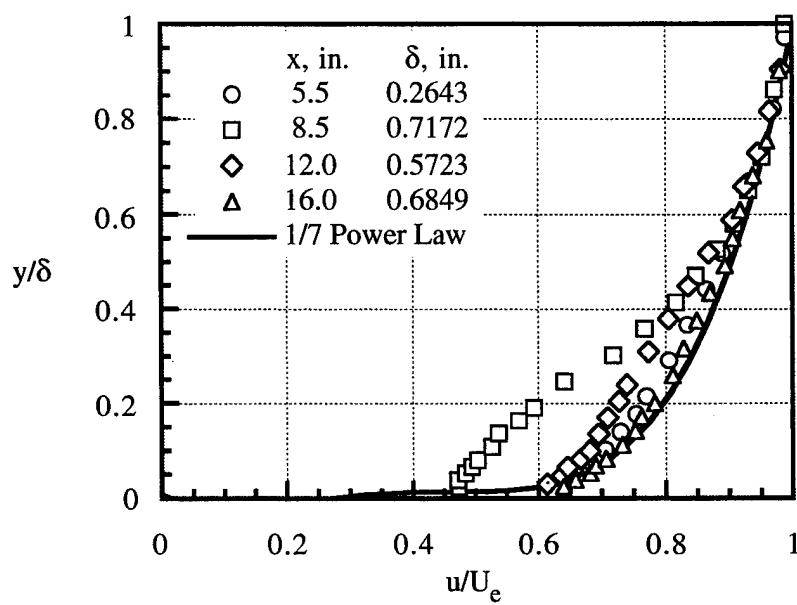


Figure D28. Boundary layer profiles for 0031o configuration.

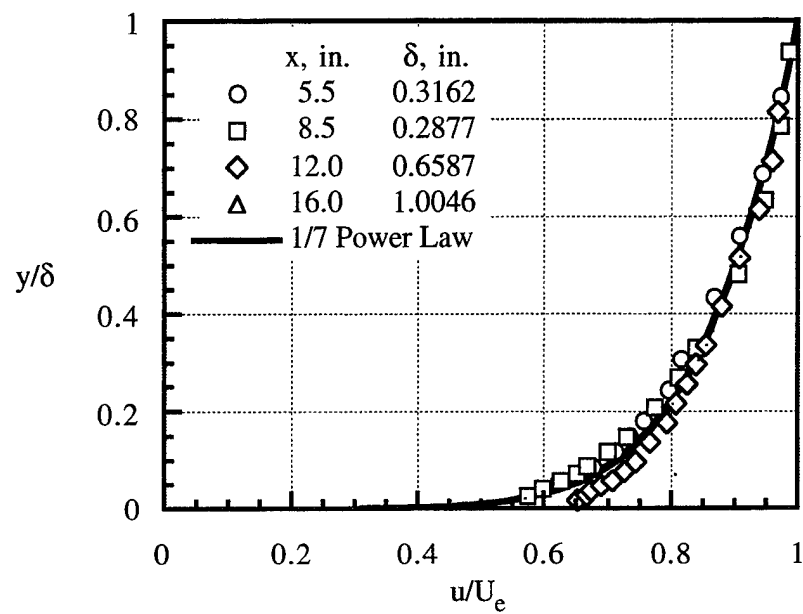


Figure D29. Boundary layer profiles for 0731c configuration.

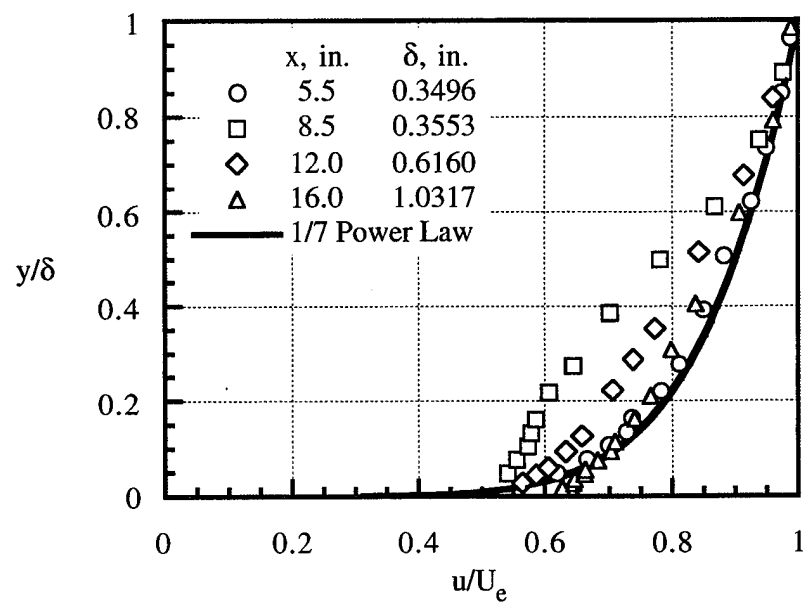


Figure D30. Boundary layer profiles for 0731o configuration.

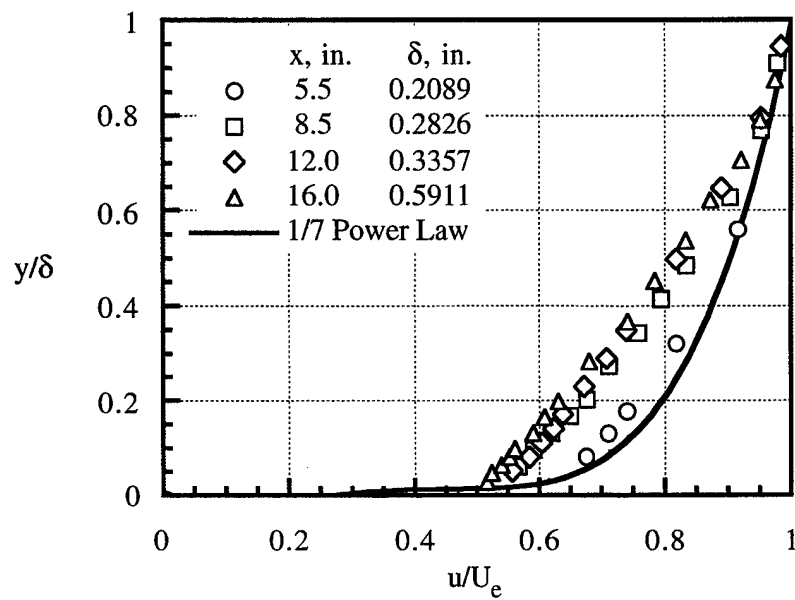


Figure D31. Boundary layer profiles for 1431c configuration.

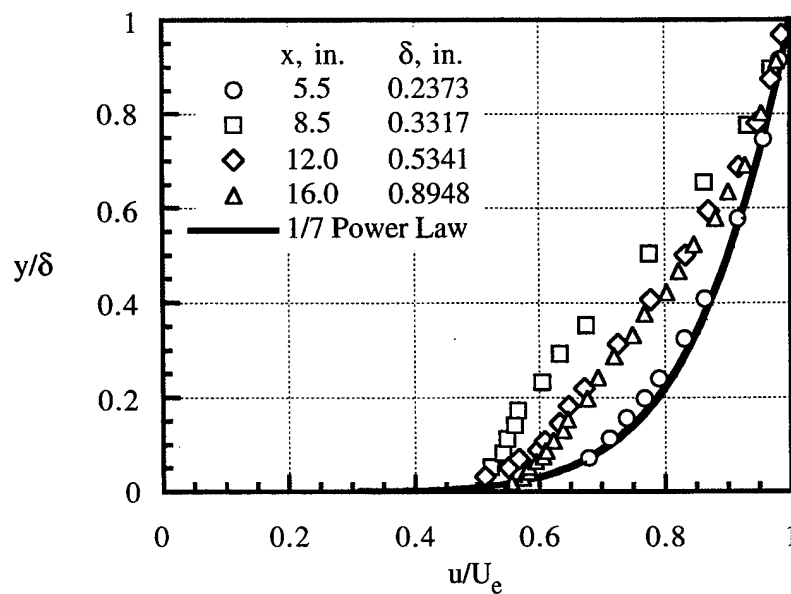


Figure D32. Boundary layer profiles for 1431o configuration.

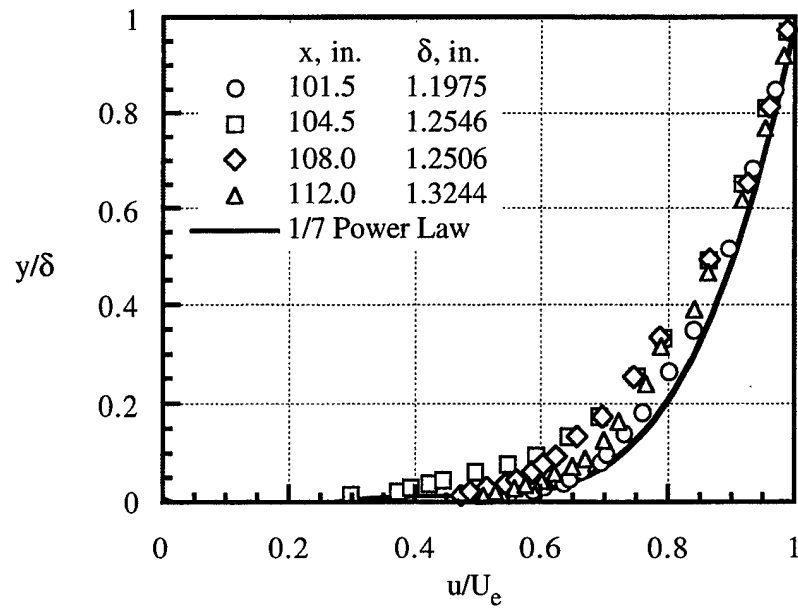


Figure D33. Boundary layer profiles for 8031c configuration.

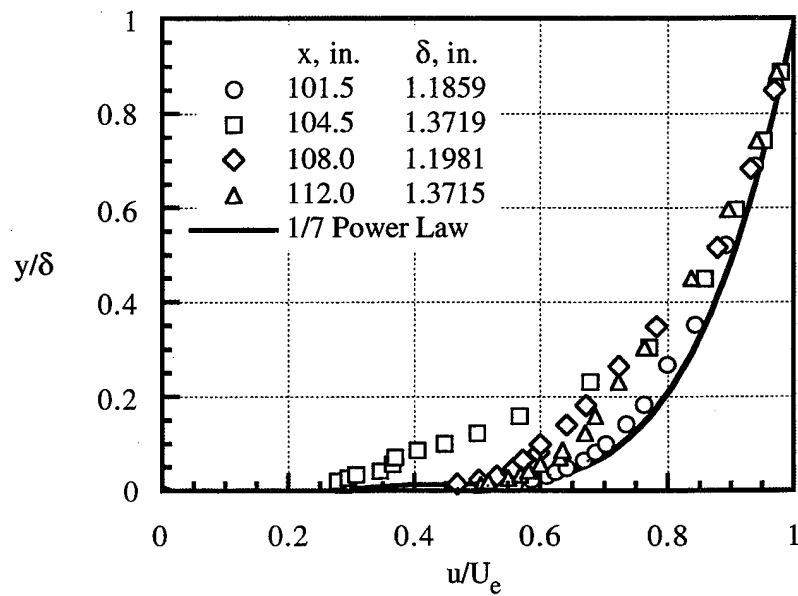


Figure D34. Boundary layer profiles for 8031o configuration.

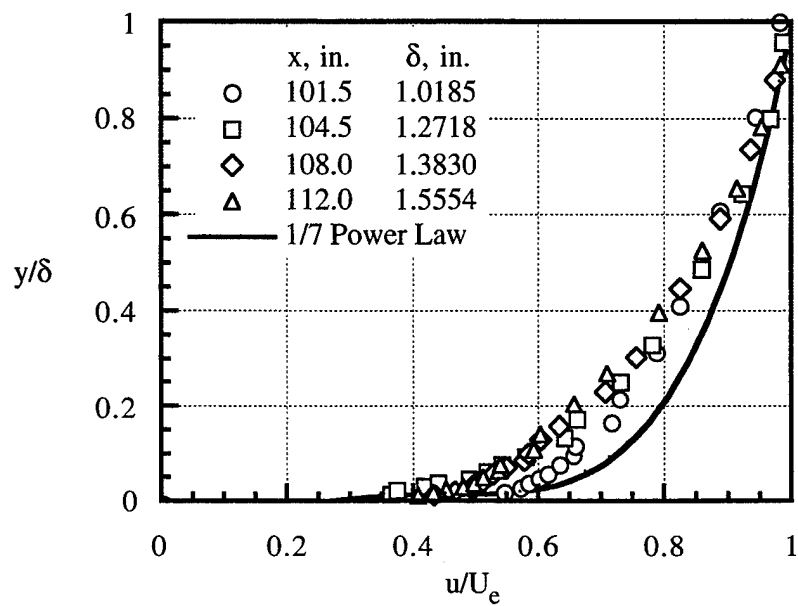


Figure D35. Boundary layer profiles for 8431c configuration.

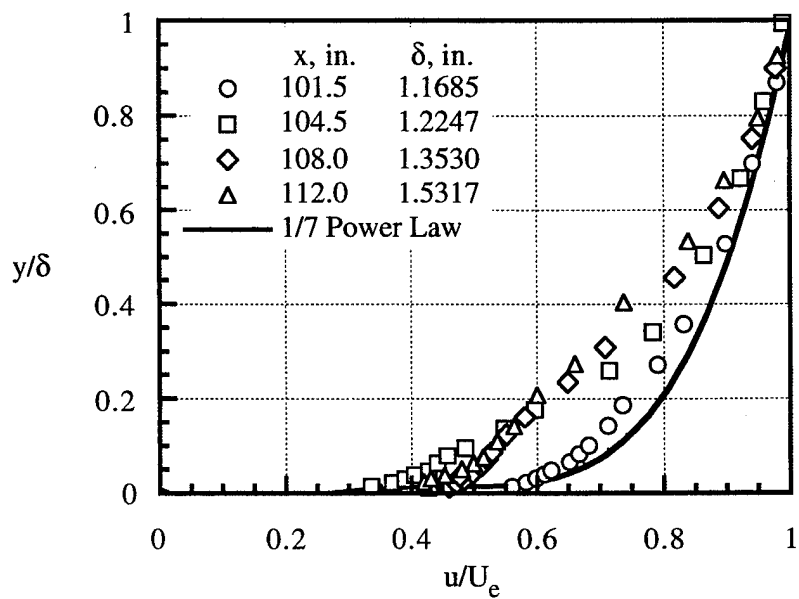


Figure D36. Boundary layer profiles for 8431o configuration.

INITIAL DISTRIBUTION LIST

1. Defense Technical Information Center 2
8725 John J. Kingman Rd., STE 0944
Ft. Belvoir, VA 22060-6218

2. Dudley Knox Library 2
Naval Postgraduate School
Monterey, California 93943-5000

3. Prof. Max F. Platzer 10
Code AA/PI
Dept. of Aeronautics and Astronautics
Naval Postgraduate School
699 Dyer Road
Monterey, CA 93943-5106

4. Gino Paglia 1
24634 Katherine Ct., Apt. 109
Harrison Twp., MI 48045

5. Prof. Nikos Mourtos 1
Department of Aerospace Engineering
San Jose State University
1 Washington Square
San Jose, CA 95192-0188

6. Prof. Dick Desautel 1
Department of Aerospace Engineering
San Jose State University
1 Washington Square
San Jose, CA 95192-0188

7. Dr. Larry E. Olson 1
Mail Stop 247-2
NASA Ames Research Center
Moffett Field, CA 94035-4003

8. Douglas Wardwell 1
Mail Stop 237-2
NASA Ames Research Center
Moffett Field, CA 94035-4003

9. Tim Naumowicz 1
 Mail Stop 247-2
 NASA Ames Research Center
 Moffett Field, CA 94035-4003

10. Tom Arledge 1
 Mail Stop 247-2
 NASA Ames Research Center
 Moffett Field, CA 94035-4003

11. Craig Hange 1
 Mail Stop 247-2
 NASA Ames Research Center
 Moffett Field, CA 94035-4003

12. Richard J. Margason 5
 12763 Lake Wildwood Drive
 Penn Valley, CA 95946

13. Robert VanDyken 1
 Code 473110D
 China Lake, CA 93555

14. Jerry Higman 1
 c/o Katsumasa Iso
 5-3 Hanazono-Cho
 Utsunomiya-Shi, Tochigi-Ken 302
 JAPAN

15. Daniel Lyons 1
 4303 Pinewood Ct.
 Morehead City, NC 28557

16. Prof. Raymond P. Shreeve 1
 Code AA/SF
 Dept. of Aeronautics and Astronautics
 Naval Postgraduate School
 699 Dyer Road - Room 137
 Monterey, CA 93943-5106

17. Dr. James A. Franklin 1
 Mail Stop 211-2
 NASA Ames Research Center
 Moffett Field, CA 94035-4003